ISSN: 2008-2010; eISSN: 2008-322X

JAN 2023
VOLUME 18
NUMBER 1

# JOURNAL OF OPHTHALMIC & VISION RESEARCH

Official Publication of the Ophthalmic Research Center
Affiliated to Shahid Beheshti University of Medical Sciences



KnowledgeE
enriching | engaging | empowering

Print ISSN 2008-2010;
E-ISSN 2008-322X

# JOURNAL OF OPHTHALMIC AND VISION RESEARCH

Official Publication of the Ophthalmic Research Center


## EDITOR-IN-CHIEF

Shahin Yazdani, *Iran*

## SENIOR EDITOR

Hamid Ahmadieh, *Iran*

## ASSOCIATE EDITORS

Touka Banaee, *USA*
Hamed Esfandiari, *USA*
Sepehr Feizi, *Iran*
Mohammad Haeri, *USA*
Mehdi Tavakoli, *USA*

## SECTION EDITORS

### Translational Eye Research

Henry J. Kaplan, *USA*
Barry E. Knox, *USA*

### Cornea and Ocular Surface

Alireza Baradaran-Rafii, *Iran*
Ali Djalilian, *USA*
Farid Karimian, Iran

### Lens and Cataract

Amir Faramarzi, *Iran*
Majid Moshirfar, *USA*

### Glaucoma

Naveed Nilforushan, *Iran*
Kouros Nouri-Mahdavi, *USA*

### Retina and Retinal cell Biology

J. Fernando Arevalo, *USA*
Mohammad Riazi-Esfahani, *Iran*
William J. Brunken, *USA*

### Uveitis

Carl P Herbort, *Switzerland*
Masoud Soheilian, *Iran*

### Pediatric Ophthalmology and Strabismus

Abbas Bagheri, *Iran*
Cameron F. Parsa, *France*
David I. Silbert, *USA*

### Neuro-Ophthalmology

Rod Foroozan, *USA*
Mohammad Pakravan, *Iran*

### Ocular Oncology

Arman Mashayekhi, *USA*
Mozhgan Rezaei Kanavi, *Iran*

### Ophthalmic Plastic & Reconstructive Surgery

Mohsen Bahmani Kashkouli, *Iran*
Bita Esmaeli, *USA*
David H. Verity, *UK*

### Ophthalmic Epidemiology

Akbar Fotouhi, *Iran*
Marzieh Katibeh, *Iran*
Mehdi Yaseri, *Iran*

### Controversies and Challenging Cases

Alireza Ramezani, *Iran*
Mohammad Reza Razeghinejad, *Iran*

### Imaging and Surgical Techniques

Khalil Ghasemi Falavarjani, *Iran*
Azadeh Doozandeh, *Iran*
Siamak Zarei-Ghanavati, *Iran*

### Photo Essay

Maryam Aletaha, *Iran*
Siamak Moradian, *Iran*

### News

Ramin Daneshvar, *Iran*
Mohammad Hosein Nowroozzadeh, *Iran*
Mehran Zarei-Ghanavati, *Iran*

## EDITORIAL BOARD

Heydar Amini, *Iran*
James Bainbridge, *UK*
Reza Dana, *USA*
Elahe Elahi, *Iran*
Ali Hafezi-Moghadam, *USA*
Pedram Hamrah, *USA*
Andrew J. W. Huang, *USA*
Martine J. Jager, *The Netherlands*
Mohammad-Ali Javadi, *Iran*
Jost B. Jonas, *Germany*
Ahmad Kheirkhah, *USA*
Timothy Lai, *China*
Alireza Lashay, *Iran*
Ian MacDonald, *Canada*
Jodhbir S. Mehta, *Singapore*
Mehdi Modarres-Zadeh, *Iran*
Yadollah Omidi, *Iran*
Mohammad-Mehdi Parvaresh, *Iran*
Zhaleh Rajavi, *Iran*
Virender S. Sangwan, *India*
Nader Sheibani, *USA*
Zahra-Soheila Soheili, *Iran*
Ramin Tadayoni, *France*
Ilkhnur Tugal-Tutkun, *Turkey*

## ADVISORY COMMITTEE

Tin Aung, *Singapore*
Hossein Baharvand, *Iran*
Ahmad-Reza Dehpour, *Iran*
Ingrid Kreissig, *Germany*
Phillip Luthert, *UK*
Neil Miller, *USA*
Gholam A. Peyman, *USA*
Jose Sahel, *France*
Mansoor Sarfarazi, *USA*
Khalid Tabbara, *Saudi Arabia*
Scheffer Tseng, *USA*
Robert Weinreb, *USA*
Marco Zarbin, *USA*

### Manager

Mohammad Ali Javadi

### Executive Editor

Sareh Safi

### Co-Executive Editor

Hamideh Sabbaghi

### Editorial Staff

Bahar Safdari

Print ISSN 2008-2010;
E-ISSN 2008-322X

JOURNAL OF
OPHTHALMIC AND VISION RESEARCH

Official Publication of the Ophthalmic Research Center

# General Information

**The journal**

The Journal of Ophthalmic and Vision Research is a peer-reviewed, open-access journal published quarterly on behalf of the Ophthalmic Research Center, Shahid Beheshti University of Medical Sciences with the mission to disseminate information, viewpoints and questions about eye diseases, research, clinical and laboratory science, and education. The journal aims to advance the science, technology, ethics and art of ophthalmology through research and education worldwide. The scope of the journal is intended to include not only clinical ophthalmology, but related disciplines in basic sciences that contribute to the knowledge and science of vision.

**Abstracting and indexing information**

The journal is registered with the following abstracting partners:
Baidu Scholar, CNKI (China National Knowledge Infrastructure), EBSCO Publishing's Electronic Databases, Exlibris - Primo Central, Google Scholar, Hinari, Infotrieve, National Science Library, ProQuest, TdNet.
The journal is indexed with, or included in, the following: DOAJ, Emerging Sources Citation Index, Index Copernicus, Index Medicus for the Eastern Mediterranean Region (IMEMR), PubMed Central, Scimago Journal Ranking, SCOPUS, Web of Science.

**Information for Authors**

There are no page charges for submissions to the journal. Please check https://knepublishing.com/index.php/JOVR/authorguidelines for details. All manuscripts must be submitted online at https://knepublishing.com/index.php/JOVR/about/submissions

**Advertising policies**

The journal accepts display and classified advertising. Frequency discounts and special positions are available. Inquiries about advertising should be sent to Knowledge E. The journal reserves the right to reject any advertisement considered unsuitable according to the set policies of the journal. The appearance of advertising or product information in the various sections in the journal does not constitute an endorsement or approval by the journal and/or its publisher of the quality or value of the said product or of claims made for it by its manufacturer.

**Copyright**

The entire contents of the Journal of Ophthalmic and Vision Research are protected under Indian and international copyrights. The Journal, however, grants to all users a free, irrevocable, worldwide, perpetual right of access to, and a license to copy, use, distribute, perform and display the work publicly and to make and distribute derivative works in any digital medium for any reasonable non-commercial purpose, subject to proper attribution of authorship and ownership of the rights. The journal also grants the right to make small numbers of printed copies for their personal non-commercial use.

**Permissions**

For information on how to request permissions to reproduce articles/information from this journal, please visit https://knepublishing.com/index.php/JOVR/authorguidelines

**Disclaimer**

The information and opinions presented in the Journal reflect the views of the authors and not of the Journal or its Editorial Board or the Society of the Publisher. Publication does not constitute endorsement by the journal. Neither the Journal of Ophthalmic and Vision Research nor its publishers nor anyone else involved in creating, producing or delivering the Journal of Ophthalmic and Vision Research or the materials contained therein, assumes any liability or responsibility for the accuracy, completeness, or usefulness of any information provided in the Journal of Ophthalmic and Vision Research, nor shall they be liable for any direct, indirect, incidental, special, consequential or punitive damages arising out of the use of the Journal of Ophthalmic and Vision Research. The Journal of Ophthalmic and Vision Research, nor its publishers, nor any other party involved in the preparation of material contained in the Journal of Ophthalmic and Vision Research represents or warrants that the information contained herein is in every respect accurate or complete, and they are not responsible for any errors or omissions or for the results obtained from the use of such material. Readers are encouraged to confirm the information contained herein with other sources.

**Addresses**

Editorial Office
Journal of Ophthalmic and Vision Research
Ophthalmic Research Center, #23, Paidarfard St., Boostan 9 St., Pasdaran Ave., Tehran, Iran
Postal code: 1666673111
Phone: +98 21 2277 0957
Fax: +98 21 2259 0607
E-mail: labbafi@gmail.com & jovrjournal@gmail.com
Website: https://knepublishing.com/index.php/JOVR

**Published by**

Knowledge E Office 4401–02 ,4404
Jumeirah Bay X2 Tower
Jumeirah Lakes Towers (JLT)
P.O. Box 488239
Dubai, UAE
Website: www.knowledgee.com

Print ISSN 2008-2010;
E-ISSN 2008-322X

JOURNAL OF
OPHTHALMIC AND VISION RESEARCH

Official Publication of the Ophthalmic Research Center

VOLUME 18, ISSUE 1, JANUARY 2023

# Contents

## EDITORIAL



## ORIGINAL ARTICLES

# Contents Contd...

Editorial

# Application of Artificial Intelligence to Improve Imaging in Ophthalmology

**Mark Christopher, PhD**

*Hamilton Glaucoma Center, Viterbi Family Department of Ophthalmology and Shiley Eye Institute, University of California San Diego, California, USA*

*J Ophthalmic Vis Res* 2023; 18 (1): 1–2

Over the past decade, the literature has witnessed major advances in the field of artificial intelligence (AI). Many of these developments have focused on applying specific AI approaches, including deep learning and convolutional neural networks (CNNs), to image datasets which have greatly improved the accuracy of general image recognition and computer vision tasks.[1] There has also been great interest and progress in adapting these methods for use on medical imaging data to detect disease, assess prognosis, and improve patient care.[2] With respect to ophthalmic images specifically, AI models have been developed for diabetic retinopathy, macular degeneration, glaucoma, and even prediction of systemic health indicators.[3] The past few years have even seen regulatory approval of autonomous AI-based systems to detect diabetic retinopathy in the US.[4, 5]

In the current issue of *Journal of Ophthalmic and Vision Research*, Razaghi et al report the use of a deep learning approach to reduce errors in optical coherence tomography (OCT) retinal nerve fiber layer (RNFL) segmentation.[6] It is known that using current standard device software, segmentation errors can be a common event.[7, 8] Errors in the resulting structural and thickness measurements may provide incorrect information on which diagnostic and treatment decisions could be based. Methods that provide accurate and robust segmentation methods are critical for ensuring that clinical decisions are based on correct information.

A number of investigators have approached OCT segmentation using deep learning techniques.[9–11] These reports have typically used manual segmentation by experts on OCT data to train CNNs designed specifically for image segmentation. Based on their intended use, these algorithms can be trained to segment individual retinal layers, optic nerve head structures, or disease markers, or be programmed to perform simultaneous segmentation of all these parameters. These techniques exhibit variations in terms of modifications of the CNN architecture, training approaches, and pre-/post-processing procedures. Razaghi et al focused on providing accurate and reliable RNFL segmentation. To achieve this, they adopted a commonly used fully convolutional CNN approach (U-Net).[12] They then applied post-processing steps to help clean up the segmentation and provide accurate estimates of mean RNFL thickness. When applied to their test

**Correspondence to:**

Mark Christopher, PhD. Hamilton Glaucoma Center, Viterbi Family Department of Ophthalmology and Shiley Eye Institute, University of California San Diego, 9415 Campus Point Dr La Jolla, California 92093, USA.
E-mail: mac157@health.ucsd.edu

Received: 29-12-2022 Accepted: 05-01-2023

Access this article online

**Website:** https://knepublishing.com/index.php/JOVR

**DOI:** 10.18502/jovr.v18i1.12719

This is an open access article distributed under the Creative Commons Attribution License, which permits unrestricted use, distribution, and reproduction in any medium, provided the original work is properly cited.

**How to cite this article:** Christopher M. Application of Artificial Intelligence to Improve Imaging in Ophthalmology . J Ophthalmic Vis Res 2023;18:1–2.

set, they have reported performances comparable to previous studies in terms of DICE (a commonly used metric for image segmentation) and even exceeding prior results in terms of $R^2$when comparing mean RNFL thickness to manual segmentation-based RNFL thickness values.

In summary, AI is already demonstrating a massive impact on ophthalmology (and medicine is general) that will only continue to grow. AI-based tools have the potential to impact and hopefully improve all aspects of patient care. It is critical, however, that clinical integration of these tools be performed responsibly. This includes emphasis on thorough evaluation of AI models on diverse datasets and mindfulness of their limitations.

## Financial Support and Sponsorship

None.

## Conflicts of Interest

There are no conflicts of interest.

## *REFERENCES*

1. Emmert-Streib F, Yang Z, Feng H, Tripathi S, Dehmer M. An introductory review of deep learning for prediction models with big data. *Front Artif Intell* 2020;3:4.
2. Aggarwal R, Sounderajah V, Martin G, Ting DSW, Karthikesalingam A, King D, et al. Diagnostic accuracy of deep learning in medical imaging: A systematic review and meta-analysis. *NPJ Digit Med* 2021;4:65.
3. Ting DSW, Pasquale LR, Peng L, Campbell JP, Lee AY, Raman R,et al. Artificial intelligence and deep learning in ophthalmology. *Br J Ophthalmol* 2019;103:167–175.
4. FDA. FDA permits marketing of artificial intelligence-based device to detect ceretain diabetes-related eye problems. Accessed January 10, 2022. https://www.fda.gov/news-events/press-announcements/fda-permits-marketing-artificial-intelligence-based-device-detect-certain-diabetes-related-eye
5. Lee KJ. Autonomous diabetic retinopathy screening system gains FDA approval. Accessed December 20, 2022. https://www.aao.org/headline/autonomous-diabetic-retinopathy-screening-system-g
6. Razaghi G, Aghsaei M, Hejazi M. Correction of retinal nerve fiber layer thickness determination on spectral-domain optical coherence tomographic images using U-net architecture. *J Ophthalmic Vis Res* 2023;18:1–11.
7. Mansberger SL, Menda SA, Fortune BA, Gardiner SK, Demirel S. Automated segmentation errors when using optical coherence tomography to measure retinal nerve fiber layer thickness in glaucoma. *Am J Ophthalmol* 2017;174:1–8.
8. Miki A, Kumoi M, Usui S, Endo T, Kawashima R, Morimoto T, et al. Prevalence and associated factors of segmentation errors in the peripapillary retinal nerve fiber layer and macular ganglion cell complex in spectral-domain optical coherence tomography images. *J Glaucoma* 2017;26:995–1000.
9. Devalla SK, Chin KS, Mari JM, Tun TA, Strouthidis NG, Aung T, et al. A deep learning approach to digitally stain optical coherence tomography images of the optic nerve head. *Invest Ophthalmol Vis Sci* 2018;59:63–74.
10. Wilson M, Chopra R, Wilson MZ, Cooper C, MacWilliams P, Liu Y, et al. Validation and clinical applicability of whole-volume automated segmentation of optical coherence tomography in retinal disease using deep learning. *JAMA Ophthalmol* 2021;139:964–973.
11. Marques R, Andrade De Jesus D, Barbosa-Breda J, Eijgen JV, Stalmans I, Walsum T, et al. Automatic segmentation of the optic nerve head region in optical coherence tomography: A methodological review. *Comput Methods Programs Biomed* 2022;220:106801.
12. Ronneberger O, Fischer P, Brox T. U-net: Convolutional networks for biomedical image segmentation. 2015:arXiv:1505.04597. https://ui.adsabs.harvard.edu/abs/2015arXiv150504597R

Original Article

# Safety and Precision of Two Different Flap-morphologies Created During Low Energy Femtosecond Laser-assisted LASIK

**Johannes Steinberg[1,2,3], MD; Juliane Mehlan[1], MD; Bulat Mudarisov[1], MD; Toam Katz[1,3], MD; Andreas Frings[4,5], MD; Vasyl Druchkiv[1,2], MS; Stephan J Linke[1,2,3], MD**

[1]*Department of Ophthalmology, University Hospital Hamburg-Eppendorf, Hamburg, Germany*
[2]*Hamburg Vision Clinic, Hamburg, Germany*
[3]*CareVision GmbH, Hamburg, Germany*
[4]*Univ.-Augenklinik Düsseldorf, Düsseldorf, Germany*
[5]*Augenarztpraxis PD Dr. Frings, Nürnberg, Germany*

**ORCID:**

*Johannes Steinberg: https://orcid.org/0000-0002-3091-9347*

## Abstract

**Purpose:** Currently, two major principles exist to create LASIK flaps: firstly, a strictly horizontal (2D) cut similar to the microkeratome-cut and secondly an angled cut with a "step-like" edge (3D). The strictly horizontal (2D) cut method can be performed using apparatus such as the low-energy FEMTO LDV Z8 laser and its predecessors which are specific to this type. Alternatively, the low-energy FEMTO LDV Z8 laser's 3D flap design creates an interlocking flap-interface surface which potentially contributes toward flap stability. In addition, the FEMTO LDV Z8 offers flap-position adjustments after docking (before flap-creation). The current study analyzed precision, safety, efficacy, as well as patient self-reported pain and comfort levels after applying two different types of LASIK flap morphologies which were created with a low-energy, high-frequency femtosecond (fs) laser device.

**Methods:** A prospective, interventional, randomized, contralateral eye, single-center comparison study was conducted from November 2019 to March 2020 at the Hamburg vision clinic/ zentrumsehstärke, Hamburg, Germany. Eleven patients and 22 eyes received low-energy fs LASIK treatment for myopia or myopic astigmatism in both eyes. Before the treatment, the eyes were randomized (one eye was treated with the 2D, the other eye with the 3D method).

**Results:** The mean central flap thickness one month after surgery was 110.7 ± 1.6 µm (2D) and 111.2 ± 1.7 µm (3D); $P$ = 0.365 (2D vs 3D). Flap thickness measured at 13 different points resulted in no statistically significant differences between any of the measurement points within/between both groups; demonstrating good planarity of the flap was achieved using both methods. Despite not being statistically significant, the surgeons recognized an increase in the presence of an opaque bubble layer in the 3D flap eyes during surgery and some patients reported higher, yet not statistically significant, pain scores in the 3D flap eyes during the first hours after the treatment. Overall, safety- and efficacy indices were 1.03 and 1.03, respectively.

**Conclusion:** In this prospective, randomized, contralateral eye study, the low-energy fs laser yielded predictable lamellar flap thicknesses and geometry at one-month follow-up. Based on these results, efficacy and safety of the corresponding laser application, that is, 2D vs 3D, are equivalent.

**Keywords:** Cornea; Femtosecond Laser; Flap Morphology; LASIK; Refractive Surgery

*J Ophthalmic Vis Res* 2023; 18 (1): 3–14

© 2023 Steinberg et al. This is an open access article distributed under the Creative Commons Attribution License | Published by Knowledge E

## INTRODUCTION

More than 30 years ago, laser in situ keratomileusis, better known as LASIK, started its journey to become the most frequently performed treatment to correct ametropia in otherwise healthy eyes. Over the past decades, several modifications were made to further improve its safety, efficacy, and predictability, as well as the comfort levels for both patients and surgeons.[1, 2] One of the improvements was to create a highly precise LASIK flap with a femtosecond (fs) laser to reduce variations in terms of flap thickness (FT) and flap-related complications when compared to microkeratome-created flaps.[3, 4]

In addition, the fs laser enables different flap-morphology designs to potentially further improve the safety of the surgery. Currently, two methods exist to create LASIK flaps: firstly, a strictly horizontal two-dimensional (2D) flap-cutting geometry, comparable to that of the microkeratome and secondly, a three-dimensional (3D) flap-cutting geometry which is in essence a combination of the horizontal cut and an angled side-cut, leading to a "step-like" edge. The first option is only possible with the use of the low-energy FEMTO LDV Z8 laser (Ziemer Ophthalmic Systems AG, Switzerland) and its predecessors. Whilst the 3D method creates a perfectly fitting angled flap, the interface morphology is believed to contribute toward flap stability and might also lead to a decreased number of flap striae and/or epithelial ingrowth.[5–7] However, due to the entrapped air emerging during the fs-laser "cutting" process of the horizontal flap-interface, the occurrence of opaque bubble layers (OBL) increases and potential tissue bridges might also occur in the 3D-flaps.[8] Therefore, the LDV Z8 fs laser creates additional "venting tunnels" during the 3D flap preparation, which lead the gas formed during the flap-cutting process into the direction of the flap bed downward and outward, to allow the gas to dissipate out of the stroma. Several FT predictability (intended versus achieved) comparisons were made in the past, where multiple fs lasers were used and were responsible for creating the flaps.[9–11]

However, the current study was done to analyze the predictability, precision, safety, efficacy, as well as the patients' pain and comfort levels when comparing the application of two different flap morphologies which were both created using the same low-energy, high-frequency fs laser.

## METHODS

This single-center (Hamburg Vision Clinic, Hamburg, Germany), prospective, interventional, randomized, contralateral eye study was conducted from November 2019 to March 2020. The study was registered in clinicaltrials.gov (NCT04426175) after Hamburg ethics committee approval and performed in accordance with the tenets of the Declaration of Helsinki. All patients signed an informed consent form after being advised in detail about the study rationale.

All patients received fs LASIK treatment for myopia or myopic astigmatism on both eyes from one of the two trained surgeons (SL/JS). The inclusion and exclusion criteria were similar to the criteria defined by the national committee defining the inclusion and exclusion criteria recommendations for refractive surgery in Germany (KRC). Hence, the inclusion criteria were: myopia up to 8 diopters, astigmatism up to 5 diopters, minimal corneal thickness of 480 µm, and a minimum of two weeks of no contact lens wearing. Patients with predicted residual stromal thickness (RST) under the flap after ablation of <250 µm, former ocular surgery, ocular diseases (including, but not limited to, signs of keratoconus),

**Correspondence to:**

Johannes Steinberg, MD. Department of Ophthalmology, University Hospital Hamburg-Eppendorf, Martinistr. 52, Hamburg 20251, Germany.
E-mail: steinberg@zentrumsehstaerke.de

Received: 01-09-2021 Accepted: 21-03-2022

**Access this article online**

**Website:** https://knepublishing.com/index.php/JOVR

**DOI:** 10.18502/jovr.v18i1.12720

This is an open access article distributed under the Creative Commons Attribution License, which permits unrestricted use, distribution, and reproduction in any medium, provided the original work is properly cited.

**How to cite this article:** Steinberg J, Mehlan J, Mudarisov B, Katz T, Frings A, Druchkiv V, Linke SJ . Safety and Precision of Two Different Flap-morphologies Created During Low Energy Femtosecond Laser-assisted LASIK. J Ophthalmic Vis Res 2023;18:3–14.

aged younger than 18 years, and concurrent participation in another ophthalmological clinical study were excluded.

Just before the treatment commenced, every patient was assigned according to our randomization list, those with a 2D flap created in one eye and those with a 3D-flap creation in the other eye. Schematic drawings of the morphology and geometry of both flap designs are displayed in Figures 1 (2D) and 2 (3D). In our study, the option of two venting tunnels (3D flap) was chosen [Figure 2].

In all eyes, the flap was created with the FEMTO LDV Z8 (Ziemer Ophthalmic Systems AG, Port) with a target thickness of 110 µm along with a superior hinge configuration. The subsequent excimer laser ablation was performed with the WaveLight® EX500 Excimer Laser (Alcon Fort Worth, USA).

An optical coherence tomography (OCT) image for flap visualization can be displayed, at the surgeon's discretion, on the screen before and/or after the flap resection. Before flap creation, flap visualization may serve as an optional safety measure confirming the flap's positioning with respect to the Bowman's layer and the stroma, or, post flap-creation, where the presence of gas bubbles can be assessed as an additional safety measure before flap lifting [Figure 3]. In addition, the intraoperative OCT feature can be useful for the visualization of the applanation area.

Antibiotic eyedrops were instilled for one week, while steroids and lubricants were reduced gradually over the course of one month.

The primary objective of this study was to compare central FT predictability in 110 µm LASIK flaps between 2D and 3D flap geometry groups with spectral domain anterior segments (AS)-OCT (Maestro 1, Topcon Medical Systems Tokyo, Japan) performed one month postoperatively. After measuring the cornea with the OCT using a scan protocol consisting of 12 B-scans in a radial pattern, the anterior surface was automatically marked in the image by the device. Three centrally located manual thickness measurements from the anterior surface to the interface were done and the average value was noted.

Secondary objectives of the study were to assess the following parameters:

Postoperative flap planarity with AS-OCT (Maestro 1, Topcon, Japan) at one month follow-up. After measuring the cornea with the OCT using a scan protocol consisting of 12 B-scans in a radial pattern, the anterior surface was automatically marked in the image by the device. Then, three manual thickness measurements from the anterior surface to the interface were done in 12 different measurement points as displayed in Figure 4. For every measurement point, three consecutive measurements were done and the average was noted.

Subjective intraoperative flap morphology assessment included: Stromal bed quality, ease of flap lifting, and presence of OBL. The grading was given by the surgeon directly after the completion of the treatment and was based on their assessment during/after the flap lift.

Self-reported pain perception and visual experience with 2D and 3D flap geometries during the early postoperative period. During the one-day follow-up examination, patients were asked to respond to three different questions.

Safety and Efficacy index (EI) defined as the best-corrected visual acuity (BCVA) after treatment divided by corrected distance visual acuity (CDVA) before treatment (BCVA post/BCVA pre), and uncorrected visual acuity (UCVA) after treatment divided by BCVA before treatment (uncorrected distance acuity (UDVA) post/BCVA pre), respectively, were calculated.

## Statistical Analysis

Statistical analyses were performed using the SAS® software version 9.4 and R software (https://www.r-project.org). A two-sided *t*-test was used to test the primary hypothesis. Further two-sided *t*-tests were used to test the difference between the 2D and 3D flap geometries for continuous parameters, while Fisher's exact test was used to test categorical parameters. In the case of multiple comparisons (for instance, between the regions or distances) the *P*-values were adjusted with Holm's method.

The sample size was estimated using nQuery® V4.0.

## RESULTS

Eleven patients (22 eyes) were included in our study. Seven (63.6%) patients were female, while four (36.4%) were male. The mean age

at the time of surgery was 37.27 ± 10.32 years (range: 21 to 54). Preoperative refraction and corneal thickness data are displayed in Table 1. None of the analyzed demographic, refractive or tomography parameters, displayed statistically significant differences between the 2D and 3D group (for all $P > 0.05$).

## Primary Objective

Postoperative central FT for the 2D and 3D cutting geometries were measured at the one-month follow-up visit. Target FT was 110 µm. The results are displayed in Table 2.

Figure 4 displays the differences from the target FT (110 µm). Based on the equivalence test and the null-hypothesis test combined, we can conclude that the observed effect is statistically not different from zero nor statistically equivalent to zero for 2D and 3D cutting geometries.

At the one-month follow-up visit, the mean central FT ± SD measured for 2D geometry flaps was 110.67 ±1.60 µm, and for the 3D geometry flaps was 111.21 ±1.65 µm. The mean difference ± SD between the target and achieved FT for each individual cutting geometry group was 0.67 ± 1.60 µm (2D) and 1.21 ± 1.65 µm (3D). Although the 2D cutting geometry group showed a lower mean difference in terms of FT predictability, the difference was not statistically significant ($P$ = 0.440).

## Secondary Objectives

The results of the secondary objectives are displayed in Tables 3–5.

Concerning postoperative flap planarity at the one-month follow-up visit measured with AS-OCT; for both 2D and 3D flap cut geometry groups, a series of three consecutive thickness measurements were taken at four distinct measurement points (±1, ±2, and ±3 mm from the center) along four different meridians (further called subgroups), namely: superior, inferior, nasal, and temporal [Figure 5]. The mean values were taken for each point and then the averages of the means were compared in terms of subgroups.

Data of the respective means and overall averages were analyzed [Table 3].

For our analyses, we allocated the measurement points to four subgroups: superior, inferior, nasal, and temporal. When comparing these subgroups, we couldn't demonstrate any statistical relevant differences among the four subgroups for either 3D or 2D flaps, neither when comparing the totals of the four subgroups of 3D with the totals of the four subgroups of 2D (all $P > 0.05$).

We also combined all horizontal and all vertical measurement points to analyze potential differences between the 2D and 3D flaps. Again, no statistically significant differences could be demonstrated (all $P > 0.05$). Furthermore, no statistically significant changes from the central to the periphery of the cornea (i.e., potentially increasing or decreasing flap thickness) could be demonstrated either for 2D or 3D flaps.

Regarding our secondary objective of analyzing subjective intraoperative flap morphology, we used a predefined grading and surgeon's assessment during and after the procedure where the flaps were lifted [Table 4]. Eight eyes (72.7%) in the 2D group which were compared to five eyes (45.5%) in the 3D group presented with a flat stromal bed ($P$ = 0.387). Despite not being statistically significant, both surgeons found corneal stromal striae in two eyes (18.2%) ($P$ = 0.476) and "rastered" interface in one eye (9.1%) ($P$ = 1.000) in the 3D geometry group as compared to none in the 2D flap-cutting geometry group. Surgeons were able to easily lift nine flaps (81.8%) from the 2D and six flaps (54.5%) from the 3D group ($P$ = 0.361). No OBL was found in nine eyes that received 2D flaps (81.8%) or six eyes that received 3D flaps (54.5%), respectively ($P$ = 0.453).

Regarding the secondary objective of this study, analyzing postoperative subjective pain and visual perception, a questionnaire was completed during the first day follow-up visit where patients assessed their own visual quality and perceived pain levels during the first hours after the treatment.

Whereas more than half of the eyes treated with either a 2D or 3D flap morphology experienced none to moderate pain, reported during the first hours after surgery, higher pain scores were reported for some of the eyes treated with a 3D flap.

In summary, pain perception was slightly better in the 2D group, however, it was not statistically significant.

Regarding the visual assessment right after the treatment and at the beginning of the first day after surgery, no statistically or clinically

significant differences could be demonstrated. Detailed results are displayed in Table 5.

The patients were also asked to give an assessment of their visual quality and pain level at the one-week follow-up visit. None of the patients reported any noticeable differences when comparing their 3D and 2D-flap eyes.

Table 6 provides a better representation of the functional parameters. Preoperative and postoperative UCVA data for the respective follow-up examinations are presented, and converted from Snellen notation to the logarithm of the minimum angle of resolution (logMAR).

The mean UCVA ($n$ = 22) improved significantly ($P < 0.0001$) between the preoperative visit 0.97 ± 0.36 logMAR and the one-month follow-up visit 0.00 ± 0.02 logMAR.

### Safety and Efficacy

For all eyes combined, the overall mean UCVA ($n$ = 22) measured at one month after treatment was 0.00 ± 0.02 logMAR. The safety index (SI) was 1.03, and the EI was 1.03 with no statistically significant differences between the 2D and 3D flap groups (all $P > 0.05$).

## DISCUSSION

Published literature comparing microkeratome and fs laser created flaps is not a novelty anymore.[3, 4, 13] Correspondingly, various publications exist comparing the predictability of FT measurements among fs lasers.[9, 11, 14] To the best of our knowledge, this is the first study that compared the predictability of two flap-cutting geometries (2D vs 3D) created by the same low-energy high-spot density fs laser. In this prospective, randomized, contralateral, single-center study, we were able to demonstrate central FT predictability and discuss the objective and subjective intra- and postoperative flap morphology, as well as patients' visual and pain experience between the two groups. Furthermore, it was verified that both geometry groups displayed comparable overall linear and planar FTs from the center to the periphery of the cornea.

Concerning FT predictability in other studies, a retrospective series published in 2013 by Cummings et al where 120 µm intended thickness flaps were created by the FS200 fs laser (Alcon, Wavelight, Fort Worth, USA) in 162 eyes and measured by the AS-OCT (3D OCT-2000, Topcon Medical Systems Tokyo, Japan) postoperatively, showed a mean FT of 121.94 ± 10.52 µm.[9]

In another prospective study, 87 consecutive eyes received either 110 or 120 µm intended flaps created by the 200 kHz VisuMax fs laser (Carl Zeiss Meditec, Jena, Germany). Results showed a mean achieved FT of 112.3 ± 3.84 µm (range, 109.6 to 115.1) and 122.2 ± 3.93 µm (range, 115.8 to 129.0 µm) at one-month follow-up visit for the respective intended flaps created.[15]

In a study where 110 µm intended flaps were measured with FD-OCT one week postoperatively, results showed a mean central FT of 105.4 ± 3.4 µm for FS200 and 110.8 ± 3.9 µm for VisuMax-created flaps which was found to be statistically significant; $P < 0.01$.[16] In the current study, although the mean central FT measured for 2D geometry flaps (110.67 ± 1.60 µm) was closer to the 110 µm target FT as compared to the 3D geometry flaps (111.21 ± 1.65 µm) at one-month follow-up, no statistically significant difference was found between the two groups; $P$ = 0.440. Therefore, our results suggest that excellent predictability was achieved regardless of the flap geometry utilized, that is, 2D versus 3D.

One of the secondary objectives of our study was to analyze postoperative FT in both groups along 13 different data points across the horizontal and vertical meridians, starting from the center of the cornea to ±1.0, ±2.0, and ±3.0 mm. Our results seem to be in line with the literature discussed below: Jagow et al demonstrated in their prospective comparative study, where FTs were created either by a 60 kHz fs laser (Intralase, Advanced Medical Optics) or a mechanical microkeratome (Zyoptix XP, Bausch & Lomb) and assessed with an AS-OCT for 20 points measured from the corneal vertex across each flap, for an intended 100 µm FT. The mean FT achieved ranged between 108 and 124 µm, with up to 16 µm of SD.[17] Zheng et al compared flap morphology with the FD-OCT (uniformity, accuracy, predictability) of 110 µm intended flaps created by the FS200 (Alcon, Wavelight, Fort Worth, USA) ($n$ = 200 eyes) and the VisuMax fs laser (Carl Zeiss Meditec, Jena, Germany) ($n$ = 200 eyes), one week postoperatively. Nine thickness measurements were obtained across the length of the flaps at the meridians of 0°, 45°, 90°, and 135° with the cursor manually placed at ±4, ±3, ±2, and ±1 mm

**Table 1.** Descriptive summary (preoperative refraction and pachymetry) of the 2D and 3D groups.

| | 2D (n = 11) | | | 3D (n = 11) | | |
|---|---|---|---|---|---|---|
| **Parameter (unit)** | **Median (Q1/Q2)** | **Mean ± SD** | **Min/Max** | **Median (Q1/Q2)** | **Mean ± SD** | **Min/Max** |
| Sphere (D) | –2.00 (–3.25; –1.75) | –2.45 ± 1.36 | –5.50/–1.0 | –2.25 (–4.25; –1.50) | –2.61 ± 1.69 | –6.25/–0.25 |
| Cylinder (D) | –0.75 (–1.50; –0.50) | –0.93 ± 0.77 | –2.75/0.00 | –0.50 –1.00; –0.50) | –0.79 ± 0.69 | –2.50/0.00 |
| SE (D) | –2.38 (–4.00; –1.88) | –2.92 ± 1.43 | –6.00/–1.50 | –2.62 (–4.63; –1.75) | –3.01 ± 1.62 | –6.25/–1.00 |
| CCT (µm) | 566 (531; 591) | 564 ± 37 | 514/642 | 565 (533; 588) | 564 ± 34 | 516/632 |

SE, spherical equivalent; CCT, central corneal thickness
*P*-values from a two-sided *t*-test = all >0.05

**Table 2.** Postoperative central flap thickness measured with AS-OCT at one-month follow-up visit.

| | 2D | | | 3D | | | P-value* |
|---|---|---|---|---|---|---|---|
| **Characteristics (unit)** | **Median (Q1/Q3)** | **Mean ± SD** | **Min/Max** | **Median (Q1/Q3)** | **Mean ±SD** | **Min/Max** | |
| Flap thickness achieved (µm) | 110.3 (109.3/111.7) | 110.67 ± 1.60 | 108.3/114.3 | 110.7 (110.3/111.3) | 111.21 ± 1.65 | 109.3/114.3 | 0.440 |
| Achieved thickness minus Target (µm)* | 0.33 (–0.67/1.67) | 0.67 ± 1.60 | –1.7/4.3 | 0.67 (0.33/1.33) | 1.21 ±1.65 | –0.7/4.3 | 0.440 |

**P*-value from a two-sided *t*-test

**Table 3.** Mean flap thickness for 2D vs 3D flaps measured with AS-OCT from central along the superior, inferior, nasal, and temporal meridians at respective points: ±1, ±2, and ±3 mm at one-month follow-up visit.

| **2D** (*n* = 11) | **Central (µm)** Mean ± SD | **±1 mm (µm)** Mean ± SD | **±2 mm (µm)** Mean ± SD | **±3 mm (µm)** Mean ± SD |
|---|---|---|---|---|
| Superior | 110.67 ± 1.60 | 111.33 ± 1.56 | 111.85 ± 2.34 | 111.58 ± 2.80 |
| Inferior | 110.67 ± 1.60 | 111.61 ± 2.27 | 112.18 ± 1.82 | 111.76 ± 2.18 |
| Nasal | 110.67 ± 1.60 | 111.21 ± 2.30 | 110.91 ± 2.10 | 111.18 ± 2.72 |
| Temporal | 110.67 ± 1.60 | 111.12 ± 2.58 | 111.30 ± 1.64 | 110.70 ± 2.35 |
| Overall average | **110.67 ± 1.60** | **111.32 ± 1.92** | **111.56 ± 1.69** | **111.30 ± 2.17** |
| **3D** (*n* = 11) | **Central (µm)** Mean ± SD | **±1 mm (µm)** Mean ± SD | **±2 mm (µm)** Mean ± SD | **±3 mm (µm)** Mean ± SD |
| Superior | 111.21 ± 1.65 | 111.70 ± 1.74 | 111.85 ± 1.77) | 111.58 ± 2.53 |
| Inferior | 111.21 ± 1.65 | 112.85 ± 1.98 | 111.73 ± 2.11 | 111.91 ± 2.23 |
| Nasal | 111.21 ± 1.65 | 111.33 ± 2.08 | 111.06 ± 2.63 | 112.52 ± 2.83 |
| Temporal | 111.21 ± 1.65 | 112.76 ± 3.30 | 111.33 ± 2.86 | 111.55 ± 2.37 |
| Overall average | **111.21 ± 1.65** | **112.16 ± 1.85** | **111.49 ± 2.03** | **111.93 ± 2.24** |

**Table 4.** Summary of intraoperative assessments: stromal bed quality, ease of flap lift, and presence of opaque bubble layer (OBL).

| Characteristics | Category | 2D | 3D | P-value* |
|---|---|---|---|---|
| Stromal bed quality, *n* (%) | Smooth | 8 (72.7) | 5 (45.5) | 0.387 |
| | Tissue bridges | 3 (27.3) | 3 (27.3) | 0.659 |
| | Lines | 0 | 2 (18.2) | 0.476 |
| | Rastered | 0 | 1 (9.1) | 1.000 |
| Ease of flap lift, *n* (%) | Easily | 9 (81.8) | 6 (54.5) | 0.361 |
| | Sticky | 2 (18.2) | 5 (45.5) | |
| Presence of OBL, *n* (%) | No OBL | 9 (81.8) | 6 (54.5) | 0.453 |
| | <30% of flap surface | 1 (9.1) | 2 (18.2) | |
| | 30–40% of flap surface | 1 (9.1) | 3 (27.3) | |

*P-value from a Fisher's exact test
For stromal bed quality: because one eye could display more than one variable, *P*-values were given for each variable comparing 2D and 3D. In all other analyzes, the overall *P*-value for the Fisher's exact test was given.

**Table 5.** Summary of postoperative self-reported pain perception and visual experience stratified between 2D and 3D flap geometry groups on day-one follow-up visit.

| Category | 2D(n = 11) | 3D(n = 11) | Overall(n = 22) | P-value* |
|---|---|---|---|---|
| *"Rate your pain in the right eye/left eye during the hours after the treatment."* No pain | 4 (36.4) | 3 (27.3) | 7 (31.8) | 0.821 |
| Mild pain | 2 (18.2) | 1 (9.1) | 3 (13.6) | |
| Moderate pain | 3 (27.3) | 2 (18.2) | 5 (22.7) | |
| Severe pain | 2 (18.2) | 4 (36.4) | 6 (27.3) | |
| Intense pain | 0 | 1 (9.1) | 1 (4.5) | |
| *Rate your first visual experience immediately after treatment: right eye/left eye.* As good as with glasses before treatment | 2 (18.2) | 2 (18.2) | 4 (18.2) | 1.000 |
| Almost as good as with glasses before treatment | 2 (18.2) | 3 (27.3) | 5 (22.7) | |
| A little blurred | 4 (36.4) | 3 (27.3) | 7 (31.8) | |
| Blurry like seeing through foggy glasses | 3 (27.3) | 3 (27.3) | 6 (27.3) | |
| "*Rate your visual acuity a few minutes after awakening this morning for the right and the left eye."* As good as with glasses before treatment | 5 (45.5) | 5 (45.5) | 10 (45.5) | 1.000 |
| Almost as good as with glasses before treatment | 2 (18.2) | 3 (27.3) | 5 (22.7) | |
| A little blurred | 4 (36.4) | 3 (27.3) | 7 (31.8) | |

*P-value from a Fisher's exact test

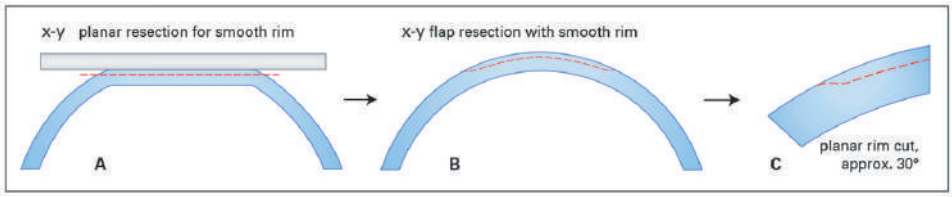


**Figure 1.** Flap morphology in planar (2D) flaps**.** Side view on the 2D LASIK flap. The flap is generated after applanation in a strictly horizontal plane leading to a minimum-angled flap edge after the applanation (A & B). Planar rim cut at approximately 30° (C).
Source: Femto LDV Z8; Surgical procedure manual Cornea; Ziemer Ophthalmology.

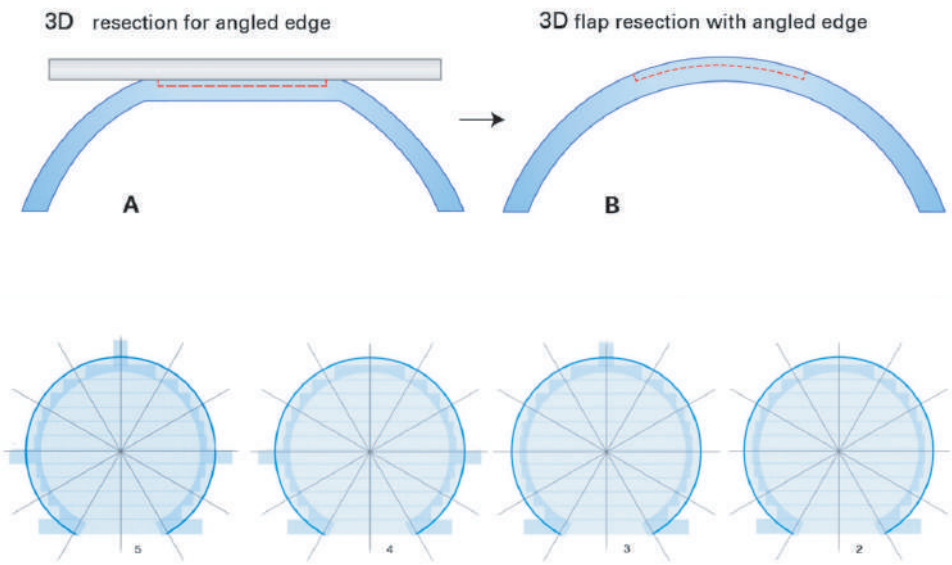


**Figure 2.** Flap morphology in planar (3D) flaps**.** Side (upper row) and top (lower row) views on the 3D LASIK flap. The flap is generated after applanation combining a strictly horizontal plane with a 90° side cut (A & B). Additional venting tunnels (optionally 2–5 tunnels, see lower row) have to be created to release the otherwise enclosed air.
Source: Femto LDV Z8; Surgical procedure manual Cornea; Ziemer Ophthalmology.

from the center of the flap. In total, 36 thickness measurements were analyzed for each flap. The mean FT achieved with the FS200 was 105.7 ± 2.6 μm, which was significantly less ($P < 0.01$) than for the VisuMax (111.2 ± 2.3 μm).[17] Although both lasers used the 3D cutting geometry, the VisuMax results were found to be closer when corresponding to our 3D group. In our study, seeing that no statistically significant differences were found between the central and overall FT (13 points) results for both cutting geometry groups, we can conclude that both 2D and 3D flap-cutting geometries demonstrated high precision in terms of FTs.

Regarding our subjective intraoperative flap morphology findings, despite no statistically significant differences between both groups, both surgeons (SL, JS) noted from a clinical perspective a tendency toward a more homogeneous interface with a less adhesive flap and less OBL in the 2D flap geometry. Regarding postoperative self-reported pain perception and visual experience stratified between 2D and 3D flap geometry groups, the patients were unaware of which eye received 2D or 3D flap morphology (i.e., blinded study design). For seven eyes (31.8%) "no pain" was reported. Four of them belonged to the 2D group. However, despite not being statistically significant in our 22 eyes-analyses, higher pain scores were reported for some of the eyes treated with the "3D-flap". Regarding the subjective visual quality assessment, no differences could be identified. Minutes after waking up the first morning post operation, for 10 eyes (equally distributed between

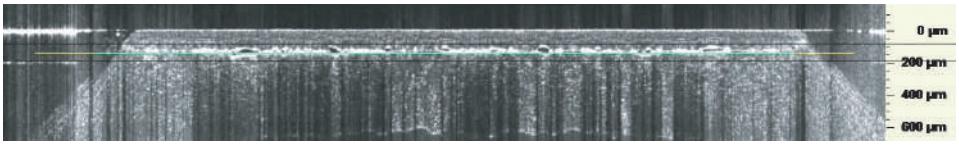


**Figure 3.** Intraoperative OCT before flap lifting. The yellow line defines the cut position.

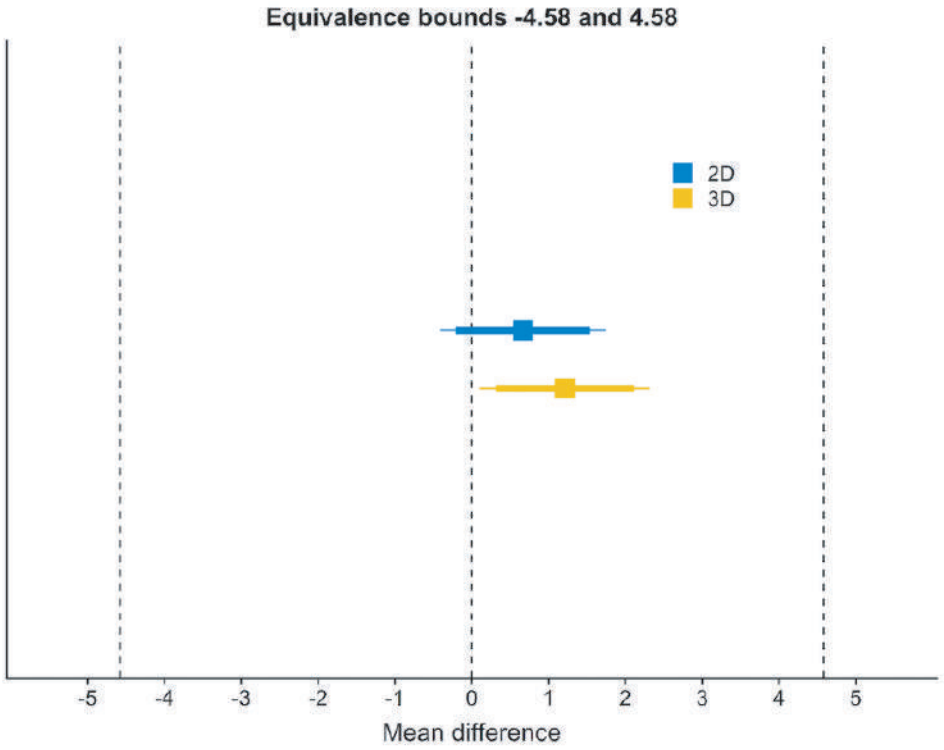


**Figure 4.** The mean differences of flap thickness from 110 µm. Squares: Mean differences from 110 µm. Dashed lines equivalence bounds (–4.58; 4.58). Thick line around differences is TOST (Two One-Sided Tests) confidence interval. 2D 90% CI (–0.207; 1.54); 3D 90% CI (0.311; 2.113). Thin line NHST (Null Hypothesis Significance Test) 95% confidence interval. 2D 95% CI (–0.407; 1.741); 3D 95% CI (0.105; 2.32).

2D and 3D eyes), patients rated their visual acuity to be "as good as with glasses before treatment". No statistically significant differences between intraoperative flap quality and patient's perception could be demonstrated during the first hours after the treatment. However, differences between both flap geometry groups regarding a tendency toward more adhesive and more OBL-prone flaps, potentially leading to the perceived (patient) discomfort in 3D flaps as compared to 2D flap geometry group, were clinically noticed.

Furthermore, it is important to keep in mind that the analyses of the intra-op flap-/interface morphology and the patients' postoperative assessments were secondary objectives of the study. Since the power analysis was based on the primary objective, that is, comparing the central FT predictability in both flap geometries and by taking the contralateral character of the study into account, we had to limit the number of eyes included in the study.

In case clinically relevant differences regarding subjective pain perception and morphology are to be assessed, bigger sample sizes would be necessary for future investigations. However, due to the low number of eyes included, the Fisher's exact test was used in these analyses. Our *P*-values > 0.05 indicate no correlation between the different categories and the 2D and 3D flap morphologies.

Technically, each flap-cutting geometry has its own special advantages. As mentioned, the 2D flap-cutting geometry only exists in the low-energy

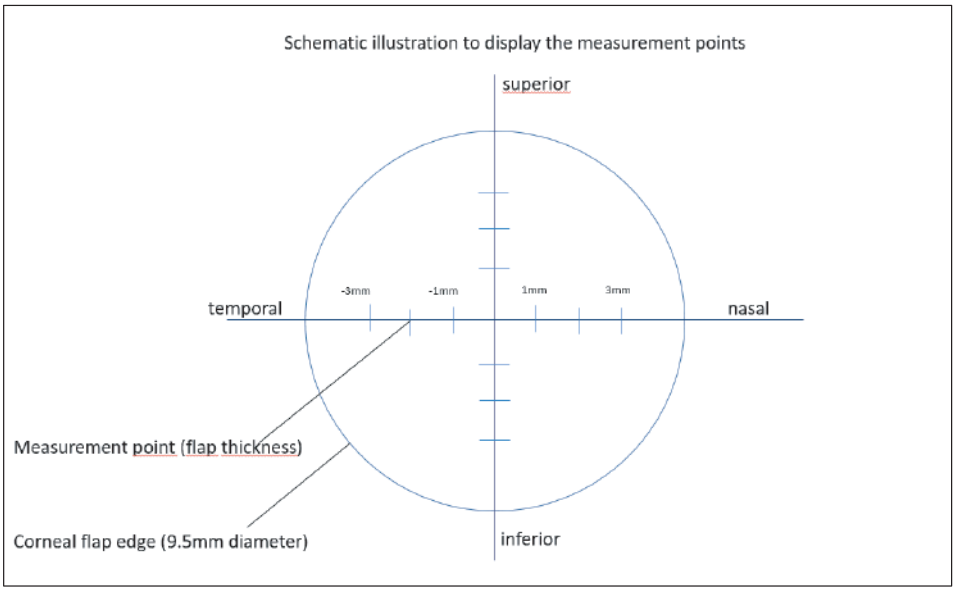


**Figure 5.** Schematic illustration to display the four measurement points in each meridian.

high-spot density FEMTO LDV Z8 laser and its predecessors.

Due to the nature of the 2D flap configuration, one would expect it to be relatively easy when lifting such a flap. With the FEMTO LDV Z8, not only are round flaps (as with the 2D) are a possibility but oval-shaped flaps can also be created with the 3D flap-cutting geometry tool. According to the patient requirements, 3D flap geometries can be resized or repositioned on the patient's eye, and side cut angles can be programmed from 30° to 150° around the globe.

The biggest advantage of the low-energy FEMTO LDV Z8 is the additional software option that exists called Optima which allows the surgeon to start with a 2D flap approach and switch intraoperatively to a 3D flap-mode after docking. As 2D flaps are generated without an angled site-cut, these flaps have to be created in the center of the applanated corneal surface. Adjusting the flap position after applanation would lead to a potentially irregular flap shape and/or a much too small or long hinge-configuration. Therefore, no such option for the surgeon exists other than in 3D flap-creation. With the 3D, angled side-cut geometry, even after applanation of the cornea, the surgeon can change settings including the flap position as well as the hinge position based on a live image. As mentioned before, the angled side cut in 3D geometry flaps creates a perfectly fitting angled flap and interface morphology believed to contribute toward flap stability which might lead to a decreased number of flap striae and/or epithelial ingrowth.[5–7]

Considering the aforementioned advantages and disadvantages of 2D versus 3D flap geometries as well as the flexibility to intraoperatively switch after docking in case the surgeon wants to shift the centration before flap-cutting commences, the low-energy FEMTO LDV Z8 seems to be the preferred choice in performing LASIK surgeries.

One of the limitations of our study was the lack of comparison of the induced corneal higher order aberrations (HOA) due to flap striaes which would be another important parameter when comparing the two flap-cutting techniques. As a result, it is recommended that we research this aspect for follow-up studies. Another limitation occurred with our small sample size as we had to limit the number of eyes included in our study to properly achieve our primary objective.

In summary, this study compared two different flap morphologies created during LASIK, whilst using the same low-energy, high-frequency OCT-equipped fs laser. Both the 2D and 3D flap-cutting geometries demonstrated comparable precision and predictability in terms of FTs combined with a high safety and efficacy performance.

**Table 6.** Summary of pre- and postoperative uncorrected visual acuity( logMAR).

| Characteristics | Category | 2D(n = 11) | 3D(n = 11) | Overall(n = 22) | P-value** |
|---|---|---|---|---|---|
| Preop UCVA | *n* (missing) | 11 (0) | 11 (0) | 22 (0) | |
| | Mean (SD) | 0.91 (0.32) | 1.03 (0.39) | 0.97 (0.36) | 0.4224 |
| | 95% CI | 0.69; 1.12 | 0.77; 1.30 | 0.81; 1.13 | |
| | Median | 1.00 | 1.00 | 1.00 | |
| | Q1; Q3 | 0.70; 1.10 | 0.88; 1.10 | 0.80; 1.10 | |
| | Min; Max | 0.2; 1.3 | 0.4; 2.0 | 0.2; 2.0 | |
| One day post-op UCVA | *n* (missing) | 11 (0) | 11 (0) | 22 (0) | |
| | Mean (SD) | 0.11 (0.08) | 0.10 (0.04) | 0.11 (0.06) | 0.5668 |
| | 95% CI | 0.06; 0.17 | 0.07; 0.13 | 0.08; 0.14 | |
| | Median | 0.10 | 0.10 | 0.10 | |
| | Q1; Q3 | 0.10; 0.18 | 0.10; 0.10 | 0.10; 0.10 | |
| | Min; Max | 0.0; 0.3 | 0.0; 0.2 | 0.0; 0.3 | |
| One week post-op UCVA | *n* (missing) | 11 (0) | 11 (0) | 22 (0) | |
| | Mean (SD) | 0.06 (0.08) | 0.06 (0.11) | 0.06 (0.09) | 1.0000 |
| | 95% CI | 0.01; 0.11 | 0.00; 0.14 | 0.02; 0.10 | |
| | Median | 0.00 | 0.00 | 0.00 | |
| | Q1; Q3 | 0.00; 0.10 | 0.00; 0.18 | 0.00; 0.10 | |
| | Min; Max | 0.0; 0.2 | 0.0; 0.3 | 0.0; 0.3 | |
| One month post-op UCVA | *n* (missing) | 11 (0) | 11 (0) | 22 (0) | |
| | Mean (SD) | 0.01 (0.03) | 0.00 (0.00) | 0.00 (0.02) | 0.3293 |
| | 95% CI | 0.00; 0.03 | 0.00; 0.00 | 0.00; 0.01 | |
| | Median | 0.00 | 0.00 | 0.00 | |
| | Q1; Q3 | 0.00; 0.00 | 0.00; 0.00 | 0.00; 0.00 | |
| | Min; Max | 0.0; 0.1 | 0.0; 0.0 | 0.0; 0.1 | |
| *P*-value* | | | | <0.0001 | |

## Financial Support and Sponsorship

None.

## Conflicts of Interest

None.

## *REFERENCES*

1. Kim TI, Alió Del Barrio JL, Wilkins M, Cochener B, Ang M. Refractive surgery. *Lancet* 2019;393:2085–2098.
2. Moshirfar M, Bennett P, Ronquillo Y. Laser in situ keratomileusis. Treasure Island, FL: StatPearls; 2021.
3. Pajic B, Vastardis I, Pajic-Eggspuehler B, Gatzioufas Z, Hafezi F. Femtosecond laser versus mechanical microkeratome-assisted flap creation for LASIK: A prospective, randomized, paired-eye study. *Clin Ophthalmol* 2014;8:1883–1889.
4. Pietilä J, Huhtala A, Mäkinen P, Salmenhaara K, Uusitalo H. Laser-assisted in situ keratomileusis flap creation with the three-dimensional, transportable Ziemer FEMTO LDV model Z6 I femtosecond laser. *Acta Ophthalmol* 2014;92:650–655.
5. dos Santos AM, Torricelli AA, Marino GK, Garcia R, Netto MV, Bechara SJ, et al. Femtosecond laser-assisted LASIK flap complications. *J Refract Surg* 2016;32:52–59.
6. Güell JL, Elies D, Gris O, Manero F, Morral M. Femtosecond laser-assisted enhancements after laser in situ keratomileusis. *J Cataract Refract Surg* 2011;37:1928–1931.
7. Letko E, Price MO, Price FW Jr. Influence of original flap creation method on incidence of epithelial ingrowth after

LASIK retreatment. *J Refract Surg* 2009;25:1039–1041.

8. Mastropasqua L, Calienno R, Lanzini M, Salgari N, De Vecchi S, Mastropasqua R, et al. Opaque bubble layer incidence in Femtosecond laser-assisted LASIK: Comparison among different flap design parameters. *Int Ophthalmol* 2017;37:635–641.
9. Cummings AB, Cummings BK, Kelly GE. Predictability of corneal flap thickness in laser in situ keratomileusis using a 200 kHz femtosecond laser. *J Cataract Refract Surg* 2013;39:378–385.
10. Prakash G, Agarwal A, Yadav A, Jacob S, Kumar DA, Agarwal A, et al. A prospective randomized comparison of four femtosecond LASIK flap thicknesses. *J Refract Surg* 2010;26:392–402.
11. Zheng Y, Zhou Y, Zhang J, Liu Q, Zhai C, Wang Y. Comparison of laser in situ keratomileusis flaps created by 2 femtosecond lasers. *Cornea* 2015;34:328–333.
12. Eldaly ZH, Abdelsalam MA, Hussein MS, Nassr MA. Comparison of laser in situ keratomileusis flap morphology and predictability by wavelight FS200 Femtosecond laser and Moria microkeratome: An anterior segment optical coherence tomography study. *Korean J Ophthalmol* 2019;33:113–121.
13. Reinstein DZ, Sutton HF, Srivannaboon S, Silverman RH, Archer TJ, Coleman DJ. Evaluating microkeratome efficacy by 3D corneal lamellar flap thickness accuracy and reproducibility using Artemis VHF digital ultrasound arc-scanning. *J Refract Surg* 2006;22:431–440.
14. Ahn H, Kim JK, Kim CK, Han GH, Seo KY, Kim EK, et al. Comparison of laser in situ keratomileusis flaps created by 3 femtosecond lasers and a microkeratome. *J Cataract Refract Surg* 2011;37:349–357.
15. Ju WK, Lee JH, Chung TY, Chung ES. Reproducibility of LASIK flap thickness using the zeiss femtosecond laser measured postoperatively by optical coherence tomography. *J Refract Surg* 2011;27:106–110.
16. Zheng Y, Zhou Y, Zhang J, Liu Q, Zhai C, Wang Y. Comparison of laser in situ keratomileusis flaps created by 2 femtosecond lasers. *Cornea* 2015;34:328–333.
17. von Jagow B, Kohnen T. Corneal architecture of femtosecond laser and microkeratome flaps imaged by anterior segment optical coherence tomography. *J Cataract Refract Surg* 2009;35:35–41.

Original Article

# Risk Factors Associated with Keratoconus in an Iranian Population

**Hossein Mohammad-Rabei[1,2], MD; Shahrokh Ramin[3], MD; Sahar Lotfi[3], MS; Hamideh Sabbaghi[3, 4], PhD; Farid Karimian[1], MD; Saeid Abdi[3], MS; Mohammad Hasan Shahriari[5], MS; Bahareh Kheiri[1], MS; Kourosh Sheibani[6], MD; Mohammad Ali Javadi[1], MD**

[1]*Ophthalmic Research Center, Research Institute for Ophthalmology and Vision Science, Shahid Beheshti University of Medical Sciences, Tehran, Iran*
[2]*Department of Ophthalmology, Torfeh Eye Hospital, Shahid Beheshti University of Medical Sciences, Tehran, Iran*
[3]*Department of Optometry, School of Rehabilitation, Shahid Beheshti University of Medical Sciences, Tehran, Iran*
[4]*Ophthalmic Epidemiology Research Center, Research Institute for Ophthalmology and Vision Science, Shahid Beheshti University of Medical Sciences, Tehran, Iran*
[5]*Department of Health Information, Technology and Management, School of Allied Medical Sciences, Shahid Beheshti University of Medical Sciences, Tehran, Iran*
[6]*Basir Eye Health Research Center, Tehran, Iran*

**ORCID:**
*Hamideh Sabbaghi: https://orcid.org/0000-0002-2627-7222*
*Hossein Mohammad-Rabei: https://orcid.org/0000-0003-3653-6272*

## Abstract

**Purpose:** To determine associated factors for keratoconus (KCN) in the Iranian population.

**Methods:** In this retrospective case-control study, 100 KCN patients and 200 age- and sex-matched individuals, who were either candidates for photorefractive keratectomy or healthy referrals from the Torfeh Eye Hospital, were included as the case and control groups, respectively. KCN patients were all registered at the Iranian National Registry of Keratoconus (KCNReg®). Demographic characteristics, patients' symptoms and their habits, as well as systemic and ocular disorders were documented. Clinical examinations included best corrected visual acuity (BCVA) and refractive error measurements, biomicroscopic examination, and corneal imaging.

**Results:** In this case group, the frequency of mild, moderate, and severe KCN was 38%, 28%, and 34%, respectively. Parental consanguinity (odds ratio [OR] = 1.758, $P = 0.029$), positive familial history in patients' first degree (OR = 12.533, $P < 0.001$) and second degree (OR = 7.52, $P < 0.001$) relatives, vernal keratoconjunctivitis (OR = 7.510, $P = 0.003$), severe eye rubbing (OR = 10.625, $P < 0.001$), and systemic diseases including migraine, hypertension, and thyroid disease (OR = 6.828, $P = 0.021$) were found as associated factors for KCN. Lesser frequency of KCN was observed in patients with Fars ethnicity (OR = 0.583, $P = 0.042$), with higher levels of wealth indices (OR = 0.31, $P < 0.001$) and higher levels of education (OR = 0.18, $P = 0.024$).

**Conclusion:** Severe eye rubbing, vernal keratoconjunctivitis, parental consanguinity and positive familial history of KCN, low socioeconomic status, and low levels of education were significantly associated with KCN in our study population.

**Keywords:** Associated Factors; Iran; Keratoconus; Population

*J Ophthalmic Vis Res* 2023; 18 (1): 15–23

© 2023 Mohammad-Rabei et al. This is an open access article distributed under the Creative Commons Attribution License | Published by Knowledge E

## INTRODUCTION

Keratoconus (KCN) is a progressive non-inflammatory corneal thinning disorder which commonly occurs bilaterally and asymmetrically. It appears in most patients between the second and fourth decades of their lives.[1–3] In previous literature, a prevalence of 50 to 2300 cases per 100,000 individuals has been reported for this disease in different geographical regions.[4–7] The annual incidence rate of KCN was reported within the range of 22.3 to 24.9 per 100,000 population in Yazd, a province of Iran with a hot and dry climate.[8] Most patients complain of reduced vision due to induced myopia and irregular astigmatism secondary to the deformation of corneal tissue into a cone-shaped structure.[1–3] The reduction of visual acuity among patients decreases activity and quality of life.[1, 9]

Various environmental, socioeconomic, and familial factors including atopic diseases and eye rubbing,[10–12] exposure to sunlight and ultraviolet radiation,[1, 10] race,[10] older age,[10, 13] low socioeconomic status or low levels of education,[14] parental consanguinity,[15] and positive familial history[10] have all been reported as the probable risk factors for KCN. However, these risk factors are controversial.[3, 10, 16–19]

Considering different geographical regions, less prevalence of KCN has been found in Northern Europe,[10,20,21] North America,[10,22,23] and Japan[10,24] as compared with India, China,[10, 25, 26] and Eastern Mediterranean countries.[10, 27, 28]

Due to the importance of KCN as a leading cause of visual impairment and the effectiveness of implementing preventive approaches in some higher risk individuals, we aimed to determine the possible associated factors for KCN among the Iranian population.

**Correspondence to:**

Hamideh Sabbaghi, PhD. Ophthalmic Epidemiology Research Center, Research Institute for Ophthalmology and Vision Science, Shahid Beheshti University of Medical Sciences, No. 23, Paidarfard St., Boostan 9 St., Pasdaran Ave., Tehran, 16666, Iran.
E-mail: Sabbaghi.opt@gmail.com

Received: 10-06-2021 Accepted: 21-03-2022

**Access this article online**

**Website:** https://knepublishing.com/index.php/JOVR

**DOI:** 10.18502/jovr.v18i1.12721

## METHODS

### Patient Enrolment

In this case–control study, a total of 300 subjects in the age range of 16 to 61 years were studied as case ($n$ = 100) and control ($n$ = 200) groups between March 2016 and October 2017. KCN patients were all registered at the Iranian National Registry of Keratoconus (KCNReg®). The study protocol adhered to the Declaration of Helsinki and was approved by the Ethics Committee of the Ophthalmic Research Center, Shahid Beheshti University of Medical Sciences via the approval number IR.SBMU.ORC.1397.12. The study details were explained to all participants and written consent was obtained prior to enrolling into the study.For the case group, we used the demographic and clinical records of 100 registered KCN patients from the KCNReg®. The control group comprised 200 age- and sex-matched individuals who were either candidates for photorefractive keratectomy or healthy referrals from the Torfeh Eye Hospital. We excluded patients who were under suspicion of having a diagnosis of KCN or any other corneal pathological disorders from the control group.

### The Questionnaire

Data collection was performed using a standard questionnaire based on the questionnaire used by Owen and Gamble,[29] which had been applied previously in other studies.[15, 28] In order for the questionnaire to be more comprehensive it was independently translated to the Persian language by two bilingual translators (an ophthalmologist and an optometrist). The two translators mutually agreed about any differences. The document was also translated back into

This is an open access article distributed under the Creative Commons Attribution License, which permits unrestricted use, distribution, and reproduction in any medium, provided the original work is properly cited.

**How to cite this article:** Mohammad-Rabei H, Ramin Sh, Lotfi S, Sabbaghi H, Karimian F, Abdi S, Shahriari MH, Kheiri B, Sheibani K, Javadi MA. Risk Factors Associated with Keratoconus in an Iranian Population. J Ophthalmic Vis Res 2023;18:15–23.

English by another translator and compared to the original questionnaire to check the consistency of the translation. It was then presented to an expert panel which included ophthalmologists, biostatisticians, and research methodologists to assess its format and content validity. Finally, we asked 10 patients to read the questionnaire to determine whether there were any items that they could not understand. No shortcomings were detected by these individuals. In this questionnaire, demographic characteristics such as age, sex, occupation, birthplace, ethnicity, parental consanguinity, patients' education and socioeconomic status were questioned. Patients' symptoms (blurred vision, diplopia, and dry eye) and their habits (smoking, eye rubbing, duration of sunlight exposure, and wearing of contact lens or sunglasses) were also documented. Comorbidities of either general or systemic disorders (diabetes, atopic diseases, mitral valve prolapse, collagen diseases, renal dysfunction, and any other systemic disorders) and/or ocular diseases (vernal keratoconjunctivitis and glaucoma) among patients were also recorded in both groups. In addition, family history of KCN as well as any history of previous corneal surgery was recorded. For both the case and control groups, the questionnaires were filled either on paper, online, telephone, or via face-to-face interviews in order to increase the response rate.

## Visual and Ocular Examinations

Clinical examinations included measurements of the best corrected visual acuity (BCVA), refractive error, biomicroscopic examination, and corneal imaging using Tomey topography (TMS-4, Tomey, Nishi-Ku, Japan) and Pentacam (WaveLight Allegro Topolyzer Vario, Alcon, United States). Funduscopy was also conducted by an indirect binocular ophthalmoscope through dilated pupil using a 78D lens.

## Definitions

KCN was diagnosed if any of the following signs were observed in any of the examination steps; presence of scissor reflex in retinoscopy, as well as Vogt's striae, Fleischer ring, Munson's sign, stromal thinning, corneal scar, and hydrops in biomicroscopy. KCN diagnosis was also determined based on the corneal topography in cases with a Sim k > 45.57D, corneal irregularity measurement (CIM) between 0.69 and 100 µm, surface regularity index (SRI) higher than 0.56, inferior–superior (I–S) asymmetry >1.8, and KCN severity index (KSI) >30%.[30]

The severity of KCN was determined based on the Rabinowitz classification[30] by an experienced cornea and anterior segment specialist (HMR). Subjects were included in the control group if none of the KCN signs were observed in their examination. First-degree relatives were considered as the patients' offspring, siblings, or their parents while the second-degree relatives included their uncles, aunts, nephews, nieces, grandparents, grandchildren, half-siblings, and double cousins. We asked the patients to determine the duration of eye rubbing during a day, where it was classified as high in cases with a duration of 10 to 180 s, low with eye rubbing of <10 s, and never in cases with no reports of eye rubbing during a day.[10]

## Statistical Analysis

To present data, we used mean, standard deviation, median, range, frequency, and percentage. To evaluate the differences between the groups, we used the Fisher's Exact Test and the Chi-square Test. We also used generalized estimating equations when needed to consider the possible correlation of the results in the eyes. To assess the effect of the associated factor on the incidence of KCN, we first entered the associated factor in the model as univariate then each variable which had a *P*-value of <0.2 was entered into the model as multivariate. All statistical analyses were performed using the SPSS software version 25 (IBM Corp. Armonk, NY: IBM Corp.). *P*-values < 0.05 were considered statistically significant.

# RESULTS

In total 100 KCN patients and 200 controls with a mean age of 30.14 ± 7.93 years participated in the present case–control study. In the case group, the frequency of mild, moderate, and severe KCN was 38%, 28%, and 34%, respectively. Table 1 represents the comparison of baseline characteristics between the case and the control groups. As shown, no significant difference was

**Table 1.** Comparison of demographic characteristics between case and control groups.

| Factors | Level | Total | Groups | | OR | 95% CI | | P-value* |
|---|---|---|---|---|---|---|---|---|
| | | | KCN (n = 100) | Control (n = 200) | | Lower | Upper | |
| Age (yr) | Mean ± SD | 30.14 ± 7.93 | 29.54 ± 8.54 | 30.44 ± 7.61 | 0.985 | 1.017 | 0.955 | 0.356 |
| | Median (Range) | 29 (16 to 61) | 28 (16 to 61) | 29 (16 to 55) | | | | |
| Sex | Male | 150 (50.0%) | 50 (50.0%) | 100 (50.0%) | 1 | 0.619 1.616 | | >0.999 |
| | Female | 150 (50.0%) | 50 (50.0%) | 100 (50.0%) | 1 | | | |
| Birthplace | North | 24 (8.0%) | 7 (7.0%) | 17 (8.5%) | 0.961 | 0.378 2.443 | | 0933 |
| | South | 9 (3.0%) | 4 (4.0%) | 5 (2.5%) | 1.867 | 0.483 7.207 | | 0.365 |
| | West | 66 (22.0%) | 31 (31.0%) | 35 (17.5%) | 2.067 | 1.164 3.671 | | 0.013 |
| | East | 10 (3.3%) | 1 (1.0%) | 9 (4.5%) | 0.259 | 0.032 2.094 | | 0.205 |
| | Center | 191 (63.7%) | 57 (57.0%) | 134 (67.0%) | 1 | | | |
| Patient's ethnicity | Fars | 108 (36.0%) | 28 (28.0%) | 80 (40.0%) | 0.583 | 0.347 | 0.981 | 0.042 |
| | Others | 192 (64.0%) | 72 (72.0%) | 120 (60.0%) | 1 | | | |
| Parental consanguinity | Yes | 95 (31.7%) | 40 (40.0%) | 55 (27.5%) | 1.758 | 1.059 | 2.916 | 0.029 |
| | No | 205 (68.3%) | 60 (60.0%) | 145 (72.5%) | 1 | | | |
| Patient's education (yr) | 0–6 | 8 (2.7%) | 5 (5.0%) | 3 (1.5%) | 1 | | | |
| | 6–12 | 162 (54.0%) | 65 (65.0%) | 97 (48.5%) | 0.402 | 0.093 | 1.741 | 0.223 |
| | >12 | 130 (43.3%) | 30 (30.0%) | 100 (50.0%) | 0.18 | 0.041 | 0.797 | 0.024 |
| Patient's occupation | Indoor | 200 (66.7%) | 67 (67.0%) | 133 (66.5%) | 1 | | | |
| | Outdoor | 100 (33.3%) | 33 (33.0%) | 67 (33.5%) | 0.978 | 0.587 | 1.628 | 0.931 |
| Wealth index | Rich | 102 (34.0%) | 19 (19.0%) | 83 (41.5%) | 0.31 | 0.165 | 0.583 | <0.001 |
| | Normal | 92 (30.7%) | 36 (36.0%) | 56 (28.0%) | 0.871 | 0.493 | 1.539 | 0.635 |
| | Poor | 106 (35.3%) | 45 (45.0%) | 61 (30.5%) | 1 | | | |
| Sunlight exposure during a day (hr) | 0–2 | 112 (37.3%) | 37 (37.0%) | 75 (37.5%) | 1 | | | |
| | 3–4 | 88 (29.3%) | 30 (30.0%) | 58 (29.0%) | 1.048 | 0.581 | 1.893 | 0.875 |
| | 5–6 | 34 (11.3%) | 11 (11.0%) | 23 (11.5%) | 0.969 | 0.427 | 2.2 | 0.941 |
| | >6 | 66 (22.0%) | 22 (22.0%) | 44 (22.0%) | 1.014 | 0.531 | 1.933 | 0.968 |
| Wearing of sunglasses | Yes | 128 (42.7%) | 40 (40.0%) | 88 (44.0%) | 0.841 | 0.516 | 1.37 | 0.487 |
| | No | 172 (57.3%) | 60 (60.0%) | 112 (56.0%) | 1 | | | |

KCN, keratoconus; OR, odds ratio; CI, confidence interval; SD, standard deviation
*Based on binary logistic regression

**Table 2.** Comparison of clinical characteristics between case and control groups to find the probable associated factors.

| Factors | Level | Total | Groups | | OR | 95% CI | | P-value* |
|---|---|---|---|---|---|---|---|---|
| | | | KCN (n = 100) | Control (n = 200) | | Lower | Upper | |
| KCN in family | First-degree | 35 (11.7%) | 28 (28.0%) | 7 (3.5%) | 12.533 | 5.21 30.148 | | <0.001 |
| | Second-degree | 17 (5.7%) | 12 (12.0%) | 5 (2.5%) | 7.52 | 2.54 | 22.21 | <0.001 |
| | No | 248 (82.7%) | 60 (60.0%) | 188 (94.0%) | 1 | | | |
| Systemic diseases | Diabetes | 3 (1%) | 2 (2.0%) | 1 (0.5%) | 4.552 | 0.405 | 51.200 | 0.22 |
| | MVP | 6 (2.0%) | 2 (2.0%) | 4 (2.0%) | 1.138 | 0.203 | 6.388 | 0.883 |
| | Renal | 3 (1.0%) | 2 (2.0%) | 1 (0.5%) | 4.552 | 0.405 | 51.200 | 0.220 |
| | Asthma | 7 (2.3%) | 1 (1.0%) | 6 (3.0%) | 0.379 | 0.045 | 3.222 | 0.374 |
| | Eczema | 18 (6.0%) | 8 (8.0%) | 10 (5.0%) | 1.821 | 0.684 | 4.849 | 0.231 |
| | Allergy | 65 (21.7%) | 21 (21.0%) | 44 (22.0%) | 1.086 | 0.593 | 1.988 | 0.789 |
| | Others | 8 (2.7%) | 6 (6.0%) | 2 (1.0%) | 6.828 | 1.338 | 34.841 | 0.021 |
| | No | 190 (63.3%) | 58 (58.0%) | 132 (66.0%) | 1 | | | |
| Ocular diseases | Glaucoma | 17 (5.7%) | 7 (7.0%) | 10 (5.0%) | 1.577 | 0.58 | 4.286 | 0.372 |
| | VKC | 13 (4.3%) | 10(10.0%) | 3 (1.5%) | 7.510 | 2.015 | 27.997 | 0.003 |
| | No | 270 (90.0%) | 83 (83.0 %) | 187 (93.5%) | 1 | | | |
| Eye rubbing | Never | 110 (36.7%) | 25 (25.0%) | 85 (42.5%) | 1 | | | |
| | Low | 157 (52.3%) | 50 (50.0%) | 107 (53.5%) | 1.589 | 0.909 | 2.776 | 0.104 |
| | High | 33 (11.0%) | 25 (25.0%) | 8 (4.0%) | 10.625 | 4.266 | 26.463 | <0.001 |
| Dry eye | Never | 177 (59.0%) | 53 (53.0%) | 124 (62.0%) | 1 | | | |
| | Mild | 90 (30.0%) | 31 (31.0%) | 59 (29.5%) | 1.229 | 0.716 | 2.111 | 0.454 |
| | Moderate | 28 (9.3%) | 13 (13.0%) | 15 (7.5%) | 2.028 | 0.903 | 4.555 | 0.087 |
| | Severe | 5 (1.7%) | 3 (3.0%) | 2 (1.0%) | 3.509 | 0.570 | 21.614 | 0.176 |
| Smoking | Yes | 35 (11.7%) | 7 (7.0%) | 28 (14.0%) | 0.46 | 0.193 | 1.093 | 0.079 |
| | No | 265 (88.3%) | 93 (93.0%) | 172 (86.0%) | 1 | | | |

KCN, keratoconus; OR, odds ratio; CI, confidence interval; MVP, mitral valve prolapse; VKC, vernal keratoconjunctivitis; NA, not available

*Based on binary logistic regression; **Not available because of zero observation in one of the levels

found between the two studied groups regarding age, sex, ethnicity, occupation, sunlight exposure, and wearing of sunglasses. However, it was found that patients living in the west regions of Iran were at a higher risk of KCN as compared to the controls (odds ratio [OR] = 2.067, $P$ = 0.013). Furthermore, parental consanguinity (OR = 1.758, $P$ = 0.029) was also found as another associated factor for KCN.

**Table 3.** Comparison of topo- and tomographic findings in case and control groups.

| Factors | KCN (n = 100) | | | | P-value* | Pairwise comparison | Control (n = 200) | P-value** |
|---|---|---|---|---|---|---|---|---|
| | Total | Severe (1) | Moderate (2) | Mild (3) | | | | |
| Kmin (D) | 48.04 ± 4.53 | 50.46 ± 5.09 | 48.21 ± 3.23 | 44.63 ± 1.9 | <0.001 | (1,3) (2,3) | 43.24 ± 1.62 | <0.001 |
| | 47.3 (39, 65.05) | 49.7 (39, 65.05) | 48.15 (42.6, 57.87) | 45.35 (39.8, 46.95) | | | 43.35 (38.4, 46.7) | |
| Kmax (D) | 51.57 ± 5.02 | 54.2 ± 5.71 | 51.93 ± 3.76 | 47.71 ± 1.42 | <0.001 | (1,3) (2,3) | 44.26 ± 1.96 | <0.001 |
| | 50.8 (40.28, 64.14) | 54.2 (40.28, 62.0) | 51.1 (45.63, 64.14) | 47.92 (45, 49.8) | | | 44.3 (38.8, 55.7) | |
| Kmeans (D) | 49.81 ± 4.28 | 52.33 ± 4.42 | 50.07 ± 3.25 | 46.17 ± 1.54 | <0.001 | (1,3) (2,3) | 43.74 ± 1.67 | <0.001 |
| | 49 (40.7, 61.0) | 52.35 (40.7, 59.5) | 49.3 (46.75, 61.0) | 46.3 (42.85, 48.3) | | | 43.75 (38.6, 50.7) | |
| CCT (µm) | 468.75 ± 47.89 | 429.26 ± 41.61 | 476 ± 34.79 | 499.56 ± 35.88 | <0.001 | (1,2) (1,3) | 543.32 ± 32.5 | <0.001 |
| | 469 (352, 574) | 430 (352, 551) | 472 (401, 539) | 499 (437, 574) | | | 541.5 (405, 623) | |

KCN, keratoconus; K, keratometry; D, diopter; CCT, central corneal thickness; µm, micrometer
*Based on ANOVA (Bonferroni Post Hoc Multiple comparison); **Based on independent *T*-test

However, less frequency of KCN was observed in patients with Fars ethnicity (OR = 0.583, $P = 0.042$), higher levels of wealth indices (OR = 0.31, $P < 0.001$), and higher levels of education (OR = 0.18, $P = 0.024$).

Table 2 shows the comparison of clinical characteristics between the case and the control groups. As presented, higher risk of KCN was observed in patients who had a positive familial history in their first- (OR = 12.533, $P < 0.001$) and second-degree (OR = 7.52, $P < 0.001$) relatives, and in cases who had systemic diseases including migraine, hypertension, and thyroid disease (OR = 6.828, $P = 0.021$). In addition, patients with vernal keratoconjunctivitis (OR = 7.510, $P = 0.003$) and severe eye rubbing (OR = 10.625, $P < 0.001$) were found to be at a higher risk of KCN as compared with the healthy controls. No significant differences were observed when comparing the other factors between the two groups.

Description of topographic findings at different stages of KCN and the control group is summarized in Table 3. As shown, higher keratometric values (Kmin, Kmax, and K-means) and thinner central corneal thickness were observed in severe KCN patients as compared with the other stages of KCN and the normal controls ($P < 0.001$ for both).

Table 4 represents the effect of various factors on different stages of KCN. As shown, low wealth index was the only variable identified as associated factor among patients with severe KCN ($P = 0.019$). No statistically significant association was found when investigating other factors.

## DISCUSSION

In the present study, parental consanguinity, positive familial history in patients' first- and second-degree relatives, vernal keratoconjunctivitis, severe eye rubbing, and systemic diseases including migraine, hypertension, and thyroid disease were found as associated factors for KCN. On the other hand, lesser frequency of KCN was observed in patients with Fars ethnicity, higher levels of wealth indices and education.

We observed that KCN is more prevalent in cases who have positive familial history of KCN. It has been reported that 14% of patients with KCN have an affected family member which could be considered as evidence for the hereditary nature of KCN, which is in line with our observation.[31] Hashemi et al identified this significant association between the incidence of KCN and positive familial history.[32]

Furthermore, we observed that KCN patients had higher percentages of parental consanguinity, which is in line with previous studies reporting a high prevalence of KCN among populations of Pakistan, Western Mediterranean countries, and India who have a high percentage of consanguine marriages.[10, 15, 33, 34] Due to the

**Table 4.** The stages of keratoconus and possible associated factors for severity.

| Factors | Level | Total | Severity of KCN (n = 100) | | | P-value* |
|---|---|---|---|---|---|---|
| | | | Severe (n = 38) | Moderate (n = 28) | Mild (n = 34) | |
| Birthplace | North | 7 (7.0%) | 1 (2.6%) | 4 (14.3%) | 2 (5.9%) | 0.476 |
| | South | 4 (4.0%) | 1 (2.6%) | 2 (7.1%) | 1 (2.9%) | |
| | West | 31 (31.0%) | 13 (34.2%) | 7 (25.0%) | 11 (32.4%) | |
| | East | 1 (1.0%) | 0 (0.0%) | 1 (3.6%) | 0 (0.0%) | |
| | Center | 57 (57.0%) | 23 (60.5%) | 14 (50.0%) | 20 (58.8%) | |
| Patient's ethnicity | Fars | 28 (28.0%) | 11 (28.9%) | 7 (25.0%) | 10 (29.4%) | 0.916 |
| | Others | 72 (72.0%) | 27 (71.1%) | 21 (75.0%) | 24 (70.6%) | |
| Parental Consanguinity | Yes | 40 (40.0%) | 18 (47.4%) | 12 (42.9%) | 10 (29.4%) | 0.280 |
| | No | 60 (60.0%) | 20 (52.6%) | 16 (57.1%) | 24 (70.6%) | |
| Patient's education (yr) | 0–6 | 5 (5.0%) | 3 (7.9%) | 2 (7.1%) | 0 (0.0%) | 0.559 |
| | 6–12 | 65 (65.0%) | 25 (65.8%) | 17 (60.7%) | 23 (67.6%) | |
| | >12 | 30 (30.0%) | 10 (26.3%) | 9 (32.1%) | 11 (32.4%) | |
| Wealth index | Rich | 19 (19.0%) | 2 (5.3%) | 5 (17.9%) | 12 (35.3%) | 0.019 |
| | Normal | 36 (36.0%) | 14 (36.8%) | 10 (35.7%) | 12 (35.3%) | |
| | Poor | 45 (45.0%) | 22 (57.9%) | 13 (46.4%) | 10 (29.4%) | |
| KCN in family | No | 60 (60.0%) | 24 (63.2%) | 18 (64.3%) | 18 (52.9%) | 0.096 |
| | First-degree | 28 (28.0%) | 13 (34.2%) | 7 (25.0%) | 8 (23.5%) | |
| | Second-degree | 12 (12.0%) | 1 (2.6%) | 3 (10.7%) | 8 (23.5%) | |
| Ocular diseases | Glaucoma | 7 (7.0%) | 2 (5.3%) | 4 (14.3%) | 1 (2.9%) | 0.826 |
| | VKC | 10 (10.0%) | 4 (10.5%) | 2 (7.1%) | 4 (11.8%) | |
| | No | 83 (83.0%) | 32 (84.2%) | 22 (78.6%) | 29 (85.3%) | |
| Eye rubbing | Never | 25 (25.0%) | 8 (21.1%) | 6 (21.4%) | 11 (32.4%) | 0.373 |
| | Low | 50 (50.0%) | 19 (50.0%) | 13 (46.4%) | 18 (52.9%) | |
| | High | 25 (25.0%) | 11 (28.9%) | 9 (32.1%) | 5 (14.7%) | |

KCN, keratoconus; VKC, vernal keratoconjunctivitis
*Based on Chi-square test

prevalence of consanguine marriages registering as high as 40% among the Iranian population,[35] more comprehensive investigations of the Iranian population might be necessary to better understand the role of inter family marriage on KCN.

In the present study, we did not detect significant associations between allergy, asthma, eczema, and KCN, however atopic diseases have been reported as one of the probable risk factors for KCN.[10, 12, 32] This association was not detected in a study by Bawazeer et al,[36] who believed that KCN is not directly related to atopic diseases. They believed, however, that it happens secondary to eye rubbing, which was also a factor significantly associated with KCN in our study. Furthermore, eye rubbing was reported as a known risk factor of KCN in a meta-analysis and systematic review conducted by Hashemi et al.[32]

Naderan et al[37] have reported that KCN patients with vernal keratoconjunctivitis or allergic conjunctivitis have significantly thinner and steeper corneas in comparison with non-allergic KCN patients. It was concluded that these patients

experience more severe KCN and should be closely followed-up and intensively treated.

Regarding the geographical location, it was found that people living in the west regions of Iran were at a higher risk of KCN. However, Kelly et al[18] and Millodot et al[38] showed higher prevalence of KCN among individuals living in tropical countries located around the equator, in comparison with European and North American countries. It can be considered as strong evidence of the significant association between KCN and exposure to sunlight and ultraviolet radiation. However, this significant relationship has not been found in other studies.[16, 17]

Regarding different Iranian ethnicities, Fars people were found to be at lesser risk of KCN, which is in line with the findings reported by Hashemi et al,[39] showing a higher prevalence of KCN among Arab, Turk, Kurd, and Lur ethnicities as compared to the Fars population.

Regardless of the sunlight exposure, some studies have reported less prevalence of KCN in several geographical regions like Northern Europe,[10, 20, 21] Northern America,[10, 22, 23] and Japan[10, 24] as compared to India, China,[10, 25, 26] and Eastern Mediterranean countries.[10, 27, 28]

In addition, a strong relationship was found in children who live in families with low socioeconomic status or low levels of education,[14] as children living in poor families will be dealing with problems of contaminations found in the air, water, and waste.[40] We also noticed less frequency of KCN among people with higher levels of wealth indices and education.

Age is another probable associated factor with a positive relationship with the progression of KCN. Due to the incomprehensible visual symptoms in the early stages of KCN, patients are usually diagnosed in older ages with more severe stages of the disease.[10, 13, 41]

In the current study, a significant association was found between KCN and some systemic diseases including migraine, hypertension, and thyroid diseases. This finding was inconclusive due to the limited numbers of affected patients.

One of the possible drawbacks of the present study is the selection bias regarding the participation of KCN patients with different levels of wealth status.

In summary, based on our findings, severe eye rubbing, vernal keratoconjunctivitis, parental consanguinity and positive familial history of KCN, low socioeconomic status and low levels of education were significantly associated with KCN in the Iranian population.

## Acknowledgements

This article is taken from the disease registry, titled "The Iranian National Registry of Keratoconus (KCNReg®)", code number IR.SBMU.ORC.REC.1397.12 from the ethics committee, which was supported by the Deputy of Research and Technology at Shahid Beheshti University of Medical Sciences, Tehran, Iran (http://dregistry.sbmu.ac.ir).

## Financial Support and Sponsorship

None.

## Conflicts of Interest

The authors have no conflict of interest with the subject matter of this manuscript.

## *REFERENCES*

1. Davidson AE, Hayes S, Hardcastle AJ, Tuft SJ. The pathogenesis of keratoconus. *Eye* 2014;28:189–195.
2. Krachmer JH, Feder RS, Belin MW. Keratoconus and related noninflammatory corneal thinning disorders. Surv Ophthalmol 1984;28:293–322.
3. Rabinowitz YS. Keratoconus. *Surv Ophthalmol* 1998;42:297–319.
4. Kennedy RH, Bourne WM, Dyer JA. A 48-year clinical and epidemiologic study of keratoconus. *Am J Ophthalmol* 1986;101:267–273.
5. Jonas JB, Nangia V, Matin A, Kulkarni M, Bhojwani K. Prevalence and associations of keratoconus in rural Maharashtra in central India: The central India eye and medical study. *Am J Ophthalmol* 2009;148:760–765.
6. Gokhale NS. Epidemiology of keratoconus. *Indian J Ophthalmol* 2013;61:382–383.
7. Woodward MA, Blachley TS, Stein JD. The association between sociodemographic factors, common systemic diseases, and keratoconus: An analysis of a nationwide healthcare claims database. *Ophthalmology* 2016;123:457–65.e2.
8. Ziaei H, Jafarinasab MR, Javadi MA, Karimian F, Poorsalman H, Mahdavi M, et al. Epidemiology of keratoconus in an Iranian population. *Cornea* 2012;31:1044–1047.
9. Aydin Kurna S, Altun A, Gencaga T, Akkaya S, Sengor T. Vision related quality of life in patients with keratoconus. *J Ophthalmol* 2014;2014:694542.

10. Gordon-Shaag A, Millodot M, Shneor E, Liu Y. The genetic and environmental factors for keratoconus. *Biomed Res Int* 2015;2015:795738.
11. Carlson AN. Expanding our understanding of eye rubbing and keratoconus. *Cornea* 2010;29:245.
12. Kaya V, Karakaya M, Utine CA, Albayrak S, Oge OF, Yilmaz OF. Evaluation of the corneal topographic characteristics of keratoconus with orbscan II in patientswith and without atopy. *Cornea* 2007;26:945–948.
13. Ihalainen A. Clinical and epidemiological features of keratoconus genetic and external factors in the pathogenesis of the disease. *Acta Ophthalmol Suppl* 1986;178:1–64.
14. Naderan M, Shoar S, Rezagholizadeh F, Zolfaghari M, Naderan M. Characteristics and associations of keratoconus patients. *Cont Lens Anterior Eye* 2015;38:199–205.
15. Gordon-Shaag A, Millodot M, Essa M, Garth J, Ghara M, Shneor E. Is consanguinity a risk factor for keratoconus? *Optom Vis Sci* 2013;90:448–454.
16. Georgiou T, Funnell CL, Cassels-Brown A, O'Conor R. Influence of ethnic origin on the incidence of keratoconus and associated atopic disease in Asians and white patients. *Eye* 2004;18:379–383.
17. Pearson AR, Soneji B, Sarvananthan N, Sandford-Smith JH. Does ethnic origin influence the incidence or severity of keratoconus? *Eye* 2000;14:625–628.
18. Kelly TL, Williams KA, Coster DJ, Australian Corneal Graft Registry. Corneal transplantation for keratoconus: A registry study. *Arch Ophthalmol* 2011;129:691–697.
19. Rabinowitz YS. The genetics of keratoconus. *Ophthalmol Clin North Am* 2003;16:607–620.
20. Gorskova EN, Sevost'ianov EN. Epidemiology of keratoconus in the Urals. *Vestn Oftalmol* 1998;114:38–40. In Russian
21. Nielsen K, Hjortdal J, Pihlmann M, Corydon TJ. Update on the keratoconus genetics. *Acta Ophthalmol* 2013;91:106–113.
22. Kennedy RH, Bourne WM, Dyer JA. A 48-year clinical and epidemiologic study of keratoconus. *Am J Ophthalmol* 1986;101:267–273.
23. Hofstetter HW. A keratoscopic survey of 13,395 eyes. *Am J Optom Arch Am Acad Optom* 1959;36:3–11.
24. Tanabe U, Fujiki K, Ogawa A, Ueda S, Kanai A. Prevalence of keratoconus patients in Japan. *Nihon Ganka Gakkai Zasshi* 1985;89:407–411. In Japanese
25. Jonas JB, Nangia V, Matin A, Kulkarni M, Bhojwani K. Prevalence and associations of keratoconus in rural Maharashtra in central India. *American J Ophthalmol* 2009;148:760–765.
26. Xu L, Wang YX, Guo Y, You QS, Jonas JB. Prevalence and associations of steep cornea/keratoconus in greater Beijing. *PLoS One* 2012;7:e39313.
27. Mohd-Ali B, Abdu M, Yaw CY, Mohidin N. Clinical characteristics of keratoconus patients in Malaysia: A review from a cornea specialist centre. *J Optom* 2012;5:38–42.
28. Shneor E, Millodot M, Gordon-Shaag A, Essa M, Anton M, Barbara R, et al. Prevalence of keratoconus amoung young Arab students in Israel. *Int J keratoconus Ectatic Corneal Dis* 2014;3:9–14.
29. Owens H, Gamble G. A profile of keratoconus in New Zealand. *Cornea* 2003;22:122–125.
30. Alio J-L, Vega-Estrada A, Sanz-Garcia P, Duran-Garcia M-L, Maldonado M. keratoconous management guidelines. *Int J Keratoconous Ectatic Corneal Dis* 2015;4:1–39.
31. Karimian F, Aramesh S, Rabei HM, Javadi MA, Rafati N. Topographic evaluation of relatives of patients with keratoconus. *Cornea* 2008;27:874–878.
32. Hashemi H, Heydarian S, Hooshmand E, Saatchi M, Yekta A, Aghamirsalim M, et al. The prevalence and risk factors for keratoconous: A systematic review and meta-analysis. *Cornea* 2020;39:263–270.
33. Al-Gazali L, Hamamy H. Consanguinity and dysmorphology in Arabs. *Hum Hered* 2014;77:93–107.
34. Saadat M, Ansari-Lari M, Farhud DD. Consanguineous marriage in Iran. *Ann Hum Biol* 2004;31:263–269.
35. Najmabadi H, Hu H, Garshasbi M, Zemojtel T, Abedini SS, Chen W, et al. Deep sequencing reveals 50 novel genes for recessive cognitive disorders. *Nature* 2011;478:57–63.
36. Bawazeer AM, Hodge WG, Lorimer B. Atopy and keratoconus: A multivariate analysis. *Br J Ophthalmol* 2000;84:834–836.
37. Naderan M, Rajabi MT, Zarrinbakhsh P, Bakhshi A. Effect of allergic diseases on keratoconus severity. *Ocul Immunol Inflamm* 2017;25:418–423.
38. Millodot M, Shneor E, Albou S, Atlani E, Gordon-Shaag A. Prevalence and associated factors of keratoconus in Jerusalem: A cross-sectional study. *Ophthalmic Epidemiol* 2011;18:91–97.
39. Hashemi H, Khabazkhoob M, Fotouhi A. Topographic keratoconus is not rare in an Iranian population: The Tehran Eye Study. *Ophthalmic Epidemiol* 2013;20:385–391.
40. Powell DL, Stewart V. Children. The unwitting target of environmental injustices. *Pediatr Clin North Am* 2001;48:1291–1305.
41. Weed KH, MacEwen CJ, McGhee CN. The variable expression of keratoconus within monozygotic twins: Dundee University Scottish Keratoconus Study (DUSKS). Cont Lens Anterior Eye 2006;29:123–126.

Original Article

# Histopathology of Corneal Lenticules Obtained from Small Incision Lenticule Extraction (SMILE) versus Microkeratome Excision

**Salwa Abdelkawi Ahmed[1], PhD; Ibrahim Mohi Eldin Taher[2], MD; Dina Fouad Ghoneim[2], PhD; Mohammed Ahmed Elnaggar[2], MRCsEd; Aziza Ahmed Hassan[2], PhD**

*[1]Department of Vision Science, Biophysics and Laser Science Unit, Research Institute of Ophthalmology, Giza, Egypt*
*[2]Ophthalmic Unit, National Institute of Laser Enhanced Science, Cairo University, Egypt*

**ORCID:**

*Salwa Abdelkawi Ahmed: https://orcid.org/0000-0002-3649-8328*

## Abstract

**Purpose:** To study the alterations on the lenticules extracted after femtosecond (Femto) small incision lenticule extraction (SMILE) versus the corneal free cap removed using a microkeratome.

**Methods:** The visuMax (500 kHz; laser energy: 180 nJ) was used for small-incision lenticule extraction. Free caps from human cadaveric corneas were excised by microkeratome. The collected lenticules were examined with the light and transmission electron microscope (TEM) for histological analysis, DNA fragmentation was assessed by agarose gel electrophoresis, DNA damage was evaluated using comet assay, and corneal proteins secondary structure was assessed by Fourier transform infrared spectroscopy (FTIR).

**Results:** Light microscopic examination showed the presence of more edematous stroma under Femto SMILE than under free cap with a percentage change of 101.6%. In the Femto SMILE group, TEM examination showed pyknotic keratocytes, disruption, and cavitation of the collagen arrays stromal area under Femto SMILE. The DNA fragmentation for the Femto SMILE group revealed one undefined band with a size of 1.1 Kbp. The comet assay analysis indicated the presence of 3% and 8.0% tailed cells for the free cap and Femto SMILE groups, respectively. The tail lengths were 1.33 $\pm$ 0.16 and 1.67 $\pm$ 0.13 µm ($P < 0.01$), the percentage of tail DNA was 1.41 $\pm$ 0.18% ($P < 0.01$) and 1.72 $\pm$ 0.15%, and the tail moments were 1.88 $\pm$ 0.12 AU and 2.87 $\pm$ 0.14 AU ($P < 0.001$) for the free cap and Femto SMILE groups, respectively. FTIR spectroscopy of the Femto smile group revealed disorders in the secondary and tertiary structure of the proteins.

**Conclusion**: Femto SMILE technique induced more structural changes, DNA fragmentation, DNA damage, and corneal proteins secondary structure alteration than those induced by a microkeratome cutting. These changes may be attributed to the deep penetration of high energy levels to the corneal layer. These findings may highlight the potential impact of the Femto SMILE on the cornea and the necessity for managing the laser parameters used.

**Keywords:** Comet Assay; DNA Fragmentation; Femto SMILE; Fourier Transform Infrared Spectroscopy; Histological Analysis

*J Ophthalmic Vis Res* 2023; 18 (1): 24–33


© 2023 Ahmed et al. This is an open access article distributed under the Creative Commons Attribution License | Published by Knowledge E

## INTRODUCTION

Recently, considerable attention has been paid to the Femtosecond laser (FS) in the infrared range (1053 nm and pulse duration $10^{--15}$ s). FS laser causes photodisruption and photoionization effects on sensitive ocular tissues such as cornea,[1]which generate an intensifying cloud of ionized molecules and free electrons that disrupt the treated tissue.[2] The femtosecond (Femto) small incision lenticule extraction (SMILE) technique in refractive surgery has excellent cutting accuracy and safety as compared with the microkeratome flap creation in laser in-situ keratomileusis.[3]

FS laser has been employed in many applications, such as laser-assisted anterior and posterior lamellar keratoplasty, excision of donor buttons in endothelial keratoplasty, customized trephination in penetrating keratoplasty, wound construction, capsulorhexis, and cataract surgery.[4–6] In addition, FS laser is used in corneal refractive surgeries such as LASIK flap creation, implantation of intrastromal corneal ring segments, astigmatic keratotomy, femtosecond lenticule extraction (FLEx), intrastromal presbyopia correction, and small-incision lenticule extraction (SMILE).[7, 8]

The SMILE technique has gained importance for its application in corneal refractive surgery. It is performed entirely with the FS laser, without flap creation, avoiding all flap-related complications and reducing the inflammation and postoperative dry eye syndrome.[9–11]

Previous researches on the Femto SMILE technique were focused only on the ultrastructure change or the efficacy and safety at the clinical levels without considering the change in the protein levels or the genetic damage of lenticules.[12–14]

**Correspondence to:**

Salwa Abdelkawi Ahmed, PhD. Department of Vision Science, Biophysics and Laser Science Unit, Research Institute of Ophthalmology, Giza 12511, Egypt.
E-mail: saelkawi@yahoo.com

Received: 23-05-2022 Accepted: 05-12-2022

**Access this article online**

**Website:** https://knepublishing.com/index.php/JOVR

**DOI:** 10.18502/jovr.v18i1.12722

Several studies have investigated the refractive, optical, and histological outcomes of Femto smile procedures.[15] Other studies determined the best cutting parameters by using high frequency, small spot distances, and low pulse energy.[16, 17]

The earliest scanning electron microscope study (SEM) showed smooth cuts by applying 500 nJ pulse energy, 200 kHz, and a spot distance of 5.0 μm (WaveLight UltraFlap– Femtosecond laser).[18] However, using 200 kHz, 185 nJ pulse energy, and 9.0 $\mu m^2$ spot separation (VisuMax laser) showed lower surface quality for the lenticules of an animal model than those obtained with a mechanical microkeratome.[19]

Although using a higher frequency at 500 kHz (VisuMax femtosecond), 130 nJ pulse energy, and 9.0 $\mu m^2$ spot separation improved the surface quality viewed in 12 cadaveric eyes, cavitation bubbles and rough patches were still seen in their samples.[12, 20]

In another recent study by Ziebarth et al using the VisuMax femtosecond laser at 500 kHz, 130 nJ pulse energy, and a closer spot separation of 2.5×2.5 μm, the procedure showed an easy extraction and smooth lenticules surfaces.[20, 21] Another study by Ang et al on 30 Femto SMILE lenticules of human corneas compared with the microkeratome cuts assessed by the SEM and TEM[12, 21] found that Femto SMILE lenticules showed more surface roughness, tissue bridges, and cavitation changes which was in contrast with the study of Ziebarth et al.[20, 21] A comparison among those three previous studies on SMILE lenticules is not possible, as different spot sizes were used.[12, 20, 21]

The current study aimed to evaluate the morphological differences, DNA fragmentation, DNA damage, and the deformation in proteins' structure in human corneal lenticules after the Femto SMILE laser procedure versus the corneal free cap procedure using the microkeratome.

This is an open access article distributed under the Creative Commons Attribution License, which permits unrestricted use, distribution, and reproduction in any medium, provided the original work is properly cited.

**How to cite this article:** Ahmed SA, Taher IME, Ghoneim DF, Elnaggar MA, Hassan AA. Histopathology of Corneal Lenticules Obtained from Small Incision Lenticule Extraction (SMILE) versus Microkeratome Excision. J Ophthalmic Vis Res 2023;18:24–33.

## METHODS

Ten corneas of human cadavers' donors were obtained from Al-Kaser Elaini eye bank. The mean donor age was 50 ± 10 years, the death-to-tissue harvest time was <24 hr, and the mean time from death to the surgical procedure was 6 ± 5 days. Ten myopic patients (–4 D to –9 D) were assigned for Femto SMILE laser (*n* = 20 eyes) using VisuMax femtosecond laser system for SMILE at 100 µm depth. This work was conducted per the Declaration of Helsinki as revised in 2013 and accepted by the local Scientific Research Ethics Committee of our institute (Approval no. CU-NILES/01/22). The removed lenticules were examined by light microscopy, transmission electron microscope (TEM), agarose gel electrophoresis for DNA fragmentation analysis, comet assay for DNA damage, and Fourier transform infrared spectroscopy (FTIR) for analysis of corneal proteins secondary structure.

### Creation of Free Caps from the Donor Cornea

The donor cornea was placed with the epithelial side facing upward on the tissue pedestal of the artificial anterior chamber (Coronet, Network Medical product Ltd., UK). Centration of the cornea was adjusted by using the cross-hair, and the tissue retainer was selected. The tissue retainer was dropped gently onto the tissue pedestal, and the compression head was placed over the tissue retainer and secured. As soon as the desired pressure was achieved, the flow regulator was locked. Free caps with a thickness of 130 µm were created using a microkeratome (Moria Surgical M2, Antony, France) and stored in cornea storage medium "Optisol" ( Bausch & Lomb Incorporated – Rochester, NY, USA) at 4°C .

### Small-incision Lenticule Extraction (Smile)

Femto SMILE operations were performed using the VisuMax® femtosecond laser system (Carl Zeiss Meditec AG, Jena, Germany) with a laser frequency of 500 kHz and laser energy of 180 nJ and multiple pulses duration of 220–280 fs. The obtained cap thickness was 130 µm, 7.5 mm cap diameter, and 6.3 mm optical zone of lenticule.[20]

### Histological Examination

The cornea specimens were fixed by immersion in formaldehyde (4%) and glutaraldehyde (1%) for 3 hr in phosphate buffer solution (PBS, pH 7.2) at 4°C. Then, samples were post-fixed in 2% Osmic oxide in the PBS at 4°C for 2 hr. After washing the specimen in the PBS and dehydrating at 4°C using a graded series of ethanol, they were embedded in pre-labeled (plastic) capsules to be polymerized for 48 hr. The specimens were trimmed and cut to semi-thin sections (1 µm) using Lab Knife Blade (LKB) ultra-microtome to be visualized by the light microscope. For TEM, thin sections were cut (30–100 nm) using an ultramicrotome and mounted on copper grids. Next, the grids were stained with uranyl acetate for 20 min and lead citrate for 10 min. The grids were then examined by JEOL 100 CX TEM ( JEOL Inc., Peabody, Massachusetts, USA). The area percentage and the means ± standard deviation of the edematous areas in each group were measured using ImageJ software (NIH, USA).[22]

### DNA Fragmentation Analysis

Agarose gel electrophoresis was employed to compare fragmented and intact DNA fractions of the human corneal lenticules according to Dash et al.[23] Twenty microliters of the DNA samples and markers were loaded on the 1% agarose gel wells containing 0.5 mg/ml of ethidium bromide in TBE buffer (pH 8.0). A gel electrophoresis device **(**Model Horizon 58, Gibco BRL, USA) was used to run the electrophoresis and viewed using a Bio-Rad$^{TM}$ gel documentation system with the analysis software Quantity One®.

### Comet Assay for DNA Damage

Comet assay was employed according to Olive and Banáth to evaluate the extent of DNA damage.[24] Briefly, corneas were minced in phosphate buffer saline ($Ca^{2+}$- and $Mg^{2+}$-free) to form a single-cell suspension ($2\times10^5$ cell/ml) and kept in an ice-cold medium. Next, agarose slides were prepared by covering the slides with a thin layer of 1% low-gelling-temperature agarose (Sigma Uldrich, USA) and allowed to dry.

The cornea cells suspension (0.4 ml) was mixed with 1.2 ml of 1% agarose at 40°C. Then, 1.2 ml from

the mixture was spread on the precoated agarose slides and allowed to solidify.

Cell lysis was performed using a cold fresh alkaline solution (pH > 13) at 4°C overnight in the dark. The slides were removed and rinsed with an alkaline solution (pH > 13) for 20 min. Then, the slides were immersed in the electrophoresis chamber and operated for 25 min at 0.7 V/cm, 40 mA, and 20 V.

The slides were then removed and stained with propidium iodide solution (2.5 μg/ml) for 20 min (Sigma Uldrich; USA). Next, the DNA comets were visualized and photographed using a Nikon Optiphot-2 epifluorescence microscope with an attached camera (Sony CCD-IRIS, Minato, Tokyo, Japan) and connected to comet assay II software (Perceptive Instruments, UK). The software analyzes duplicate comet images for tail length (μm), percent of DNA in the tail (%), and tail moment. The results of the tail length, % tail DNA, and tail moments were calculated as the mean and standard deviation (Mean ± SD) for all experimental groups. A one‐way analysis of variance and the Student (*t*) test were employed to assess the contrast between the free cap and Femto SMILE groups.

### FTIR Spectroscopic Analysis of Corneal Proteins

In order to verify the validity of both agarose electrophoresis and comet assay, FTIR spectroscopy for corneal proteins was carried out. FTIR spectroscopy delivers evidence about the secondary and tertiary structure of corneal proteins by aiming radiation into the infrared range which is absorbed by the sample. Each sample has a distinct group of absorption bands in its infrared spectrum. The most characteristic bands found in the infrared spectra of corneal proteins and polypeptides are Amide I and Amide II. These ascend from the amide bonds that link the amino acids. The absorption related to the Amide I band leads to stretching vibrations of the C = O bond of the amide, and absorption related to the Amide II band leads primarily to bending vibrations of the N–H bond. Both C = O and the N–H bonds are involved in the hydrogen bonding between these two different elements of the secondary structure. Moreover, the change in the vibrational frequencies of both the Amide I and Amide II bands are sensitive to the changes in the secondary and tertiary structure of the corneal proteins.[25]

Tertiary structure of the protein is originated when the elements of the secondary structure are arranged tightly together to form the well-defined three dimensional shape. The sidechains buried inside a folded protein are packed tightly together and must interact favorably in order to remain folded and function properly. Changes in the lenticules' protein tertiary structure were determined by comparing ratios of amide II to amide I bond intensities. This tertiary structural change indicates a transition from a folded to an unfolded state.[26]

First, corneas were lyophilized thoroughly by an instant insertion into liquid nitrogen (–196°C). Next, the corneas were crushed into a powder by using a Teflon hand homogenizer for proteins extraction. Finally, the KBr disks were prepared by mixing the obtained corneal powder with potassium bromide (KBr) powder (98 mg KBr: 2 mg of the powdered cornea). The FTIR spectra in the range of 4000–1000 $cm^{--1}$were obtained using a Thermo Nicolet iS5 FTIR spectrometer (USA), baseline corrected, and operated under continuous dry nitrogen gas.

### Statistical Evaluation

The area percentages of the edematous lenticules and their mean ± standard deviation were quantified using imageJ software analysis. The variations between the free cap and Femto SMILE groups were analyzed employing a one‐way analysis of variance and Student's *t*‐test for comparing between the two groups. The result was considered significant at $P < 0.05$.

## RESULTS

### Histological Examination

Light microscopic examination for corneal free caps showed slight stromal edema [Figure 1a], while the Femto SMILE samples showed homogeneous and more edematous stroma (arrows) [Figure 1b]. The area percentage was 3.19% for the free cap group and 6.43% for the SMILE group with a percentage change of 101.6%. Moreover, the mean values ± standard deviation of the edematous areas for the free cap group was 7.9 ± 6.6 $\mu m^2$and for the Femto SMILE group was 20.3 ± 13.6 $\mu m^2$with a percentage change of 157% ($P < 0.001$).

**Table 1.** Tail length, tail DNA (%), and tail moment for free cap group and Femto SMILE group obtained by comet assay images analysis.

| | Tailed% | Untailed% | Tail length (μm) | Tail DNA (%) | Tail moment (AU) |
|---|---|---|---|---|---|
| **Free cap** | 3 | 97 | 1.33 ± 0.16 | 1.41 ± 0.18 | 1.88 ± 0.12 |
| **Femto SMILE** | 8 | 92 | 1.67 ± 0.13* | 1.72 ± 0.15* | 2.87 ± 0.14* |

*Significant difference
SMILE, small incision lenticule extraction

**Table 2.** Wavenumber ($cm^{-1}$) for FTIR spectra bands for free cap and Femto SMILE laser groups, in the NH-OH, CH stretching, Fingerprint and Amide I regions.

| Bands | Free cap wavenumber ($cm^{-1}$) | Femto SMILE wavenumber ($cm^{-1}$) |
|---|---|---|
| **NH-OH** | 3452 ± 2 | 3290 ± 2 |
| **CH stretching** | 2962 ± 2 | 2938 ± 2* |
| **Amide II CH2 bending** $_{assym}PO_2$ $_{sym}PO_2$ | 1558 ± 3 1457 ± 2 1240 ± 2 1070 ± 1 | 1530 ± 2* 1450 ± 1 1388 ± 2* 1238 ± 2 1056 ± 2* |
| **Amide I** | 1643 ± 2 | 1640 ± 1 |

*Statistically significant
SMILE, small incision lenticule extraction

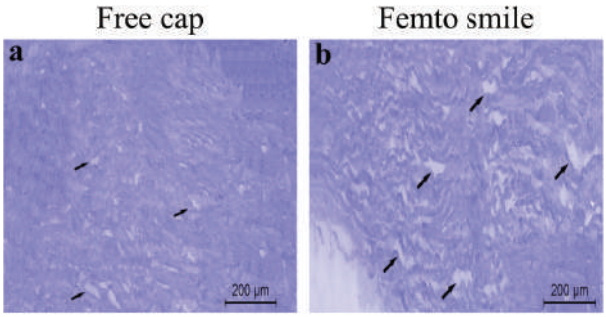


**Figure 1.** Light microscope picture for (a) free cap showing slight stromal edema and (b) Femto SMILE showing homogeneous and more edematous stroma (arrows).

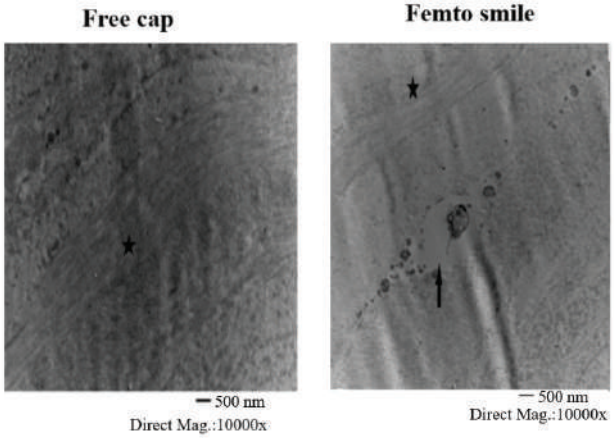


**Figure 2.** Transmission electron micrograph of (a) free cap showing more regular arrangement of the stromal lamella and intact collagen bundles and (b) Femto SMILE showing disruption of the collagen arrays (*) as well as pyknotic keratocyte (arrow).

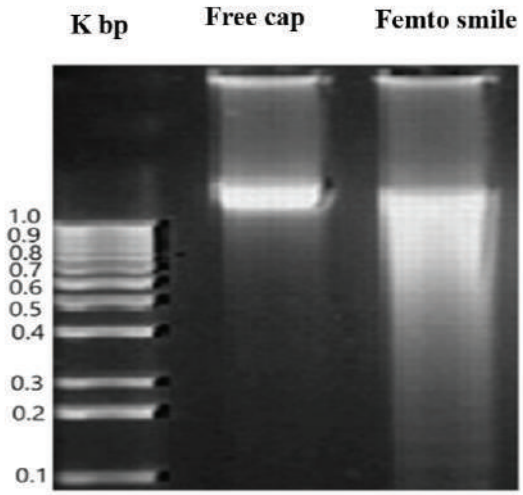


**Figure 3.** 0.1% Agarose gel electrophoresis for analysis of DNA fragmentation showed a well-defined band for the free cap and an undefined band for the Femto SMILE group. The first band represents the DNA markers.
Kbp, kilo base pair.

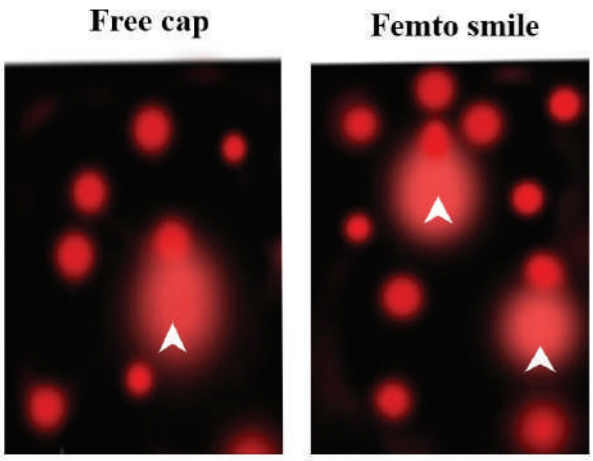


**Figure 4.** Representative Comet images of human cornea for free cap and Femto SMILE group showing a circular head corresponding to the undamaged DNA that remains in the cavity and a tail of damaged DNA (arrow head). Propidium iodide solution (2.5 µg/ml) gel Stain, Scale bars: 100 µm.

The TEM examination for the corneal free caps showed a more regular arrangement of the stromal lamella, and the collagen fibers appeared as arranged threads in contrast to the Femto SMILE specimens that showed disruption and cavitation of the collagen arrays and pyknotic keratocyte [Figure 2].

## DNA Fragmentation Analysis

Agarose gel electrophoresis for corneal DNA of the free caps and the Femto SMILE laser is shown in Figure 3. The typical ladder pattern of DNA markers was separated into 10 fragments ranging from 1.0 Kbp to 0.1 Kbp. An intense ladder was noticed for the free caps with a size of 1.150 Kbp. In comparison, the ladder reflects one undefined band with a size of 1.1 Kbp for the Femto SMILE sample.

## The Comet Assay Analysis

The photograph of the comet assay [Figure 4] shows the circular head containing the high

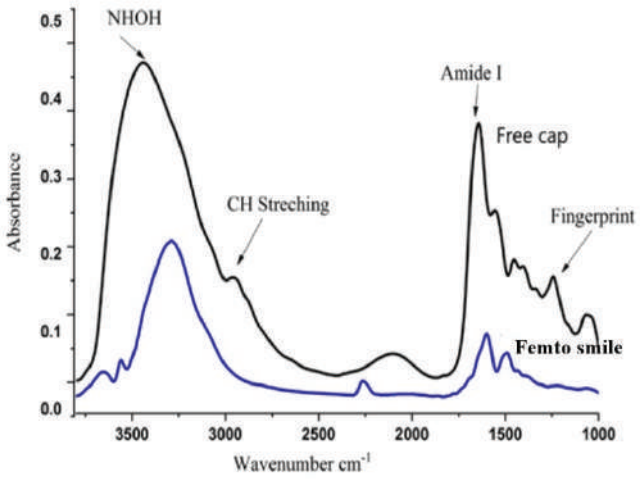


**Figure 5.** FTIR spectroscopic analysis for the corneal proteins showing the difference between the spectral profile for the free cap group and Femto SMILE groups in the NH-OH (3000–3700 $cm^{-1}$), CH stretching (2800–3000 $cm^{-1}$), Amide I (1700–1800 $cm^{-1}$), and fingerprint regions (1000–1800 $cm^{-1}$).

molecular weight of the undamaged DNA while the comet tail represents the migrating fragments of the damaged DNA (arrow head). The percentage of the tailed cell for the free cap group was less than the Femto SMILE group. Moreover, the mean tail lengths were 1.33 ± 0.16 µm and 1.67 ± 0.13 µm for the free cap and Femto SMILE groups, respectively. Additionally, the percentage of tail DNA was 1.41 ± 0.18% and 1.72 ± 0.15% for the free cap and Femto SMILE groups, respectively [Table 1]. The tail moment, which is the multiplication of the percent DNA in the tail by the tail length, was 1.88 ± 0.12 AU for free cap and 2.87 ± 0.14 AU for Femto SMILE (AU: Arbitrary unit). Furthermore, the percentage difference between the free cap group and the Femto SMILE group was 22.7% ($P < 0.01$) for the tail lengths, 19.8% ($P < 0.01$) for the percentage of DNA in the tail, and 41.7% ($P < 0.001$) for the tail moment, respectively.

### FTIR Spectroscopic Analysis for the Lenticules' Proteins

The lenticular proteins were analyzed for the spectral regions at 3700–3000 $cm^{-1}$, 3000–2800 $cm^{-1}$, 1800–1000 $cm^{-1}$, and 1700–1600 $cm^{-1}$, corresponding to NH-OH stretching, CH stretching, fingerprint, and amide I regions, respectively. The profile of the free cap group [Figure 5] revealed the presence of two peaks centered at 3452 $cm^{-1}$ and 2962 $cm^{-1}$ corresponding to the NH-OH group and CH stretching group, respectively. Moreover, another five peaks were centered at 1558 $cm^{-1}$, 1457 $cm^{-1}$, 1240 $cm^{-1}$, 1070 $cm^{-1}$, and 1643 $cm^{-1}$ concerning amide II, CH2 bending, $_{assym}PO_2$, and $_{sym}PO_2$ and amide I, respectively. In the Femto SMILE group, the NH–OH wavenumber had significantly changed and shifted to 3290 $cm^{-1}$, and the CH stretching region had shifted to 2938 $cm^{-1}$. Moreover, the fingerprint region showed several significant changes in wavenumber at 1558 $cm^{-1}$ (Amide II) and was shifted to 1530 $cm^{-1}$; 1070 $cm^{-1}$ corresponding to $_{sym}PO_2$was shifted to 1056 $cm^{-1}$, the appearance of 1388 $cm^{-1}$ corresponding to $COO_{sym}$[Table 2]. In addition, ratios of amide II to amide I bond intensities were 0.95 and 0.93 for the free cap group and Femto SMILE group, respectively.

## DISCUSSION

In this study, we concluded that the histological analysis of human corneal lenticules could be a model of the alteration in the rest of the cornea. Using the light microscope, the Femto SMILE samples showed more stromal edema than the free cap samples with an area percentage of 6.43% and 3.19%, respectively. Moreover, pyknotic keratocytes, and disrupted

collagen were detected in the Femto SMILE group with TEM examination. Furthermore, both light microscope and TEM results for the lenticules

have been promising as they have shown lower surface quality cavitation bubbles, more surface roughness, and tissue bridges than those obtained with a mechanical microkeratome.[12, 19, 20]

This work focused not only on the histological changes that occurred in the extracted lenticules after Femto SMILE laser and free cap procedures but also on the alteration in the corneal proteins through DNA fragmentation analysis, comet assay, and FTIR spectroscopy.

The agarose gel electrophoresis offers a technique for the separation of the fragmented and the intact DNA fractions.[27] In the free cap group, the appearance of a distinctive band in electrophoresis analysis without any fragmentation indicates the absence of apoptotic cells or DNA cleavage. In contrast, the Femto SMILE group pattern shows a change, appearing as an undefined band without any fragmentation. So far, the significance of this finding has not been clear as it does not enable us to determine the exact effect on the DNA of the lenticule. In this regard, the comet assay has been used to analyze DNA damage in the cells of the lenticules. The amount of DNA that migrates from the nucleus cavity measures the amount of DNA damage in the cell.[28]In this study, the comet image analysis compares the two signals obtained from undamaged and damaged DNA, the longer and brighter the tail, the higher the level of damage. Based on this result, the Femto SMILE laser group has more DNA breaks than the free cap group. The DNA breaks can be induced by many factors such as exposure to ultraviolet, ionizing radiation, X-rays, chemicals, pollutants, and oxidative stress.[29–33] High oxidative stress is the most probable cause for the elevated level of DNA breaks. It ensues under a condition of light exposure, high energy consumption, or a weakening of coping ability.[34, 35]These factors result in abnormality in the cellular metabolic process.[36] Furthermore, this finding suggested that the Femto SMILE group was exposed to the laser photodisruption effect. In this process, the evaporation of microscopic volumes of tissue results in cavitation gas bubbles (carbon dioxide and water).

The vibrational frequency obtained from the FTIR spectra for the lenticules is a measure of the changes in the molecular structure. Hence, lenticular proteins were analyzed for the different spectral regions, namely NH–OH stretching, CH stretching, fingerprint, and amide I regions. Consequently, the FTIR analysis results for the two groups differ from each other. Nevertheless, the data obtained from FTIR spectroscopy are broadly consistent with the agarose gel electrophoresis and the comet assay. The significant difference between the NH–OH wavenumber in the free cap and Femto SMILE groups may be related to the instability in the formation of hydrogen bonds. On the other hand, the Femto SMILE group showed significant change in the wavenumber of the CH stretching region which appeared at 2962 $cm^{-1}$ in the free cap group and at 2938 $cm^{-1}$ in the Femto SMILE group. The decline in the wavenumber of the Femto SMILE group indicates an environmental change leading to disorder in the lipid hydrocarbon chains. Moreover, the amide II band at 1558 $cm^{-1}$ was shifted to 1530 $cm^{-1}$ causing alteration in the ratios of amide II to amide I and reveals disorder in the proteins' secondary and tertiary structure which may cause unfolding, aggregation and proteins distortion.[34] Furthermore, the change in $_{sym}PO_2$ wavenumber from 1070 $cm^{-1}$ to 1056 $cm^{-1}$ may be related to spatial changes in the positions of the phosphate groups in the proteins helix. This change may lead to several changes in the nucleic acid content of phospholipids. Therefore, it probably reveals that initial changes in the secondary and tertiary structure of the proteins also may cause changes in genetic materials.[37] Our findings may indicate that the Femto SMILE laser group has more significant DNA damage and fragmentation than the free cap group. Moreover, the slight alteration in the histological analysis and DNA analysis of the free cap group may also be related to many factors such as tissue processing, donor age, time of storage, and samples transportation.

These results are parallel with the results obtained with histological analysis and FTIR spectroscopy. Thus, the influence of the Femto SMILE laser may be due to the deep dispersion of the Femto laser into the corneal lamella. The closer the Femto laser is to the targeted area, the more exposure to the heat energy and the shock waves causes collateral damage to the cell layer.[38] Thus, it may be considered as a risk factor that may affect the rest of the corneal lamella.

Although SMILE induced slight effects on corneal lamellar cells , the advantages of the Femto SMILE laser include the corneal

biomechanical preservation, which results in excellent maintenance of the structure and low postoperative dry eye syndrome.[10, 39, 40]

Further studies on the impact of Femto SMILE laser surgery on corneal morphology and proteins using larger sample sizes, different lenticular depths, and laser parameters are essential.

In summary, the results of our research suggested that the Femto SMILE procedure induced more structural changes than those induced by a microkeratome cutting. In addition, Femto SMILE patients had a higher rate of DNA damage than the patients in the free cap group. The effect of the Femto SMILE laser technique on the DNA revealed by the corneal histological examination may be attributed to the deep penetration of high energy levels to the corneal layer. Future studies are obligatory on experimenting with using different frequencies, optimum energy, spot size, and spot distance to reach the best outcome from the Femto SMILE procedure. Moreover, additional investigations on the efficacy of administrating systemic antioxidants and DNA repair mechanism may protect the cornea from oxidative stress in the Femto SMILE patients.

## Financial Support and Sponsorship

None.

## Conflicts of Interest

None.

## *REFERENCES*

1. Chung SH, Mazur E. Surgical applications of femtosecond laser. *J Biophotonics* 2009;2:557–572.
2. Soong HK, Malta JB. Femtosecond lasers in ophthalmology. *Am J Ophthalmol* 2009;147:189–197.
3. Vestergaard A, Ivarsen A, Asp S, Hjortdal JØ. Femtosecond (FS) laser vision correction procedure for moderate to high myopia: A prospective study of ReLEx(®) flex and comparison with a retrospective study of FS-laser in situ keratomileusis. *Acta Ophthalmol* 2013;91:355–362.
4. Yoo SH, Kymionis DG, Koreishi A, Ide T, Goldman D, Karp CL, et al. Femtosecond laser assisted sutureless anterior lamellar keratoplasty. *Ophthalmology* 2008;115:1303–1307.
5. Soong HK, Mian S, Abbasi O, Juhasz T. Femtosecond laser assisted posterior lamellar keratoplasty: Initial studies of surgical technique in eye bank eyes. *Ophthalmology* 2005;112:44–49.
6. Roberts TV, Lawless M, Chan CC, Jacobs M, David Ng, Bali SJ, et al. Femtosecond laser cataract surgery: Technology and clinical practice. *Clin Exp Ophthalmol* 2013;41:180–186.
7. Binder PS. Femtosecond applications for anterior segment surgery. *Eye Contact Lens* 2010;36:282–285.
8. Kymionis GD, Kankariya VP, Plaka AD, Reinstein DZ. Femtosecond laser technology in corneal refractive surgery: A review. *J Refract Surg* 2012;28:912–920.
9. Abbey A, Ide T, Kymionis GD, Yoo SH. Femtosecond laser-assisted astigmatic keratotomy in naturally occurring high astigmatism. *Br J Ophthalmol* 2009;93:1566–1569.
10. Sekundo W, Kunert K, Russmann C, Gille A, Bissmann W, Stobrawa G, et al. First efficacy and safety study of femtosecond lenticule extraction for the correction of myopia: six-month results. *J Cataract Refract Surg* 2008;34:1513–1520.
11. Seyeddain O, Riha W, Hohensinn M, Nix G, Dexl AK, Grabner G. Refractive surgical correction of presbyopia with the Acufocus small aperture corneal inlay: Two-year follow-up. *J Refract Surg* 2010;26:707–715.
12. Osman IM, Madwar AY. Surface quality of human corneal SMILE lenticules in comparison with microkeratome free caps. *Delta J Ophthalmol* 2016;17:49–55.
13. Osman IM, Madwar AY. Scanning electron microscopy of human corneal lenticules at variable corneal depths in small incision lenticule extraction cases. *Delta J Ophthalmol* 2016;17:109–113.
14. Blum M, Kunert K, Schröder M, Sekundo W. Femtosecond lenticule extraction for the correction of myopia: Preliminary 6-month results. *Graefes Arch Clin Exp Ophthalmol* 2010;248:1019–1027.
15. Hjortdal JØ, Vestergaard AH, Ivarsen A, Ragunathan S, Asp S. Predictors for the outcome of small-incision lenticule extraction for Myopia. *J Refract Surg* 2012;28:865–871.
16. Kunert KS, Blum M, Duncker GI, Sietmann R, Heichel J. Surface quality of human corneal lenticules after femtosecond laser surgery for myopia comparing different laser parameters. *Graefes Arch Clin Exp Ophthalmol* 2011;249:1417–1424.
17. De Medeiros FW, Kaur H, Agrawal V, Chaurasia SS, Hammel J, Dupps WJ, et al. Effect of femtosecond laser energy level on corneal stromal cell death and inflammation. *J Refract Surg* 2009;25:869–874.
18. Mohrenfels CW, Khoramnia R, Maier MM, Pfäffl W, Hölzlwimmer G, Lohmann C. Cut quality of a new femtosecond laser system. *Klin Monbl Augenheilkd* 2009;226:470–474.
19. Heichel J, Blum M, Duncker GI, Sietmann R, Kunert KS. Surface quality of porcine corneal lenticules after femtosecond lenticule extraction. *Ophthalmic Res* 2011;46:107–112.
20. Ziebarth NM, Lorenzo MA, Chow J, Cabot F, Spooner GJ, Dishler J, et al. Surface quality of human corneal lenticules after SMILE assessed using environmental scanning electron microscopy. *J Refract Surg* 2014;30:388–393.
21. Ang M, Tan D, Mehta JS. Small incision lenticule extraction (SMILE) versus laser in-situ keratomileusis (LASIK): Study protocol for a randomized, non-inferiority trial. *Trials* 2012;13:75.

22. Schneider CA, Rasband WS, Eliceiri KW. NIH Image to ImageJ: 25 years of image analysis. *Nat Methods* 2012;9:671–675.
23. Dash HR, Shrivastava P, Das S. Principles and practices of DNA analysis: A laboratory manual for forensic DNA typing. New York, NY, USA: Springer Protocols Handbooks, Springer Nature; 2020.
24. Olive PL, Banáth JP. The comet assay: A method to measure DNA damage in individual cells. *Nat Protoc* 2006;1:23–29.
25. Gallagher W. FTIR analysis of protein structure. *Course Manual Chem* 2009;455:1–8.
26. Hayes KD , Ozen BF, Nielsen SS, Mauer LJ. FTIR determination of ligand-induced secondary and tertiary structural changes in bovine plasminogen. *J Dairy Res* 2003;70:461–466.
27. Compton MM. A biochemical hallmark of apoptosis: Internucleosomal degradation of the genome. *Cancer Metastasis Rev* 1992;11:105–119.
28. Pu X, Wang Z, Klaunig J E. Alkaline comet assay for assessing DNA damage in individual cells. *Curr Protoc Toxicol* 2015;65:3.12.1–3.12.11.
29. Choy CK, Benzie IF, Cho P. UV-mediated DNA strand breaks in corneal epithelial cells assessed using the comet assay procedure. *Photochem Photobiol* 2005;81:493–497.
30. Davidkova M, Juha L, Bittner M, Koptyaev S, Hajkova V, Krasa J, et al. A high-power laser-driven source of sub-nanosecond soft X-ray pulses for single-shot radiobiology experiments. *Radiat Res* 2007;168:382–387.
31. Arbillaga L, Azqueta A, Ezpeleta O, Lopez CA. Oxidative DNA damage induced by Ochratoxin A in the HK-2 human kidney cell line: Evidence of the relationship with cytotoxicity. *Mutagenesis* 2007;22:35–42.
32. Stap J, Krawczyk PM, Van Oven CH, Barendsen GW, Essers J, Kanaar R, et al. Induction of linear tracks of DNA double-strand breaks by alpha-particle irradiation of cells. *Nat Methods* 2008;5:261–266.
33. Chye SM, Hseu YC, Liang SH, Chen CH, Chen SC. Single strand dna breaks in human lymphocytes exposed to paraphenylenediamine and its derivatives. *Bull Environ Contam Toxicol* 2008;80:58–62.
34. Mozaffarieh M, Flammer J. Is there more to glaucoma treatment than lowering IOP? *Surv Ophthalmol* 2007;52:S174–S179.
35. Mozaffarieh M, Schoetzau A, Sauter M, Grieshaber M, Orgül S, Golubnitschaja O. Comet assay analysis of single-stranded DNA breaks in circulating leukocytes of glaucoma patients. *Mol Vis* 2008;14:1584–1588.
36. Li L, Jiang L, Geng C, Cao J, Zhong L. The role of oxidative stress in acrolein-induced DNA damage in HepG2 cells. *Free Radic Res* 2008;42:354–361.
37. Dovbeshko GI, Gridina NY, Kruglova EB, Pashchuk OP. FTIR spectroscopy studies of nucleic acid damage. *Talanta* .246–53:233;2000
38. Shaaban YM, Badran TA. Comparison between the effect of femtosecond laser in situ keratomileusis (FS-LASIK) and femtosecond small incision lenticule extraction (FS-SMILE) on the corneal endothelium. *Clin Ophthalmol* 2020;14:2543–2550.
39. Denoyer A, Landman E, Trinh L, Faure JF, Auclin F, Baudouin C. Dry eye disease after refractive surgery: Comparative outcomes of small incision lenticule extraction versus LASIK. *Ophthalmology* 2015;122:669–676.
40. Reinstein DZ, Archer TJ, Randleman JB. A mathematical model to compare the relative tensile strength of the cornea after PRK, LASIK, and small incision lenticule extraction. *J Refract Surg* 2013;29:454–460.

Original Article

# A Modified Formula for Intraocular Lens Power Calculation Based on Aphakic Refraction in a Pediatric Population

**Mohammad-Reza Jafarinasab[1], MD; Behrooz Khosravi[2], MD; Hamed Esfandiari[2], MD; Sadid Hooshmandi[2], MD; Kiana Hassanpour[2], MD, MPH**

*[1]Ophthalmic Epidemiology Research Center, Research Institute for Ophthalmology and Vision Science, Shahid Beheshti University of Medical Sciences, Tehran, Iran*
*[2]Ophthalmic Research Center, Research Institute for Ophthalmology and Vision Science, Shahid Beheshti University of Medical Sciences, Tehran, Iran*
*[3]Department of Ophthalmology, Northwestern University Feinberg School of Medicine, Chicago, IL, USA*

**ORCID:**
*Mohammad-Reza Jafarinasab: https://orcid.org/0000-0001-7558-0351*
*Kiana Hassanpour: https://orcid.org/0000-0002-1788-7352*

## Abstract

**Purpose:** To investigate and optimize the accuracy of aphakic refraction (AR) techniques for secondary intraocular lens (IOL) power calculation in aphakic children.
**Methods:** Thirty-three aphakic eyes of 18 patients who were candidates for secondary IOL implantation were enrolled in the present study. Axial length (AL) measured by optical biometry was used in the biometric formula (SRK-T, Holladay II, and Hoffer-Q). AR and spherical equivalent (SE) were used in two AR-based formulas (Ianchulev, Leccissotti). True power was calculated based on postoperative SE at three months' follow-up.
**Results**: Regarding the postoperative SE, 13 (40%) eyes were within ±1.00 diopters (D) and 22 (66%) were within ±2.00 D. Median absolute error (MedAE) was predicted to be 4.4 and 7.3 D with the use of Ianchulev and Leccissotti formulas, respectively. The corresponding value was 0.8 D with the biometric formula. All eyes were deemed to have myopic refraction when using the AR-based formulas except one eye with the Ianchulev formula. The coefficient of our modified formula was 1.7 instead of 2.01 in the Ianchulev formula. MedAE with the use of new formulae was 0.5 D and was comparable with the true IOL power ($P$ = 0.22).
**Conclusion:** Both Ianchulev and Leccissotti formulas resulted in a significant myopic surprise in aphakic children aged between 4.5 and 14 years. The modified formula proved to determine a more accurate SE that is comparable with biometric formulas.

**Keywords:** Aphakic Refraction; Intraocular Lens (IOL); IOL Power Calculation; Pediatric Cataract

*J Ophthalmic Vis Res* 2023; 18 (1): 34–40

**Correspondence to:**
Kiana Hassanpour, MD, MPH. Ophthalmic Research Center, Research Institute for Ophthalmology and Vision Science, Shahid Beheshti University of Medical Sciences, Paidarfard St., Boostan 9th St., Pasdaran, Ave., Tehran 16666, Iran.
E-mail: kiana.hassanpour@gmail.com

Received: 02-03-2021 Accepted: 14-09-2022

Access this article online

**Website:** https://knepublishing.com/index.php/JOVR

**DOI:** 10.18502/jovr.v18i1.12723

This is an open access article distributed under the Creative Commons Attribution License, which permits unrestricted use, distribution, and reproduction in any medium, provided the original work is properly cited.

**How to cite this article:** Jafarinasab MR, Khosravi B, Esfandiari H, Hooshmandi S, Hassanpour K. A Modified Formula for Intraocular Lens Power Calculation Based on Aphakic Refraction in a Pediatric Population. J Ophthalmic Vis Res 2023;18:34–40.


© 2023 Jafarinasab et al. This is an open access article distributed under the Creative Commons Attribution License | Published by Knowledge E

## INTRODUCTION

Intraocular lens (IOL) power calculation remains a challenging issue in the pediatric population.[1] There are two methods of IOL power calculation that are most commonly used in aphakic children including the use of either biometric formulas or refractive vergence formulas. Anatomical measurements including axial length (AL) and keratometry (K) are used in the biometric method formulas such as Sanders–Retzlaff–Kraff (SRK-T),[2] Holladay II,[3] or Hoffer-Q.[4] In aphakic refraction (AR)-based formulas, AR is applied to measure the power of the IOL.[5] The data of AL and K are not always available. AR could be used either preoperatively or- intra- and postoperatively, for both primary and secondary IOL calculations in adults and children. When using this AR method of measurement intraoperatively for primary IOL implantation, the anterior chamber should be formed after performing the lensectomy to refract the aphakic eye using either a portable auto refractometer or retinoscopy. The spherical equivalent (SE) could then be placed in the formula without further need of the AL and K measurements.

Currently, there are several available AR-based formulas including the Hug,[6] Khan,[7] Ianchulev,[8] and Leccissotti[9] formulas. In Khan's formula, AL is calculated based on the AR, and K is assumed to be 44.[7] Ianchulev et al[8] have introduced a formula that does not include AL and K measurements compared favorably with the biometric IOL power calculation. Subsequently, Leccissotti used aphakic SE in a personal formula for high myopic patients as well as in the Ianchulev formula for low myopic patients and reported a parabolic relationship between the SE and IOL power.[9] Wong et al[10] investigated the accuracy of the Iaunchulev and Leccissotti formulas in 182 eyes of adult patients undergoing cataract surgery. The authors found that the Ianchulev formula could be applied in all eyes except in those experiencing high myopia while the Leccissotti formula worked particularly poorly in short eyes but performed better in eyes with myopia.

In recent years, intraoperative wavefront aberrometry with Optiwave Refrctive Analyzer (ORA) system has shown comparable postoperative refractive outcomes when compared to conventional biometry (IOL Master) in adult patients who underwent routine cataract surgery. However, its use in the pediatric population is yet to be determined.[11]

The application of refractive vergence formulas in the pediatric population remains a controversial issue. Abdel-Aziz et al[12] compared Khan's and Hug's formulas with the Holladay I formula and found a 0.8 D reduction in the accuracy of the refractive vergence formula. Similarly, Nakhli et al reported better performance with the AL vergence formula compared to the refractive vergence formula.[13]

The current study is designed to investigate the accuracy of two refractive vergence formulas in secondary IOL calculations in children as well as the clinical outcomes when modifying the AR formulas to determine more accurate predictive results.

## METHODS

Thirty-three aphakic eyes of 18 patients who were candidates of secondary IOL implantation aged 4.5–14 years were all enrolled in this comparative case-series between October 2013 and September 2019. The exclusion criterion was a cornea that was too hazy for refraction. The study protocol was approved by the Ethics Committee of Shahid Beheshti University of Medical Sciences. The study adhered to the tenets of the Declaration of Helsinki and written informed consent was obtained from the legal guardians of the patients.

### Biometric Formulas

All measurements before and after the operations were performed by an optometrist experienced in working with the pediatric population. AL and keratometry were measured using optical biometry (Lenstar LS 900, Haag-Streit AG, Switzerland). To calculate secondary IOL power, SRKT[2] was used in eyes with AL measuring >22 mm and Hoffer-Q[4] was the formula of choice in eyes with AL measuring <22 mm.

The patient's age was used to determine the target refraction. Target refraction was set for emmetropia in children older than six and 1 D of hyperopia in children younger than six years old.

### Refractive Vergence Formulas

An experienced pediatric ophthalmologist (BK) measured the AR with the use of an autorefractor

(Nikon Instruments Inc., Melville, New York, USA) or retinoscope (Welch Allyn SureSight, Welch Allyn, Skaneateles Falls, New York). The mean of four SE autorefraction measurements was used in the refractive vergence formulas of Lanchulev and Lescilloti.

## Surgical Technique

All surgeries were performed by an experienced pediatric cataract surgeon (MRJ). Under general anesthesia, the main wound was created with a 2.8 mm keratome and intracameral diluted adrenaline (1/1000) was used for pupillary dilation. An ophthalmic viscoelastic device (OVD) was used to form the anterior chamber and release the synechiae. A three-piece foldable acrylic IOL (AcrySof MA60, Alcon Laboratories) was placed in the ciliary sulcus followed by irrigation and removal of the OVD. The wound was sutured with a 10-0 Nylon (Nylon, Ethicon Inc., Somerville, NJ) suture. Subconjunctival betamethasone and cefazolin were injected upon the conclusion of the surgery. Topical ciprofloxacin 0.3% (Ciplex, Sina Daru, Tehran, Iran) was used four times per day for one week while betamethasone 0.1% (Betasonate, Sinadaru, Tehran, Iran) eye drops were used four times per day and tapered off over a month.

Patients were followed on day one, week one, month one, and month three postoperatively. The refraction was measured at the third-month follow-up visit.

## Statistical Analysis

Frequency and percentages were used to report the descriptive data.

Postoperative refraction was used to estimate the "actual" IOL power; Regarding postoperative SE, the IOL power that would cause emmetropia was calculated for each subject. This value was considered as "true" IOL power. For each diopter of myopia, 1 D was reduced from the actual calculated IOL power. Similarly, for each diopter of hyperopia, 1.5 D were added to the actual calculated IOL power. The mean (Mean Absolute Error [MAE]) and median (MedAE) of the difference between true IOL power and calculated IOL powers were then calculated for each formula. All statistical analyses were performed using SPSS (IBM). A *P*-value < 0.05 was considered significant.

## RESULTS

Thirty-three eyes of 18 patients were included in this study. Median age of the patients was 8.7 ± 2.9 years ranging from 5 to 13.5 years. Average AL was 23.3 ± 1.8 mm ranging from 18.5 to 26.6 mm. AL was >24 in 13 eyes (39.3.5 %), between 22 and 24 mm in 14 eyes (45.4%), and <22 mm in 6 eyes (18.8%) [Table 1].

## Biometric Formulas

The mean preoperative SE was +13.2 D (range, +8.0 to +20) that improved to –0.9 D (range, – 3.00 to +4.00) postoperatively. Considering the multiple measurements of AL, the mean SE was –0.8, –0.98, and +0.62 D in ALs >24, between 22 and 24, and <22 mm, respectively. The MedAE and MAE were –0.9 ± 2 and –1.1, respectively [Table 2]. Figure 1 demonstrates the postoperative SE plotted against the preoperative SE in each patient.

## Refractive Vergence Formula

Theoretically, if the Ianchulev formula was used to assess the refractive vergence, all eyes except one would reflect myopic refraction. The mean postoperative SE would be –4.5 ± 2.6 D while one eye would have +1.50 D of hyperopic refraction. In eyes with AL >24 mm, the mean SE would have been –3.75 D (range, –1.0 to –6.0 D). The mean SE would be –5.50 (range, –10.0 to +1.50) in AL <24 mm.

Similarly, if the Leccissotti formula was utilized, it would have resulted in an average SE of –11.0 (range, –1.50 to –20.0) in AL <24 and –4.85 (range, –4.85 to 8.50 D) in AL >24 mm [Tables 2 & 3].

With the use of the Ianchulev formula, MedAE and MAE would be 4.5 and 4.4 D, respectively. The corresponding values for the Leccissotti formula were 8.7 and 7.3 D, respectively [Figure 2].

## Modified Formula

With the step-by-step reduction of the coefficient of the Ianchulev formula from 2.01 to 1.70, the mean SE improved to –0.5 ± 2 (Median –0.5, range from –4 to 5.4) D. Twenty-two (66%) eyes would reflect myopic results, while 11 (34%) would reflect hyperopic refraction [Table 2 & Figures 1 & 2]. MedAE and MAE were 0.5 and 0.5, respectively

**Table 1.** Baseline characteristics of study participants.

| Parameter | Mean ± SD | Median (Range) |
|---|---|---|
| Age (yr) | 8.7 ± 2.9 | 8.0 (5.0 to 13.50) |
| AL | 23.3 ± 1.8 | 23.5 (18.5 to 26.6) |
| Preoperative sphere | 13.8 ± 3.2 | 13.3 (8.0 to 20.0) |
| Preoperative cylinder | –1.0 ± 1.0 | –1.0 (–3.3 to 0.8) |
| Preoperative SE | 13.2 ± 3.2 | 12.3 (8.0 to 20.0) |
| Postoperative sphere | 0.1 ± 2.0 | –0.3 (–3.0 to 6.0) |
| Postoperative cylinder | –1.6 ± 1.0 | –1.5 (–4.3 to 0.8) |
| Postoperative SE | –0.9 ± 2.0 | –1.1 (–4.0 to 4.5) |

AL, axial length; SE, spherical equivalent; yr, years

**Table 2.** Mean and median of calculated IOL power with different formulas.

| Parameter | Mean | Median (Q1, Q3) | Min | Max |
|---|---|---|---|---|
| True power* | 22.0 ± 5.4 | 19.4 (18.0, 26.3) | 13.8 | 33.0 |
| Biometric formulas | 22.8 ± 4.9 | 21.5 (19.5, 28.0) | 15.0 | 32.0 |
| Postoperative SE | –0.9 ± 2.0 | –1.1 (–1.9, –0.3) | –4.0 | 4.5 |
| Leccissotti formula | 30.7 ± 10.7 | 26.5 (23.0. 39.5) | 15.9 | 54.6 |
| Error | –8.7 ± 6.0 | –7.3 (–11.7, –4.8) | –21.6 | –1.5 |
| Ianchulev formula | 26.4 ± 6.7 | 24.1 (21.6, 32.3) | 16.1 | 40.2 |
| Error | –4.5 ± 2.6 | –4.4 (–6.4, –3.1) | –10.1 | 1.5 |
| Modified formula | 22.5 ± 5.2 | 20.9 (19.3, 26.9) | 14.1 | 33.3 |
| Error | –0.5 ± 2.0 | –0.5 (–1.8, 0.6) | –4.0 | 5.4 |

IOL, intraocular lens; Q1, first quartile; Q3, Third quartile

**Table 3.** Comparison between IOL power calculated with different formulas subtracted from the true power.

| Statistics | Used – True | Leccissotti – True | Ianchulev – True | Modified – True |
|---|---|---|---|---|
| Pearson correlation | 0.931 | 0.931 | 0.931 | 0.932 |
| ICC | 0.926 | 0.751 | 0.908 | 0.931 |
| Δ Mean ± SD (Diopter) | –0.9 ± 2 | –8.7 ± 6 | –4.5 ± 2.6 | –0.5 ± 2 |
| 95% CI | –1.58 to –0.22 | –10.73 to –6.67 | –5.39 to –3.61 | –1.17 to 0.17 |
| *P*-value* | <0.001 | <0.001 | <0.001 | 0.116 |
| Δ Median (range) | –1.1 (–4 to 4.5) | –7.3 (–21.6 to 2.3) | –4.4 (–10.1 to 2.2) | –0.5 (–4 to 5.4) |
| 95% LoA | –4.82 to 3.02 | –20.46 to 3.06 | –9.6 to 0.6 | –4.42 to 3.42 |

*Based on Paired *t*-test
True indicates the calculated power based on postoperative refraction
Correlation of eyes was considered in the calculation of SD, 95% CI, and LoA
IOL, intraocular lens; ICC, intra cluster correlation; Δ, inter-formula difference; CI, confidence interval; LOA, limits of agreement

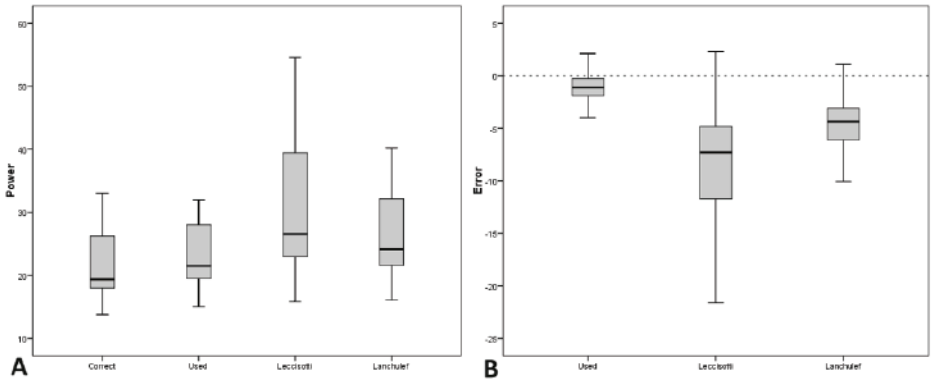


**Figure 1.** Box and whisker plot demonstrating calculated IOL powers (A) and the error using different formulas (B). Error is based on the difference between True power (Correct bar in A) and calculated powers using different formulas.

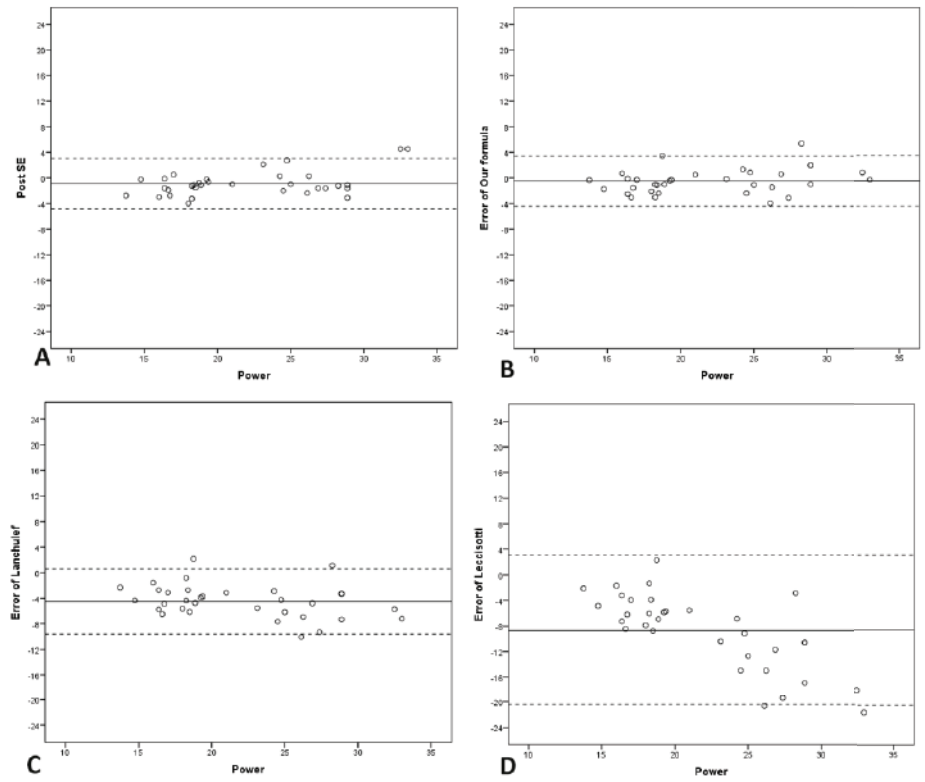


**Figure 2.** Scatter plots demonstrating postoperative spherical equivalent (SE) (A), the error of different formulas plotted against the calculated power based on the modified formula (B), lanchulev (C), and Leccissotti (D).

Table 4 demonstrates the ranges of achieved refractions with the use of different formulas.

## DISCUSSION

The refractive vergence formulas that use AR instead of AL and keratometry could be used in assessing IOL power calculations for aphakic children. IOL power calculation in an eye that is still growing is a challenging process.

Recent advances in technologies resulted in more reliable AL, and keratometry measurements improved the ability in predicting more accurate IOL power and subsequent better visual outcome in pediatric cataract surgery. In this study, we have investigated the use of two refractive vergence

**Table 4.** Achieved refraction with the use of different formulae.

| Achieved SE (D) | Used formula | Ianchulev formula | Leccissotti formula | Modified formula |
|---|---|---|---|---|
| Within ± 0.5 | 6 (18.2 %) | 0 (0%) | 0 (0%) | 7 (21.2 %) |
| Within ±1 | 13 (39.4 %) | 2 (6.1%) | 0 (0%) | 19 (57.6 %) |
| Within ±2 | 22 (66.7 %) | 4 (12.1%) | 2 (6.1%) | 27 (81.8 %) |
| –2< SE or SE > +2 | 33 (100%) | 33 (100 %) | 33 (100%) | 33 (100 %) |

SE, spherical equivalent; D, diopter

formulas in comparison to conventional formulas. In this series of 33 eyes, we demonstrated that refractive vergence formulas would result in reflecting significant myopic refraction, while the conventional formulas resulted in reflecting favorable refraction within ±0.5 D from the target refraction. Furthermore, postoperative myopic refractive error was higher in eyes with shorter AL. In high myopic patients, the Leccissotti formula was slightly closer to target refraction than the Ianchulev formula when calculated preoperatively.

Our findings are in line with previous studies on this subject, Nakhli et al[13] compared the axial vergence formulas such as Hoffer-Q, SRK-T, and Holladay with the refractive vergence formulas as presented by Ianchulev, Khan, and Mackool in 31 pediatric cataract eyes. The authors reported more accurate results to target refraction with the preoperative axial vergence formulas when compared with the true IOL calculations postoperatively. The amount of error was predicted to be –5.48 ± 3.55 diopters with the use of the Ianchulev formula, which is comparable to the predictive error calculation of 4.5 ± 2.6 D observed in our study.

Our study differs from Khan and Al Gaeed's study in which AL was estimated from the AR through the use of a complicated formula.[7] They used the estimated AL as well as 44.0 as a constant keratometry value in the Holladay formula. Results of their comparison confirmed the comparable accuracy of the AR pre-calculation of AL with the pre-calculated AL using the Holladay formula in 50 eyes where both formulas resulted in values that were close to the "true" IOP power calculation postoperatively.[7] In Nakhli et al's study, Khan's method resulted in more accurate prediction as compared to the Ianchulev formula (–1.66 ± 3.19 vs –5.48 ± 3.55 D).[13] Due to the inability to retrieve accurate measurements for AL and the limitation of using a constant to represent keratometry, we did not use this formula in our study.

In another study comparing Hug's and Khan's refractive vergence formulas, the mean error was greater by 0.8 as compared to the standard biometric methods. The mean predicted error was 2.4 ± 2.0 with both Khan's and Hug's formulas as compared to –4.5 ± 2.6 D and –8.7 ± 6.0 in the Ianchulev and Leccissotti formulas, respectively.[12] Notably, the between-study comparison of predicted errors is biased due to differences in population, measurement, and surgical techniques. Therefore, the results should be interpreted with caution.

Considering the significant myopic surprise with the Ianchulev formula, we modified the current coefficient of the formula from 2.01 to 1.70. IOL power calculation with the new coefficient proved to be comparable with the biometric formula. Our modified coefficient is close to a coefficient proposed by Mackool et al.[14] Mackool et al suggested the following formula in determining the IOL power in patients with post-LASIK cataract extraction:

IOL power = 1.75 * AR (SE).

Accurate biometry could be difficult in patients with a history of refractive surgery. The small difference between the Mackool coefficient and ours could be attributed to the position of the IOL. In our study, all the IOLs were placed into the sulcus in contrast to the bag implantation in Mackool's study.

There are several limitations to our study including an assessment on a small population of patients which may affect the results and also precludes a valuable analysis of the hypothetical prediction of postoperative refractions with the use of refractive vergence formulas.

In summary, the present study confirmed the superiority of the use of conventional biometric

formulas in the secondary IOL power calculation in aphakic children. However, since the biometric measurements are not always available in aphakic children, the presence of a comparable refractive vergence formula is critical. We found that the use of aphakic SE multiplied by our modified coefficient of 1.7 would result in favorable clinical outcomes in aphakic children aged between 4.5 and 14 years. To determine a more accurate prediction of error, the use of this formula in conjunction with testing on an expanded population in the real world is recommended.

## Financial Support and Sponsorship

None.

## Conflicts of Interest

None.

## *REFERENCES*

1. Koch CR, Kara-Junior N, Serra A, Morales M. Long-term results of secondary intraocular lens implantation in children under 30 months of age. *Eye* 2018;32:1858–1863.
2. Sanders DR, Retzlaff JA, Kraff MC, Gimbel HV, Raanan MG. Comparison of the SRK/T formula and other theoretical and regression formulas. *J Cataract Refract Surg* 1990;16:341–346.
3. Hoffer KJ. Clinical results using the Holladay 2 intraocular lens power formula. *J Cataract Refract Surg* 2000;26:1233–1237.
4. Hoffer KJ. The Hoffer Q formula: A comparison of theoretic and regression formulas. *J Cataract Refract Surg* 1993;19:700–712.
5. Sanders DR, Retzlaff J, Kraff MC. Comparison of empirically derived and theoretical aphakic refraction formulas. *Arch Ophthalmol* 1983;101:965–967.
6. Hug T. Use of the aphakic refraction in intraocular lens (IOL) power calculations for secondary IOLs in pediatric patients. *Am J Ophthalmol* 2005;139:585.
7. Khan AO, AlGaeed A. Paediatric secondary intraocular lens estimation from the aphakic refraction alone: Comparison with a standard biometric technique. *Br J Ophthalmol* 2006;90:1458–1460.
8. Ianchulev T, Hoffer KJ, Yoo SH, Chang DF, Breen M, Padrick T, et al. Intraoperative refractive biometry for predicting intraocular lens power calculation after prior myopic refractive surgery. *Ophthalmology* 2014;121:56–60.
9. Leccisotti A. Intraocular lens calculation by intraoperative autorefraction in myopic eyes. *Graefes Arch Clin Exp Ophthalmol* 2008;246:729.
10. Wong ACM, Mak ST, Tse RKK. Clinical evaluation of the intraoperative refraction technique for intraocular lens power calculation. *Ophthalmology* 2010;117:711–716.
11. Zhang Z, Thomas LW, Leu S-Y, Carter S, Garg S. Refractive outcomes of intraoperative wavefront aberrometry versus optical biometry alone for intraocular lens power calculation. *Indian J Ophthalmol* 2017;65:813.
12. Abdel-Hafez G, Trivedi RH, Wilson ME, Bandyopadhyay D. Comparison of aphakic refraction formulas for secondary in-the-bag intraocular lens power estimation in children. *J AAPOS* 2011;15:432–434.
13. Nakhli FR, Emarah K, Jeddawi L. Accuracy of formulae for secondary intraocular lens power calculations in pediatric aphakia. *J Curr Ophthalmol* 2017;29:199–203.
14. Mackool RJ, Ko W, Mackool R. Intraocular lens power calculation after laser in situ keratomileusis: Aphakic refraction technique. *J Cataract Refract Surg* 2006;32:435–437.

Original Article

# Correction of Retinal Nerve Fiber Layer Thickness Measurement on Spectral-Domain Optical Coherence Tomographic Images Using U-net Architecture

**Ghazale Razaghi[1], MS; Masoud Aghsaei Fard[2], MD; Marjaneh Hejazi[1,3], PhD**

[1]*Medical Physics and Biomedical Engineering Department, School of Medicine, Tehran University of Medical Sciences, Tehran, Iran*
[2]*Department of Ophthalmology, Farabi Eye Hospital, Tehran University of Medical Sciences, Tehran, Iran*
[3]*Research Center for Molecular and Cellular Imaging, Bio-Optical Imaging Group, Tehran University of Medical Sciences, Tehran, Iran*

**ORCID:**
*Ghazale Razaghi: http://orcid.org/0000-0003-3121-4602*
*Marjaneh Hejazi: http://orcid.org/0000-0002-1823-2876*

## Abstract

**Purpose:** In this study, an algorithm based on deep learning was presented to reduce the retinal nerve fiber layer (RNFL) segmentation errors in spectral domain optical coherence tomography (SD-OCT) scans using ophthalmologists' manual segmentation as a reference standard.
**Methods:** In this study, we developed an image segmentation network based on deep learning to automatically identify the RNFL thickness from B-scans obtained with SD-OCT. The scans were collected from Farabi Eye Hospital (500 B-scans were used for training, while 50 were used for testing). To remove the speckle noise from the images, preprocessing was applied before training, and postprocessing was performed to fill any discontinuities that might exist. Afterward, output masks were analyzed for their average thickness. Finally, the calculation of mean absolute error between predicted and ground truth RNFL thickness was performed.
**Results:** Based on the testing database, SD-OCT segmentation had an average dice similarity coefficient of 0.91, and thickness estimation had a mean absolute error of 2.23 ± 2.1 μm. As compared to conventional OCT software algorithms, deep learning predictions were better correlated with the best available estimate during the test period ($r^2$ = 0.99 vs $r^2$ = 0.88, respectively; $P < 0.001$).
**Conclusion:** Our experimental results demonstrate effective and precise segmentation of the RNFL layer with the coefficient of 0.91 and reliable thickness prediction with MAE 2.23 ± 2.1 μm in SD-OCT B-scans. Performance is comparable with human annotation of the RNFL layer and other algorithms according to the correlation coefficient of 0.99 and 0.88, respectively, while artifacts and errors are evident.

**Keywords:** Deep Learning; Optical Coherence Tomography; Retinal Nerve Fiber Layer

*J Ophthalmic Vis Res* 2023; 18 (1): 41–50

**Correspondence to:**

Marjaneh Hejazi, PhD. Medical Physics and Biomedical Engineering Department, University of Medical Sciences, Tehran 1417613151, Iran.
E-mail: mhejazi@sina.tums.ac.ir

Received: 26-12-2021 Accepted: 10-11-2022

**Access this article online**

**Website:** https://knepublishing.com/index.php/JOVR

**DOI:** 10.18502/jovr.v18i1.12724

This is an open access article distributed under the Creative Commons Attribution License, which permits unrestricted use, distribution, and reproduction in any medium, provided the original work is properly cited.

**How to cite this article:** Razaghi G, Aghsaei M, Hejazi M. Correction of Retinal Nerve Fiber Layer Thickness Measurement on Spectral-Domain Optical Coherence Tomographic Images Using U-net Architecture. J Ophthalmic Vis Res 2023;18:41–50.

## INTRODUCTION

Treatment of retinal diseases can be greatly improved by early diagnosis and monitoring of optic neuropathies. Glaucoma and other optic neuropathies can be diagnosed based on assessing the thickness of the retinal nerve fiber layer (RNFL).[1−−3]RNFL thickness can now be measured quantitatively with optical coherence tomography (OCT) software which is a convoluted imaging technology.

RFNL thickness is currently measured automatically by spectral domain OCT (SD-OCT) using segmentation algorithms. However, despite improvements in SD-OCT hardware and software, RNFL segmentation errors are still rather common. According to the literature, artifacts or segmentation errors can be found anywhere from 19.9% to 46.3% of SD-OCT scans of the RNFL.[4, 5]There are several factors associated with these segmentation errors in OCT images, which include image decentration, epiretinal membranes, long axial lengths, and poor visual acuity.[5] Although manually correcting the segmentation errors is possible, accomplishing this in a busy clinical practice could be infeasible due to the lengthy time commitment.[6]

SD-OCT has been applied in the diagnosis and segmentation of RNFL throughout several recent studies that used deep learning (DL) models.[7]Devalla et al developed a DL technique that allowed for more precise optic nerve head tissue segmentation than the manual method.[8] A higher level of accuracy (ACC) was achieved by the algorithm as compared to manual segmentation performed by two graders. Accordingly, this algorithm yielded 8.85 ± 3.40% and 9.01 ± 4.20% errors for RNFL thicknesses calculations, while between the two graders, 5.94 ± 2.30% errors were observed. Thompson et al in their article demonstrated that glaucomatous eyes could be distinguished from healthy eyes by training a DL algorithm on raw SDOCT B-scans.[9] With an area under the receiver operating characteristic (ROC) curve of 0.96, the proposed algorithm is superior to the conventional RNFL thickness parameters used in the instrument's printout ($P < 0.001$).

In another study by Ma et al,[10] U-net with residual block for RNFL thickness estimation was used in raw OCT images. They achieved an acceptable correlation, and the Dice Similarity Index was 0.92 for test samples. In order to quantify the thickness of the retinal nerve fiber layer on OCT images for three test set groups, Mariottoni et al[11] provided a DL segmentation-free method based on ResNet34 that had been pre-trained on the ImageNet dataset. The 2D-OCT scan has been used without a training mask and any previous biomarker definition as input in segmentation-free approaches. Also, Medeiros et al[12] and An et al[13] obtained the average thickness directly without segmentation according to their network design on thickness maps and fundus images. The clinical relevance of examining trends in retinal layer thickness changes and retinal structure deformation is due to the fact that for some diseases, changes in RNFL thickness for a specific period are less than the axial resolution of OCT. This thickness change cannot be determined by OCT software, but DL is able to do so. Therefore, DL-based methods let clinicians explore the disease progression in the early stages. Accordingly, some studies have concentrated on segmenting more than one layer. Fang et al used a hybrid convolutional neural network (CNN) model for segmenting nine retinal layer boundaries in age-related macular degeneration (AMD) patients,[14] and Pekala et al designed CNN in DenseNet architecture for retinal OCT segmentation.[15]

To reduce the segmentation error, we used a DL algorithm based on convolution to determine the average RNFL thickness in this study. Our proposed method can be considered as a more robust method of RFNL thickness estimation than the conventional segmentation algorithms as DL segmentation according to our hypothesis, would provide more accurate measurements of RNFL thickness for images which have segmentation errors.

To develop and evaluate a system that is reliable at measuring RNFL layer thickness, this study aims at developing and evaluating a DL system. With enough database of SD-OCT images to prevent overfitting, DL models were trained on OCT images to illustrate the algorithm's ACC and reliability in analyzing and quantifying the thickness of the RNFL.

## METHODS

This study used DL to develop an algorithm for measuring RNFL thickness. Figure 1 summarizes

our proposed workflow. The first step involved reducing speckle noise using a preprocessing method. CNNs were then used to delineate RNFL contours. A morphological method was applied to remove any inappropriate patterns in segmentation results. Finally, RNFL thickness was determined according to our DL rules.

## Data Collection

From 90 left eyes and 62 right eyes of participants (age range of 20–80 years), SD-OCT images of healthy and unhealthy (glaucomatous optic neuropathy) patients were collected. The Heidelberg OCT machine at the Farabi Eye Hospital captured all of the data, which was anonymized to fulfill the Human Ethics criteria of the Tehran University of Medical Sciences. All 500 images in the dataset were randomly divided into training (80%, 400 OCT images) and validation (20%, 100 OCT images) groups, and 50 OCT images were used in the test group.

## Pre-processing

To prepare OCT images for segmentation, we applied a preprocessing step after extracting each image. Preprocessing was primarily focused on reducing the speckle noise. To minimize these image artifacts, morphological opening filters (square and kernel size 3×3) in OpenCV (version 4.5.1, https://opencv.org, Gary Bradsky 1999) were used. The image signal-to-noise ratio factor improved from 25 to 40 dB as a result of this method.

Images must match the input size of a network in order to train it and make predictions on test data. Therefore, images were resized to 256×256 pixels with zero padding. Preprocessing becomes more crucial if the dataset contained a limited amount of data. In our study, reducing speckle noise allowed the network to learn useful information like RNFL boundaries efficiently.

## Retinal Nerve Fiber Layer Segmentation

After preprocessing the image, it is first necessary to segment RNFL accurately to measure the thickness of the fiber layer. An established image segmentation network, U-net, is used to segment RNFL accurately in this study. The U-net created by Ronneberger et al[16] (https://lmb.informatik.uni-freiburg.de/people/ronneber/u-net) has robust performance in the absence of adequate training data. The U-net has advantages in performing segmentation tasks. First, this model allows for simultaneously using global location and context. Second, it performs better for segmentation tasks even with a few training images. Another advantage is that U-net uses a loss function for each image pixel, which helps quickly identify individual cells within the segmentation map.

U-net's detailed network architecture is shown in Figure 2. As input, X is passed to the network, and at the last convolution layer, a binary mask is emitted by the network that includes the RNFL region. The U-net architecture has skip connections to connect encoders and decoders. X's resolution is downsized by a factor of two in the encoder module using Max-pooling for the purpose of capturing contextual details at different resolution steps, and then by up-sampling using Up-Convolution, the resolution is restored in the decoder module, enabling precise localization. Moreover, the architecture shows that the input images are passed through the model and then followed by a series of convolutional layers with the ReLU activation function. In the encoder architecture, we also have multiple convolutional layers with an increasing number of filters (16, 32, 64, 128, 256). We notice that, as we progress toward the decoder, the number of filters in the convolutional layers decreases along with a gradual upsampling of the following layers toward the top. The neural network was carried out with Python programming language (Python 3.5 Software Foundation, https://www.python.org/).

In our U-net network, we used Adam with a default learning rate as an optimizer and binary cross entropy as a loss function. The batch size was equal to 16 with 100 epochs, and we saved the network weights from the "best" epoch by checkpoint and earlystop function.

The training images were manually segmented under the supervision of an expert ophthalmologist using Labelme (http://labelme.csail.mit.edu) to create ground truth masks. With the RNFL OCT images and their respective ground truth masks which were prepared by Labelme, at the last step, the U-net model was trained and validated. We used our trained and validated model to predict the output of the RNFL images in the test set without the corresponding label. Predictions were

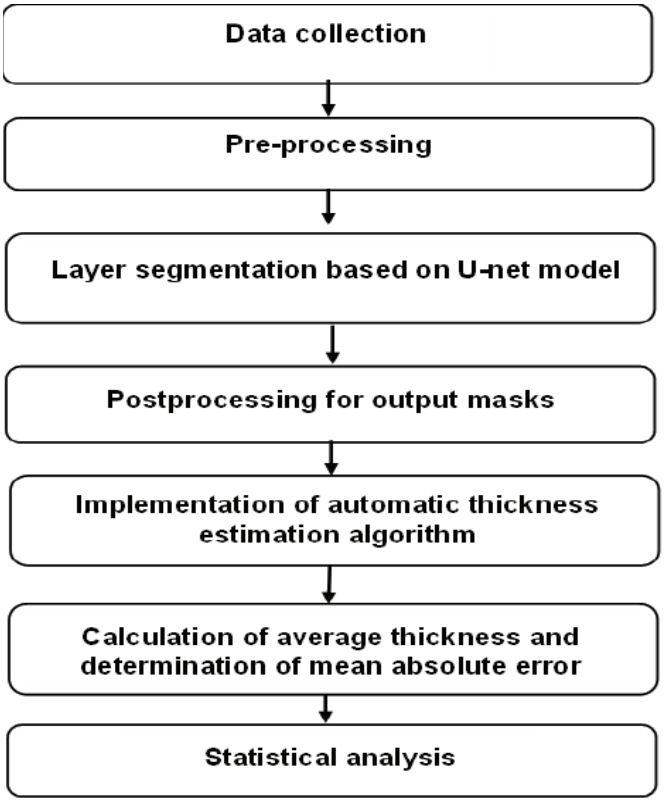


**Figure 1.** Flowchart for steps in material and methods.

compared with ground truth masks for analyzing and determining model operation on the test set.

## Postprocessing

The generated binary masks may contain gaps and speckles as a consequence of implementing the segmentation algorithm. Morphological algorithms were applied as post-processing methods to fill the gaps. After applying edge detection filters such as the binary threshold or Canny on binary masks to detect white objects from a black background, the ”findCountours” function in OpenCV can be used to find continuous contours. It looks for borders and pixels with similar intensities to identify contours.

## Average Thickness Estimation

Following the post-processing phase, the average thickness of the RNFL was determined using the Python environment and the Euclidean distance transform (EDT)[17, 18] approach.

A binary digital image was subjected to the EDT to determine the distance between each non-feature (non-zero pixels) and each feature (zero pixels, i.e., RNFL contour). A numerical value is assigned to each binary image pixel by the EDT method indicating how far the black pixel is from the nearest white pixel of the image. For the 2D cases with 256×256 pixels, the EDT metric is fast enough to create a distance map for output binary masks.

To find the centerline of the RNFL, we implemented the Skeleton algorithm on EDT outputs. Skeleton is a thinning operation that reduces an object region in EDT output to a matrix of one row. This matrix preserves the significant pixel information (maximum pixel value in EDT results) of the RNFL region.

As stated in the formulas below, the average thickness of RNFL is calculated according to Eq. 2 and as it indicates the mean of maximum values are determined based on Eq. 1. If $a_1$, $a_2$,...$a_n$ is the maximal distance values that were extracted by the skeleton algorithm from the EDT result, to get the thickness diameter, the mean distance value calculated in Eq. 1 was multiplied by two in Eq. 2. In Eq. 1 “*n*” is the total number of maximum values (“*n*” is equal to the number of columns in output mask). In Eq. 2, *F* is the factor that depends on the

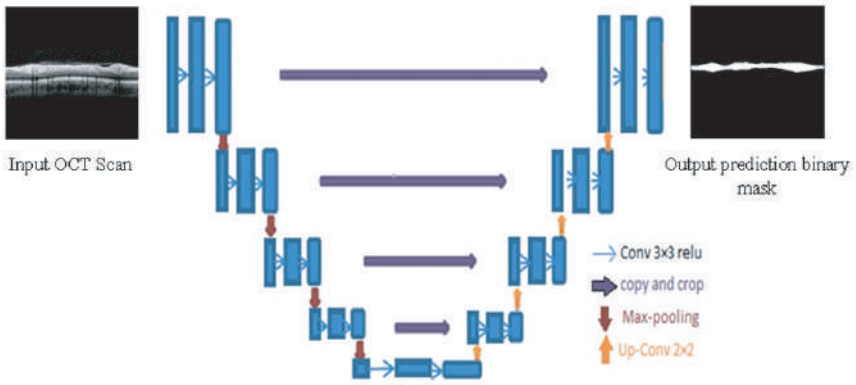


**Figure 2.** Summary of the U-net architecture. The network receives input X and generates a prediction mask.

resolution of the OCT system. In our study, the axial resolution was 2.8 µm.

$$mean\ of\ maximum\ values = \frac{a_1 + a_2 + \cdots + a_n}{n} \quad (1)$$

$$average\ thickness = mean \times 2 \times F \quad (2)$$

## Performance Metrics

We used a variety of metrics to measure the OCT segmentation model's performance, including ACC, sensitivity (SEN), specificity (SPE), and dice similarity coefficient (DSC). In the resulting binary mask, SEN, and SPE correspond to the percentages of correctly classified pixels. According to Eq. 3 and Eq. 4, SEN and SPE depend on pixels classification by the number of true positive (TP), false negative (FN), true negative (TN), and false positive (FP) pixels. The significant alert here is that >50% of the pixels in our output masks are black and are in the background class, so if the U-net model only predicted background correctly, the ACC, SPE, and SEN are more than 0.5, and it can lead to a huge mistake. Since DSC is a combination of SEN and SPE, it stands out more from the other metrics for measuring this task.

$$SEN = \frac{TP}{TP + FN} \quad (3)$$

$$SPE = \frac{TN}{TN + FP} \quad (4)$$

The DSC is another established metric for comparing binary masks resulting from image segmentation with their ground truth counterparts. The equations of the DSC metric are written as:

$$DSC = \frac{2 \times SEN \times SPE}{SEN + SPE} \quad (5)$$

Figure 3 shows the DSC metric by an example. As shown in Figure 3, the DSC Index was calculated by multiplying the overlap (between the prediction and the ground truth) and dividing it by both areas (of the prediction and the ground truth).

## RESULTS

To predict the average thickness of the RNFL, we developed a DL algorithm based on U-net and trained using SDOCT B-scans. To compare algorithm results with the best estimate of RNFL average thickness determined by the ophthalmologist, dice coefficients and mean absolute errors (MAE) were calculated.

We have two steps for effective examination, the first step being the DL model evaluation, and the second being consideration of the thickness measurement algorithm performance. Figure 4 shows some examples generated by the proposed methodology on the dataset validation, where it was observed that our U-net model was able to extract the boundary of RNFL at different thicknesses. To prove the validity of the proposed, the test set was used, and Figure 5 shows the segmentation results for two samples in the test set.

To evaluate quantitatively the U-net performance on the validation and the test sets,

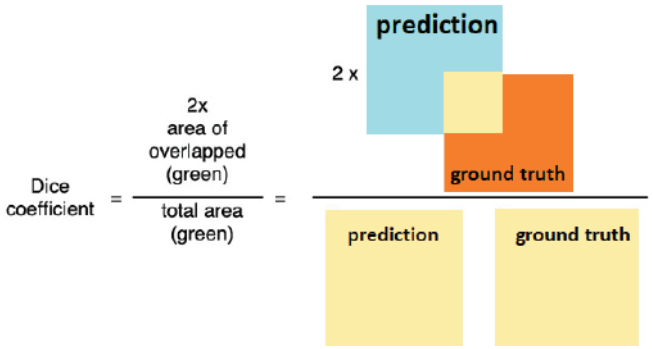


**Figure 3.** Dice coefficient calculation formula.

SEN, SPE, and DSC were utilized as evaluation metrics. Table 1 lists the evaluation results obtained by using the proposed framework on validation and test sets.

Testing and validating images with the U-net model demonstrated a high level of performance. As shown in Table 1, the DSC Index between segmentation results and manual segmentation by an expert was 0.93, and for the test images, the DSC Index was 0.91.

In the second step, the average RNFL thickness resulting from the model and thickness determined by the conventional algorithm were compared with the reference RNFL thickness measured by the expert on the test images. A strong correlation was found between the DL segmentation estimates of RNFL thickness and the best measurement of RNFL thickness (Pearson's $r$ = 0.996; $P < 0.001$), with an MAE of 2.23 ± 2.1 µm. Figure 6 shows the fluctuation of absolute error for the test images. In addition, the algorithm was not affected by other factors, such as gender or race.

Figure 7 presents a scatter plot between the U-net prediction thickness values and measured thickness values by an expert from 50 SD-OCT B-scans. Based on the test data, a linear regression model is fitted with an R-squared value of 0.9919. As a result, the predicted values are highly linearly related to the measured values, showing that despite the small variance, the predicted thickness values are reliable.

To demonstrate OCT software function, average thicknesses resulting from conventional software were compared with the thicknesses which were estimated by an expert. Figure 8 illustrates the relation between OCT software thickness prediction and the best thickness value recognized by an ophthalmologist.

A linear regression model fitted to the data yields an R-square of 0.8811 and MAE was 9.12 ± 6.9 µm which has a significant error according to RNFL thickness in normal and abnormal OCT images.

## DISCUSSION

In the present study, we developed a segmentation DL algorithm capable of predicting RNFL average thickness from B-scans in this study. There was a strong correlation between algorithm estimates of RNFL average thickness and expert measurements of RNFL thickness. On normal images without artifacts, conventional software performed well, but DL-based segmentation estimated RNFL average thickness that is significantly closer to the ground truth values for RNFL thickness than conventional segmentation software. On the test set, the dice coefficient is 0.91, and the MAE is 2.23 ± 2.1 µm in this study.

Several U-net-based models have recently been proposed with promising results for retinal layer segmentation. Devalla et al developed DRUnet for retinal segmentation.[8] The resulting RNFL thickness provided by this algorithm had an error of 8.85 ± 3.40% and at 9.01± 4.20% when compared to each grader, while the graders had an error of 5.94 ± 2.30% between each other. Thompson et al found an area under the ROC curve of 0.96 vs 0.87 for the global peripapillary RNFL thickness ($P < 0.001$). Ben-Cohen et al detected four retinal boundaries using a combination of U-net's fully convolutional network, Sobel's edge detection, and graph search.[19] The Dice index in this study for RNFL was 0.95, and the mean difference for thickness was 1.12 pixels. Also, the mean difference for OCT explorer was 3.65

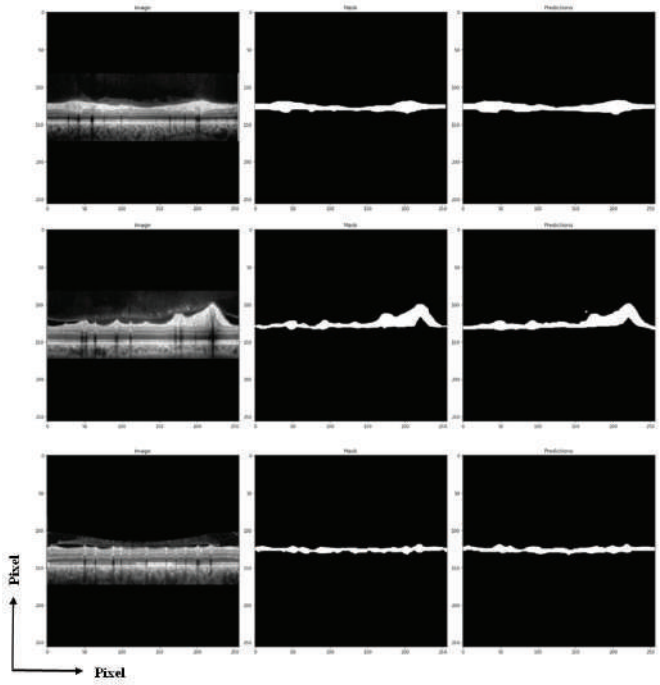


**Figure 4.** U-net output on validation data. Original image, manually segmented image, and output image, in that order.

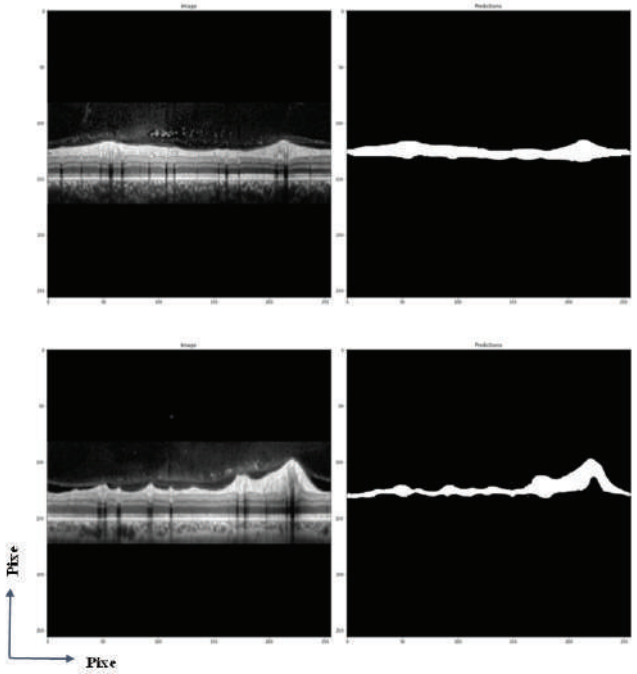


**Figure 5.** U-net prediction for two samples of the test set. Original image and U-net prediction.

pixels. LF-Unet,[20] U-net++,[21] and ResU-net[22] are other models for segmentation of more than one layer in retinal images; dice scores were 0.83, 0.88, and 0.92, respectively, in comparison to our Dice index that is equal to 0.91. Ma et al proposed U-net with residual blocks and received 0.92 for Dice when adding transfer learning to the model and $R^2$ was 0.98 in this study, but we found 0.99 for DSC.[10] Whereas prior SD-OCT segmentation methods based on

**Table 1.** DSC, SPE, and SEN value for U-net model on validation and test images.

| Metric | SEN | SPE | Dice |
|---|---|---|---|
| Validation | 0.94 | 0.93 | 0.93 |
| Test | 0.93 | 0.90 | 0.91 |

SEN, sensitivity; SPE, specificity; DSC, dice similarity coefficient

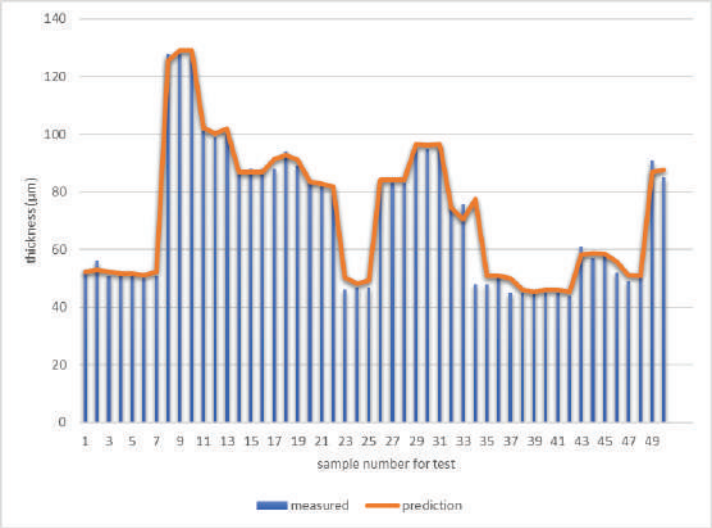


**Figure 6.** Thickness absolute error between prediction results and best measurement by the expert for each sample in the test set. MAE for 50 samples is equal to 2.23 ± 2.1(μm)..

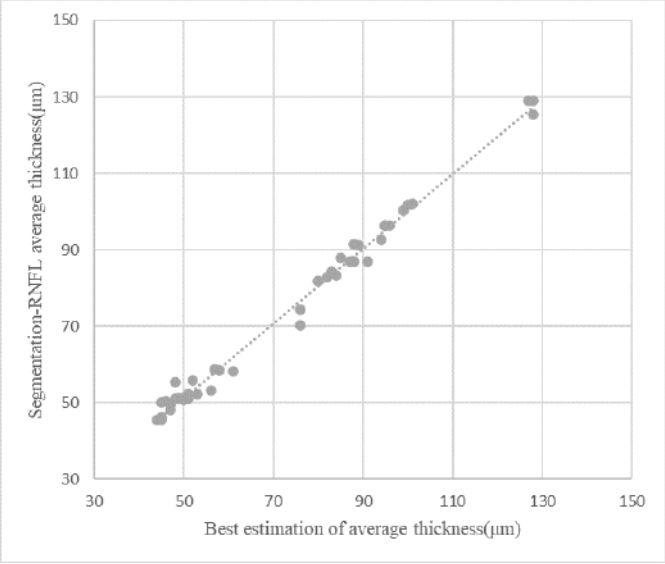


**Figure 7.** Scatterplot illustrating the relationship between the prediction thickness value and best estimation thickness measurement by the expert for the test set.

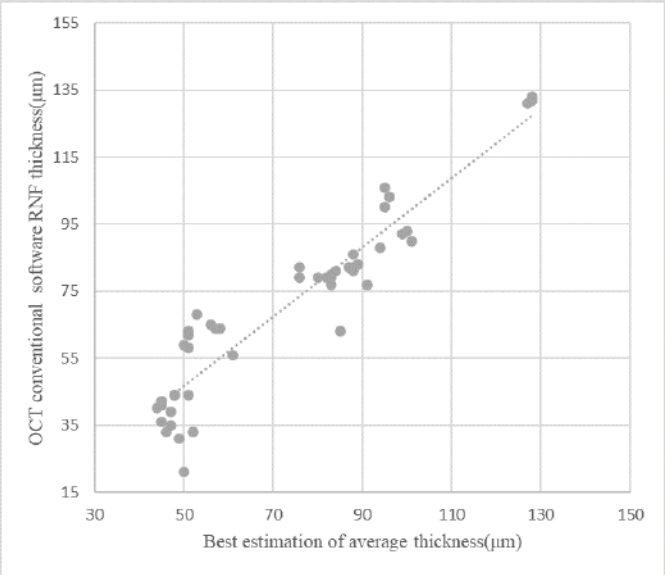


**Figure 8.** Scatterplot illustrating the relationship between the conventional OCT software and the best estimation thickness measurement by an expert for the test set.

DL mostly focused on enhancing segmentation performance, our research demonstrates that efficient thickness estimate algorithms are also crucial.

Other studies that work with OCT images received reliable results but U-net model is easier for clinical application because U-net does not have complexity and does not need much space in memory and GPU systems. The response of U-net is fast enough and results are accurate in comparison to conventional software. As you can see in Figure 5, at least 15–20% of images have an unavoidable error in thickness estimation via conventional software.

Our findings imply that segmentation based on DL technique can offer reliable RNFL thickness estimations in both images with and without segmentation error by using U-net network and thickness measurement algorithm. We achieved MAE 2.23 ± 2.1 µm that is less than axial resolution 2.8 µm for OCT conventional algorithms. According to our hypothesis, the proposed method segmented RNFL similarly to ophthalmologists by a DSC score of 0.91. Such a method could prove useful in clinical practice to determine RNFL thickness without the need to refine segmentation, thus avoiding the time-consuming process of segmentation.

## Ethical Considerations

All procedures implemented in studies involving human participants were done in accordance with the ethical standards of the Research Ethics Committees of School of Medicine, Tehran University of Medical Sciences under "IR.TUMS.MEDICINE.REC.1398.827".

## Financial Support and Sponsorship

None.

## Conflicts of Interest

None.

All authors read and approved the final manuscript.

## *REFERENCES*

1. Pierro L, Gagliardi M, Iuliano L, Ambrosi A, Bandello F. Retinal nerve fiber layer thickness reproducibility using seven different OCT Instruments. *Invest Ophthalmol Vis Sci* 2012;53:5912–5920.
2. Asrani S, Essaid L, Alder BD, Santiago-Turla C. Artifacts in spectral-domain optical coherence tomography measurements in glaucoma. *JAMA Ophthalmol* 2014;132:396–402.
3. Liu Y, Simavli H, Que CJ, Rizzo JL, Tsikata E, Maurer R, et al. Patient characteristics associated with artifacts in spectralis optical coherence tomography imaging of the

retinal nerve fiber layer in glaucoma. *Am J Ophthalmol* 2015;159:565–576.

4. Jammal AA, Thompson AC, Ogata NG, Mariottoni EB, Urata CN, Costa VP, et al. Detecting retinal nerve fibre layer segmentation errors on spectral domain-optical coherence tomography with a deep learning algorithm. *Sci Rep* 2019;9:1–9.
5. Mansberger SL, Menda SA, Fortune BA, Gardiner SK, Demirel S. Automated segmentation errors when using optical coherence tomography to measure retinal nerve fiber layer thickness in glaucoma. *Am J Ophthalmol* 2017;174:1–8.
6. Shen D, Wu G, Suk HI. Deep learning in medical image analysis. *Annu Rev Biomed Eng* 2017;19:221–248.
7. Christopher M, Bowd C, Belghith A, Goldbaum MH, Weinreb RN, Fazio MA, et al. Deep learning approaches predict glaucomatous visual field damage from Oct optic nerve head en face images and retinal nerve fiber layer thickness maps. *Ophthalmology* 2020;127:346–356.
8. Devalla SK, Renukanand PK, Sreedhar BK, Subramanian G, Zhang L, Perera S, et al. DRUNET: A dilated-residual U-Net Deep Learning Network to segment optic nerve head tissues in optical coherence tomography images. *Biomed Opt Express* 2018;9:3244–3265.
9. Thompson AC, Jammal AA, Berchuck SI, Mariottoni EB, Medeiros FA. Assessment of a segmentation-free deep learning algorithm for diagnosing glaucoma from optical coherence tomography scans. *JAMA Ophthalmol* 2020;138:333–339.
10. Ma R, Liu Y, Tao Y, Alawa KA, Shyu M-L, Lee RK. Deep learning–based retinal nerve fiber layer thickness measurement of murine eyes. *Transl Vis Sci Technol* 2021;10:21.
11. Mariottoni EB, Jammal AA, Urata CN, Berchuck SI, Thompson AC, Estrela T, et al. Quantification of retinal nerve fibre layer thickness on optical coherence tomography with a deep learning segmentation-free approach. *Sci Rep* 2020;10:1–9.
12. Medeiros FA, Jammal AA, Thompson AC. From machine to machine: An OCT-trained deep learning algorithm for objective quantification of glaucomatous damage in fundus photographs. *Ophthalmology* 2019;126:513–521.
13. An G, Omodaka K, Hashimoto K, Tsuda S, Shiga Y, Takada N, et al. Glaucoma diagnosis with machine learning based on optical coherence tomography and color fundus images. *J Healthc Eng* 2019;2019:1–9.
14. Fang L, Cunefare D, Wang C, Guymer RH, Li S, Farsiu S. Automatic segmentation of nine retinal layer boundaries in OCT images of non-exudative AMD patients using deep learning and graph search. *Biomed Opt Express* 2017;8:2732–2744.
15. Pekala M, Joshi N, Liu TYA, Bressler NM, DeBuc DC, Burlina P. Deep Learning based retinal OCT segmentation. *Comput Biol Med* 2019;114:103445.
16. Ronneberger O, Fischer P, Brox T. U-net: Convolutional networks for biomedical image segmentation. *Med Image Comput Assist Interv* 2015;234–241.
17. Kipli K, Enamul Hoque M, Thai Lim L, Afendi Zulcaffle TM, Kudnie Sahari S, Hamdi Mahmood M. Retinal image blood vessel extraction and quantification with Euclidean distance transform approach. *IET Image Process* 2020;14:3718–3724.
18. Tang X, Zheng R, Wang Y. Distance and edge transform for skeleton extraction. *IEEE/CVF ICCVW* 2021;2136–2141.
19. Ben-Cohen A, Mark D, Kovler I, Zur D, Barak A, Iglicki M, et al. Retinal layers segmentation using fully convolutional network in OCT images. *RSIP Vision* 2017;1–8.
20. Lu D, Heisler M, Ma D, Dabiri S, Lee S, Ding GW, et al. Cascaded deep neural networks for retinal layer segmentation of optical coherence tomography with fluid presence. *arXiv* preprint arXiv:1912.03418.
21. Zhou Z, Siddiquee MMR, Tajbakhsh N, Liang J. UNet++: A nested U-net architecture for medical image segmentation. *Deep Learn Med Image Anal Multimodal Learn Clin Decis Support* 2018;11045:3–11.
22. Matovinovic IZ, Loncaric S, Lo J, Heisler M, Sarunic M. Transfer learning with U-net type model for automatic segmentation of three retinal layers in optical coherence tomography images. *11th International Symposium on Image and Signal Processing and Analysis (ISPA)* 2019;49–53.

Original Article

# Adenosine Receptors Expression in Human Retina and Choroid with Age-related Macular Degeneration

**Collin P. Goebel[1], MD; Yong-Seok Song[1,2], MS; Ismail S. Zaitoun[1,2], PhD; Shoujian Wang[1], MD, PhD; Heather A. D. Potter[1], MD; Christine M. Sorenson[1,2], PhD; Nader Sheibani[1,2,3,4], PhD**

*[1]Department of Ophthalmology and Visual Sciences, University of Wisconsin School of Medicine and Public Health, Madison, WI, USA*
*[2]McPherson Eye Research Institute, University of Wisconsin School of Medicine and Public Health, Madison, WI, USA*
*[3]Department of Cell and Regenerative Biology, University of Wisconsin School of Medicine and Public Health, Madison, WI, USA*
*[4]Department of Biomedical Engineering, University of Wisconsin, Madison, WI, USA*

**ORCID:**
*Nader Sheibani: https://orcid.org/0000-0003-2723-9217*

## Abstract

**Purpose:** Adenosine signaling modulates ocular inflammatory processes, and its antagonism mitigates neovascularization in both newborns and preclinical models of ocular neovascularization including age-related macular degeneration (AMD). The adenosine receptor expression patterns have not been well characterized in the human retina and choroid.
**Methods:** Here we examined the expression of adenosine receptor subtypes within the retina and choroid of human donor eyes with and without AMD. Antibodies specifically targeting adenosine receptor subtypes A1, A2A, A2B, and A3 were used to assess their expression patterns. Quantitative real-time PCR analysis was used to confirm gene expression of these receptors within the normal human retina and choroid.
**Results:** We found that all four receptor subtypes were expressed in several layers of the retina, and within the retinal pigment epithelium and choroid. The expression of A1 receptors was more prominent in the inner and outer plexiform layers, where microglia normally reside, and supported by RNA expression in the retina. A2A and A2B showed similar expression patterns with prominent expression in the vasculature and retinal pigment epithelium. No dramatic differences in expression of these receptors were observed in eyes from patients with dry or wet AMD compared to control, with the exception A3 receptors. Eyes with dry AMD lost expression of A3 in the photoreceptor outer segments compared with eyes from control or wet AMD.
**Conclusion:** The ocular presence of adenosine receptors is consistent with their proposed role in modulation of inflammation in both the retina and choroid, and their potential targeting for AMD treatment.

**Keywords:** Caffeine; Choroid; Inflammation; Neovascularization; Neurodegeneration; Retina

*J Ophthalmic Vis Res* 2023; 18 (1): 51–59

**Correspondence to:**
Nader Sheibani, PhD. Department of Ophthalmology and Visual Sciences, University of Wisconsin School of Medicine and Public Health, 1111 Highland Ave., 9453 WIMR, Madison, WI 53705-2275, USA.
E-mail: nsheibanikar@wisc.edu

Received: 09-06-2022 Accepted: 08-09-2022

Access this article online

**Website:** https://knepublishing.com/index.php/JOVR

**DOI:** 10.18502/jovr.v18i1.12725

This is an open access article distributed under the Creative Commons Attribution License, which permits unrestricted use, distribution, and reproduction in any medium, provided the original work is properly cited.

**How to cite this article:** Goebel PG, Song Y-S, Zaitoun IS, Wang S, Potter HAD, Sorenson CM, Sheibani N. Adenosine Receptors Expression in Human Retina and Choroid with Age-related Macular Degeneration. J Ophthalmic Vis Res 2023;18:51–59.

## INTRODUCTION

Age-related macular degeneration (AMD) is an inflammatory driven neurodegenerative disorder that develops in the elderly due to a combination of genetics, the environment, and other factors. It contributes to substantial irreversible central vision loss in the industrialized countries and was present in an estimated 6.5% of all American adults over the age of 40 as of 2011.[1] AMD is characterized by the deposition of cellular debris, called drusen between the retina and choroid, and divided into the categories of wet and dry AMD.[2] In patients with wet AMD, subretinal neovascularization occurs, which may lead to edema and hemorrhage. In contrast, dry AMD is characterized by drusen and retinal degeneration without neovascularization or hemorrhage. Currently, treatment for AMD, especially dry AMD, is very limited. Antibodies against vascular endothelial growth factor (VEGF) improve visual outcomes in most patients with wet AMD.[3, 4] In addition, antioxidant vitamins and minerals slow down the progression of moderate or severe dry AMD but fail to prevent the development of moderate AMD from mild AMD.[5] Thus, these therapeutics are best for preventing progression in patients who have already developed moderate or severe disease and are unable to halt or reverse the disease process.

To develop better therapeutic targets for patients with AMD, a more complete understanding of its pathophysiology is required. The dysfunction and death of retinal pigment epithelial (RPE) cells and degeneration of photoreceptors are observed in AMD. However, the detailed cellular and molecular mechanisms driving this degeneration needs further investigation. Several hypotheses have been proposed, including accumulation of toxins, dysfunction of mitochondria, and damage from reactive oxygen species in the RPE cells and choroidal vasculature.[5–8] Recently, immune and inflammatory regulatory pathways have been proposed to be the central components in the pathophysiology of AMD, and preclinical models have demonstrated complement and IgG deposition in the RPE and choroid of mice with AMD.[5, 8–10]

Recent investigations indicate the importance of adenosine receptors in modulation of ocular inflammatory processes. Adenosine elicits its effects through its G-protein coupled receptors: A1, A2A, A2B, and A3.[11] Adenosine receptor A1 activation inhibits calcium influx-induced release of neurotransmitters in the central nervous system (CNS) under hypoxic conditions, creating a neuroprotective effect.[12] Adenosine receptor A3 engagement has both pro- and anti-inflammatory properties throughout the body, including the lung, cardiac, and gastrointestinal systems.[10] Blockade of the adenosine A2A receptor in microglial cells reduces inflammatory responses and photoreceptor cell loss in cultured human cells. Furthermore, adenosine receptors A2A and A2B expression are upregulated by hypoxia-inducible factor during hypoxic conditions and inflammation in the eye,[13, 14] and their antagonism blocks ischemia-mediated retinal neovascularization.[15] Thus, the process of inflammation and angiogenesis in dry and wet AMD could be linked with adenosine receptor signaling. However, the function of these receptors in the RPE and choroid, and their potential activity in pathophysiology of AMD, needs further evaluation.

The importance of adenosine receptor signaling pathways in ocular inflammatory and neovascular diseases has been further supported by studies of caffeine, an adenosine receptor antagonist, in both preclinical models and humans.[16] Maugeri and colleagues found evidence that caffeine decreases the permeability of the RPE layer and thus may inhibit the development of macular edema.[17] In addition, caffeine administered to infants born prematurely for apnea diminishes the severity of retinopathy of prematurity.[18] We recently showed that caffeine is efficacious in mitigating choroidal neovascularization in a preclinical model of wet AMD.[19] However, the identity of adenosine receptor(s) involved in these activities remains unknown, and results have yet to be verified in humans. Here we assessed the presence of specific adenosine receptors in the retina and choroid of human donor eye samples from control and patients with wet and dry AMD. These studies, to the best of our knowledge, are the first to demonstrate the presence of specific adenosine receptors in the human retina and choroid and examine whether their expression pattern is altered under AMD conditions.

## METHODS

### Human Donor Eyes and Other Materials

Deidentified human ocular samples were from the Lion Gift of Sight (St. Paul, MN). The eyes were collected by written consent from donors or donors' family for medical research as delineated by the Declaration of Helsinki. We were provided with a list of 28 potential donor samples with histological evaluations, of which 13 were control eyes and 15 were eyes with AMD. Eyes from two donors with wet AMD, two donors with dry AMD, and two donors with no AMD were selected by the help of our

ocular pathologist from the available samples. Each experimental group contained samples matched by age and gender, and all samples included the macula. Presumptive diagnoses were confirmed histologically. Anti-ADORA1 (55026-1-AP, Proteintech, Rosemont, IL), anti-ADORA2A (PA1-042), anti-ADORA2B (PA5-72850), and anti-ADORA3 (PA5-36350) were obtained from Thermo Fisher Scientific (Carlsbad, CA). Anti-collagen IV antibody was from Southern Biotech (1340-01; Birmingham, AL). Cy5-labeled anti-goat (705-175-147) and Cy2-labelled anti-rabbit (305-225-045) were obtained from Jackson ImmunoResearch Laboratories (West Grove, PA).

## Antibody Staining and Microscopic Analysis of Eye Sections

Four paraffin sections, taken from each donor eye, were placed on glass slides. Sections were washed with xylene four times for five min. This was followed by two washes in 100% and 95% ethanol for 10 min, and the pure water for 5 min. Slides were then heated in a citrate solution (H-3300, Vector Laboratories, Burlingame, CA) for 11 min to retrieve epitopes. For each set of samples, slides were then stained overnight with 750 $\mu$L ADORA1, ADORA2A, ADORA2B, and ADORA3 primary antibodies, diluted in blocking buffer (1:500; PBS with 1% bovine serum albumin, 0.2% skim milk powder, and 0.3% Triton-X100). Diluted Anti-collagen IV antibody (1:500) was added to each sample to target vasculature in the samples, and DAPI diluted 1:1000 was added to each sample to visualize the cellular nuclei of the retina and choroid. The slides were then rinsed with PBS buffer three times for 5 min, and 750 $\mu$L of appropriate secondary antibodies (diluted 1:500 in PBS blocking buffer) were added to each sample. Slides were incubated at room temperature for 4 h allowing the visualization of collagen in the vasculature and adenosine receptor expression.

Following staining with primary and secondary antibodies, the expression of the A1, 2A, 2B, and A3 receptors in donor eyes with wet AMD, dry AMD, or no AMD were compared using fluorescence microscopy. Light intensity and exposure time were standardized for each group of slides under the microscope. Photographs were taken of fluorescence emission patterns for the adenosine receptor, collagen IV, and DAPI located within the macula and underlying choroid. The fluorescence intensity in each sample was then compared to determine the predominant location of each adenosine receptor in the retina and choroid, as well as look for differences in adenosine receptor expression between wet and dry AMD compared to control.

## RNA Isolation and Quantitative PCR (qPCR) Analysis

The retina and RPE/choroid were dissected from at least three non-diseased human eyes of similar age (male and female) and cut into smaller pieces in cold PBS. The tissue samples were snap frozen in liquid nitrogen and stored at –80°C for RNA preparation. Tissue samples (50–100 mg) were dissolved in 1 mL of Trizol reagent (Invitrogen, San Diego, CA). Total RNA was extracted using RNeasy mini kit as recommended (Qiagen, Valencia, CA). Complementary DNA was prepared using 1 µg of total RNA and the RNA to cDNA EcoDry Premix (TaKaRa, Mountain View, CA) and diluted 1:10. qPCR was conducted in triplicates using a Mastercycler Realplex (Eppendorf, Enfield, CT) and TB-Green qPCR Premix (TaKaRa). The cycles for amplification were 95°C for 2 min; 40 cycles of amplification (95°C for 15 s, 60°C for 40 s); and dissociation curve step (95°C for 15 s, 60°C for 15 s, 95°C for 15 s). The relative fluorescent units (RFUs) at a threshold fluorescence value (Ct) were used for linear regression line and assessment of nanograms of DNA. The target gene expression levels were determined by comparing the RFU at the Ct to the standard curve and normalized by the housekeeping gene ribosomal protein L13α (RPL13A). The primer sequences used in this study are listed in Table 1. Each sample was run in triplicates.

## Statistical Analysis

Differences between the expression level of ADORA in the retina and RPE/Choroid were evaluated using *t*-tests and GraphPad Prism version 8 (GraphPad Software, La Jolla, CA). $P < 0.05$ was considered significant. Data are the mean ± standard deviation.

# RESULTS

## Adenosine Receptors Expression in Retina and Choroid

Each eye section selected for fluorescent staining was from a patient between the ages of 76 and 100 years old at the time of death. One male and one female sample was chosen for each of the AMD and control groups. Each sample was preserved within 28 h of the patient's death. All samples demonstrated

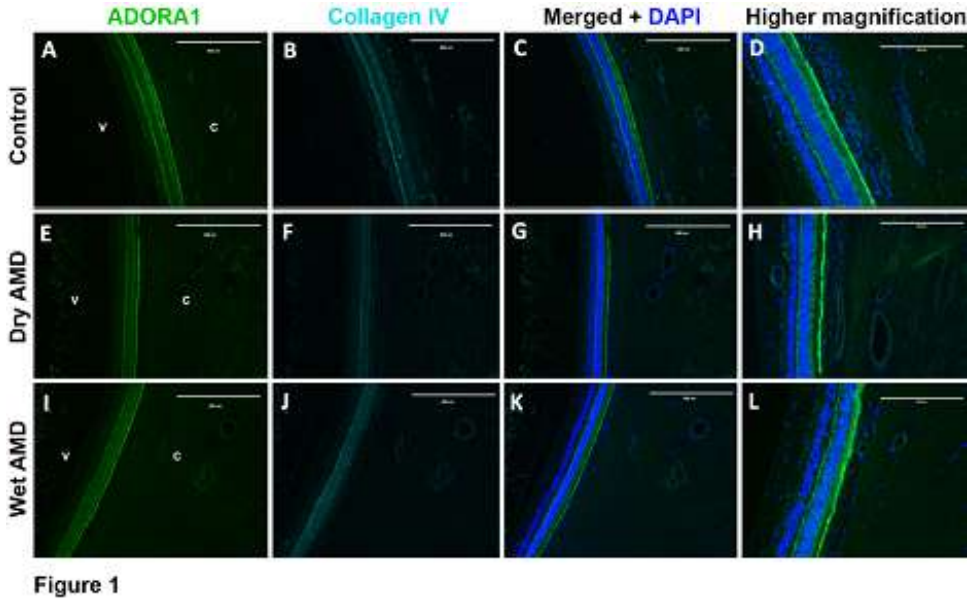


Figure 1

**Figure 1.** Expression of ADORA1 in retinal and choroidal cross sections. (A) ADORA1, (B) collagen IV, and (C) merged images and DAPI staining of eye sections with no AMD (Control). (D) A higher magnification of C. (E) ADORA1, (F) collagen IV, and (G) merged images and DAPI staining of eye sections with dry AMD. (H) A higher magnification of G. (I) ADORA1, (J) collagen IV, and (K) merged images and DAPI staining of eye sections with wet AMD. (L) Higher magnification of K. Scale bar = 400 µm (A, B, C, E, F, G, I, J, and K) and 200 µm (D, H, and L).
V, vitreous; C, choroid.

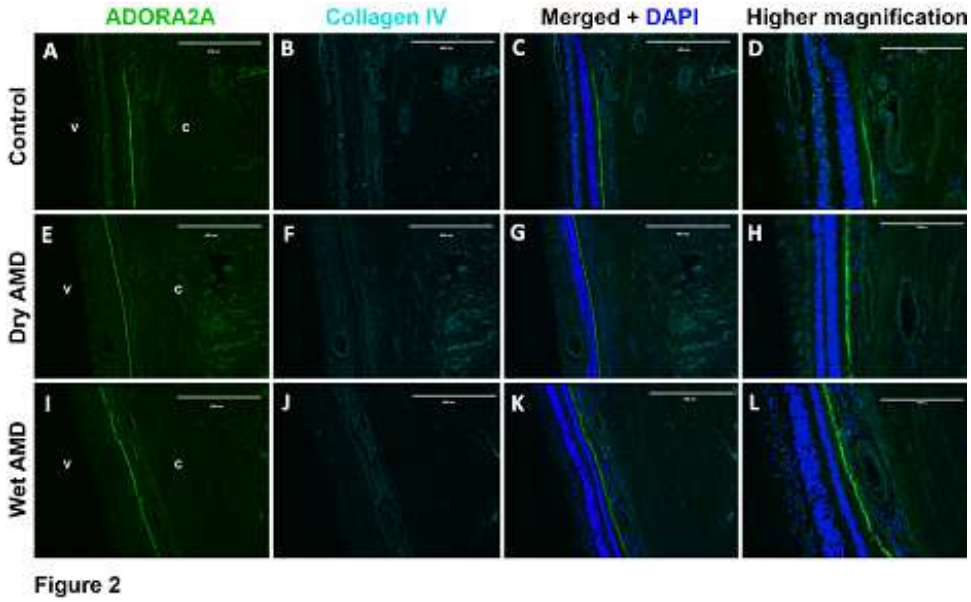


Figure 2

**Figure 2.** Expression of ADORA2A in retinal and choroidal cross sections. (A) ADORA2A, (B) collagen IV, (C) merged images and DAPI staining of eye sections with no AMD (Control). (D) A higher magnification of C. (E) ADORA2A, (F) collagen IV, and (G) merged images and DAPI staining of eye sections with dry AMD. (H) A higher magnification of G. (I) ADORA2A, (J) collagen IV, and (K) merged images and DAPI staining of eye sections with wet AMD. (L) A higher magnification of K. Scale bar = 400 µm (A, B, C, E, F, G, I, J, and K) and 200 µm (D, H, and L).
V, vitreous; C, choroid.

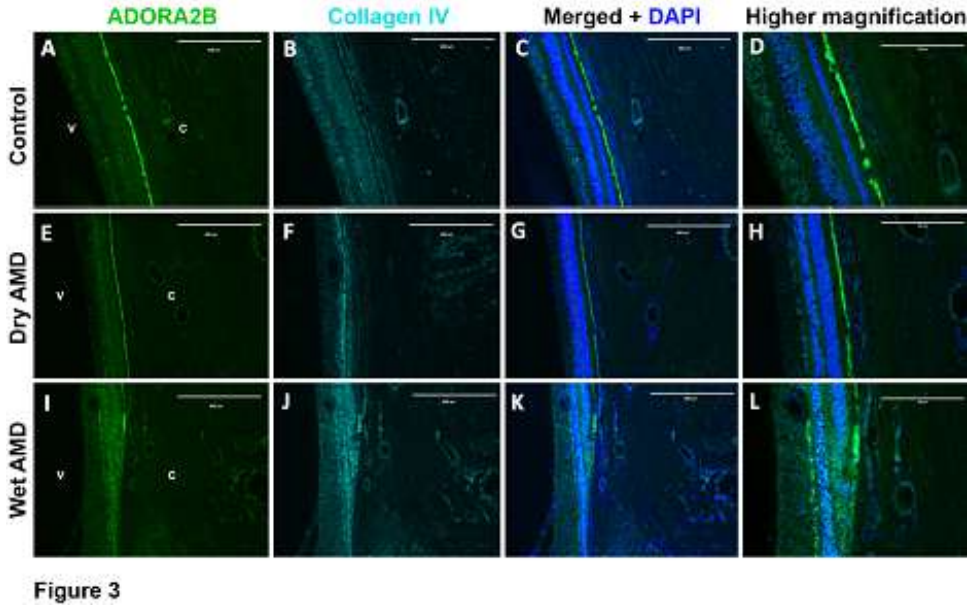


Figure 3

**Figure 3.** Expression of ADORA2B in retinal and choroidal cross sections. (A) ADORA2B, (B) collagen IV, and (C) merged images and DAPI staining of eye sections with no AMD (Control). (D) A higher magnification of C. (E) ADORA2B, (F) collagen IV, (G) merged images and DAPI staining of eye sections with dry AMD. (H) A higher magnification of G. (I) ADORA2B, (J) collagen IV, and (K) merged images and DAPI staining of eye sections with wet AMD. (L) A higher magnification of K. Scale bar = 400 µm (A, B, C, E, F, G, I, J, and K) and 200 µm (D, H, and L).
V, vitreous; C, choroid.

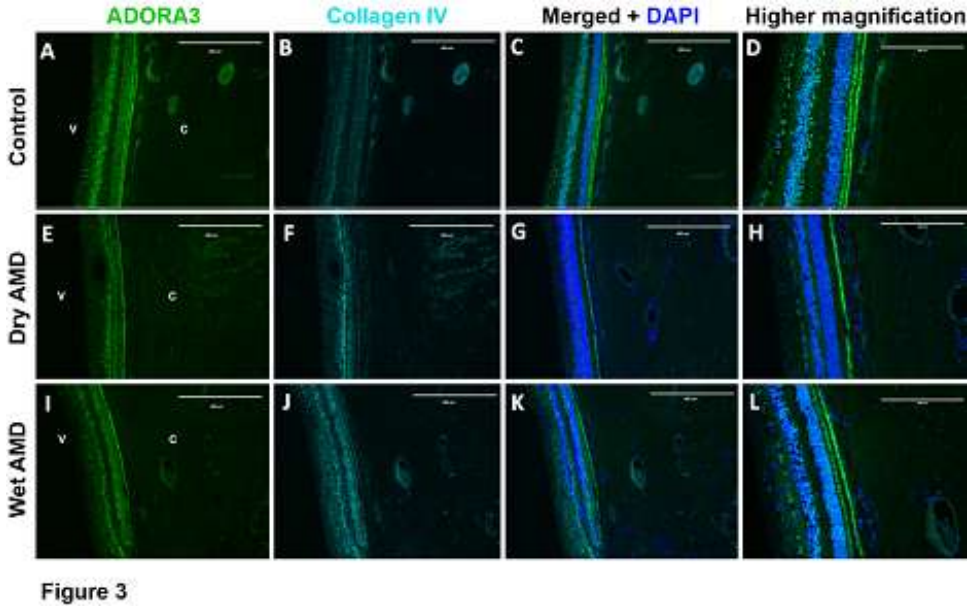


Figure 3

**Figure 4.** Expression of ADORA3 in retinal and choroidal cross sections. (A) ADORA3, (B) collagen IV, and (C) merged images and DAPI staining of eye sections with no AMD (Control). (D) Higher magnification of C. (E) ADORA3, (F) collagen IV, and (G) merged images and DAPI staining of eye sections with dry AMD. (H) higher magnification of F. (I) ADORA3, (J) collagen IV, and (K) merged images and DAPI staining of eye sections with wet AMD. (L) Higher magnification of K. Scale bar = 400 µm (A, B, C, E, F, G, I, J, and K) and 200 µm (D, H, and L).
V, vitreous; C, choroid.

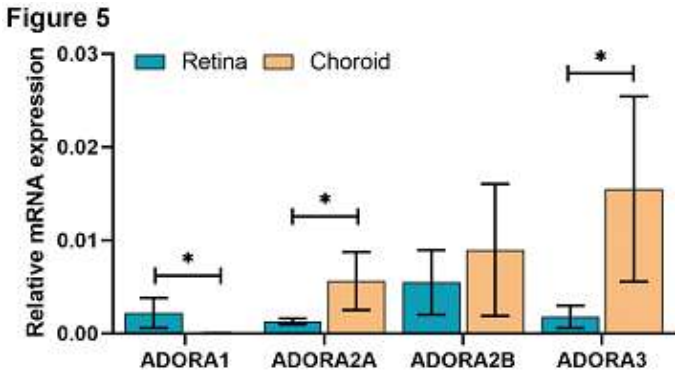


**Figure 5.** Quantitative PCR results demonstrating relative mRNA expression of adenosine receptor subtypes in a human eye sample without AMD. Blue bars display mRNA expression for each receptor in the retina, and orange bars display mRNA expression for each receptor in the choroid. ADORA1 and ADORA2B showed significantly higher levels in the retina, while ADORA2A and ADORA3 showed significantly higher levels in the choroid. *$P < 0.05$, $n = 3$.

**Table 1.** List of primers.

| Gene | Forward (5' to 3') | Reverse (5' to 3') |
|---|---|---|
| ADORA1 | gtccggtcctcatcctcac | ccaccatcttgtaccggaga |
| ADORA2A | cacaccactctccctagactctc | ttcctcacacttacatttttcctg |
| ADORA2B | cactgcttataatgctggtgatcta | gggtggtcctcgagtggt |
| ADORA3 | cccaattatatctcccccact | aagtcaggcctccaaaacact |
| RPL13A | aagcggatgaacaccaacc | tgtggggcagcatacctc |

successful staining with each of the adenosine receptor antibodies. Furthermore, vascular staining with collagen IV antibody and nuclear staining with DAPI were performed for each of the samples.

Adenosine receptor A1 demonstrated expression throughout the retina. A1 expression was particularly prominent in the outer plexiform layer (OPL), inner photoreceptor layer, and inner plexiform layer (IPL) of the retina. Retinal pigment epithelium (RPE) was also positive. No noticeable differences in choroidal vascular or retinal expression of the A1 were appreciated between patients with AMD compared to control patients regardless of sex. Representative images of A1 receptor staining in the retina and choroid are shown in Figure 1.

Receptor A2A primarily demonstrated expression within the retinal and choroidal vasculature, with a modest expression within the outer (ONL) and inner nuclear layers (INLs). The expression of the A2A was also detected in the RPE and was similar in patients with AMD compared to control eyes. However, there did appear to be a modest decrease in A2A receptor expression in retinal and choroidal vasculature in samples from patients with wet and dry AMD. There did not appear to be a dramatic difference in receptor A2A expression between patients with wet AMD compared with dry AMD [Figure 2].

Receptor A2B demonstrated expression throughout the retina in all samples, particularly the ganglion cell layer, ONL, and INL, and RPE. Receptor A2B was also strongly expressed in the retinal and choroidal vasculature in all samples. However, there was no dramatic difference in A2B receptor staining in the retina, retinal vasculature, or choroidal vasculature of patients with AMD compared with control eyes. Representative images of retinal and choroidal staining with antibodies to the A2B receptor are shown in Figure 3.

Receptor A3 was expressed primarily within the ganglion cell layer, INL, and ONL of the retina, and RPE. There was also some A3 receptor expression in the retinal and choroidal vasculature of each sample. A dramatic differences in A3 staining was observed in dry AMD samples compared with control and wet AMD samples. The dry AMD samples lost the expression of A3 receptor in the photoreceptor outer segments, which was prominently present in control and wet AMD samples. However, no additional differences in the intensity of staining were observed in retina or choroid in patients with AMD compared

to those with no AMD. Representative images of A3 receptor staining are shown in Figure 4.

### Adenosine Receptors mRNA Expression in Retina and RPE/Choroid Tissues

Quantitative PCR of cDNA prepared from the retinal and choroidal/RPE tissues from normal human eyes demonstrated notable expression of adenosine receptors within both the retina and choroid. Adenosine receptor A1 displayed gene expression primarily within the retina, with little to no choroidal expression. This was consistent with predominant immunostaining of A1 receptor in IPL and OPL, where microglia are normally residing. We previously showed predominant expression of A1 receptor in mouse microglia and retinal vascular cells.[19] Receptors A2A, A2B, and A3 displayed gene expression within both the retina and choroid. Although A1 receptor expression was significantly lower, the expression of A2A and A3 were significantly higher in the choroid/RPE compared with the retina, as we previously reported in human and mouse tissue samples.[19] The average relative expression of each adenosine receptor in both the retina and choroid/RPE is shown in Figure 5.

## DISCUSSION

The role of adenosine receptors in inflammatory pathways, as well as prior clinical and preclinical studies of their antagonism with caffeine suggest that these receptors may play important roles in the development of neurodegenerative diseases such as AMD. However, previous literature has not sufficiently examined the distribution of the adenosine receptor subtypes in the human retina and choroid. Furthermore, this is the first study to compare the expression patterns of adenosine receptors in the eyes of patients with and without AMD.

Collectively, our qPCR and antibody staining experiments demonstrated that adenosine receptors are widely expressed throughout the human eye and are present within both the human retina and choroid. Antibody staining suggested that receptors A1, A2A, A2B, and A3 are widely expressed in multiple layers of the human retina, providing further support for the importance of these receptors in the human ocular homeostasis and pathophysiology of AMD. A recent study involving zebrafish studied the expression of all four adenosine receptor subtypes, reporting A2A and A2B receptors in both the inner and outer plexiform and nuclear layers, and the ganglion cell layer.[20] Our results demonstrated similar distribution of the A2B receptors throughout the retina, but we primarily observed the A2A receptors expressed within the vasculature. Much like our results, A3 receptors were primarily in the inner and ONLs and A1 receptors were primarily in the inner and OPLs.[20] Therefore, our results indicate some overlap with the preclinical models mapping the expression of adenosine receptors in the retina, but we did find differences in human retinal expression compared to animal models.

Prior human studies have examined the location of adenosine A1 receptors in the retina of humans and other mammals. Like our results, these studies demonstrated A1 expression in both the inner and outer retina, with expression in the inner plexiform, ganglion cell, inner nuclear, and photoreceptor layers.[21, 22] A separate study demonstrated the presence of A2 receptors within the human RPE but did not attempt to map the A2 receptors throughout the retina.[23]

In addition to the human neuroretina, receptors A2A, A2B, and A3 were strongly expressed within the retinal and choroidal vasculature. Studies have suggested that the loss of the inner choroidal vascular layer is associated with the development of AMD and likely to occur due to inflammation within the choroid.[24] Our observation of adenosine receptors within the choroidal vasculature and their involvement in inflammation suggests they may also have a role in hallmark AMD changes within the choroid.

We hypothesized that altered A2A expression in patients with wet and dry AMD could contribute to pathophysiology of AMD. Prior studies have suggested that A2A receptor stimulation is pro-inflammatory, and antagonism of the A2A receptor can prevent neovascularization in the retina.[13–15] Interestingly, our results suggest there may be a modest decrease in the expression of the A2A receptor in patients with AMD disease process, which requires further verification in future studies. Therefore, a change in the A2A receptor levels in the human retina and choroid may disrupt normal signaling in the eye potentially contributing to pathogenesis of AMD.

A previous study in our lab examined the effect of caffeine, an adenosine receptors antagonist, and istradefylline, a specific A2A receptor antagonist, on choroidal neovascularization after laser-induced rupture of Bruch's membrane. These studies demonstrated that antagonism of adenosine receptors, particularly A2A, was successful in

inhibiting choroidal neovascularization. We also demonstrated that caffeine inhibits the migration of retinal and choroidal endothelial cells.[19] Thus, the results of the current study suggesting that the A2A receptor may have altered expression in human eyes with AMD fits well with prior findings. Together these results suggest a potential role for adenosine receptor antagonism in preventing changes associated with AMD.

In our previous study we noted variable and limited expression of A3 receptor in retina and choroid/RPE tissues from mouse eyes.[19] However, here we noted significant expression of A3 receptor in human eye sections with predominant expression in the choroid/RPE. The immune staining of the eye sections from dry AMD patients lacked A3 staining in the photoreceptor outer segments, which was predominantly present in eye sections from control and wet AMD patients. Thus, downregulation of A3 receptor expression may specifically contribute to loss of photoreceptor cells in dry AMD and awaits future studies of its significance in pathophysiology of dry AMD.

Overall, this study suggests that adenosine receptors are present throughout the retina and choroidal vasculature and supports the potential role of adenosine as a key signaling molecule and inflammatory mediator in pathophysiology of AMD. Furthermore, there may be changes in the levels of adenosine receptor A2A and A3 expression in patients who have AMD. However, the number of samples evaluated here were limited and awaits further confirmation of these results using additional samples in future studies as more suitable samples become available. We propose it is possible that the adenosine receptors contribute to the development of both wet and dry AMD and are suitable candidates to be targeted in the ongoing search for AMD therapeutics in future studies.

## Ethical Considerations

The human eyes were obtained from Lions Gift of Sight (formerly known as Minnesota Lions Eye Bank, Saint Paul, MN) with the written consent of the donor or the donor's family for use in medical research in accordance with the Declaration of Helsinki. Lions Gift of Sight is licensed by the Eye Bank Association of America (accreditation #0015204) and accredited by the FDA (FDA Established Identifier 3000718528). Donor tissue is considered pathological specimens and is therefore exempt from the process of Institutional Review Board approval.

## Acknowledgements

The authors would like to thank the Lion Gift of Sight (St. Paul, MN) personnel for obtaining the eyes and preparing the tissues for immunostaining. They are also thankful to the donors and their families for their valuable contributions to the research.

## Financial Support and Sponsorship

This work and/or the investigator(s) were supported by an unrestricted award from Research to Prevent Blindness to the Department of Ophthalmology and Visual Sciences, Retina Research Foundation, RRF/Daniel M. Albert chair, and by National Institutes of Health grants P30 EY016665, R01 EY026078, EY030076, EY032543, and HL158073. CPG was recipient of a VitreoRetinal Surgery Foundation research award, Edina, MN.

## Conflicts of Interest

The authors declare no conflict of interest.

## *REFERENCES*

1. Klein R, Chou CF, Klein BE, Zhang X, Meuer SM, Saaddine JB. Prevalence of age-related macular degeneration in the US population. *Arch Ophthalmol* 2011;129:75–80.
2. Bhutto I, Lutty G. Understanding age-related macular degeneration (AMD): Relationships between the photoreceptor/retinal pigment epithelium/Bruch's membrane/choriocapillaris complex. *Mol Aspects Med* 2012;33:295–317.
3. Hernandez-Zimbron LF, Zamora-Alvarado R, Ochoa-De la Paz L, Velez-Montoya R, Zenteno E, Gulias-Canizo R, et al. Age-related macular degeneration: New paradigms for treatment and management of AMD. *Oxid Med Cell Longev* 2018;2018:8374647.
4. Martin DF, Maguire MG, Ying GS, Grunwald JE, Fine SL, Jaffe GJ. Ranibizumab and bevacizumab for neovascular age-related macular degeneration. *N Engl J Med* 2011;364:1897–1908.
5. Handa JT, Bowes Rickman C, Dick AD, Gorin MB, Miller JW, Toth CA, et al. A systems biology approach towards understanding and treating non-neovascular age-related macular degeneration. *Nat Commun* 2019;10:3347.
6. Jabbehdari S, Handa JT. Oxidative stress as a therapeutic target for the prevention and treatment of early age-related macular degeneration. *Surv Ophthalmol* 2020.
7. Jager RD, Mieler WF, Miller JW. Age-related macular degeneration. *N Engl J Med* 2008;358:2606–2617.
8. Hollyfield JG, Bonilha VL, Rayborn ME, Yang X, Shadrach KG, Lu L, et al. Oxidative damage-induced inflammation initiates age-related macular degeneration. *Nat Med* 2008;14:194–198.

9. Sakurai E, Anand A, Ambati BK, van Rooijen N, Ambati J. Macrophage depletion inhibits experimental choroidal neovascularization. *Invest Ophthalmol Vis Sci* 2003;44:3578–3585.
10. Nozaki M, Raisler BJ, Sakurai E, Sarma JV, Barnum SR, Lambris JD, et al. Drusen complement components C3a and C5a promote choroidal neovascularization. *Proc Natl Acad Sci U S A*. 2006;103:2328–2333.
11. Auchampach JA. Adenosine receptors and angiogenesis. *Circ Res* 2007;101:1075–1077.
12. Effendi WI, Nagano T, Kobayashi K, Nishimura Y. Focusing on adenosine receptors as a potential targeted therapy in human diseases. *Cells* 2020;9:785.
13. Madeira MH, Rashid K, Ambrosio AF, Santiago AR, Langmann T. Blockade of microglial adenosine A2A receptor impacts inflammatory mechanisms, reduces ARPE-19 cell dysfunction and prevents photoreceptor loss in vitro. *Scientific Reports* 2018;8:2272.
14. Aherne CM, Kewley EM, Eltzschig HK. The resurgence of A2B adenosine receptor signaling. *Biochim Biophys Acta* 2011;1808:1329–1339.
15. Merighi S, Borea PA, Stefanelli A, Bencivenni S, Castillo CA, Varani K, et al. A2a and a2b adenosine receptors affect HIF-1alpha signaling in activated primary microglial cells. *Glia* 2015;63:1933–1952.
16. Daly JW, Shi D, Nikodijevic O, Jacobson KA. The role of adenosine receptors in the central action of caffeine. *Pharmacopsychoecologia* 1994;7:201–213.
17. Maugeri G, D'Amico AG, Rasà DM, La Cognata V, Saccone S, Federico C, et al. Caffeine prevents blood retinal barrier damage in a model, in vitro, of diabetic macular edema. *J Cell Biochem* 2017;118:2371–2379.
18. Chen JF, Zhang S, Zhou R, Lin Z, Cai X, Lin J, et al. Adenosine receptors and caffeine in retinopathy of prematurity. *Mol Aspects Med* 2017;55:118–125.
19. Sorenson CM, Song Y-S, Zaitoun IS, Wang S, Hanna BA, Darjatmoko SR, et al. Caffeine inhibits choroidal neovascularization through mitigation of inflammatory and angiogenesis activities. *Front Cell Dev Biol* 2021;9:737426.
20. Grillo SL, McDevitt DS, Voas MG, Khan AS, Grillo MA, Stella SL, Jr. Adenosine receptor expression in the adult zebrafish retina. *Purinergic Signal* 2019;15:327–342.
21. Blazynski C, Perez MT. Adenosine in vertebrate retina: Localization, receptor characterization, and function. *Cell Mol Neurobiol* 1991;11:463–484.
22. Braas KM, Zarbin MA, Snyder SH. Endogenous adenosine and adenosine receptors localized to ganglion cells of the retina. *Proc Natl Acad Sci U S A* 1987;84:3906–3910.
23. Friedman Z, Hackett SF, Linden J, Campochiaro PA. Human retinal pigment epithelial cells in culture possess A2-adenosine receptors. *Brain Res* 1989;492:29–35.
24. Farazdaghi MK, Ebrahimi KB. Role of the choroid in age-related macular degeneration: A current review. *J Ophthalmic Vis Res* 2019;14:78–87.

Original Article

# The Role of TRiC-enhanced Actin Folding in Leber Congenital Amaurosis

**Silke Berger[1,2], BS; Peter D. Currie[1,2] BS; Joachim Berger[1,2], MS**

*[1]Australian Regenerative Medicine Institute, Monash University, Clayton, Australia*
*[2]Victoria Node, EMBL Australia, Clayton, Australia*

**ORCID:**
*Silke Berger: https://orcid.org/0000-0002-6887-317X*
*Joachim Berger: https://orcid.org/0000-0002-7859-545X*

## Abstract

**Purpose:** Mutations in TCP-1 ring complex (TRiC) have been associated with Leber Congenital Amaurosis (LCA). TRiC is involved in protein folding and has 8 essential subunits including CCT5. Herein, we studied the retina of TRiC mutant zebrafish to evaluate the possible role of impaired actin and tubulin folding in LCA.
**Methods:** The *cct5*$^{tf212b}$ retina was histologically studied using Toluidine Blue staining as well as TUNEL, BrdU-labeling, and Phalloidin assays. Retinal organisation was assessed by quantification of the cellularity utilising DAPI.
**Results:** Laminar organization of *cct5*$^{tf212b}$ retinas was intact. Enhanced apoptosis throughout the *cct5*$^{tf212b}$ retina was not compensated by higher proliferation rates, leaving the *cct5*$^{tf212b}$ retina smaller in size. Quantification of retinal layer cellularity demonstrated that specifically the numbers of the amacrine and the retinal ganglion cells were depleted, suggesting that the *cct5*$^{tf212b}$ retina was not uniformly affected by the reduced actin folding.
**Conclusion:** Whereas the current literature suggests that LCA is predominantly affecting retinal photoreceptor cells and the retinal pigment epithelium, *cct5*$^{tf212b}$ analyses demonstrated the important role of folding of actin by TRiC, suggesting that *cct5*$^{tf212b}$ is a useful tool to specifically analyze the role of F-actin filaments in the context of LCA.

**Keywords:** Actin; *cct5*; Leber Congenital Amaurosis; Retina; TRiC; Zebrafish

*J Ophthalmic Vis Res* 2023; 18 (1): 60–67

**Correspondence to:**
Joachim Berger, MS. Australian Regenerative Medicine Institute, 15 Innovation Walk, Clayton, VIC 3800, Australia.
E-mail: Joachim.Berger@monash.edu

Received: 14-05-2022 Accepted: 05-11-2022

**Access this article online**

**Website:** https://knepublishing.com/index.php/JOVR

**DOI:** 10.18502/jovr.v18i1.12726

This is an open access article distributed under the Creative Commons Attribution License, which permits unrestricted use, distribution, and reproduction in any medium, provided the original work is properly cited.

**How to cite this article:** Berger S, Currie PD, Berger J. The Role of TRiC-enhanced Actin Folding in Leber Congenital Amaurosis. J Ophthalmic Vis Res 2023;18:60–67.



© 2023 Berger et al. This is an open access article distributed under the Creative Commons Attribution License | Published by Knowledge E

## INTRODUCTION

Leber Congenital Amaurosis (LCA) is an early-onset congenital retinal dystrophy causing severe visual impairment. Over 38 disease-causing variants involving various pathological mechanisms have been associated with LCA, which consequently presents with a broad clinical spectrum, typically including poor to near-absent pupillary responses, nystagmus, photophobia, and severe visual impairment.[1] Diagnosis is made within the first year of life usually based on extinguished electroretinograms, detecting little if any retinal activity.

Compound heterozygous missense mutations in *CCT2* have been identified in individuals suffering from LCA.[2] Computational modeling combined with biochemical studies suggested that these mutations combined induce partial, and not complete, loss of TRiC functionality.[2] *CCT2* is a subunit of the eukaryotic TCP-1 ring complex (TRiC, also called chaperonin containing TCP-1 [CCT]); an ATP-driven chaperonin that aids mis- or unfolded proteins in their folding. TRiC has a barrel-shaped structure with two back-to-back rings, each comprising of eight paralogous subunits (CCT1 - 8).[3] Whereas several substrates have been described for TRiC,[4] actin as well as all $\alpha$- and $\beta$-tubulin are the main folding substrates.[5, 6] Accordingly, genetic analysis of TRiC in the zebrafish vertebrate model system *in vivo* revealed that loss of TRiC function leads to severe muscle and neuronal defects provoked by deficits in folding of actin and tubulin.[7, 8] The notion from structural data that loss of a single subunit leads to full loss of TRiC function was confirmed by genetic analysis of single and compound mutants.[3, 7] In a forward genetic screen, the zebrafish mutant *tf212b* was isolated based on its abnormal locomotion behavior and later reported to harbor a missense mutation leading to G422V replacement within the Cct5 subunit of TRiC.[7, 9] In contrast to mutants with a full loss of TRiC function, the missense mutation in *cct5*$^{tf212b}$ leads to actin misfolding by TRiC, whereas tubulin folding is not affected.[7]

In order to assess the role of impaired actin folding in retinal development, the retina of *cct5*$^{tf212b}$ was studied. As tubulin folding is intact in *cct5*$^{tf212b}$ homozygotes, defects of the retina within *cct5*$^{tf212b}$ homozygotes can be attributed to impaired actin folding. According to the impaired folding of actin within *cct5*$^{tf212b}$, retina analyses revealed that the formation of F-actin filaments is reduced in the *cct5*$^{tf212b}$ retina. Although proliferation was enhanced within the ciliary marginal zone, the retina in *cct5*$^{tf212b}$ mutants was smaller in size, likely due to enhanced apoptosis. Further cellularity quantification of the retinal layers revealed a reduction number of retinal ganglion cells and amacrine cells, indicating that these cell types are specifically affected by reduced actin folding.

## METHODS

### Maintenance and Genotyping of Zebrafish

The zebrafish lines *cct5*$^{tf212b}$ and *cct4*$^{-14}$ were maintained in the TU (Tübingen) background under the ERM/22161 breeding license of the Monash Animal Service. Genotyping of *cct4*$^{-14}$ mutants was achieved by using the oligonucleotides cct4_F (5'-cccgagtttcttgaccacgttg) and cct4_R (5'-ctccacctcgctctgctctaag) in a PCR resulting in a 131 bp amplicon for the *cct4*$^{-14}$ allele. For *cct5*$^{tf212b}$, the oligonucleotides Cct5_Bst_F (5'-acctggtgagggataatcgtatccagtat) and gCCT5_R1 (5'-cgggcactgaacacaagacaatc) were used in a PCR followed by restriction digestion with BstXI as reported[7].

### Immunohistochemistry and Histological Analysis

Immunohistochemistry as well as the stains with Toluidine Blue, DAPI, and H&E were performed according to standard methods. Only retinal cross sections with optic nerve were analyzed. Retinal areas were measured on H&E or Toluidine Blue-stained cross sections using the software ImageJ. BrdU labeling was performed by soaking larvae in 1% bromodeoxyuridine (BrdU) dissolved in fish water followed by 14 µm cryostat cross sectioning and treatment with fluorescein conjugated BrdU monoclonal antibodies (BMC9318, Merck) as described.[10] Apoptosis was detected using the *in situ* Cell Death Detection Kit as recommended by the manufacturer (Roche). All fluorescence images were recorded on a Zeiss ImagerZ1 fluorescence microscope (Zeiss, Germany). Images within figures show representatives of a minimum of six analyzed larvae per genotype.

## Comparison of F-actin Levels

F-actin was detected on 14 µm cryostat cross sections with phalloidin conjugated with AlexaFluor-568 (A12380, Life Technologies). To compare F-actin levels, phalloidin-stained sections were imaged on a Zeiss ImagerZ1 fluorescence microscope (Zeiss, Germany) under constant conditions and subsequently analyzed for their brightness values. Utilizing the software Fiji, the area of the inner plexiform layer (IPL) was selected and the mean of all grey values of the pixels within this area was measured, resulting in a single grey value per quantified IPL. To enable comparison of the brightness of the IPL from different genotypes, obtained grey values were rescaled to siblings set to 100%. To rescale grey values of siblings, measured grey values ($A_1$ to $A_n$) of individual IPL were multiplied by 100 and divided by the average of all measured grey values of siblings using $\frac{A_i \times 100}{\sum_{i=1}^{n} A_i/n}$. To normalize values of mutants, measured grey values ($B_1$ to $B_n$) of individual IPL were multiplied by 100 and divided by the average of the measured grey values of the siblings using $\frac{B_i \times 100}{\sum_{i=1}^{n} A_i/n}$. Only IPL from retinal cross sections were analyzed that showed the optic nerve. Ten IPL were analyzed per genotype ($n$ = 10).

## Quantification of Cellularity of Retinal Layers

At six days post fertilization (dpf), transverse sections were stained with DAPI to label cell nuclei. Subsequent to imaging using a Zeiss ImagerZ1 fluorescence microscope (Zeiss, Germany), images were converted to 8-bit format and adjusted for contrast, brightness, and threshold. The outer nuclear layer, the inner nuclear layer, and the ganglion cell layer were distinguished based on their separation by the plexiform layers. The inner nuclear layer was further subdivided into a basal and an apical layer based on the difference in the fluorescence intensity of their nuclei. All DAPI-marked cell nuclei in individual layers were counted as described earlier.[11] Five sections per genotype on the level of the optic nerve were included in the quantification ($n$ = 5).

## Statistical Analysis

Significance between two groups was determined by Student's *t*-test. Statistical significance was calculated using the software Prism (GraphPad Software). Presented data are mean ± standard error of the mean (SEM).

## RESULTS

To document the retinal degeneration at larval stages within zebrafish, *cct4*$^{-14}$ mutants were utilized that feature loss of TRiC function due to their lack of the Cct4 subunit.[7] Semi-thin cross sections of retinas from *cct4*$^{-14}$ homozygotes were generated and stained with Toluidine Blue at six dpf [Figure 1A]. In contrast to the highly organized layers of the sibling retina, within *cct4*$^{-14}$ homozygous only a rudimentary lens and dispersed pigments mainly accumulated in a band shape were present. Defined cell structures were absent between a rudimentary lens and clustered pigment, indicating a full degeneration of the *cct4*$^{-14}$ retina. In contrast, the retina of *cct5*$^{tf212b}$ homozygotes, in which folding of actin but not tubulin is impaired, showed defined nuclei and largely intact layering comparable to their siblings [Figure 1B]. However, whereas signs of retinal degeneration were not obvious on Toluidine Blue-stained sections, the *cct5*$^{tf212b}$ homozygous retina seemed reduced in size compared to their sibling retina, indicating that minor defects could be apparent within the *cct5*$^{tf212b}$ retina.

To study the retina of *cct5*$^{tf212b}$ homozygotes in more detail, the retinal area was quantified on H&E-stained cross sections. Quantification of the retinal area revealed that the retina of *cct5*$^{tf212b}$ homozygotes was significantly reduced in size compared to their siblings at three dpf as well as six dpf [Figure 2A]. To further study the reduced retinal size of *cct5*$^{tf212b}$ homozygotes, cells in the S phase were labeled using a single 1-hr pulse of the thymidine analogue bromodeoxyuridine (BrdU) prior to fixation at three dpf. Subsequent analysis of BrdU-labeled cells on cross sections revealed that although the location of the proliferating cells within the retinal ciliary marginal zone was not altered in *cct5*$^{tf212b}$ homozygotes [Figure 2B], significantly more cells were proliferating during the 1-hr BrdU pulse within *cct5*$^{tf212b}$ homozygotes compared to siblings [Figure 2C]. To assess if the significantly smaller *cct5*$^{tf212b}$ retinal area despite their higher proliferation rate could be attributed to increased cell death, apoptotic cells were labeled on sections using the TUNEL assay (TdT-mediated dUTP-biotin nick end labeling). With an

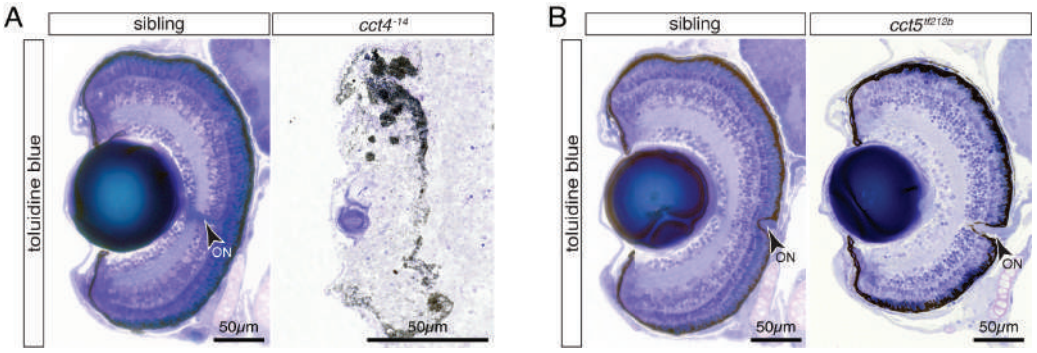


**Figure 1.** The eye develops in *cct5*$^{tf121b}$ but not *cct4*$^{-14}$ mutants. (A) Toluidine Blue-stained sections of six-dpf-old siblings revealed the typical layered structure of the retina. In contrast, the eye of TRiC loss-of-function *cct4*$^{-14}$ mutants was severely degraded and only rudimentary structures of lens and pigmented retina were recognisable. (B) At six dpf, homozygotes of the missense mutant *cct5*$^{tf212b}$ featured a structured eye and the layering of the retina appeared comparable to siblings. Arrowheads indicate optic nerves (ON).

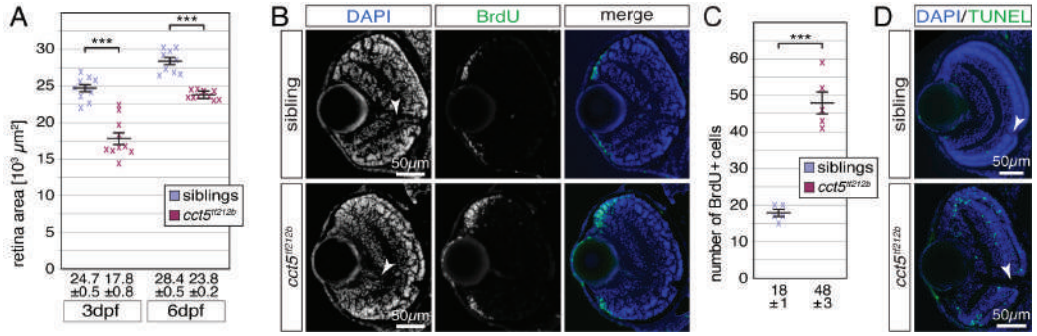


**Figure 2.** The retina of *cct5*$^{tf121b}$ mutants is smaller and characterised by enhanced proliferation and apoptosis. (A) Quantification of the retina sizes revealed that the retinal area of *cct5*$^{tf121b}$ homozygotes was significantly smaller compared to siblings. The mean retinal area of *cct5*$^{tf121b}$ homozygotes was 17.8 ± 0.8 (×10$^3$ µm$^2$) at three dpf and 23.8 ± 0.2 (×10$^3$ µm$^2$) at six dpf compared to siblings that featured mean retinal areas of 24.7 ± 0.5 (×10$^3$ µm$^2$) at three dpf and 28.4 ± 0.5 (×10$^3$ µm$^2$) at six dpf; *n* = 10 per genotype and stage. (B) In contrast to three-dpf-old siblings, more BrdU-positive cells (green) were detected at the periphery of the retina within the ciliary marginal zone of *cct5*$^{tf121b}$ homozygotes. (C) Quantification of the number of BrdU-positive cells within individual retinas revealed that significantly more cells were proliferating within the ciliary marginal zone of *cct5*$^{tf121b}$ homozygotes at three dpf. Whereas *cct5*$^{tf121b}$ had 48 ± 3 BrdU-positive cells per retinal cross section, 18 ± 1 were proliferating in siblings (*n* = 5). (D) In contrast to the retina of three-dpf-old siblings, in which apoptotic cells were rarely labelled by the TUNEL assay (green), apoptosis was frequently observed throughout the entire retina of *cct5*$^{tf121b}$ homozygotes.
Data are mean ± SEM; ***$P < 0.001$ by Student's *t*-test. Arrowheads indicate optic nerves (ON).

average of 1.2 ± 0.3 TUNEL-positive cells per retinal cross section, apoptotic cells were rarely found on retinal sections of three-dpf-old siblings [Figure 2D]. In contrast, sections from *cct5*$^{tf212b}$ homozygotes harbored significantly more TUNEL-positive cells with an average of 60 ± 6 per section, indicating that apoptosis was greatly enhanced in *cct5*$^{tf212b}$ mutants ($n$ = 10, $P < 0.0001$). In summary, the significantly reduced size of the retinal area of *cct5*$^{tf212b}$ homozygotes could be attributed to the greatly enhanced apoptosis that could not be compensated by the significantly higher proliferation within the ciliary marginal zone.

Residual actin-based thin filaments are formed within the sarcomeres of *cct5*$^{tf212b}$ skeletal muscle cells, as TRiC only enhances actin folding but is not absolutely required.[7] In order to unveil F-actin filament assembly within the *cct5*$^{tf212b}$ retina, cross sections were stained with the F-actin marker phalloidin and counterstained with DAPI at three dpf. As F-actin mainly locates on the inner surface of cell membranes, the inner and the outer plexiform layers of the sibling retina are strongly marked by phalloidin due to the high neurite densities within these regions [Figure 3A]. In comparison, the phalloidin signal of both plexiform layers appeared weaker in

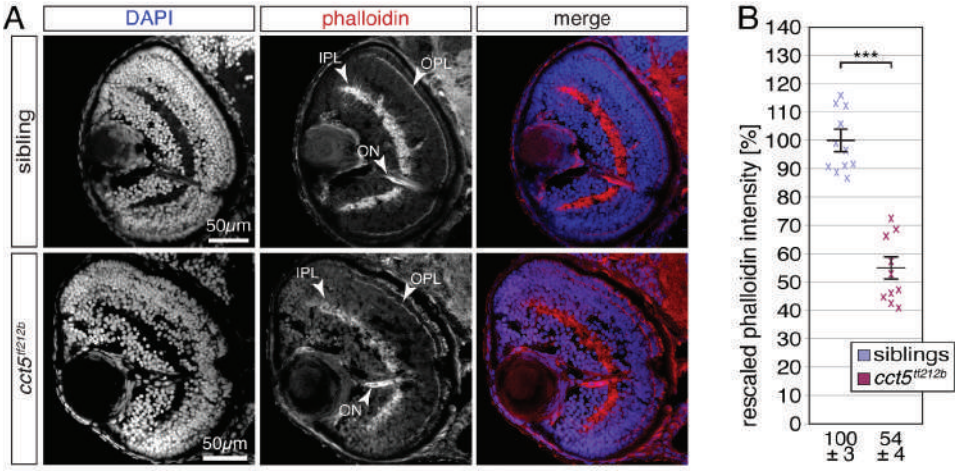


**Figure 3.** F-actin is significantly reduced in the retina of *cct5*$^{tf121b}$ mutants. (A) At three dpf, F-actin was labelled with phalloidin (red) on cross sections counterstained with DAPI (blue). Whereas the inner and outer plexiform layers of the retina (IPL and OPL, respectively) were prominently stained by phalloidin within siblings, the signal from *cct5*$^{tf121b}$ homozygotes appeared weaker. Phalloidin also marked the optic nerve (ON). (B) Quantification of the brightness of the phalloidin signal within the IPL revealed that *cct5*$^{tf121b}$ homozygotes showed a significant reduction in signal intensity to 54 ± 4% in relation to their siblings, which were rescaled to 100 ± 3%. Data are mean ± SEM; ***$P$ < 0.001 by Student's $t$-test; $n$ = 10.

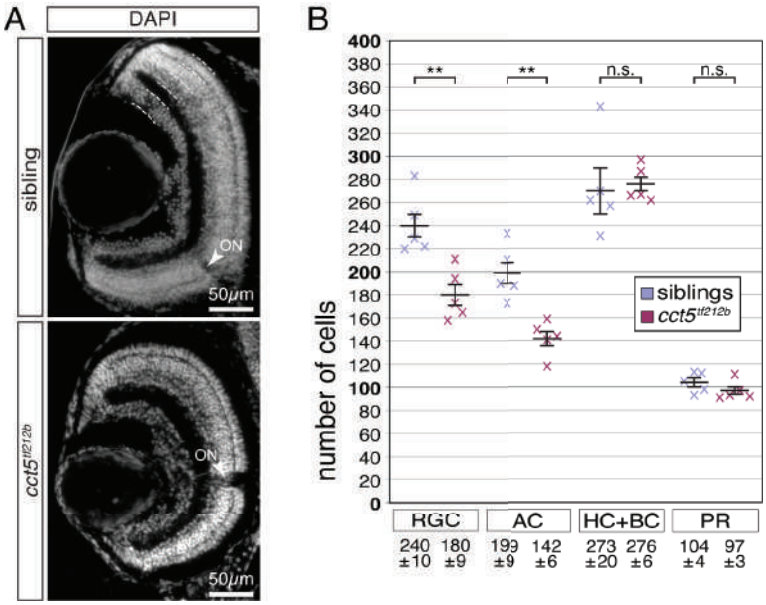


**Figure 4.** Retinal ganglion and amacrine cells are reduced in number in *cct5*$^{tf121b}$ mutants. (A) At six dpf, the retinal nuclei of siblings and *cct5*$^{tf121b}$ mutants were marked at the level of the optic nerve using the nuclear stain DAPI. Indicated by the dotted lines, the outer nuclear layer contains the photoreceptor cells (PR). The inner nuclear layer harbours the apical horizontal cells (HC) and the bipolar cells (BC) as well as the basally located amacrine cells (AC). The most basal layer contains the retinal ganglion cells (RGC). Arrowheads indicate optic nerves (ON). (B) Quantification of the cellularity of the different retinal layers within siblings and *cct5*$^{tf121b}$ homozygotes at six dpf. The cell number of the RGC and the AC were significantly reduced in *cct5*$^{tf121b}$ homozygotes. Per retinal cross section, siblings had 240 ± 10 RGC and 199 ± 9 AC in contrast to 180 ± 9 RGC and 142 ± 6 AC in *cct5*$^{tf121b}$ homozygotes. The number of HC and BC as well as PR remained unchanged. Siblings had 273 ± 20 HC and BC as well as 104 ± 24 PR and *cct5*$^{tf121b}$ homozygotes had 276 ± 6 HC and BC as well as 97 ± 3 PR. Data are mean ± SEM; **$P$ < 0.01 by Student's $t$-test; n.s., not significant; n, 5.

*cct5*$^{tf212b}$ homozygotes [Figure 3A]. To quantify the signal intensity of phalloidin from both genotypes, staining of retinal sections and imaging were performed under constant conditions for both *cct5*$^{tf212b}$ homozygotes and siblings. Subsequent quantification of the brightness of the IPL revealed that the mean signal intensity from *cct5*$^{tf212b}$ homozygotes was significantly reduced compared to their siblings, indicating a reduced level of F-actin filaments within *cct5*$^{tf212b}$ mutants. Taken together, in accordance with the reduced actin folding detected in skeletal muscle of *cct5*$^{tf212b}$ homozygotes,[7] biogenesis of F-actin filaments was also impaired within the retina, although F-actin filaments were still assembled within *cct5*$^{tf212b}$ mutants.

Using the nuclear stain DAPI, the laminar organization of the retina can be visualized that includes the outer nuclear layer, the inner nuclear layer, and the ganglion cell layer [Figure 4A]. The inner nuclear layer can further be subdivided into the basal positioned amacrine cells and the apical compartment with the bipolar and horizontal cells.[12] To further characterize the retinal defects, the cell number within individual retinal layers were counted at six dpf. Quantification of the cellularity of the outer nuclear layer with photoreceptor cells as well as the apical inner nuclear layer with the horizontal cells and the bipolar cells revealed that the number of these cell types remained unchanged between siblings and *cct5*$^{tf212b}$ mutants [Figure 4B]. However, quantification of the cellularity of the basal inner nuclear layer and the ganglion cell layer revealed that both layers of *cct5*$^{tf212b}$ homozygotes contained significantly less nuclei compared to their siblings, suggesting that amacrine cells as well as retinal ganglion cells were diminished within *cct5*$^{tf212b}$ homozygotes [Figure 4B]. Taken together, these results indicate that specifically the amacrine and the retinal ganglion cells of *cct5*$^{tf212b}$ mutants are affected by the reduced biogenesis of F-actin filaments.

## DISCUSSION

Analysis of zebrafish *cct5*$^{tf212b}$ mutants revealed that their retinas were reduced in size and their level of F-actin filaments. Enhanced proliferation was not able to compensate for the enhanced apoptosis and numbers of the amacrine and the retinal ganglion cells were depleted.

LCA is a severe congenital retinal dystrophy with over 38 disease-causing variants, including *CCT2*.[1, 2] Mutations in the zebrafish ortholog Cct2 as well as other TRiC subunits have been reported to result in retinal degeneration.[7, 8, 13] Retinal ganglion and amacrine cells are reduced in number in *cct5*$^{tf121b}$ mutants. (A) At six dpf, the retinal nuclei of siblings and *cct5*$^{tf121b}$ mutants were marked at the level of the optic nerve using the nuclear stain DAPI. Indicated by the dotted lines, the outer nuclear layer contains the photoreceptor cells (PR). The inner nuclear layer harbours the apical horizontal cells (HC) and the bipolar cells (BC) as well as the basally located amacrine cells (AC). The most basal layer contains the retinal ganglion cells (RGC). Arrowheads indicate optic nerves (ON). (B) Quantification of the cellularity of the different retinal layers within siblings and *cct5*$^{tf121b}$ homozygotes at six dpf. The cell number of the RGC and the AC were significantly reduced in *cct5*$^{tf121b}$ homozygotes. Per retinal cross section, siblings had 240 ± 10 RGC and 199 ± 9 AC in contrast to 180 ± 9 RGC and 142 ± 6 AC in *cct5*$^{tf121b}$ homozygotes. The number of HC and BC as well as PR remained unchanged. Siblings had 273 ± 20 HC and BC as well as 104 ± 24 PR and *cct5*$^{tf121b}$ homozygotes had 276 ± 6 HC and BC as well as 97 ± 3 PR. Data are mean ± SEM; $^{**}P < 0.01$ by Student's *t*-test; n.s., not significant; n, 5. However, these mutants were full or partial loss-of-function mutants of individual TRiC subunits resulting in full or partial loss of TRiC function. Consequently, these studied mutants featured deficiencies in folding of both actin and tubulin, the main substrates of TRiC. Accordingly, retinal degeneration within *cct4*-deficient mutants, with only a rudimentary lens and clustered pigment remaining, was confirmed at six dpf in this study.

In order to specifically distinguish the effects of impaired actin folding from the other functions of TRiC in the context of LCA, the retina of the mutant *cct5*$^{tf212b}$ was assessed. Although the size of the retina was reduced at three and six dpf, the six-dpf-old *cct5*$^{tf212b}$ retina was organized in defined layers and appeared largely intact. Although proliferation of the *cct5*$^{tf212b}$ retina was enhanced, abundant apoptosis was detected as well, suggesting that the smaller retinal area might be attributed to the greatly increased apoptosis. These findings are in accordance with zebrafish *cct2*$^{L394H-7del}$ mutants that showed a higher number of retinal S phase cells.[13]

Residual folded actin can be detected in the absence of TRiC, suggesting that TRiC enhances the folding of actin but is not absolutely required.[7] Compared to other retinal layers, the IPL contains a high level of F-actin filaments due to its high membrane density with interlaced dendrites from cells of the inner nuclear layer and the retinal ganglion cells. Accordingly, the number of F-actin filaments within the *cct5*$^{tf212b}$ IPL was found to be reduced, although F-actin filaments were still detected. The intact organization of the *cct5*$^{tf212b}$ retinal layers suggested that areas of low actin contents were not notably affected in *cct5*$^{tf212b}$ mutants. Thus, the reduced biogenesis of F-actin filaments predominantly within the IPL could be explained by the high levels of F-actin filaments within this layer that require TRiC to enhance the folding of actin.

Retinal organization was further analyzed by the quantification of the cellularity of individual retinal layers, which revealed that specifically the amacrine cells and the ganglion cells were reduced in numbers. Amacrine cells are interneurons that modulate the signal from the rod photoreceptors to the retinal ganglion cells, which transport the visual information through the optic nerve to the brain. Thus, although ocular function was not further elucidated given the severely impaired musculature of *cct5*$^{tf212b}$ that would hamper analysis of behavioral responses to visual stimuli,[7] an impaired functionality of the *cct5*$^{tf212b}$ eye resulting in visual impairment would be expected from the disrupted anatomical structure of the *cct5*$^{tf212b}$ retina. It is noteworthy that LCA is mainly recognized as a disease of the retinal pigment epithelium and photoreceptors[14] and only two sibling patients with variants in *CCT2* resulting in disruption of TRiC were implicated in LCA to date.[2] Variants in *CCT5* have not been associated with patients suffering from LCA as yet, making further studies necessary to fully understand the consequences of impaired F-actin filament formation for LCA.

Taken together, the analysis of the *cct5*$^{tf212b}$ retina demonstrated that defects in the enhancement of actin folding by TRiC could potentially contribute to TRiC-associated LCA and that zebrafish *cct5*$^{tf212b}$ mutants might be a valuable tool to study the role of F-actin filaments in the context of LCA.

## Ethical Considerations

The Monash Animal Service approved the treatment of zebrafish males with N-ethyl-N-nitrosourea (MAS/2009/05) and the maintenance of zebrafish lines (ERM/22161).

## Financial Support and Sponsorship

JB was supported by the Angior Family Foundation. The Australian Regenerative Medicine Institute is supported by grants from the State Government of Victoria and the Australian Government.

## Conflicts of Interest

None declared.

## *REFERENCES*

1. Huang CH, Yang CM, Yang CH, Hou YC, Chen TC. Leber's congenital amaurosis: Current concepts of genotype-phenotype correlations. *Genes* 2021;12:1261.
2. Minegishi Y, Sheng X, Yoshitake K, Sergeev Y, Iejima D, Shibagaki Y, et al. CCT2 mutations evoke Leber congenital amaurosis due to chaperone complex instability. *Sci Rep* 2016;6:33742.
3. Munoz IG, Yebenes H, Zhou M, Mesa P, Serna M, Park AY, et al. Crystal structure of the open conformation of the mammalian chaperonin CCT in complex with tubulin. *Nat Struct Mol Biol* 2011;18:14–19.
4. Hein MY, Hubner NC, Poser I, Cox J, Nagaraj N, Toyoda Y, et al. A human interactome in three quantitative dimensions organized by stoichiometries and abundances. *Cell* 2015;163:712–723.
5. Gao Y, Thomas JO, Chow RL, Lee GH, Cowan NJ. A cytoplasmic chaperonin that catalyzes beta-actin folding. *Cell* 1992;69:1043–1050.
6. Yaffe MB, Farr GW, Miklos D, Horwich AL, Sternlicht ML, Sternlicht H. TCP1 complex is a molecular chaperone in tubulin biogenesis. *Nature* 1992;358:245–248.
7. Berger J, Berger S, Li M, Jacoby AS, Arner A, Bavi N, et al. In vivo function of the chaperonin TRiC in alpha-actin folding during sarcomere assembly. *Cell Rep* 2018;22:313–322.
8. Matsuda N, Mishina M. Identification of chaperonin CCT gamma subunit as a determinant of retinotectal development by whole-genome subtraction cloning from zebrafish no tectal neuron mutant. *Development* 2004;131:1913–1925.
9. Granato M, van Eeden FJ, Schach U, Trowe T, Brand M, Furutani-Seiki M, et al. Genes controlling and mediating locomotion behavior of the zebrafish embryo and larva. *Development* 1996;123:399–413.

10. Berger J, Berger S, Hall TE, Lieschke GJ, Currie PD. Dystrophin-deficient zebrafish feature aspects of the Duchenne muscular dystrophy pathology. *Neuromuscul Disord* 2010;20(:826–832.
11. Wood AJ, Lin CH, Li M, Nishtala K, Alaei S, Rossello F, et al. FKRP-dependent glycosylation of fibronectin regulates muscle pathology in muscular dystrophy. *Nat Commun* 2021;12:2951.
12. Richardson R, Tracey-White D, Webster A, Moosajee M. The zebrafish eye-a paradigm for investigating human ocular genetics. *Eye* 2017;31:68–86.
13. Minegishi Y, Nakaya N, Tomarev SI. Mutation in the zebrafish cct2 gene leads to abnormalities of cell cycle and cell death in the retina: A model of CCT2-related Leber congenital amaurosis. *Invest Ophthalmol Vis Sci* 2018;59:995–1004.
14. Noel NCL, MacDonald IM, Allison WT. Zebrafish models of photoreceptor dysfunction and degeneration. *Biomolecules* 2021;11:78.

Original Article

# The Antitumor Effect of Topotecan Loaded Thiolated Chitosan-Dextran Nanoparticles for Intravitreal Chemotherapy: A Xenograft Retinoblastoma Model

**Elham Delrish[1], PhD; Mahmoud Jabbarvand[1], MD; Fariba Ghassemi[1,2],MD; Fahimeh Asadi Amoli[3], MD; Fatemeh Atyabi[4,5], PhD; Saeed Heidari Keshel[6], PhD; Alireza Lashay[1],MD; Farnaz Sadat Mirzazadeh Tekie[4], PhD; Masoud Soleimani[7], PhD, Rassoul Dinarvand[4,5], PhD**

*[1]Translational Ophthalmology Research Centre (TORC), Farabi Eye Hospital, Tehran University of Medical Sciences, Tehran, Iran*
*[2]Retina & Vitreous Service, Farabi Eye Hospital, Tehran University of Medical Sciences, Tehran, Iran*
*[3]Department of pathology, Farabi Eye Hospital, Tehran University of Medical Sciences, Tehran, Iran*
*[4]Nanotechnology Research Centre, Faculty of Pharmacy, Tehran University of Medical Sciences, Tehran, Iran*
*[5]Department of Pharmaceutics, Faculty of Pharmacy, Tehran University of Medical Sciences, Tehran, Iran*
*[6]Department of Tissue Engineering and Applied Cell Science, School of Advanced Technologies in Medicine, Shahid Beheshti University of Medical Sciences, Tehran, Iran*
*[7]Department of Hematology, School of Medical Sciences, Tarbiat Modares University, Tehran, Iran*

**ORCID:**
*Elham Delrish: https://orcid.org/0000-0003-4993-7593*
*Fariba Ghassemi: https://orcid.org/0000-0001-9423-9650*

## Abstract

**Purpose:** This research intended to fabricate the thiolated chitosan-dextran nanoparticles (NPs) containing topotecan (TPH-CMD-TCS-NPs) to assess the ability of NPs in improving the efficacy of intravitreal chemotherapy of retinoblastoma in a rabbit xenograft model.

**Methods:** The coacervation process was used to produce the NPs. The cellular uptake of Cyanine-3 (CY3)-labeled NPs were investigated in human retinoblastoma Y79 cells using confocal microscopy. Also, the prepared TPH-CMD-TCS-NPs were tested *in vitro* by the tetrazolium dyes II (XTT) and flow cytometry in order to assess their cytotoxicity. In addition, a rabbit xenograft model of retinoblastoma was developed to test the antitumor effectiveness of TPH-CMD-TCS-NPs through intravitreal administration.

**Results:** NPs had a mean diameter, polydispersity index, and zeta potential of 30 ± 4 nm, 0.24 ± 0.03 and +10 ± 3 mV, respectively. NPs (IC50s 40.40 compared to 126.20 nM, $P = 0.022$) were more effective than free topotecan as a dose-based feature. The tumor reaction to intravitreal chemotherapy with NPs was measured by evaluating the percentage of necrosis in the tumor tissue (91 ± 2%) and vitreous seeds (89 ± 9%) through hematoxylin and eosin (H&E) staining. In comparison with the control group, the TPH-CMD-TCs-NPs treated group showed a significant decrease in tumor volume seven days after the intravitreal injection ($P = 0.039$). No significant changes were found in the ERG parameters after the intravitreal injection of TPH-CMD-TCs-NPs or TPH ($P > 0.05$).

**Conclusion:** This investigation revealed definitive antitumor efficacy of TPH-CMD-TCS-NPs by intravitreal administration in the rabbit xenograft retinoblastoma model.

**Keywords:** Chemotherapy; Intravitreal; Nanoparticles; Ocular Malignancy; Retinoblastoma; Topotecan

*J Ophthalmic Vis Res* 2023; 18 (1): 68–80


© 2023 Delrish et al. This is an open access article distributed under the Creative Commons Attribution License | Published by Knowledge E

## INTRODUCTION

For several decades, external beam radiation (EBR) was the only possible way to preserve an eye with retinoblastoma (Rb) vitreous seeding. Intravenous chemotherapy (IVC) was an approach used for treating Rb without the increased rate of secondary malignancies related to the EBR procedure. However, at least half of the eyes with vitreous seeding treated with IVC were eventually enucleated.[1, 2] In recent decades, intra-arterial chemotherapy (IAC) which uses a maximal local concentration of chemotherapy agents by direct application to the tumor site has significantly improved the management of Rb.[3–8] Although, most eyes with vitreous seeding can be saved with this method, vitreous seeding still remains the main drawback leading to enucleation in IAC-treated eyes. Therefore, the use of intravitreal chemotherapy (IVitC) has been selected as an option to increase the globe salvage rate.[9–12] Although a few chemotherapy molecules have been effective in the treatment of Rb, these medications have not achieved the optimal concentrations needed within the ocular malignant tissue. Insufficient delivery of these small molecular drugs causes dose-limiting side effects including toxicity and limited bioavailability. For more efficient drug delivery and targeting of Rb, nanotechnology may be an implementable strategy. Nano-carrier material has been shown to be a successful drug delivery system (DDS).

Applying non-degradable drug carrier materials can give rise to an additional problem of proper elimination of such particles from the vitreous after release of the medication. Chitosan (Cs) is a biocompatible, biodegradable, and non-toxic linear polysaccharide. Since it has free –OH and $–NH_2$ groups in its construction, it is also amenable to chemical modifications for potentiating some of its features for particular purposes[13, 14] Trimethyl chitosan (TMC) is a water-soluble derivative of Cs fabricated by N-methylation of some of Cs's free amine groups using iodomethane.[15, 16] Centered on the immobilization of the thiol group on the TMC backbone, thiolated chitosan (TCs) is synthesized, leading to improved biopolymer mucoadhesive properties.[17] Carboxymethyl dextran (CMD) is a hydrophilic polymer made of many glucose molecules, often consisting of α-1, 6-glycosidic bonds,[18] which is used to enhance the bioavailability of anticancer drugs in malignant tissue. High degrees of methylation (DQ%) in TMC-cysteine conjugates (TCs) used in this study might have led to high rates of O-methylation that resulted in less solubility of TCs-NPs. Therefore, using CMD improves stability and impedes O-methylation. It also contributes to NP's reactivity owing to its carboxyl and hydroxyl groups.[19, 20]

Topotecan hydrochloride (TPH) is approved for the prevention of cervical cancer, breast cancer, and small cell lung cancer.[21–23] Additionally, TPH is also identified as a potent drug against Rb with a safe toxicity profile.[24–27] TPH has been used as a systemic chemotherapy for resistant intraocular Rb.[28] Periocular injection of topotecan has been handled in patients with recurrent tumors and in those who are not inclined to systemic chemotherapy.[29] However, efficiency limitations have shown that TPH's active lactone form is vulnerable to pH-dependent hydrolysis of the biologically inactive carboxylate species under physiological conditions, which presents a barrier to its therapeutic efficacy.[28, 29] By encapsulating topotecan in CMD-TCs-NPs, the stability concern of the topotecan might be solved. In addition, the bioavailability of TPH in malignant tissues may be improved due to CMD-based surface stabilization, which decreases agglomeration after the intravitreal NP injection. In the present analysis, TCs and CMD were used to create an efficient

**Correspondence to:**

Fariba Ghassemi, MD. Translational Ophthalmology Research Center (TORC), Farabi Eye Hospital, Tehran University of Medical Sciences, Qazvin Square, Tehran 13366, Iran.
E-mail: faribaghassemi@yahoo.com

Received: 16-06-2021 Accepted: 05-06-2022

Access this article online

**Website:** https://knepublishing.com/index.php/JOVR

**DOI:** 10.18502/jovr.v18i1.12727

This is an open access article distributed under the Creative Commons Attribution License, which permits unrestricted use, distribution, and reproduction in any medium, provided the original work is properly cited.

**How to cite this article:** Delrish E, Jabbarvand M, Ghassemi F, Amoli FA, Atyabi F, Keshel SH, Lashay A, Tekie FSM, Dinarvand R. The Antitumor Effect of Topotecan Loaded Thiolated Chitosan-Dextran Nanoparticles for Intravitreal Chemotherapy: A Xenograft Retinoblastoma Model . J Ophthalmic Vis Res 2023;18:68–80.

topotecan carrier to increase the bioavailability and avoid the agglomeration of intravitreal TPH-loaded NPs.

## METHODS

Cs medium-molecular-weight Chi with a degree of deacetylation of about 89% was purchased from Primex (Karmoy, Norway). TPH was supplied by Yangzhou Huaxing Chemical Company, China. CMD sodium salt (10–20 KD, 1.1–1.5 mmol carboxyl/g), dialysis tubing (molecular weight cut-off 2 and 12 kDa), N-ethylcarbodiimide hydrochloride (EDC), N-hydroxysuccinimide (NHS), Ellman's reagent, RPMI-1640 tissue culture medium, and fetal bovine serum (FBS) were purchased from Sigma-Aldrich Company (Missouri, USA). N-methyl-2-pyrrolidone (NMP) and hydrochloric acid (HCl), sodium chloride, and sodium hydroxide (NaOH) were purchased from Merck Company (Darmstadt, Germany). The human Rb cell line (Y79) was obtained from Pasteur Institute (Tehran, Iran) and cell-counting solution (Orangu TM) was prepared by Cambridge Bioscience. All chemicals were of analytical grade.

### Synthesis and Characterization of TMC

The synthesized TMC followed the process defined by Sieval et al.[30]A suspension of Cs (2 gr) was prepared in NMP (80 ml) and was immersed for 5 min – a short period of time. Eleven ml of 15% NaOH and 11.5 ml of methyl iodide and 4.8 gr of NaI were applied to this solution, followed by a reflux at 60°C for 2 hr. Then, 2.5 ml of methyl iodide and 0.7 gr pellets of NaOH were added and stirred for 1 hr and precipitated by adding 200 ml of ethanol. The derivative was centrifuged, washed, and dried to obtain trimethyl Cs iodide which was dissolved in 40 ml solution of 10% NaCl to interchange iodide with chloride. Afterward, the solution was precipitated with ethanol again and the mixture was centrifuged, washed, and dried. The degree of quaternization (%DQ) of TMC was calculated using $^1$H NMR spectrum recorded by a 600 MHz spectrometer (Bruker-Biospin, Germany). Data analysis was performed using the Topspin software. The %DQ was calculated by the following formula: DQ = [[(CH3)3 / [H] × 1/9] × 100.

DQ is the degree of quaternization; (CH3)3 is the integral of chemical shift of the hydrogens of trimethyl amino groups at 3.4 ppm; H is the integral of H-1 peaks between 4.7 and 5.7 ppm.[31]

### Synthesis and Characterization of TMC-cysteine Conjugates (TMC-cys)

The method of synthesis was adapted according to Margit et al.[32] In the first step, 200 mgr of prepared TMC was dissolved in 10 ml of distilled water (DI) and then 400 mgr of cysteine was poured and stirred until dissolved. Then, EDC and NHS were added in a final concentration of 200 mM, and the mixture was kept at room temperature and pH was adjusted to 5. Then, the solution was incubated for 3 hr in the dark under constant stirring at room temperature. Afterward, the solution was dialyzed (membrane dialysis MW cut-off = 2 kDa) using 1 mM HCl for three days at 4°C and then dialyzed again for two times utilizing the same medium but containing 1% NaCl. Finally, the mixture was lyophilized and the conjugates kept at 4°C. Determination of free thiol groups immobilized on the polymer backbone was performed via photometry with Ellman's reagent while the quantitative amount of the thiol groups was determined using the thioglycolic acid standards curve.[32, 33] FT-IR spectra of TCs were recorded on a Bruker FTIR spectrophotometer (Vectore 22, Germany).

### Preparation of CMD-TCs Nanoparticles (NPs)

The nanoparticles (NPs) were made by a simple coacervation technique where CMD was used as the cross-linking agent.[34] The NPs were prepared by adding CMD solutions to TCs solutions which contain TPH. Then, an immediate vortex stirring was performed and samples were incubated at room temperature for 2 hr. The formed NPs were then washed by DI through an Amicon® filter with a cut of 30 nm to eliminate untrapped TPH.

### NP Characteristics

The particle size and polydispersity index (PDI) of NPs were determined using dynamic light scattering (DLS) on a Malvern Zetasizer Nano-ZS (Worcestershire, United Kingdom). Surface charges of the NPs were measured by laser Doppler anemometry using a Zetasizer Nano Series (Malvern Instruments). The morphology of NPs was

distinguished by field emission scanning electron microscopy (FESEM; ZEISS, EVo 18). To prepare samples for the FESEM study, 100 µl of the nanoparticle suspension was placed on a glass, dried, and then coated with gold layer for 30 s. NPs were also stained by phosphotungstic acid (2%, w/v) and observed by transmission electron microscopy (TEM, Zeiss, EM 900) to reveal the particle size and morphology. The Fourier-Transformation Infrared (FT-IR) spectroscopy analysis was performed on a Bruker FTIR Fourier transform spectrophotometer (Vectore 22, Germany). The scanning range was from 4000 to 400 $cm^{-1}$. X-ray diffraction analysis was used to distinguish the crystallinity of the pure TPH and TPH in NP-based drug formulations, which was conducted using a StoeStidy-mp x-ray diffractometer (XRD). Differential scanning calorimetry (DSC; DSC823e, Mettler) was utilized to determine the physical state of TPH in NPs. Approximately 5 mg of the sample was measured, placed into an aluminum pan, and analyzed at a scanning temperature of 24–400°C at a heating rate of 10°C/min. The entrapment efficiency (EE) of TPH was determined by a centrifugation method. The drug-loaded NPs were cold centrifuged at 4°C for a period of 30 min at 3000 rpm via Amicon® ultra centrifugal filter (Millipore 30kDa).[35] The supernatant liquid was collected to ascertain the non-bound drug concentration by using ultraviolet-visible spectrophotometry (UV-vis)[36] (Aquarius, CE 7500) at λmax 275 nm. The %EE and drug loading (%DL) were computed using the following formulas:

$$\%\ EE = weight\ of\ drug\ incorporated\ in\ nanoparticles/weight\ of\ drug\ fed\ initially * 100.$$

$$\%\ DL = \frac{weight\ of\ drug\ incorporated\ in\ nanoparticles}{weight\ of\ nanoparticle} * 100.$$

Cumulative release experiments were operated in BSS (balanced salt solution) medium (pH =7.5) to verify the amount of TPH released from CMD-TCs-NPs. NPs were dispersed into 10 ml of BSS, then incubated at 37°C under 150 rpm. At determined time intervals, a 500 µl of the medium was withdrawn, centrifuged at 12000 rpm for 20 min to separate NPs from supernatant, and then replaced with an equal amount of fresh media to maintain sink conditions. The supernatant was used for UV examination at 275 nm (λ max).

## Evaluation of $IC_{50}$

The cancerous Y79 human Rb cells were obtained from the Pasteur Institute and used in this research to elucidate cell viabilities of TPH-loaded CMD-TCs-NPs. Cells were seeded at a concentration of $5\times 10^3$ cells/well on a 96-well plate and maintained at 37°C in a humidified, 5% $CO_2$ atmosphere. After overnight cultivation, cells were treated with TPH-loaded CMD-TCs-NPs, CMD-TCs-NPs, and free TPH with equivalent TPH concentrations of 5, 10, 20, 50, 100, and 200nM, respectively, for 24 hr at 37°C. Cell counting solution (2,3-bis-(2-methoxy- 4-nitro-5-sulfophenyl)-2H-tetrazolium-5-carboxanilide, Orangu™, Bioscience) was used to determine the cell viability per standard protocol suggested by the manufacturer. The cells viability of Y79 cells was defined as:

$$\frac{OD_{NPs\ treated} - OD_{Blank}}{OD_{Control} - OD_{Blank}} \times 100,$$

where, OD NPs treated, OD blank, and OD control represent the optical densities of treated, blank, and control samples, respectively [Table 1].

## Flow Cytometry Measurement

Apoptosis analysis using flow cytometry was used to quantitatively confirm the $IC_{50}$ determined by XTT assay. Y79 cells were seeded at a concentration of $2.5 \times 10^5$ cells/well on a six-well plate and when reaching 70% confluence treated with 50 µM concentration of TPH-CMD-TCs-NPs and TPH for 48 hr. The extent of apoptosis was determined by Annexin-V-FITC staining using Annexin-V-Phosphatidyl serine apoptosis detection kit (IQ Products; Netherlands) as directed by the manufacturer.

## In vitro Cellular Uptake of NPs

Qualitative cellular uptake of TPH-loaded CMD-TCs-NPs was investigated with a confocal laser-scanning microscope (Nikon, Eclipse). For this, the Y79 cells were cultured in a six-well configuration at the density of 2.5 × 105 cells/well. The cells were then incubated for 2 hr with Cyanine-3 (CY3)-labeled TPH-CMD-TCs-NPs suspension medium at concentrations of 200 µg/ml to follow the uptake of them in Y79 cells. Afterward, the cells were fixed with 2% paraformaldehyde and cell nuclei were stained with DAPI (4′,6-diamidino-2-phenylindole) and endosomes/lysosomes were stained with LysoTracker Red, respectively. The fluorescence of the CY3-labeled TPH-CMD-TCs-NPs was monitored applying a confocal microscope (excitation 640.8 nm/emission 662–737 nm).

## Rabbit Xenograft Model of Rb

All animals in this survey were used according to the Association for Research in Vision and Ophthalmology Statement in a protocol approved by Tehran University of Medical Sciences. Fifteen male New Zealand albino rabbits with a mean initial weight around 1 kg purchased from Pasteur Institute of Iran (Karaj, Iran) were used for this study. The rabbits were immunosuppressed with daily intramuscular injections of cyclosporin A (CsA; Sandimmune 50 mg/mL; Novartis Pharmaceuticals, Germany). Animal study groups were conducted with a sample size of $n$ = 5, except for the tumor control group ($n$ = 2). To avoid spontaneous tumor regression, CsA administration had been continued during the 10-week study period. All injections were performed by the same surgeon (FG). The dosage schedule was 15 mg/kg per day for 5 days before cell inoculation and followed by 10 mg/kg per day for the next 10 weeks of the investigation.[37] During the 10-week follow-up, the animals were monitored daily for signs of CsA toxicity (weight loss, gingival hyperplasia, and diarrhea). Fifty µl of sterile PBS (phosphate buffered saline; Gibco, Germany) containing 2.5 × $10^6$ Y79 cancerous human Rb cells was injected intravitreally using a 30-gauge needle. At week eight, after intraocular tumor inoculation, the rabbits were anesthetized, examined, and ultrasound examinations were performed on the eyes using 10-MHz B-scan (Ultrasonix Medical; TOUCH ultrasound system, Canada, Richmond). Then, TPH-CMD-TCs-NPs (100 µg/ml) were injected intravitreally to Rb eyes (100 µL). Control eyes received intravitreal topotecan at the same concentration (10 µg) (positive control) and the tumor group (negative control) received 100 µL of saline solution. The tumor size was estimated with indirect ophthalmoscopy. The length, width, and height of the mass were all measured both clinically using a lens magnifier and ultrasonically. The results obtained from both methods were in good agreement in determining the length, width, and height. The results reported in Table 2 are related to the results of measuring the dimensions by an ultrasonic system. To estimate the mass volume, we used the approximate formula of tumor length * tumor width * tumor height. Dark-adapted bright flash ERG was done on all rabbits before the intravitreal injection at baseline and then seven days after the intravitreal injection of TPH or TPH-CMD-TCs-NPs prior to sacrificing the rabbits. All surviving animals were euthanized seven days after treatments. Enucleation was performed and paraffin-embedded tissue was cut, stained with hematoxylin and eosin (H&E), and immunostained with Bcl-2 antibody. Vitreous seeds cytologic analysis by H&E staining was also performed. Slides were quantified by an experienced pathologist (FAA) to assess the percentage of tumor necrosis and immunohistochemistry.

## Statistical Analyses

To describe the data, we used mean and standard deviation. In order to evaluate the changes within groups, we used Wilcoxon signed-rank test. Comparison between groups was performed using the Kruskall–Wallis test. In addition, multiple comparisons were performed using the Bonferroni method. We used the Kruskal–Wallis test to compare the groups within different treatment groups. In addition, any statistically significant test was followed by the Bonferroni post hoc test. In order to estimate IC50, we used linear regression analysis within each treatment group. All statistical analyses were performed by SPSS software (IBM Corp. Version 25.0. Armonk, NY: IBM Corp.). $P$-value < 0.05 was considered statistically significant. All other experiments were done in triplicate.

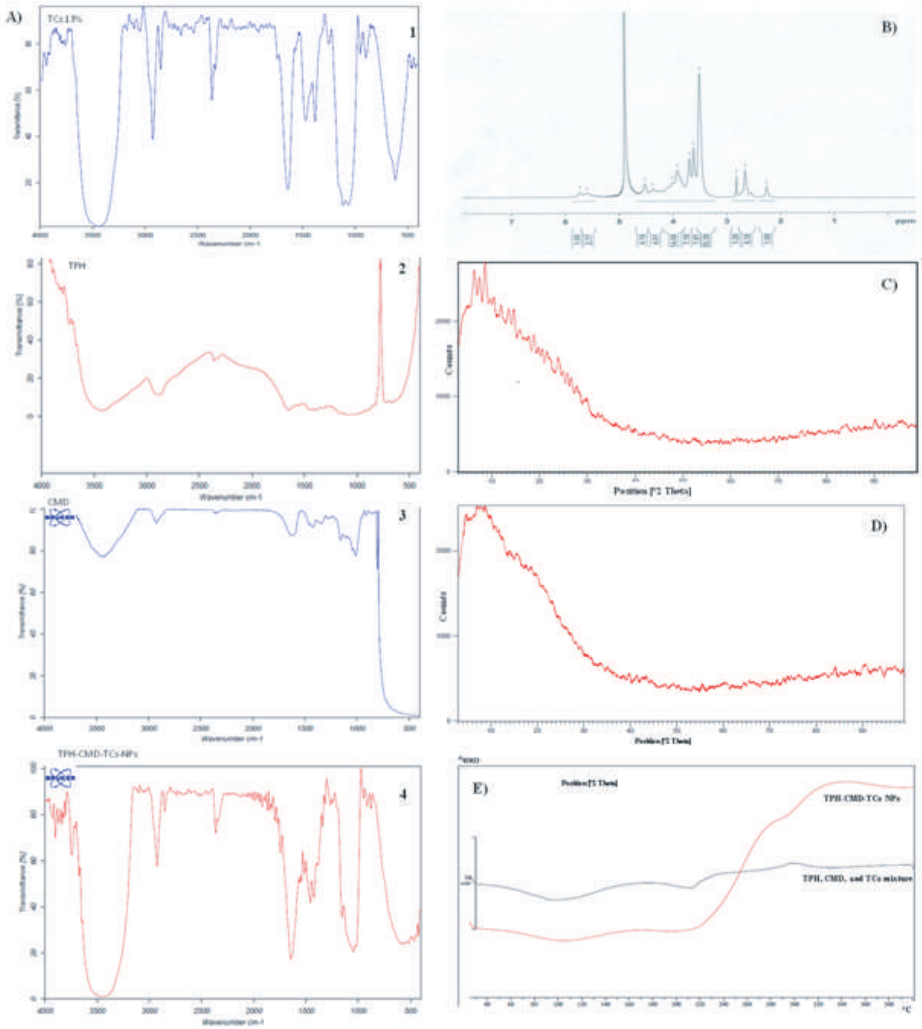


**Figure 1.** Characteristics of TPH-CMD-TCs-NPs. (A) FT-IR spectra of TCs 10% (1), TPH (2), CMD(3), and TPH-CMD-TCS-NPs (4). (B) $^{1}$H-NMR spectrum of TMC-cysteine conjugates in D2O. (C) X-ray diffraction pattern of TPH. (D) X-ray diffraction pattern of TPH-CMD-TCs-NPs. (E) Differential scanning calorimetric of physical mixture of TPH, CMD, and TCs, and TPH-CMD-TCs-NPs.

## RESULTS

### Characterization of TPH-CMD-TCs NPs

The proton nuclear magnetic resonance ($^{1}$H NMR) spectrum of TMC-cysteine conjugates (TCs) is displayed in Figure 1B. In the TMC $^{1}$H NMR spectrum [Figure S1], the signal at 3.4–3.6 ppm corresponds to the methyl group at the N,N,N-trimethylated site.[38]The TMC-cys conjugate was synthesized based on the amide bond formation between the amino group of Cs and the carboxylic of cysteine. Comparative FT-IR spectra of native Cs and TCs are shown in Figure S2. TCs shows the three characteristic peaks at 1250, 1640, and 2500 $cm^{-1}$ which correspond to C–SH stretching, C = O double bonds of the amido bond, and –SH stretching, respectively [Figure 1A-1 and Figure S2].[39] In addition, the degree of thiol substitution was determined at 11% using Ellman's protocol. The coacervation technique was used to obtain the NPs' suspensions. The EE and drug loading of NPs were found to be 62.41 ± 3 and 10.23 ± 0.03 %, respectively. Additionally, TPH-loaded CMD-TCs-NPs exhibited diameters of 30 ± 4 (PDI: 0.24 ± 0.03) and zeta potentials of 10 ± 3 (mV) while using DLS. As revealed by the SEM images [Figures 2A & 2B] and TEM image [Figures 2C], TPH-CMD-TCs-NPs were spherical with a compact structure. IR spectrum of TCs, TPH, CMD, and TPH-CMD-TCs-NPs exhibits their functional groups as shown in Figure 1A-1–4. The obtained peaks

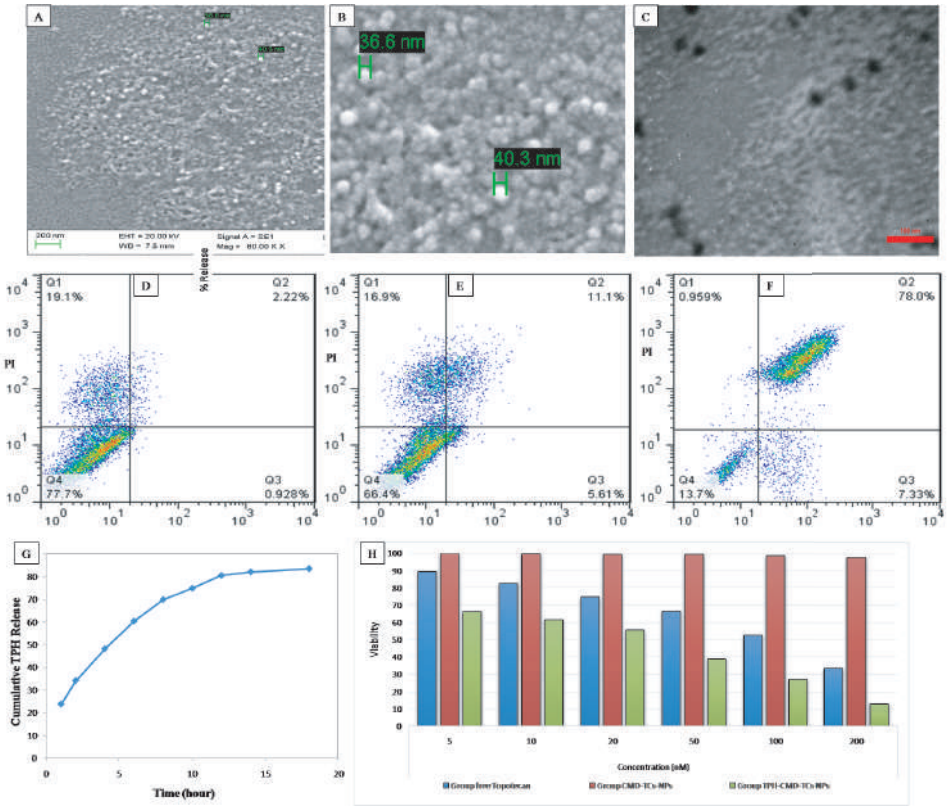


**Figure 2.** SEM images of TPH-CMD-TMC-Nps (A & B); TEM images of TPH-CMD-TMC-Nps (C); analysis of apoptosis by flow cytometry in Y79 cells (D–F). Cells were treated with 50 µM of TPH (E) and TPH-CMD-TMC-Nps (F) for 48 hr. Cumulative TPH-CMD-TCs-NPs release behaviors in BSS medium at 37°C (G). Determination of the IC50 value of the TPH, CMD-TCs-NPs, and TPH-CMD-TCs-NPs in retinoblastoma cell line (Y79) by XTT Cell Viability Assay (H).

disclosed that there was no remarkable conversion in the polymers and drug structure in NPs and their structural integrity was maintained [Figure 1A-4]. XRD pattern of the TPH and TPH-CMD-TCs-NPs are exhibited in Figures 1C and 1D, respectively. The presence of partly sharp peaks in the diffractogram of pure TPH suggested its crystalline nature being shown, while in the case of TPH-loaded NPs there were no sharp peaks, suggesting its amorphous nature. It was clear that a broad peak was presented in the TPH-loaded CMD-TCs-NPs, indicating that NPs were amorphous and lacked crystalline peaks. Compared to the pure TPH that was represented by broad peaks, a reduction in the peak intensity could be explained by a lower loading.

Figure 1E shows DSC thermo grams of a physical mixture of TPH, TCs, and CMD, and TPH-CMD-TCS NPs, respectively. As shown in Figure 1E, topotecan in the physical mixture has a melting point of 210.66°C, and after its encapsulation into the biopolymeric NPs, this peak has disappeared, showing that TPH is in a totally amorphous form. Results of DSC and XRD indicated that in the prepared NPs, the drug was present in the amorphous phase and might have been homogeneously dispersed in the biopolymeric matrix. As shown in Figure 2G, TPH could be approximately 70% released from the TPH-CMD-TCs-NPs in the initial 8 hr.

## Assessment of Modified NP Cytotoxicity

After TPH encapsulation into the TPH-CMD-TCs NPs, the cytotoxicity of TPH increased remarkably. As a function of the dosage, TPH-CMD-TCs-NPs were more efficacious than free TPH, following 24 hr of treatment as determined by XTT assay (IC50s 40.40, relative to 126.28 nM, $P = 0.022$) [Table 1; Figure 1H].

## Flowcytometric Analysis

XTT viability assay outcomes were further validated by quantitative detection with flow

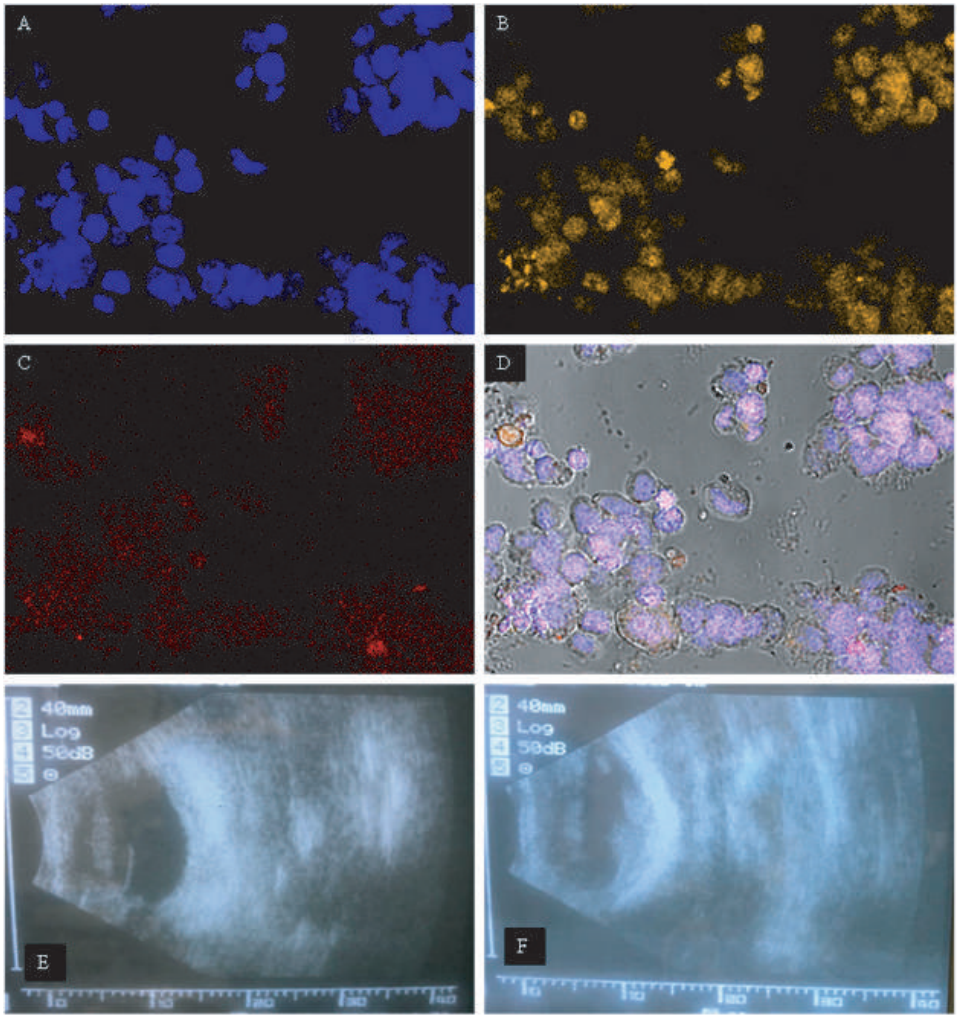


**Figure 3.** Intracellular localization of TPH-CMD-TCs-NPs in Y79 cells using CY3-labeled NPs (B) and lysosomes labeled with LysoTracker Red dye (C) observed by confocal laser scanning microscopy (A–D). Lysosomes and CY3-labeled NPs appear in red and yellow in the confocal microscopy fluorescence images, respectively. Normal Y79 cells used as control (untreated Y79 cells) (A) and nuclei stained by DAPI. Colocalization of TPH-CMD-TCs-NPs and Lysosomes in Y79 cells (D). Ultrasound image at post-injection eight weeks. The B-scan image shows an intraocular tumor in a rabbit eye (E, F).

**Table 1.** The cytotoxicity test was conducted on the Y79 cells exposed to TPH (1), CMD-TCs-NPs (2), and TPH-CMD-TCs-NPs (3) ($n$ = 3, mean ± standard error of the mean). The statistical analysis was conducted using Kruskal–Wallis and Bonferroni post hoc test.

| Concentration (nM) | Viability of treatment groups (Mean ± Standard Deviation) | | | P-value | Multiple comparison | | |
|---|---|---|---|---|---|---|---|
| | Free TPH (1) | CMD-TCs-NPs (2) | TPH-CMD-TCs-NPs (3) | | 1 vs 2 | 1 vs 3 | 2 vs 3 |
| 5 | 89.43 ± 0.94 | 99.93 ± 0.13 | 66.19 ± 0.9 | 0.027 | 0.534 | 0.021 | 0.534 |
| 10 | 82.41 ± 0.88 | 99.72 ± 0.24 | 61.51 ± 1.23 | 0.027 | 0.539 | 0.022 | 0.539 |
| 20 | 74.83 ± 1.45 | 99.3 ± 0.14 | 55.56 ± 0.99 | 0.027 | 0.539 | 0.022 | 0.539 |
| 50 | 66.59 ± 1.57 | 99.35 ± 0.08 | 38.88 ± 1.85 | 0.027 | 0.539 | 0.022 | 0.539 |
| 100 | 52.72 ± 1.45 | 98.53 ± 0.53 | 27.08 ± 1.56 | 0.027 | 0.539 | 0.022 | 0.539 |
| 200 | 33.53 ± 1.88 | 97.72 ± 0.43 | 12.86 ± 1.61 | 0.027 | 0.539 | 0.022 | 0.539 |

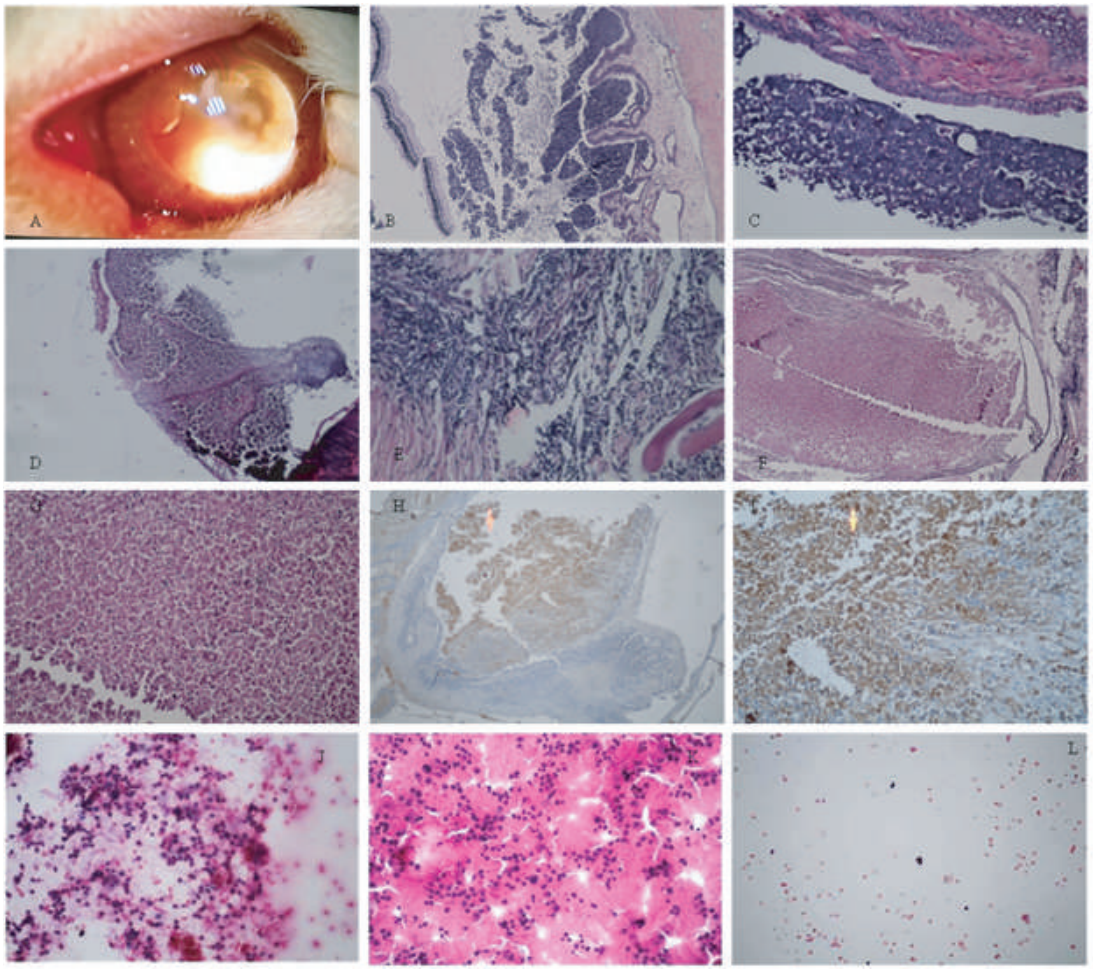

**Figure 4.** Macroscopic view of a retinoblastoma-induced eye where the tumors are seen (A). Histological findings at post-injection 10 weeks (hematoxylin-eosin) (B–F). Section from tumor control (untreated) (B & C). Section from TPH-treated tumor (D, E). Section from TPH-CMD-TCs-NPs-treated tumor (G, F). Representative light micrographs of IHC staining for BCL2 sections from TPH-CMD-TCs-NPs-treated tumor (H, I). Pathological results after the treatment of RB-induced eye with intravitreal injection of saline ( J), TPH (K), and TPH-CMD-TCs-NPs (L). The ICC results showed that there was a highly significant difference in the percentage of necrosis in vitreous seeds between the NPs-treated group (89 ± 9%) and the control group (10%) ($P$ = 0.046).

cytometry. To that end, cell apoptosis was evaluated to compare the cytotoxicity induced by TPH-CMD-TCs-Nps and the TPH [Figures 2D & 2F].

## Uptake of Topotecan-loaded TCs NPs By Y79 Cells

The cellular uptake of Cy3-labeled NPs by Y79 cells was visualized using confocal microscope after a 2-hr exposure (3 A-D). For observation of the internalized TPH-CMD-TCs-NPs location, the nucleus was stained using DAPI (blue fluorescence), while the lysosomes were stained with LysoTracker red.

## In vivo Tumor Inhibition Study in the Rabbit Xenograft Model of Rb

Animals developed an Rb eight weeks post-injection [Figure 3E, 3F, & 4A]. The histological analysis of Rb necrosis after applying different treatments by H&E staining is shown in Figures 4B–4G. For immunohistochemistry, sections were obtained from paraffin-embedded tissue blocks and then applied for BCL2 immunostaining [Figures 4H & 4I].Vitreous seeds cytologic analysis by H&E staining detected remarkable reduction of tumor cells in seeds treated by TPH-CMD-TCs-NPs as compared with other groups [Figures 4J–4L]. In addition, Bonferroni post hoc test showed that there was a statistically significant

difference in the percentages of necrotic cells in the control and NPs-treated groups *in vivo* ($P$ = 0.046). Furthermore, as a function of the tumor necrosis percentage, TPH-CMD-TCs-NPs (91 ± 2%) were more efficacious than TPH (23 ± 15%). Based on Kruskall–Wallis test, there was a statistically significant difference among groups regarding the tumor necrosis value ($P$ = 0.044). Wilcoxon signed-rank test revealed that the difference in tumor volume was significant in comparison with the TPH-CMD-TCs-NPs treated with tumor control group ($P$ = 0.039). Safety studies were performed in rabbits to assess the potential ocular toxicity after intravitreal injections of either TPH or TPH-CMD-TCs-NPs. No significant changes were found in the ERG parameters between the non-treated (tumor control) eyes and the eyes to which either TPH-CMD-TCs-NPs or TPH was injected ($P$ > 0.05) [Table 2]. In addition, as shown in Table 2, eyes showed little or no change in a- and b-waves of amplitude and implicit times values among all groups with no statistically significant difference among groups before any injection and after intravitreal TPH and TPH-CMD-TCs-NPs injections ($P$ > 0.05) [Table 2].

## DISCUSSIONS

Nanotechnology-mediated chemotherapy has been an important development in clinical research that can enhance bioavailability and therapeutic effectiveness with negligible side effects on normal tissues. The key feature of nano-carrier innovation in this research was the development of a successful anti-cancer DDS based on biopolymers, thanks to the desirable characteristics of these nano-carriers. Chemical characteristics of Cs were employed to synthesize a water-soluble derivative that is dissolved in neutral pH. The NPs were fabricated by two hydrophilic polymers – TMC-cys (TCs) and CMD – to optimize the delivery system of topotecan for intravitreal chemotherapy. Similar to Cs, TMC also possesses muco-adhesion potential.[40] It has been proven that DQ has a significant effect on the muco-adhesive properties of TMC. Snyman et al observed that the muco-adhesiveness of TMC decreased with an improvement of DQ between 22.1 and 48.8%.[41] Therefore, the TMC-cys conjugate was fabricated to solve the problem and increase the muco-adhesion properties of fabricated NPs. Additionally, the solubility of TCs-NPs may decrease as a result of high rates of O-methylation in TMC-cys conjugates. Therefore, a new strategy of combinations of CMD and TMC-cys conjugates as polymeric matrices in NPs fabrication was used in this study to increase the solubility and prevent agglomeration of NPs [Figures 2C & 2G).[19, 42, 43]Accordingly, in the present study, we prepared TPH-CMD-TCs NPs by electrostatic interaction between positively charged amine groups of TCs and negatively charged CMD. The results of FTIR spectroscopy confirmed the TPH-CMD–TCs NPs formation [Figure 1A].

The optimal formulation of CY3-labeled TPH-CMD–TCs NPs showed effective cellular uptake in the Y79 cell line [Figures 3A–3D]. Therefore, by the addition of CMD to TCs, NPs with proper particle size, zeta potential, and high cellular uptake were created. Herein, we explored the possible utility of TPH-CMD-TCs to induce apoptosis in Y79 cells in order to improve the effectiveness of Rb therapy. As shown in Figure 2H, provided that apoptosis induced in Y79 cells increased significantly in the presence of TPH-CMD–TC NPs as compared to TPH, the administration of these NPs has been shown to be more efficient in the management of Rb.

We then assessed the treatment efficacy of TPH-CMD-TCs-NPs following intravitreal administration in the xenograft Rb model in rabbits. The tumor size was measured just before the intravitreal injection and seven days after the intravitreal injection of NPs. As shown in Table 2, increased and decreased tumor size over time in animals was observed in the control tumor and TPH-CMD-TCs-NPs-treated groups, respectively. As a result, apparent suppression of Rb tumor growth in NPs-treated rabbits was observed. The H&E staining findings [Figures 4B–4G] revealed that the sections of the tumor of saline-treated rabbits were densely cellular, while those of the TPH-CMD-TCs-NPs-treated population were less cellular. Light microscopic assessments revealed no histologic evidence of retinal damage induced by intravitreal administration of NPs. Also, no significant differences were found in the ERG parameters between the tumor control eyes and the eyes that received intravitreal injections of NPs ($P$ > 0.05). Therefore, TPH-CMD-TCs-NPs could be considered safe for the retina.

**Table 2.** Clinical examinations and electroretinogram (ERG) before and after intravitreal injection of TPH or TPH-loaded NPs. Data are presented as Mean ± Standard Deviation (SD). Time 0 and 7 correspond to animal response before and seven days after the intravitreal injection of TPH or TPH-NPs, respectively.

| Parameter | Time (day) | Treatment groups | | | P-value† | Multiple comparison | | |
|---|---|---|---|---|---|---|---|---|
| | | TPH | TPH-CMD-TCs-NPs | Tumor Control | | P1 | P2 | P3 |
| Tumor Necrosis % | 7 | 23 ± 15 | 91 ± 2 | 15 ± 7 | **0.018** | **0.044** | 1 | 0.076 |
| Cytologic Necrosis % | 7 | 15 ± 6 | 89 ± 9 | 10 ± 0 | **0.015** | 0.06 | 1 | **0.046** |
| Tumor Length (mm) | 0 | 3.5 ± 1.3 | 5.8 ± 1.6 | 3.3 ± 3.9 | 0.271 | – | – | – |
| Tumor Length (mm) | 7 | 3.2 ± 1.2 | 3.2 ± 3 | 5 ± 4.2 | 0.636 | – | – | – |
| Tumor Length (mm) | Change | 0.33 ± 0.29 | 2.2 ± 1.3 | –1.75 ± 0.35 | **0.049** | 0.658 | 0.658 | **0.047** |
| | P‡ | 0.157 | 0.063 | 0.18 | | | | |
| Tumor Width (mm) | 0 | 2.8 ± 0.3 | 4.8 ± 1.3 | 2.3 ± 2.5 | 0.103 | – | – | – |
| Tumor Width (mm) | 7 | 2.3 ± 0.3 | 2.7 ± 2.6 | 4 ± 4.2 | 0.911 | – | – | – |
| Tumor Width (mm) | Change | 0.5 ± 0 | 2.1 ± 1.78 | –1.75 ± 1.77 | 0.107 | – | – | – |
| | P‡ | 0.083 | 0.078 | 0.18 | | | | |
| Tumor Height (mm) | 0 | 4.2 ± 2.5 | 4.8 ± 1.5 | 1.8 ± 1.8 | 0.203 | – | – | – |
| Tumor Height (mm) | 7 | 3.3 ± 1.9 | 2.3 ± 1.6 | 2.5 ± 2.1 | 0.579 | – | – | – |
| Tumor Height (mm) | Change | 0.83 ± 0.58 | 2.5 ± 1.17 | –0.75 ± 0.35 | **0.037** | 0.432 | 0.82 | **0.041** |
| | P‡ | 0.102 | **0.042** | 0.18 | | | | |
| Tumor estimated Volume (mm) | 0 | 49.208 ± 48.651 | 153.4 ± 109.439 | 36.063 ± 50.823 | 0.203 | – | – | – |
| Tumor estimated Volume (mm) | 7 | 29.167 ± 28.466 | 56.7 ± 95.487 | 113 ± 156.978 | 0.803 | – | – | – |
| Tumor estimated Volume (mm) | Change | 20.04 ± 20.2 | 96.7 ± 91.72 | –76.94 ± 106.15 | **0.033** | 0.351 | 0.916 | **0.039** |
| | P‡ | 0.109 | **0.043** | 0.18 | | | | |
| a-wave | | | | | | | | |
| Implicit time (ms) | 0 | 15.5 ± 0.57 | 16.6 ± 1.13 | 16.07 ± 0.19 | 0.243 | – | – | – |
| Implicit time (ms) | 7 | 15.23 ± 0.18 | 16.25 ± 2.06 | 16.07 ± 0.23 | 0.243 | – | – | – |
| Implicit time (ms) | Change | 0.27 ± 0.38 | 0.35 ± 1.29 | 0 ± 0.42 | 0.92 | – | – | – |
| | P‡ | 0.317 | 0.715 | 1 | | | | |
| b-wave | | | | | | | | |
| Implicit time (ms) | 0 | 33.6 ± 0 | 35.4 ± 1.1 | 35.3 ± 1.1 | 0.119 | – | – | – |
| Implicit time (ms) | 7 | 34.95 ± 0.64 | 36.83 ± 3.05 | 34.23 ± 0.89 | 0.472 | – | – | – |
| Implicit time (ms) | Change | –1.35 ± 0.64 | –1.43 ± 2.92 | 1.07 ± 2.02 | 0.223 | – | – | – |
| | P‡ | 0.18 | 0.465 | 0.655 | | | | |
| a-wave | | | | | | | | |
| Amplitude (mv) | 0 | 51.83 ± 7.35 | 66.1 ± 7.06 | 66.72 ± 2.85 | 0.135 | – | – | – |
| Amplitude (mv) | 7 | 57.65 ± 5.3 | 63.63 ± 15.18 | 66.99 ± 6.2 | 0.57 | – | – | – |
| Amplitude (mv) | Change | –5.82 ± 2.05 | 2.47 ± 8.2 | –0.27 ± 9.05 | 0.21 | – | – | – |
| | P‡ | 0.18 | 0.465 | 0.655 | | – | – | – |
| b-wave | | | | | | | | |
| Amplitude (mv) | 0 | 83.98 ± 8.09 | 73.43 ± 12.1 | 71.3 ± 1.13 | 0.400 | – | – | – |
| Amplitude (mv) | 7 | 92.9 ± 15.7 | 83.67 ± 18.48 | 72.96 ± 7.71 | 0.274 | – | – | – |
| Amplitude (mv) | Change | –8.92 ± 7.61 | –10.24 ± 23.24 | –1.66 ± 8.85 | 0.779 | – | – | – |
| | P‡ | 0.18 | 0.465 | 0.655 | | | | |

‡Based on Wilcoxon-singed rank test; †Based on Kruskall–Wallis test; ¥Multiple comparison based on Bonferroni method. P1, comparison of TPH and TPH-CMD-TCs-NPs groups; P2, comparison of TPH and tumor control groups; P3, comparison of TPH-CMD-TCs-NPs and tumor control groups

Cs-based NPs are particularly valuable due to their low toxicity and biocompatibility. These nano-carriers demonstrate high efficacy and safety for cancer therapy both *in vitro* and *in vivo*.[44] In this study, NPs with proper particle size and zeta potential for intravitreal chemotherapy, low toxicity and high cell uptake were manufactured by adding CMD to TCs.[42, 44]Further research is required to ensure the effectiveness and safety of TPH-CMD-TCs-NPs *in vivo*.

In conclusion, the TMC-cys conjugate was fabricated through covalent attachment of TMC with cysteine in the present study. Fabricated via self-assembly, the TCs-dextran NPs containing topotecan (TPH-CMD-TCs-NPs) had uniform particle size, spherical morphology, appropriate positive zeta potentials, and adequate topotecan EEs. The obtained results showed that NPs could efficiently deliver TPH into Y79 cells. Through thiolation of TMC, the advantages of TMC and thiomers for ocular delivery of drugs were combined, including permeation enhancing effects and muco-adhesion. The data obtained suggests a great potential for these self-assembled NPs as a promising medium for intravitreal drug delivery that offers an efficient technique for topotecan-assisted Rb chemotherapy.

## Acknowledgment

The authors wish to thank the staff of the Department of Pharmaceutics of Tehran University of Medical Sciences and the Stem Cell Preparation Unit at Farabi Eye Hospital of Tehran University of Medical Sciences.

## Financial Support and Sponsorship

This study was funded by the research deputy of Tehran University of Medical Sciences (TUMS).

## Conflicts of Interest

The authors report no conflicts of interest in this work.

## *REFERENCES*

1. Friedman DL, Himelstein B, Shields CL, Shields JA, Needle M, Miller D, et al. Chemoreduction and local ophthalmic therapy for intraocular retinoblastoma. *J Clin Oncol* 2000;18:12–17.
2. Antoneli CB, Ribeiro KC, Steinhorst F, R S Novaes PE, Chojniak MM, Malogolowkin M. Treatment of retinoblastoma patients with chemoreduction plus local therapy: Experience of the AC Camargo Hospital, Brazil. *J Pediatr Hematol Oncol* 2006;28:342–345.
3. Shields CL, Kaliki S, Al-Dahmash S, Rojanaporn D, Leahey A, Griffin G, et al. Management of advanced retinoblastoma with intravenous chemotherapy then intra-arterial chemotherapy as alternative to enucleation. *Retina* 2013;33:2103–2109.
4. Munier FL, Gaillard MC, Balmer A, Soliman S, Podilsky G, Moulin AP, et al. Intravitreal chemotherapy for vitreous disease in retinoblastoma revisited: From prohibition to conditional indications. *Br J Ophthalmol* 2012;96:1078–1083.
5. Shields CL, Fulco EM, Arias JD, Alarcon C, Pellegrini M, Rishi P, et al. Retinoblastoma frontiers with intravenous, intraarterial, periocular, and intravitreal chemotherapy. *Eye* 2013;27:253–264.
6. Shields CL, Manjandavida FP, Lally SE, Pieretti G, Arepalli SA, Caywood EH, et al. Intra-arterial chemotherapy for retinoblastoma in 70 eyes: Outcomes based on the international classification of retinoblastoma. *Ophthalmology* 2014;121:1453–1460.
7. Gobin YP, Dunkel IJ, Marr BP, Brodie SE, Abramson DH. Intra-arterial chemotherapy for the management of retinoblastoma: Four-year experience. *Arch Ophthalmol* 2011;129:732–737.
8. Shields CL, Honavar SG, Meadows AT, Shields JA, Demirci H, Singh A, et al. Chemoreduction plus focal therapy for retinoblastoma: Factors predictive of need for treatment with external beam radiotherapy or enucleation. *Am J Ophthalmol* 2002;133:657–664.
9. Abramson DH, Fabius AW, Francis JH, Marr BP, Dunkel IJ, Brodie SE, et al. Ophthalmic artery chemosurgery for eyes with advanced retinoblastoma. *Ophthalmic Genet* 2017;38:16–21.
10. Francis JH, Marr BP, Brodie SE, Gobin YP, Abramson DH. Tethered vitreous seeds following intravitreal melphalan for retinoblastoma. *JAMA Ophthalmol* 2014;132:1024–1025.
11. Francis JH, Brodie SE, Marr B, Zabor EC, Mondesire-Crump I, Abramson DH. Efficacy and toxicity of intravitreous chemotherapy for retinoblastoma: Four-year experience. *Ophthalmology* 2017;124:488–495.
12. Ghassemi F, Shields CL. Intravitreal melphalan for refractory or recurrent vitreous seeding from retinoblastoma. *Arch Ophthalmol* 2012;130:1268–1271.
13. Rinaudo M. Chitin and chitosan: Properties and applications. *Prog Polym Sci* 2006;31:603–632.
14. Azuma K, Izumi R, Osaki T, Ifuku S, Morimoto M, Saimoto H, et al. Chitin, chitosan, and its derivatives for wound healing: Old and new materials. *J Funct Biomater* 2015;6:104–142.
15. Zhang C, Ding Y, Yu LL, Ping Q. Polymeric micelle systems of hydroxycamptothecin based onamphiphilic N-alkyl-N-trimethyl chitosan derivatives. *Colloids Surf B Biointerfaces* 2007;55:192–199.
16. Bei YY, Yuan Z-Q, Zhang L, Zhou X-F, Chen W-L, Xia P, et al. Novel self-assembled micelles based on palmitoyl-trimethyl-chitosan for efficient delivery of harmine toliver cancer. *Expert Opin Drug Deliv* 2014;11:843–854.

17. Bernkop-Schnurch A. Thiomers: A new generation of mucoadhesive polymers. *Adv Drug Deliv Rev* 2005;57:1569–1582.
18. Nácher-Vázquez M, Ballesteros N, Canales A, Saint-Jean SR, ]Pérez-Prieto SI, Prieto A, et al. Dextrans produced by lactic acid bacteria exhibit antiviral and immunomodulatory activity against salmonid viruses. *Carbohydr Polym* 2015;124:292–301.
19. Shin JM, Song SH, Vijayakameswara Rao N, Lee ES, Ko H, Park JH. A carboxymethyl dextran-based polymeric conjugate as the antigen carrier for cancer immunotherapy. *Biomater Res* 2018;22:21.
20. Vasić K, Knez Ž, Konstantinova EA, Kokorin AI, Gyergyek S, Leitgeb M. Structural and magnetic characteristics of carboxymethyl dextran coated magnetic nanoparticles: From characterization to immobilization application. *React Funct Polym* 2020;104481.
21. Brave M, Dagher R, Farrell A, Abraham S, Ramchandani R, Gobburu J, et al. Topotecan in combination with cisplatin for the treatment of stage IVB, recurrent, or persistent cervical cancer. *Oncology* 2006;20:1401–1404.
22. Nicum SJ, O'Brien ME, Topotecan for the treatment of small-cell lung cancer. *Expert Rev Anticancer Ther* 2007;7:795–801.
23. Wethington SL, Wright JD, Herzog TJ. Key role of topoisomerase I inhibitors in the treatment of recurrent and refractory epithelial ovarian carcinoma. *Expert Rev Anticancer Ther* 2008;8:819–831.
24. Laurie NA, Gray JK, Zhang J, Leggas M, Relling M, Egorin M, et al. Topotecan combination chemotherapy in two new rodent models of retinoblastoma. *Clin Cancer Res* 2005;11:7569–7578.
25. Chantada GL, Fandiño AC, Casak SJ, Mato G, Manzitti J, Schvartzman E. Activity of topotecan in retinoblastoma. *Ophthalmic Genet* 2004;25:37–43.
26. Mallipatna AC, Dimaras H, Chan HS, Héon E, Gallie BL. Periocular topotecan for intraocular retinoblastoma. *Arch Ophthalmol* 2011;129:738–745.
27. Ghassemi F, Shields CL, Ghadimi H, Khodabandeh A, Roohipoor R. Combined intravitreal melphalan and topotecan for refractory or recurrent vitreous seeding from retinoblastoma. *JAMA Ophthalmol* 2014;132:936–941.
28. Padhi S, Mirza MA, Verma D, Khuroo T, Panda AK, Talegaonkar S, et al. Revisiting the nanoformulation design approach for effective delivery of topotecan in its stable form: An appraisal of its in vitro behavior and tumor amelioration potential. *Drug Deliv* 2015;23:1–11.
29. Zhang L, Hu Y, Jiang X, Yang C, Lu W, Yang YH. Camptothecinderivativeloaded poly(caprolactone-co- lactide)-b-PEG-b-poly(caprolactone-co-lactide) nanoparticles and their biodistribution in mice. *J Control Release* 2004;96:135–148.
30. Sieval AB, Thanou M, Kotze AF, Verhoef JC, Brussee J, Junginger HE. NMR preparation characterization of highly substituted N-trimethyl chitosan chloride. *Carbohydr Polym* 1998;36:157–165.
31. Snyman D, Hamman JH, Kotze JS, Rollings JE. The relationship between the absolute molecular weight and the degree of quaternization of N-trimethyl chitosan chloride. *Carbohydr Polym* 2002;50:145–150.
32. Margit DH, Constantia EK, Bernkop-Schnürch A. In vitro evaluation of the viscoelastic properties of chitosan–thioglycolic acid conjugates. *Eur J Pharm Biopharm* 2003;55:185–190.
33. Roldo M, Hornof M, Caliceti P, Bernkop-Schnürch A. Mucoadhesive thiolated chitosans as platforms for oral controlled drug delivery: synthesis an in vitro evaluation. *Eur J Pharm Biopharm* 2004;57:115–121.
34. Tekie FSM, Kiani M, Zakerian A, Pilevarian F, Assali A, Soleimani M, et al. Nano polyelectrolytecomplexes of carboxymethyl dextran and chitosan to improve chitosan-mediated delivery of miR-145. *Carbohydr Polym* 2017;159:66–75.
35. Nagarajana E , Shanmugasundarama P, Ravichandirana V, Vijayalakshmi A, Senthilnathan B, Masilamani K. Development and evaluation of chitosan based polymeric nanoparticles of an antiulcer drug lansoprazole. *J Appl Pharm Sci* 2015;5:020–025.
36. Liu Y, Chen X, Ding J, Yu L, Ma D, Ding J. Improved solubility and bioactivity of camptothecin family antitumor drugs with supramolecular encapsulation by water soluble pillar[6]arene. *ACS Omega* 2017;2:5283–5288.
37. Kang SJ, Grossniklaus HE. Rabbit model of retinoblastoma. *J Biomed Biotechnol* 2011;394730:1–6.
38. De Britto D, Celi Goy R, CampanaFilho SP, Assis OBG. Quaternary salts of chitosan: History, antimicrobial features, and prospects. *Int J Carbohydr Chem* 2011;312539:12.
39. Zhu X, Su M, Tang S, Wang L, Liang X, Meng F, et al. Synthesis of thiolated chitosan and preparation nanoparticles with sodium alginate for ocular drug delivery. *Mol Vis* 2012;18:1973–1982.
40. Mourya VK, Inamdar NN. Chitosan-modifications and applications: Opportunities galore. *React Funct Polym* 2008;68:1013–1051.
41. Snyman D, Hamman JH, Kotze AF. Evaluation of the mucoadhesive properties of N-trimethyl chitosan chloride. *Drug Dev Ind Pharm* 2003;29:61–69.
42. Kamalzare S, Noormohammadi Z, Rahimi P, Atyabi F, Irani S, Tekie FSM, et al. Carboxymethyl dextran-trimethyl chitosan coated superparamagnetic iron oxide nanoparticles: An effective siRNA delivery system for HIV-1 Nef. *J Cell Physiol* 2019;1–12.
43. Vasić K, Knez Ž, Konstantinova EA, Kokorin AI, Gyergyek S, Leitgeb M. Structural and magnetic characteristics of carboxymethyl dextran coated magnetic nanoparticles: From characterization to immobilization application. *React Funct Polym* 2020:104481.
44. Jadidi-Niaragh F, Atyabi F, Rastegari A, Kheshtchin N, Arab S, Hassannia H, et al. CD73 specific siRNA loaded chitosan lactate nanoparticles potentiate the antitumor effect of a dendritic cell vaccine in 4T1 breast cancer bearing mice. *J Control Release* 2017;246:46–59.

Original Article

# Incidence and Risk Factors for Retinopathy of Prematurity at a Rural Tertiary Hospital in Thailand

**Mantapond Ittarat[1], MD; Supakorn Chansaengpetch[2], MD; Sunee Chansangpetch[3], MD**

[1]*Surin Hospital and School of Ophthalmology, Suranaree University of Technology, Surin, Thailand*
[2]*Queen Savang Vadhana Memorial Hospital, Chonburi, Thailand*
[3]*Center of Excellence in Glaucoma, Faculty of Medicine, Chulalongkorn University and King Chulalongkorn Memorial Hospital, Thai Red Cross Society, Bangkok, Thailand*

**ORCID:**
*Mantapond Ittarat: https://orcid.org/0000-0001-8177-1234*
*Sunee Chansangpetch: https://orcid.org/0000-0002-8996-2868*

## Abstract

**Purpose**: To estimate the incidence and identify the factors affecting retinopathy of prematurity (ROP) in a rural tertiary hospital in Thailand.
**Methods**: This retrospective chart review included all infants screened for ROP. The study included all infants with gestational age (GA) ≤ 30 weeks or birth weight (BW) ≤ 1,500 gr or selected larger infants with an unstable clinical course. Retinal findings were classified according to the revised International Classification of ROP. Data were analyzed using univariate and multivariable logistic regression analyses.
**Results**: Of the 113 screened infants, the incidences of any ROP and ROP requiring intervention were 17.7% and 8.8%, respectively. In univariate analysis, lower GA, lighter BW, total days of supplemental oxygen, days of continuous positive airway pressure (CPAP), presence of apnea, and intraventricular hemorrhage (IVH) were associated with the development of any ROP. In the stepwise multivariable logistic regression analysis, lighter BW, male gender, and bronchopulmonary dysplasia (BPD) were significant risk factors for the development of any ROP. Lower GA and being either a twin or triplet were significant risk factors for ROP requiring intervention. However, no antenatal condition was identified as a risk factor for ROP.
**Conclusion:** The incidence of ROP in rural tertiary hospitals was relatively high as compared with previously published data from urban tertiary hospitals. Lighter BW, male gender, and BPD were significantly associated with the development of ROP in a local context. Epidemiological studies are necessary to prevent ophthalmic morbidities.

**Keywords:** Incidence; Retinopathy of Prematurity; Risk-factors; Thailand

*J Ophthalmic Vis Res* 2023; 18 (1): 81–87

**Correspondence to:**
Mantapond Ittarat, MD. Surin Hospital and School of Ophthalmology, Suranaree University of Technology, 68 Lak Muaeng Road, Muaeng, Surin 32000, Thailand.
E-mail: mantapornittarat@gmail.com

Received: 04-08-2021 Accepted: 01-08-2022

Access this article online

**Website:** https://knepublishing.com/index.php/JOVR

**DOI:** 10.18502/jovr.v18i1.12728

This is an open access article distributed under the Creative Commons Attribution License, which permits unrestricted use, distribution, and reproduction in any medium, provided the original work is properly cited.

**How to cite this article:** Ittarat M, Chansaengpetch S, Chansangpetch S. Incidence and Risk Factors for Retinopathy of Prematurity at a Rural Tertiary Hospital in Thailand . J Ophthalmic Vis Res 2023;18:81–87.

© 2023 Ittarat et al. This is an open access article distributed under the Creative Commons Attribution License | Published by Knowledge E

## INTRODUCTION

Retinopathy of prematurity (ROP) is one of the leading causes of childhood preventable blindness worldwide. Globally, it was estimated that 184,700 infants developed ROP in 2010.[1] Subsequently 20,000 became blind or suffered from severe visual impairment, which could have been avoided with timely screening and interventions for ROP.[1, 2] Many nations are now addressing ROP as one of the major public health concerns.[3]

Various factors have demonstrated to be associated with the development of ROP, some of which also influence its severity. Gestational age (GA), birth weight (BW), and use of supplemental oxygen showed the strongest association with ROP.[4, 5] Other neonatal comorbidities such as respiratory distress syndrome (RDS), bronchopulmonary dysplasia (BPD), intraventricular hemorrhage (IVH), and necrotizing enterocolitis are also well recognized as relevant risk factors for ROP development.[5–7]

Recent advances in neonatal care have improved the survival rate of premature infants, leading to an increase in the incidence of ROP.[3, 8, 9] However, the current situation in developing and Asian countries, including Thailand, is now considered an epidemic.[2, 3] The incidence of ROP in any stage varies among different countries. Even in the same country, the incidence and risk factors of ROP differ from region to region, as there are differences in regional ethnicities and characteristics of antenatal and neonatal care between urban and rural areas. According to an urban tertiary hospital in Bangkok, 40.7% of premature infants who underwent screening examinations during 2006–2009 developed ROP.[10] Worse, epidemiological data on ROP in Thailand are still lacking, particularly in rural areas; very few studies on ROP have been published in the past decade. Pinpointing our study to a regional context can provide key information for the further identification and investigation of more specific factors for ROP. Therefore, this study aimed to estimate the incidence of ROP and identify potential risk factors for ROP in a rural tertiary hospital in Thailand.

## METHODS

This study was a retrospective chart review conducted at Surin Hospital, northeastern Thailand. Surin Hospitals are rural tertiary care hospitals that provide neonatal intensive care units with qualified neonatologists. This study was performed by reviewing the charts of consecutive patients who underwent screening examinations for ROP between October 2019 and September 2020. Ethical review approval was obtained from the Institutional Review Board of Surin Hospital on March 2021 (IRB No. 06/2564). This study was conducted in accordance with the principles of the Declaration of Helsinki. All charts were reviewed by the primary author and no personal data of the patients were disclosed.

The study included all infants who met one of the following criteria: GA $\leq$ 30 weeks or BW $\leq$ 1,500 gr; GA $>$ 30 weeks or BW $>$ 1500 gr with an unstable clinical course and believed by their attending pediatrician or neonatologist to be at risk for ROP. These inclusion criteria followed the recommendations of the American Academy of Pediatrics, American Academy of Ophthalmology, and American Association for Pediatric Ophthalmology and Strabismus.[11] Patients lost to follow-up before the screening date were excluded. All examinations were performed by qualified ophthalmologists using binocular indirect ophthalmoscopy. Infants underwent a screening examination at four weeks postnatal age or a corrected GA of 31 weeks, whichever occurred later. Retinal findings and ROP stages were recorded according to the revised International Classification of Retinopathy of Prematurity.[12] The intervals of subsequent examinations were determined by the examining ophthalmologist in accordance with the severity of the findings. Interventions were performed when ROP reached type-1 pre-threshold disease or a diagnosis of aggressive posterior retinopathy of prematurity (APROP) was noted.

The primary outcome was to estimate the incidence of any stage of ROP (stages I–V) and ROP requiring intervention. The identification of risk factors for the development of any ROP and ROP requiring intervention was the secondary outcome. The variables collected were as follows:

(1) Demographic information: sex, BW, and multiple gestations (twins or triplets).

(2) Antenatal factors: GA, maternal age, number of gestations, inadequate number of antenatal care (ANC) visits (less than four visits), maternal diabetes mellitus, premature rupture of membranes, and severe preeclampsia.

**Table 1.** Univariable analysis – Risk factors for ROP.

| | No ROP | Any ROP | P-value[a] | ROP requiring intervention | P-value[b] |
|---|---|---|---|---|---|
| | *N* = 93 | *N* = 20 | | *N* = 10 | |
| Gender: male | 45 (48.4) | 14 (70.0) | 0.079* | 8 (80.0) | 0.065* |
| Birth weight (gr) | 1656.1 (500.9) | 1294 (246.8) | 0.002† | 1287 (227.2) | 0.037* |
| Twin/triplet | | | 0.067* | | 0.001x |
| Twin | 15 (16.1) | 4 (20.0) | | 4 (40.0) 2 (20.0) | |
| Triplet | 1 (1.1) | 2 (10.0) | | | |
| **Antenatal factors** | | | | | |
| Gestational age (wk) | 32.2 (2.9) | 30 (3.2) | 0.002† | 28.7 (1.3) | 0.004 |
| Maternal age (yr) | 25.4 (7.1) | 27.5 (7.9) | 0.103† | 28.7 (8.7) | 0.266† |
| Number of gestations | 2 (1 to 3) | 1 (1 to 2) | 0.912‡ | 1 (1 to 4) | 0.780‡ |
| Inadequate number of ANC visits | 2 (2.3) | 1 (5.9) | 0.446x | 1 (14.3) | 0.192x |
| Maternal diabetes mellitus | 4 (4.7) | 1 (5.9) | 1.000x | 0 (0.0) | 1.000x |
| Premature rupture of membranes | 8 (9.3) | 1 (5.9) | 1.000x | 0 (0.0) | 1.000x |
| Severe preeclampsia | 4 (4.7) | 0 (0.0) | 1.000x | 0 (0.0) | 1.000x |
| **Neonatal factors** | | | | | |
| 1-min Apgar score | 7.2 (2.4) | 6.6 (3.0) | 0.382† | 7.1 (1.7) | 0.953† |
| 5-min Apgar score | 8.8 (2.0) | 8.4 (2.8) | 0.502† | 9.4 (1.3) | 0.277† |
| 10-min Apgar score | 9.4 (1.5) | 9.1 (1.9) | 0.432† | 9.8 (0.4) | 0.292† |
| Apnea | 11 (11.8) | 7 (35.0) | 0.012x | 4 (40.0) | 0.041x |
| Hypoglycemia | 22 (23.7) | 5 (25.0) | 0.766* | 2 (20.0) | 1.000x |
| Sepsis | 41 (44.1) | 11 (55.0) | 0.228* | 7 (70.0) | 0.085x |
| Hypothermia | 8 (8.6) | 2 (10.0) | 0.672x | 0 (0.0) | 1.000x |
| Osteopenia of prematurity | 4 (4.3) | 2 (10.0) | 0.261x | 1 (10.0) | 0.414x |
| Hypotension | 5 (5.4) | 1 (5.0) | 1.000x | 0 (0.0) | 1.000x |
| Thrombocytopenia | 3 (3.2) | 1 (5.0) | 0.523x | 0 (0.0) | 1.000x |
| Respiratory distress syndrome | 38 (40.9) | 10 (50.0) | 0.299* | 5 (50.0) | 0.507* |
| Bronchopulmonary dysplasia | 3 (3.2) | 3 (15.0) | 0.057* | 1 (10.0) | 0.414x |
| Necrotizing enterocolitis | 18 (19.4) | 2 (10.0) | 0.516* | 1 (10.0) | 1.000x |
| Intraventricular hemorrhage | 8 (8.6) | 5 (25.0) | 0.029x | 2 (20.0) | 0.214x |
| Heart disease (including PDA) | 23 (24.7) | 5 (25.0) | 0.844* | 1 (10.0) | 0.441x |
| Hematocrit level | 40.5 (6.3) | 38.2 (7.3) | 0.164† | 35.1 (4.2) | 0.015† |
| Days of total oxygen (days) | 6 (2 to 17) | 14.5 (6 to 33.5) | 0.045‡ | 11.5 (8 to 23) | 0.313‡ |
| Days of mechanical ventilation (days) | 2 (0 to 7) | 4 (5 to 8) | 0.343‡ | 3 (1 to 6) | 0.930‡ |
| Days of CPAP (days) | 1 (0 to 3) | 2 (1 to 5.5) | 0.021‡ | 2 (1 to 4) | 0.207‡ |
| Use of surfactant | 15 (16.1) | 3 (15.0) | 1.000x | 2 (20.0) | 0.789x |

ROP, retinopathy of prematurity; PDA, patent ducts arteriosus.
[a]Comparison between No ROP and Any ROP; [b]Comparison between ROP requiring intervention and Others (no intervention).
*Data shown as *n* (%); *P*-value was obtained from Chi-squared test; †Data shown as mean (SD); *P*-value was obtained from *t*-test; ‡Data shown as median (IQR); *P*-value was obtained from Mann–Whitney U test; xData shown as *n* (%); *P*-value was obtained from Fisher's exact test.

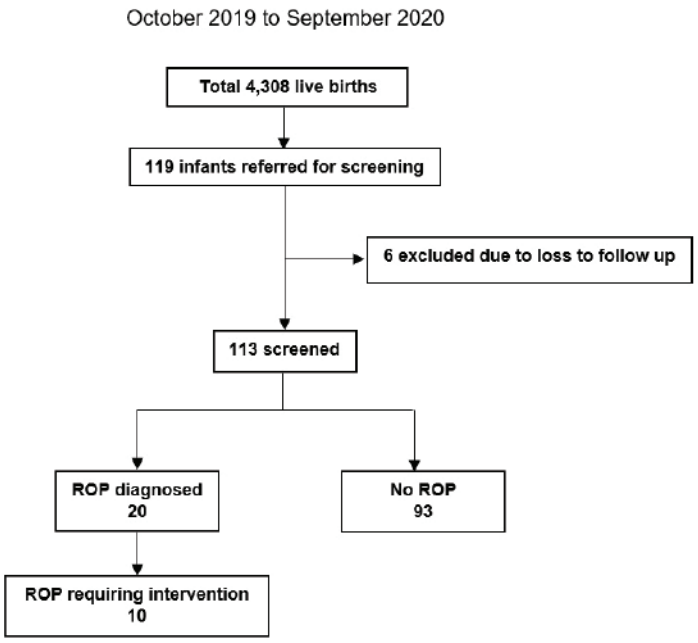


**Figure 1.** Schematic diagram of study recruitment. ROP, retinopathy of prematurity.

**Table 2.** Stepwise multivariable logistic regression – Risk factors for any ROP.

| | Odds ratio | 95% CI | P-value |
|---|---|---|---|
| Birth weight | 0.997 | 0.994–0.999 | 0.005* |
| Gender: male | 4.907 | 1.079–22.325 | 0.040* |
| Bronchopulmonary dysplasia | 17.047 | 1.453–199.946 | 0.024* |

ROP, retinopathy of prematurity; CI, confidence interval
*Statistically significant.

(3) Neonatal factors: Apgar scores at 1, 5, and 10 min, apnea of prematurity, hypoglycemia, neonatal sepsis (culture-positive or antibiotic administration for more than seven days), hypothermia, osteopenia of prematurity, hypotension, thrombocytopenia, RDS, BPD, necrotizing enterocolitis, IVH, heart disease including patent ductus arteriosus, hematocrit level (on the date of discharge), use of surfactant, total days of oxygen therapy, days of mechanical ventilation, and days of continuous positive airway pressure (CPAP).

## Statistical Analysis

All analyses were performed using Stata 13.0 (StataCorp, College Station, TX, USA). In the antenatal factor analysis, only one participant with multiple pregnancies was randomly selected to eliminate duplication of the data. Univariable comparisons of risk factors between the groups were analyzed. For variables with univariable *P*-value < 0.2, forward stepwise multivariable logistic regression was then used to establish the association between risk factors and the development of any ROP and ROP requiring intervention. The significance level for adding a variable was set as 0.05. Demographic, antenatal, and neonatal factors were explored using a stepwise model. Regression analysis was performed to define associations. Odds ratios (ORs) and 95% confidence intervals (CIs) were also calculated. Continuous variables are shown as means with standard deviations (SD) or medians with interquartile ranges. Categorical variables were presented as counts and percentages.

**Table 3.** Stepwise multivariable logistic regression – Risk factors for ROP that required intervention.

| | Odds ratio | 95% CI | P-value |
|---|---|---|---|
| GA | 0.552 | 0.366–0.830 | 0.004* |
| Twin/Triplet | 10.530 | 1.629–68.058 | 0.013* |

ROP, retinopathy of prematurity; GA, gestational age; CI, confidence interval.
*Statistically significant.

Continuous data were analyzed using the *t*-test or Mann–Whitney U test depending on the distribution of data. Categorical data were analyzed using the Chi-squared test or Fisher's exact test, as appropriate. For all tests, a *P*-value < 0.05 was considered statistically significant.

## RESULTS

During the study period, 119 infants met the criteria for the ROP examination. Of the 119 infants, 40 (33.6%) had a GA of 30 weeks or below, and 53 (44.5%) had a BW of 1500 gr or below. Thirty-three infants (27.7%) had a GA ≤ 30 weeks and BW ≤ 1500 gr. A total of 59 infants (49.6%) had a GA > 30 weeks and BW > 1500 gr. These infants underwent ROP screening because of an unstable clinical course, including RDS in 18 infants, pneumonia in 16 infants, and sepsis in 25 infants. Of these, six patients were lost to follow-up before the date of screening; thus, they were excluded. Subsequently, 113 participants underwent ROP screening and were included in the present study [Figure 1]. Of the no ROP-diagnosed infants, subsequent examinations were performed every 4 weeks until a postmenstrual age of at least 45 weeks, averaging 3.5 examinations. Of the ROP-diagnosed infants, subsequent examinations were performed every 2 weeks until a postmenstrual age of at least 54 weeks and were examined until total regression of ROP was observed, which averaged approximately 12.3 examinations.

The incidence rate of ROP was 17.7% (20/113). Of the ROP-diagnosed patients, 40% (8/20), 10% (2/20), 15% (3/20), and 5% (1/20) developed stages 1, 2, 3, and 4 ROP, respectively, and 30% (6/20) had APROP. None of them developed stage 5 ROP. Meanwhile, the incidence of ROP requiring intervention was 8.8% (10/113) among all infants undergoing the examination and 50% (10/20) of known patients with ROP. All patients with ROP who required intervention achieved satisfactory anatomical outcomes after treatment.

Table 1 shows the results of the univariate analysis. Infants with any stage of ROP had significantly lower GA, lighter BW, higher incidence of IVH, higher incidence of apnea, longer duration of total supplemental oxygen, and longer duration of CPAP than infants without ROP. The mean GA and BW of infants with ROP were 30 ± 3.2 weeks and 1294 ± 246.8 gr, respectively. While the mean GA and the mean BW of infants without ROP were 32.2 ± 2.9 weeks and 1656.1 ± 500.9 gr, respectively. Using stepwise multivariable logistic regression [Table 2], the following were significant risk factors for ROP development: lighter BW (OR 0.997, 95% CI 0.994–0.999, *P* = 0.005), male gender (OR 4.907, 95% CI 1.079–22.325, *P* = 0.040), and BPD (OR 17.047, 95% CI 1.453–199.946, *P* = 0.024). Lower GA (OR 0.552, 95% CI 0.366–0.830, *P* = 0.004) and being a twin/triplet (OR 10.530, 95% CI 1.629–68.058, *P* = 0.013) were significant risk factors for the development of ROP requiring intervention as shown in the multivariable logistic regression analysis [Table 3]. No antenatal factor was identified as a predictor or risk factor of ROP development.

## DISCUSSION

The incidence of ROP at any stage varies among countries, with reported figures ranging from 18.5% to 47%.[3, 8, 9] This was comparable to the result of Hong Kong's study (any ROP incidence of 18.5%).[9] In Thailand, there are few published studies on the incidence of ROP. A large study from an urban tertiary hospital in Bangkok revealed that the incidence of ROP during the last decade (2006–2009) was 40.7%; among these, 72% required intervention.[10] More recently, in 2020, a study conducted by another urban tertiary hospital showed that the incidence of ROP and ROP requiring intervention was 10% and 3%,

respectively.[13] The current incidence of ROP reported by rural tertiary hospitals ranges from 20.1 to 31.7%, and that of ROP requiring intervention is 10.8%.[14, 15] It signifies that the incidence of ROP varies considerably among local literature and this may be a reflection of the modification of ROP screening criteria and the improvement of antenatal and neonatal cares over the past decade. Additionally, evidence shows that the incidence of ROP is higher in rural than in urban tertiary hospitals. The differences in specific risk factors, particularly the characteristics of neonatal care, could play a role in the disparity in the ROP incidence between these two areas.

To the best of our knowledge, lower GA and lighter BW are widely regarded as the major risk factors for ROP development.[5] Our univariable analysis showed that infants with any stage of ROP had significantly lower GA and lighter BW than those without ROP; however, only lighter BW was statistically significant in the multivariable logistic regression model. Similarly, a recent Korean nationwide population-based study demonstrated that the incidence of ROP (317.14 per 1000 newborns) and the rate of visual impairment (4.5 per 100 person-years) were the highest among very low BW infants.[16] Moreover, lower GA was the significant risk factor for both ROP and ROP requiring intervention, in stepwise analysis. This finding is consistent with the results of most studies.[4, 17–19]

Male gender was the other risk factor for any ROP development in this study. Yang et al also found a similar relationship in their analysis.[20] One possible explanation is male vulnerability. It has been described that morbidity and mortality are frequently reported to be higher in male gender than female gender in early life.[21]

BPD was one of the important risk factors for any stage of ROP in this study. Our result was in line with two previous local studies.[13, 15] Gebeşçe et al, Holmström et al, and Wu et al also found a similar relationship in multivariable analysis.[22–24] Furthermore, Singh and colleagues revealed the association between moderate-to-severe BPD and severe ROP.[6] Interestingly, it has been proposed that both BPD and ROP may share common molecular mechanisms predisposing to dysregulation of angiogenesis.[25]

Being a twin or triplet was significantly correlated with the development of ROP requiring intervention in our study; however, this condition was not associated with any ROP development. Likewise, Port and colleagues identified multiple gestations as a risk factor for treatment requiring ROP.[26] There is evidence that twins could exist in placental-sharing nutrition and blood supply situations, which may reduce BW discordance.[27] It is well-known that the proportion of infants with extremely low BW is greater in twins than in singletons.[28] The extreme low BW has been frequently identified as a major risk factor for ROP requiring intervention.[8]

The present study has some limitations that should be considered. This was a single-center retrospective study. Further multicenter studies with larger sample sizes are still needed to provide generalizable epidemiological data on ROP in Thailand.

In summary, the incidence of ROP at any stage and ROP requiring intervention was 17.7% and 8.8%, respectively, at a rural tertiary hospital in Thailand. Lighter BW, male gender, and BPD were significant risk factors for the development of any ROP. Lower GA and being a twin or triplet were other relevant conditions affecting ROP requiring intervention. As the survival rates of preterm infants are increasing annually, investigation of the incidence of ROP and its risk factors is critical for identifying potential hotspots for ROP and establishing a screening protocol to prevent ophthalmic morbidities. Guidelines must be updated in a local context, and further epidemiological studies are imperative.

## Financial Support and Sponsorship

The authors did not receive support from any organization for the submitted work.

## Conflicts of Interest

The authors have no relevant financial or non-financial interests to disclose.

## *REFERENCES*

1. Blencowe H, Lawn JE, Vazquez T, Fielder A, Gilbert C. Preterm-associated visual impairment and estimates of retinopathy of prematurity at regional and global levels for 2010. *Pediatr Res* 2013;74:35–49.
2. Adams GGW. ROP in Asia. *Eye* 2020;34:607–608.
3. Bowe T, Nyamai L, Ademola-Popoola D, Amphornphruet A, Anzures R, Cernichiaro-Espinosa LA, et al. The current

state of retinopathy of prematurity in India, Kenya, Mexico, Nigeria, Philippines, Romania, Thailand, and Venezuela. *Digit J Ophthalmol* 2019;25:49–58.

4. Bas AY, Demirel N, Koc E, Ulubas Isik D, Hirfanoglu iM, Tunc T. Incidence, risk factors and severity of retinopathy of prematurity in Turkey (TR-ROP study): A prospective, multicentre study in 69 neonatal intensive care units. *Br J Ophthalmol* 2018;102:1711–1716.
5. Kim SJ, Port AD, Swan R, Campbell JP, Chan RVP, Chiang MF. Retinopathy of prematurity: a review of risk factors and their clinical significance. *Surv Ophthalmol* 2018;63:618–637.
6. Singh JK, Wymore EM, Wagner BD, Thevarajah TS, Jung JL, Kinsella JP, et al. Relationship between severe bronchopulmonary dysplasia and severe retinopathy of prematurity in premature newborns. *J AAPOS* 2019;23:209.e1–.e4.
7. Watts P, Adams GG, Thomas RM, Bunce C. Intraventricular haemorrhage and stage 3 retinopathy of prematurity. *Br J Ophthalmol* 2000;84:596–599.
8. Shah VA, Yeo CL, Ling YL, Ho LY. Incidence, risk factors of retinopathy of prematurity among very low birth weight infants in Singapore. *Ann Acad Med Singap* 2005;34:169–178.
9. Yau GS, Lee JW, Tam VT, Liu CC, Yip S, Cheng E, et al. Incidence and risk factors of retinopathy of prematurity from 2 neonatal intensive care units in a Hong Kong Chinese population. *Asia Pac J Ophthalmol* 2016;5:185–191.
10. Thitiratsanont U, Supangkasen I, Wutthiworavong B. Screening for retinopathy of prematurity in Queen Sirikit Nation Institute of Child Health: Bangkok, Thailand. *Thai J Ophthalmol* 2011;25:9–16.
11. Fierson WM; American Academy of Pediatrics Section on Ophthalmology; American Academy of Ophthalmology; American Association for Pediatric Ophthalmology and Strabismus; American Association of Certified Orthoptists. Screening examination of premature infants for retinopathy of prematurity. *Pediatrics* 2018;142:e20183061.
12. The International Classification of Retinopathy of Prematurity revisited. *Arch Ophthalmol* 2005;123:991–999.
13. Poovichayasumlit C. Retinopathy of prematurity at Thammasat University Hospital. *Thammasat Med J* 2020;20:297–306.
14. Paopongsawan P, Jirapradittha J, Kiatchoosakun P, Wongwai P. Retinopathy of prematurity in 5 neonatal units at the 7th Health District of Thailand. *J Med Assoc Thai* 2018;101:1263–1267.
15. Saleewan K. Incidence and risk factors of retinopathy of prematurity (ROP). *Med J Srisaket Surin Buriram Hosp* 2016;31:99–110.
16. Na KH, Kim KH, Kang TU, Hann HJ, Ahn HS, Kim HJ. Incidence, long-term visual outcomes, and mortality in retinopathy of prematurity in Korea: A nationwide population-based study. *Invest Ophthalmol Vis Sci* 2020;61:14.
17. Araz-Ersan B N, Kir, Akarcay K, Aydinoglu-Candan O, Sahinoglu-Keskek N, Demirel A, et al. Epidemiological analysis of retinopathy of prematurity in a referral centre in Turkey. *Br J Ophthalmol* 2013;97:15–17.
18. Ying GS, Bell EF, Donohue P, Tomlinson LA, Binenbaum G. Perinatal risk factors for the retinopathy of prematurity in postnatal growth and rop study. *Ophthalmic Epidemiol* 2019;26:270–278.
19. Freitas AM, Mörschbächer R, Thorell MR, Rhoden EL. Incidence and risk factors for retinopathy of prematurity: A retrospective cohort study. *Int J Retina Vitreous* 2018;4:20.
20. Yang MB, Donovan EF, Wagge JR. Race, gender, and clinical risk index for babies (CRIB) score as predictors of severe retinopathy of prematurity. *J AAPOS* 2006;10:253–261.
21. Wells JC. Natural selection and sex differences in morbidity and mortality in early life. *J Theor Biol* 2000;202(1):65–76.
22. Gebeşçe A, Uslu H, Keleş E, Yildirim A, Gürler B, Yazgan H, et al. Retinopathy of prematurity: Incidence, risk factors, and evaluation of screening criteria. *Turk J Med Sci* 2016;46:315–320.
23. Holmström G, Broberger U, Thomassen P. Neonatal risk factors for retinopathy of prematurity–a population-based study. *Acta Ophthalmol Scand* 1998;76:204–207.
24. Wu T, Zhang L, Tong Y, Qu Y, Xia B, Mu D. Retinopathy of prematurity among very low-birth-weight infants in China: Incidence and perinatal risk factors. *Invest Ophthalmol Vis Sci* 2018;59:757–763.
25. Stark A, Dammann C, Nielsen HC, Volpe MV. A pathogenic relationship of bronchopulmonary dysplasia and retinopathy of prematurity? A review of angiogenic mediators in both diseases. *Front Pediatr* 2018;6:125.
26. Port AD, Chan RV, Ostmo S, Choi D, Chiang MF. Risk factors for retinopathy of prematurity: Insights from outlier infants. *Graefes Arch Clin Exp Ophthalmol* 2014;252(10):1669–1677.
27. Lewi L, Cannie M, Blickstein I, Jani J, Huber A, Hecher K, et al. Placental sharing, birthweight discordance, and vascular anastomoses in monochorionic diamniotic twin placentas. *Am J Obstet Gynecol* 2007;197:587.e1-8.
28. Blondel B, Kogan MD, Alexander GR, Dattani N, Kramer MS, Macfarlane A, et al. The impact of the increasing number of multiple births on the rates of preterm birth and low birthweight: An international study. *Am J Public Health* 2002;92:1323–1330.

Original Article

# Epidemiological and Clinical Features of Pediatric Open Globe Injuries: A Report from Southern Iran

**Ali Azimi[1], MD; Fardad Abdollahi[1], MD; Elham Sadeghi[1], MD; Amir Reza Farsiani[2], MD; Shadi Moshksar[1], MD; Maryam Nadi[1], MD**

*[1]Poostchi Ophthalmology Research Center, Department of Ophthalmology, School of Medicine, Shiraz University of Medical Sciences, Shiraz, Iran*
*[2]Department of Ophthalmology, Zanjan University of Medical Sciences, Zanjan, Iran*

**ORCID:**
*Ali Azimi: https://orcid.org/0000-0001-7744-5858*
*Elham Sadeghi: https://orcid.org/0000-0003-3802-3219*

## Abstract

**Purpose:** To evaluate the epidemiological features of open globe injury (OGI) in a tertiary ophthalmic center in the south of Iran.
**Methods:** The medical files of pediatric patients diagnosed with OGI between March 2014 and March 2019 were reviewed retrospectively. Demographic data, laterality, time of injury, cause of trauma, location and mechanisms, complications, and the involved tissues, visual acuity, type of operation, and antibiotic therapy were all analyzed. Data were processed using the SPSS.
**Results:** In total, 110 eyes of 108 patients were included. Ages <7 years comprised 49.1%, 7–12 years 26.4%, and 13–18 years 24.5% of cases. Of the 108 patients, 76 (70.3%) were males. No significant difference between right versus left eyes was seen. The incidence of OGI was lowest in winter and highest in spring, and it had more prevalence on the weekends. Sharp objects were the most common cause of OGI in ages <7 years, while blunt objects, accidents and falls, and guns and fireworks were more prevalent in older children. Home was the most common place of injury overall. The most common type of injury was penetrating trauma. Upon arrival, most of the children had a visual acuity <0.1 decimal. Primary wound closure was the most prevalent type of surgery done predominantly within 24 hr from admission time.
**Conclusion:** Ages <7 years and male gender were the most common age and sex of pediatric OGI, respectively, and sharp objects were the predominant etiology. Early management and primary repair are essential for prevention of complications such as endophthalmitis and amblyopia.

**Keywords:** Eye Injury; Ocular Trauma; Pediatric; Open Globe Injury; Epidemiology

*J Ophthalmic Vis Res* 2023; 18 (1): 88–96

**Correspondence to:**
Elham Sadeghi, MD. Poostchi Clinic, Zand St., Shiraz 71349, Iran.
E-mail: elham.sadeghi@rocketmail.com

Received: 12-09-2021 Accepted: 30-08-2022

**Access this article online**

**Website:** https://knepublishing.com/index.php/JOVR

**DOI:** 10.18502/jovr.v18i1.12729

This is an open access article distributed under the Creative Commons Attribution License, which permits unrestricted use, distribution, and reproduction in any medium, provided the original work is properly cited.

**How to cite this article:** Azimi A, Abdollahi F, Sadeghi E, Farsiani AR, Moshksar S, Nadi M. Epidemiological and Clinical Features of Pediatric Open Globe Injuries: A Report from Southern Iran . J Ophthalmic Vis Res 2023;18:88–96.


© 2023 Azimi et al. This is an open access article distributed under the Creative Commons Attribution License | Published by Knowledge E

## INTRODUCTION

Twenty to fifty percent of all ocular injuries occur in the pediatric age group. Due to a lack of cooperation and poor compliance for assessment and therapy, this group's management is complicated.[1] Pediatric ocular trauma is the most leading cause of acquired unilateral vision loss in childhood, especially in developing countries.[2] Despite all that has been done to reduce the risk of trauma in children, it remains common worldwide.[3]

Ocular injuries are divided into two main groups: closed globe injuries and open globe injuries (OGIs). An OGI is a severe form of trauma leading to a full-thickness defect in the cornea, sclera, or both, exposing the intraocular compartments to the external environment. OGIs are classified into four groups: penetrating injury (only an entrance wound or same entrance/exit wound), perforating injury (separate entrance and exit wounds), rupture (resulting from blunt trauma causing a full-thickness defect at the weakest point of the eyewall), and intraocular foreign body (IOFB). The lack of treatment in childhood trauma may lead to various complications such as cataract, retinal detachment, vitreous hemorrhage, corneal opacity, amblyopia, IOFB and toxicity due to chronic foreign bodies, endophthalmitis, and sympathetic ophthalmia.[4]

Knowledge of the epidemiological characteristics of the OGI can assist in the prevention of catastrophic damage to children's physiological and psychological health. World Health Organization (WHO) has recognized childhood blindness as one of the leading causes of preventable blindness.

Determination of epidemiologic risk factors and prognosis of OGIs are essential in achieving a healthier outcome and also reducing its prevalence.[5] Therefore, we carried out a retrospective study to evaluate the clinical course and outcomes in all patients younger than 18 years old who were admitted to this tertiary referral university-affiliated ophthalmology center in the south of Iran due to OGI.

## METHODS

In this retrospective study, the medical charts of pediatric patients suffering from OGIs were reviewed. The medical records of 110 eyes of 108 children (age ≤18 years) admitted to this hospital due to ocular trauma and diagnosed by slit-lamp examination or examination under anesthesia from March 2014 to March 2019 were evaluated. Patients who had a full-thickness ocular injury repaired at other centers were excluded.

In the medical charts, the initial ophthalmology examination sheets, hospital records, details of the operation notes, and outpatient follow-up were all reviewed. Demographic data were collected on age, sex, injured eye, ocular status before the trauma, laterality, place of trauma, month and year of injury, and mechanism of trauma.

The initial best corrected distance visual acuity (BCDVA), evaluated by Snellen chart, was recorded. No light perception (NLP) visual acuity (VA) was confirmed using an indirect ophthalmoscope with a bright and highest intensity light source. Clinical data such as intraocular pressure (IOP) with Goldman tonometer, location of injury (home, school, and street), type of injury, uvea and pupil status, hyphema, lens status, vitreous, retina and choroidal conditions, involvement of orbit, presence of uveitis or endophthalmitis, and types of required surgeries were all recorded. Based on the Birmingham Eye Trauma Terminology (BETT), cases were classified into penetrating, perforating, or IOFB injury.

The study protocol was approved by the ethics committee of the university hospital. It adhered to the tenants of the Declaration of Helsinki.

Continuous parameters were reported as mean ± SD. Chi-square and Fisher's exact tests were used to compare the categorical data, and independent *t*-test and ANOVA tests were used to compare the continuous data. Statistical analysis was performed using the SPSS for Windows (SPSS Inc, Chicago, IL). Data analysis was interpreted using a significance level of $P < 0.05$.

## RESULTS

A total of 110 eyes of 108 pediatric patients initially diagnosed as OGI was included in this five-year study period (from March 2014 to March 2019). Patients' mean age was 7.8 ± 5.2 years (range, 6 months to 18 years) with a median of 7 years and a mode of 2 years. The mean age was 8.7 ± 5.4 years for boys, while the girls' mean age was 5.8 ± 4.1 years ($P = 0.006$).

Patients' eyes were divided into three different age groups: <7 years (49.1% $n = 54$), 7–12 years

(26.4% *n* = 29), and 13–18 years (24.5% *n* = 27). The majority of our cases were in the preschool age (<7years) group ($P < 0.001$).

In our study, 69.1% of eyes were related to the male gender (*n* = 76) and 30.9% were related to females (*n* = 34). Boys were statistically more susceptible to experience OGI than girls (ratio 2.2:1; $P < 0.001$). This predominance rose sharply from preschool children to older children 13–18 years old (1.57:1 to 8:1) ($P < 0.001$).

As shown in Figure 1, there is a negative correlation between age and incidence of OGI in girls.

The rate of right eye involvement was 53.6% (*n* = 59), and the left eye was 46.3% (*n* = 51) with no statistically significant difference. There were two cases with bilateral eye involvement caused by motor vehicle accident and mine explosion.

As shown in Table 1, the incidence of OGI was lowest in winter and highest in spring with no statistically significant difference by season ($P = 0.76$). Incidences were more on the weekends, but there were no significant differences regarding the day of the week (weekdays vs weekends; $P = 0.37$) [Table 2].

Most of the injuries were caused by sharp objects (37.3% *n* = 41), followed by blunt objects (35.3% *n* = 39), accidents and falls (17.3% *n* = 19), and guns and fireworks (10% *n* = 11). A statistically significant difference was identified between causative objects of the injuries and different age groups ($P = 0.027$). Sharp objects comprised a greater number of OGI in the preschool age group (<7 years), while blunt objects, accidents and falls, and guns and fireworks accounted for more injuries in older children (7–18 years). Knives and wooden sticks were the most common tools among the sharp and blunt objects that provoked OGI in all children [Table 3].

Home was the most predominant place of injury (54% *n* = 60), followed by outdoor environment (street 25.5% *n* = 28, farm 7.3% *n* = 8, industrial places 0.9% *n* = 1) and school (11.8% *n* = 13). Home was the top place that injuries occurred amid the preschool age group (<7), while the outdoor environment was more frequent in older ages (All *P*s < 0.001) [Table 4].

Most of the injuries (68% *n* = 75) occurred while playing. In decreasing order of frequency, accidents (17.3% *n* = 19), assaults (10% *n* = 11), and occupation-related factors (4.5% *n* = 5) were the other activities that led to injuries ($P < 0.001$).

The majority of the injuries in both boys and girls happened during playing, but assaults and occupation-related factors encompassed a higher percentage of injuries in boys (boys to girls' ratio for assaults is 7.3:2.7, and for occupational is 3.6:0.9) ($P < 0.001$).

The most common types of injury, according to BETT, were penetrating injuries (60.9% *n* = 67), followed by rupture (7.3% *n* = 8), IOFB (6.4% *n* = 7) and perforating injury (0.9% *n* = 1). Of the 110 traumatized eyes, 25 (22.7%) had multiple eye involvement and could not be categorized based on the BETT system. Two (1.8%) cases only had a partial-thickness laceration of the eye.

Penetrating traumas were the primary type of injuries in all age groups and genders, however, rupture injuries were observed mainly in boys and children over seven years of age (87%, seven out of eight rupture cases). We had only one case of perforating injury; a 16-year-old boy hit by a shotgun while playing on the farm.

Laceration layers in penetrating injuries were mostly corneoscleral (47.7% *n* = 32), followed by corneal (29.8% *n* = 20) and scleral (22.3% *n* = 15) layers. Corneoscleral involvement rose sharply in boys as compared to girls (25:10 cases). There were no significant statistical differences in penetrating injuries between different genders ($P = 0.38$) and age ($P = 0.16$) according to the laceration layers.

The mean size of lacerations in corneal penetrating injuries was 5.7 ± 3.1 mm with a median of 5 mm, while it was 3.47 ± 2.3 mm in scleral penetrating injuries with a median of 3 mm.

In 57 cases of corneal penetrating injuries, the main site of laceration was nasal (35% *n* = 20), followed by temporal (28% *n* = 16), central (15.8% *n* = 9), superior (12.3% *n* = 7), and inferior (8.8% *n* = 5).

In 52 cases of scleral penetrating injuries, the most common site of laceration was nasal (36% *n* = 19), followed by temporal (28% *n* = 15), inferior (17% *n* = 9), superior (15% *n* = 8), and central (1.9% *n* = 1) [Table 5].

Upon arrival, VA could not be evaluated in 36.4% (*n* = 40) of the cases because they were uncooperative. In four cases, VA was recorded using the CSM method (central, steady, and maintained eye position), which all of them presented C+S+M+VA.

BCDVA upon arrival was categorized into three groups: 0.5–1, 0.1–0.49, and under 0.1 decimal. In

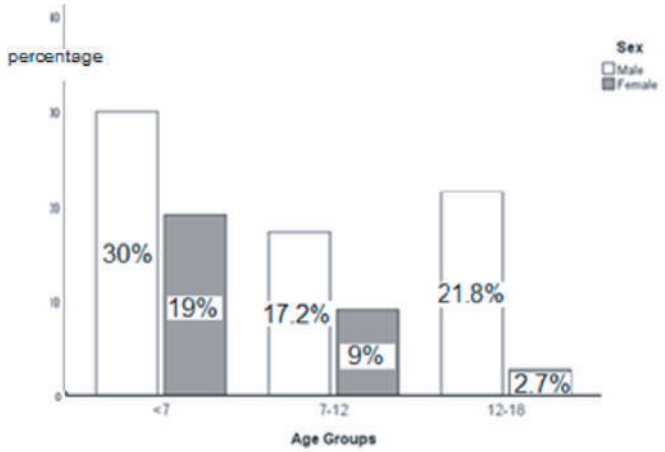


**Figure 1.** Distribution of trauma according to sex and age groups.

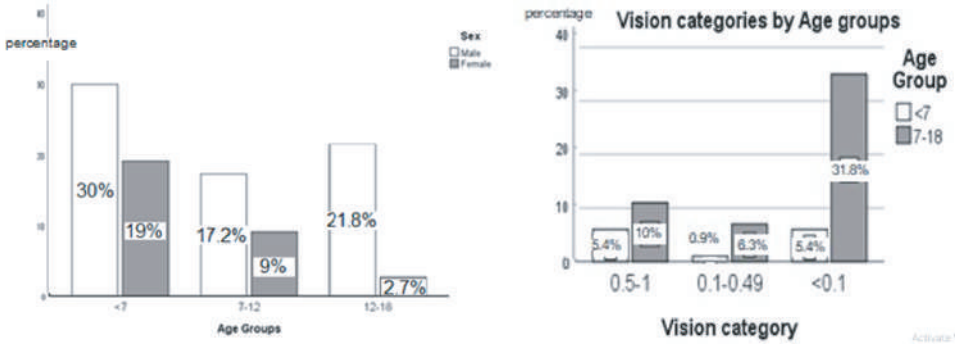


**Figure 2.** Vision categories by sex and age groups.

**Table 1.** Number of OGI by season.

| Season | Number | Percentage | |
|---|---|---|---|
| Spring | 34 | 30.9 | *P* = 0.76 |
| Summer | 28 | 25.5 | |
| Fall | 25 | 22.7 | |
| Winter | 23 | 20.9 | |

OGI, open globe injury

**Table 2.** Distribution of trauma by days of the week.

| Days of the week | N | Percentage | |
|---|---|---|---|
| Saturday | 14 | 12.7 | *P* = 0.37 |
| Sunday | 18 | 16.4 | |
| Monday | 15 | 13.6 | |
| Tuesday | 12 | 10.9 | |
| Wednesday | 11 | 10.0 | |
| Thursday | 19 | 17.3 | |
| Friday | 21 | 19.1 | |

**Table 3.** Causative objects of open globe injuries in children.

| Objects | N (%) | Objects | N (%) |
|---|---|---|---|
| Knife | 23 (20.9%) | Belt | 3 (2.7%) |
| Accidents | 16 (14.5%) | Eye glass | 3 (2.7%) |
| Wood | 12 (10.9%) | Fall | 3 (2.7%) |
| Metal, wire, nails | 8 (7.2%) | Fist | 3 (2.7%) |
| Stone | 7 (6.4%) | Animal horn | 2 (1.8%) |
| Gun | 5 (4.5%) | Pen | 2 (1.8%) |
| Fireworks | 5 (4.5%) | Explosion | 1 (0.9%) |
| Needle | 4 (3.6%) | Others | 13 (11.8%) |

**Table 4.** Place of injury according to age groups.

| Age groups (yr) | Place of injury | | | |
|---|---|---|---|---|
| | Home | School | Outdoor | P-value |
| | N (%) | | | |
| <7 | 43 (39.1) | 1 (0.9) | 10 (9.1) | <0.001 |
| 7–18 | 17 (15.5) | 12 (10.9) | 27 (24.5) | <0.001 |

66 eyes, which had registered VA upon arrival, most of the eyes had VA under 0.1 (62.1% *n* = 41), followed by 0.5–1 (25.7% *n* = 17) and 0.1–0.49 (12.1% *n* = 8).

In under 0.1 categories, VA was counting fingers in 13 cases, hand-motion in 6 cases, light perception in 9 cases, and NLP in 13 cases. As shown in Figure 2, in the male group, the VA under 0.1 was clearly higher than the female group. Additionally, the cases between 7 and 18 years old, compared to patients <7 years old, significantly presented the VA under 0.1 upon arrival.

Operation was performed on 93.6% of the cases (*n* = 103) with an initial diagnosis of OGI. Ninety-five percent of the operations (*n* = 98) were performed within 24 hr from the admission time. Five children only had an examination under sedation (EUS). Three children were discharged voluntarily despite the physicians' recommendation for surgery.

Out of the 98 patients who underwent surgery, 47.3% were operated on once; 33.6% (*n* = 37) had two surgeries; and 12.7% (*n* = 14) had more than two surgeries. Primary repair of lacerations was the most common type of the initial operation (75.7% *n* = 78). Peritomy comprised 24.2 % (*n* = 25) of the initial operations. Table 6 shows operations that were done after the initial surgeries. Of the 110 eyes with OGI, injuries finally led to the enucleation of the eyes in 7.2% of the cases (*n* = 8).

About 88% of the patients received antibiotics during admission to the hospital. Children in preschool-age received more intravitreal antibiotics or a combination of both intravitreal and intravenous antibiotics, while antibiotic therapy in older aged children was mainly via the intravenous route (*P* = 0.008) [Table 7]. About 84% of the patients (*n* = 93) received intravenous antibiotics. The mean days of receiving antibiotics were 3.4 ± 1.2 days, with a median of three days. A combination of ceftazidime and vancomycin were the most common antibiotics used intravenously (75% *n* = 70), followed by cefazolin and gentamicin (22% *n* = 21) and ceftriaxone and vancomycin (2.1% *n* = 2). From 20 cases who received intravitreal antibiotics during operation, cefazoline was the main choice (18 out of 20), and two other cases received intravitreal gentamycin and imipenem.

## DISCUSSION

Pediatric OGI can cause lifelong complications and unilateral blindness.[6] Since prevention is better than cure, solutions must be found to reduce it. Our study revealed an increase in OGI in preschool-aged children (<7 years). This is similar to the

**Table 5.** Complications and eye layers involvement.

| Complication | N (%) | Complication | N (%) |
|---|---|---|---|
| Corneal laceration | 59 (53) | Retina: hemorrhage | 5 (4.5) |
| Scleral laceration | 55 (50) | Retina: edema | 3 (2.7) |
| Uvea in wound | 5 (4.5) | Retina: tear | 2 (1.8) |
| Hyphema | 76 (69) | Retina: dialysis/detachment | 3 (2.7) |
| Iris injury | 28 (25) | External muscles | 2 (1.8) |
| Hypotony | 108 (98.18) | Lid | 19 (17.2) |
| Optic nerve injury | 26 (23) | Lacrimal system | 2 (1.8) |
| Lens: cataract | 40 (36) | Orbit: fracture | 5 (4.5) |
| Lens: subluxated/dislocated | 3 (2.7) | Orbit: foreign body | 1 (0.9) |
| Vitreous: hemorrhage | 17 (15.4) | Orbit: hemorrhage | 4 (3.6) |
| Vitreous: prolapse | 2 (1.8) | Inflammation: uveitis | 9 (8.1) |
| Choroid: hemorrhage | 2 (1.8) | Inflammation: endophthalmitis | 5 (4.5) |
| Choroid: rupture | 1 (0.9) | | |

**Table 6.** Operations after the initial surgeries.

| Operation | N (%) | Operation | N (%) |
|---|---|---|---|
| Lensectomy | 21 (19) | Pupiloplasty | 4 (3.6) |
| Deep Viterectomy | 21 (19) | Phaco | 2 (1.8) |
| Anterior Viterectomy | 2 (1.8) | Tarsoplasty | 2 (1.8) |
| Suture removal | 9 (8.1) | Iris cystectomy | 2 (1.8) |
| Enucleation | 8 (7.2) | Lateral canaloplasty | 1 (0.9) |
| IOFB removal | 6( 5.4) | Dacryocystorhinostomy | 1 (0.9) |
| IOL implantation | 5 (4.5) | ERMs removal | 1 (0.9) |
| PCIOL implantation | 3 (2.7) | Posterior capsulectomy | 1 (0.9) |
| Lid reconstruction | 4 (3.6) | Orbital wall repair | 1 (0.9) |

study by El-Sebaity et al,[7] but some reports have found increasing OGI risk in the 7–12 years old age group.[8–10]

Different studies showed different ratios of female OGL, but all agree that males' injury is statistically higher than females' injury, which is related to the propensity of the male gender to higher risk activities with less parental supervision as part of their natural growth.[4, 11–15] Besides, the differences between the sexes among the older age groups (12–18 years) increased significantly, and there was a negative correlation between age and incidence of OGI in females. It suggests that girls' dangerous and risky activities may reduce with aging.

There was no significant difference between the right and the left eyes. This is similar to the results of the study by Tan et al,[16] however, some reports have revealed that in adult cases, the right eye is more susceptible to injuries because, in adults, most injuries occur in the workplace.[17, 18] It must also be kept in mind that severe traumatic accidents, explosions, or intentional assault injuries may induce bilateral ocular involvement.

We have reported the OGI trend during vacation, as mentioned in other studies.[19, 20] A higher incidence of OGI on Fridays shows that children have more dangerous activities on the weekend. The risk increase in spring is a result of Norouz holidays in Iranian culture. At this time, the weather becomes warmer, and children tend

**Table 7.** Route of antibiotic injection by age groups.

| Age groups (yr) | Route of antibiotic | | | P-value |
|---|---|---|---|---|
| | Intravitreal N (%) | Intravenous | Both | 0.008 |
| <7 | 11 (11.3) | 27 (27.8) | 12 (12.4) | |
| 7–18 | 3 (3.1) | 39 (40.2) | 5 (5.2) | |

to play outdoor group games without parental supervision. It may be avoided with parental supervision, keeping dangerous devices out of children's reach, and educating children about proper safety considerations.

The prevailing etiological agent causing OGI in the preschool age group is sharp material such as knives, which correlates with previous studies.[6, 21, 22] Ocular trauma with knives usually happens accidentally. It is crucial to either decrease access to sharp objects or replace them with round blunt-tipped knives.[1] Older children are injured more by blunt objects, accidental falls, guns, and fireworks, predominantly in males related to practicing more aggressive behavior. These injuries can be prevented with proper training and using protective eyewear. Ocular trauma during car and motor accidents were the cause of 14.5% of OGI, and it is usually due to glass particles or blunt trauma. Using seatbelts and helmets may reduce the risk of experiencing ocular trauma during a road accident.

Prior studies have revealed that ocular injuries most frequently occur at home.[4, 12, 23] In this study, home was the main place for the incidence of ocular injuries occurring in preschool-aged children. As this age group spends most of their time at home, the use of toys with blunt edges and increased parental supervision may reduce the ocular trauma risk. Covering the sharp edges of household items with protective equipment may also be useful. Further awareness of parents and babysitters is recommended to prevent preschool-age OGI.[24] Some reports have shown that outdoor spaces are the most common place for OGI occurrences in pediatrics.[25, 26] In our study, the outdoor environment is the primary place for older children, especially in the male group, due to accidents, assaults, and occupation-related factors. Educating children to follow safety principles and practice anger management can be useful in reducing the occurrence of accidents, assaults, and occupational hazards that may lead to OGI.

Analysis of OGI in this report revealed that penetrating injuries were the most common type of ocular trauma (60.9%), which was consistent with data published by Puodžiuvienė et al.[8] The rate of globe ruptures was 7.3%, which was lower than the data reported by Court et al.[27] OGI with IOFB is more often experienced in adults. However, it is not rare in children.[28] The rate of IOFB injuries in our study was 6.4%. Compared to other types of OGI in pediatrics, perforating injury is not common in this group[29] as this type of injury is most often caused by shotgun usage which is not normally used in this age group. In our study, one patient was 16 years old with perforating OGI caused by firing a shotgun while playing on the farm.

The majority of wounds involve both cornea and sclera (47.3%), and hypotony is the most common presentation (98.18%). Two patients did not have hypotony because the laceration was partial thickness. Hyphema was the second most common sign (69%). One study had shown that hyphema was significantly related to closed globe injuries.[30] The other prevalent signs in OGI are traumatic cataract, iris injury, optic nerve injury, lid laceration, and vitreous hemorrhage.

In this study, 37.3% of cases had <0.1 VA upon arrival where 78% were males. This measurement is justified as more severe injuries occur in males due to their inherently more aggressive behavior.

Primary repair of the wound and repositioning of the prolapsed tissue is the most common surgery performed initially, usually within 24 hr from admission.[4] Endophthalmitis is one of the most serious and poor prognosis complications after OGI, which is preventable by primary wound closure.[31] About one-third (33.6%) of cases underwent surgeries twice, and 12.7% of them underwent surgeries three times. Lensectomy and deep vitrectomy were the most common types of surgery performed after the initial operation. In

an effort to prevent sympathetic ophthalmia, 7.2% of cases underwent enucleation and conformer placement surgery due to devastating injury and NLP VA.

Antibiotics administration plays a role in prophylaxis and treatment of endophthalmitis.[32] Traumatic endophthalmitis is usually seen in delayed wound closure, IOFB, posterior capsule rupture, delayed initiation of prophylactic antibiotic therapy after 24 hr from ocular trauma, and wound contamination with organic material.[33, 34] The antibiotic selected for treatment should have a broad spectrum acting against a larger group of microorganisms.[35]

The visual prognosis in pediatric OGI is not good. Statistics show that patients with ocular trauma in one eye are susceptible to trauma in the fellow eye.[36] Assessing ocular trauma is more important in the pediatric group due to longer lifespans and the more incidence of ocular complications in this group including cataract, retinal detachment, vitreous hemorrhage, corneal opacity, amblyopia, IOFB and toxicity due to chronic foreign bodies, endophthalmitis, and sympathetic ophthalmia; hence emphasizing that prevention is better than treatment. Education of parents, babysitters, and school teachers about children's supervision and choosing suitable toys according to child's age is needed. Keeping dangerous objects with sharp edges out of the reach of children is essential. Using protective eye glasses may play a useful role in preventing ocular trauma, while playing or working with sharp objects. To prevent eye injuries during an accident, using safety measures like suitable child seats, seat belts, and helmets are effective. Older children should be educated to avoid using guns, fireworks, and explosive devices.

This report is a retrospective and non-randomized study with some limitations because it was limited to medical files during hospitalization. Further studies may be needed to determine the overall burden of disease, post-discharge follow-up data, final VA, and delayed complications.

The second limitation is that as ocular trauma patients were referred to multiple centers, the actual number of patients with OGI recorded in this report is incomplete.

In summary, the results suggest the importance of prevention in reducing the frequency of ocular trauma in children due to longer lifespan. Also, it has recommended early primary wound closure to reduce or prevent devastating ocular complications. Additionally, it has counsel that extended follow-up is necessary to reduce and manage further complications such as amblyopia. More studies are recommended to accurately evaluate the prognosis of OGI in the long-term.

## Acknowledgements

This work was supported by Shiraz University of Medical Sciences and Poostchi Ophthalmology Research Center.

## Financial Support and Sponsorship

None.

## Conflicts of Interest

The authors declare that they have no conflict of interest.

## *REFERENCES*

1. Hosseini H, Masoumpour M, Keshavarz-Fazl F, Razeghinejad MR, Salouti R, Nowroozzadeh MH. Clinical and epidemiologic characteristics of severe childhood ocular injuries in southern Iran. *Middle East Afr J Ophthalmol* 2011;18:136–140.
2. Ilhan HD, Bilgin AB, Cetinkaya A, Unal M, Yucel I. Epidemiological and clinical features of paediatric open globe injuries in southwestern Turkey. *Int J Ophthalmol* 2013;6:855–860.
3. Batur M, Seven E, Akaltun MN, Tekin S, Yasar T. Epidemiology of open globe injury in children. *J Craniofac Surg* 2017;28:1976–1981.
4. Li X, Zarbin MA, Bhagat N. Pediatric open globe injury: A review of the literature. *J Emerg Trauma Shock* 2015;8:216–223.
5. Ojabo CO, Malu KN, Adeniyi OS. Open globe injuries in Nigerian children: Epidemiological characteristics, etiological factors, and visual outcome. *Middle East Afr J Ophthalmol* 2015;22:69–73.
6. AlDahash F, Mousa A, Gikandi PW, Abu El-Asrar AM. Pediatric open-globe injury in a university-based tertiary hospital. *Eur J Ophthalmol* 2020;30:269–274.
7. El-Sebaity DM, Soliman W, Soliman AM, Fathalla AM. Pediatric eye injuries in upper Egypt. *Clin Ophthalmol* 2011;5:1417–1423.
8. Puodžiuvienė E, Jokūbauskienė G, Vieversytė M, Asselineau K. A five-year retrospective study of the epidemiological characteristics and visual outcomes of pediatric ocular trauma. *BMC Ophthalmol* 2018;18:10.
9. Shoja M, MIR AA. Pediatric ocular trauma. 2006.

10. Sofi RA, Wani JS, Keng MQ, Sofi RA. Profile of children with ocular trauma. *JK-Practitioner* 2012;17:44–50.
11. Baiyeroju-Agbeja AM, Olurin-Aina OI. Penetrating eye injuries in children in Ibadan. *Afr J Med Med Sci* 1998;27:13–15.
12. Ahmadabadi MN, Alipour F, Tabataei SA, Karkhane R, Rezaei H, Ahmadabadi EN. Sharp-object-induced open-globe injuries in Iranian children admitted to a major tertiary center: A prospective review of 125 cases. *Ophthalmic Res* 2011;45:149–154.
13. Liu X, Liu Z, Liu Y, Zhao L, Xu S, Su G, et al. Determination of visual prognosis in children with open globe injuries. *Eye* 2014;28:852–856.
14. Saxena R, Sinha R, Purohit A, Dada T, Vajpayee RB, Azad RV. Pattern of pediatric ocular trauma in India. *Indian J Pediatr* 2002;69:863–867.
15. Choovuthayakorn J, Patikulsila P, Patikulsila D, Watanachai N, Pimolrat W. Characteristics and outcomes of pediatric open globe injury. *Int Ophthalmol* 2014;34:839–844.
16. Tan A, Mallika P, Asokumaran T, Mohamad Aziz S, Intan G. Paediatric ocular trauma in Kuching, Sarawak, Malaysia. *Malays Fam Physician* 2011;6:68–71.
17. Unterlauft JD, Rehak M, Wiedemann P, Meier P. Firework-related eye trauma in Germany. *Curr Eye Res* 2018;43:1522–1528.
18. Unterlauft JD, Wiedemann P, Meier P. [Firework-related eye trauma from 2005 to 2013]. *Klin Monbl Augenheilkd* 2014;231:915–920.
19. Madan AH, Joshi RS, Wadekar PD. Ocular trauma in pediatric age group at a tertiary eye care center in central Maharashtra, India. *Clin Ophthalmol* 2020;14:1003–1009.
20. Maurya RP, Srivastav T, Singh VP, Mishra CP, Al-Mujaini A. The epidemiology of ocular trauma in Northern India: A teaching hospital study. *Oman J Ophthalmol* 2019;12:78–83.
21. Lee CH, Lee L, Kao LY, Lin KK, Yang ML. Prognostic indicators of open globe injuries in children. *Am J Emerg Med* 2009;27:530–535.
22. Xu YN, Huang YS, Xie LX. Pediatric traumatic cataract and surgery outcomes in eastern China: A hospital-based study. *Int J Ophthalmol* 2013;6:160–164.
23. Dulal S, Ale JB, Sapkota YD. Profile of pediatric ocular trauma in mid western hilly region of Nepal. *Nepal J Ophthalmol* 2012;4:134–137.
24. Gunes A, Kalayc M, Genc O, Ozerturk Y. Characteristics of open globe injuries in preschool children. *Pediatr Emerg Care* 2015;31:701–703.
25. Skiker H, Laghmari M, Boutimzine N, Ibrahimy W, Benharbit M, Ouazani B, et al. [Open globe injuries in children: Retrospective study of 62 cases]. *Bull Soc Belge Ophtalmol* 2007:57–61.
26. Tok O, Tok L, Ozkaya D, Eraslan E, Ornek F, Bardak Y. Epidemiological characteristics and visual outcome after open globe injuries in children. *J AAPOS* 2011;15:556–561.
27. Court JH, Lu LM, Wang N, McGhee CNJ. Visual and ocular morbidity in severe open-globe injuries presenting to a regional eye centre in New Zealand. *Clin Exp Ophthalmol* 2019;47:469–477.
28. Zhang T, Zhuang H, Wang K, Xu G. Clinical features and surgical outcomes of posterior segment intraocular foreign bodies in children in east China. *J Ophthalmol* 2018;2018:5861043.
29. Jandeck C, Kellner U, Bornfeld N, Foerster MH. Open globe injuries in children. *Graefes Arch Clin Exp Ophthalmol* 2000;238:420–426.
30. El-Sebaity DM, Soliman W, Soliman AM, Fathalla AM. Pediatric eye injuries in upper Egypt. *Clin Ophthalmol* 2011;5:1417–1423.
31. Zheng L, Tan J, Liu R, Yang X, He H, Xiao H, et al. The impact of primary treatment on post-traumatic endophthalmitis in children with open globe injuries: A study in China. *Int J Environ Res Public Health* 2019;16.
32. Abouammoh MA, Al-Mousa A, Gogandi M, Al-Mezaine H, Osman E, Alsharidah AM, et al. Prophylactic intravitreal antibiotics reduce the risk of post-traumatic endophthalmitis after repair of open globe injuries. *Acta Ophthalmol* 2018;96:e361–e365.
33. Schmidseder E, de Kaspar HM, Kampik A, Klauß V. Post-traumatic endophthalmitis after penetrating eye injury. Risk factors, microbiological diagnosis and functional outcome. *Ophthalmologe* 1998;95:153–157.
34. Dehghani AR, Rezaei L, Salam H, Mohammadi Z, Mahboubi M. Post traumatic endophthalmitis: Incidence and risk factors. *Glob J Health Sci* 2014;6:68–72.
35. Ahmed Y, Schimel A, Pathengay A, Colyer M, Flynn HW. Endophthalmitis following open-globe injuries. *Eye* 2012;26:212–217.
36. Ozturk T, Cetin Dora G, Ayhan Z, Kaya M, Arikan G, Yaman A. Etiology and visual prognosis in open globe injuries: Results of a tertiary referral center in Turkey. *Sci Rep* 2019;9:17977.

Review Article

# Clinical Applications of Artificial Intelligence in Glaucoma

**Siamak Yousefi, PhD**

*Department of Ophthalmology, University of Tennessee Health Science Center, Memphis, TN, USA*
*Department of Genetics, Genomics, and Informatics, University of Tennessee Health Science Center, Memphis, TN, USA*

**ORCID:**
*Siamak Yousefi: https://orcid.org/0000-0001-8633-5730*

## Abstract

Ophthalmology is one of the major imaging-intensive fields of medicine and thus has potential for extensive applications of artificial intelligence (AI) to advance diagnosis, drug efficacy, and other treatment-related aspects of ocular disease. AI has made impressive progress in ophthalmology within the past few years and two autonomous AI-enabled systems have received US regulatory approvals for autonomously screening for mid-level or advanced diabetic retinopathy and macular edema. While no autonomous AI-enabled system for glaucoma screening has yet received US regulatory approval, numerous assistive AI-enabled software tools are already employed in commercialized instruments for quantifying retinal images and visual fields to augment glaucoma research and clinical practice. In this literature review (non-systematic), we provide an overview of AI applications in glaucoma, and highlight some limitations and considerations for AI integration and adoption into clinical practice.

**Keywords:** Artificial Intelligence; Convolutional Neural Network (CNN); Deep Learning; Glaucoma; Machine Learning; Ophthalmology

*J Ophthalmic Vis Res* 2023; 18 (1): 97–112

## INTRODUCTION

Artificial Intelligence (AI) applications in ophthalmology have shown significant advancements due mainly to the availability of computational platforms, generation of large annotated ocular images, and emergence of AI algorithms. Several landmark studies have highlighted the effectiveness of AI applications in screening, referral, and diagnosis of different ocular conditions.[1–3]

**Correspondence to:**
Siamak Yousefi, PhD. 930 Madison Ave., Suite 726, Memphis, TN 38163, USA.
E-mail: siamak.yousefi@uthsc.edu

Received: 16-10-2022 Accepted: 05-11-2022

Access this article online

**Website:** https://knepublishing.com/index.php/JOVR

**DOI:** 10.18502/jovr.v18i1.12730

AI is a broad term encompassing a wide range of subfields including image processing and expert systems, in which models are preprogrammed and thus require domain knowledge (i.e., human expertise to guide the programmer). In contrast, another subfield of AI, machine learning, can learn from data and identify the outcome of new circumstances without being explicitly programmed. Machine learning models can be further sub-divided to include *supervised learning* in which the label of data is available

This is an open access article distributed under the Creative Commons Attribution License, which permits unrestricted use, distribution, and reproduction in any medium, provided the original work is properly cited.

**How to cite this article:** Yousefi S. Clinical Applications of Artificial Intelligence in Glaucoma. J Ophthalmic Vis Res 2023;18:97–112.

and *unsupervised learning* in which the labels of the data are unknown. *Deep convolutional neural networks* (CNNs) are supervised machine learning models that utilize a stack of hidden layers composed of artificial neurons to emulate human brain in the learning and recognizing process.

Figure 1 shows a broad timeline of major retinal imaging instruments and AI applications in glaucoma. The ophthalmoscope was invented by Helmholtz in the 1850s, which revolutionized ophthalmology, as it allowed direct visualization of the retina and optic disc. Introduction of fundus photography in the 1910s allowed documentation of the status of the retina, thus enhancing the monitoring and management of glaucoma patients. AI was born in the 1940s and some researchers attempted to apply some AI techniques, including classical image processing, to locate the optic disc in retinal frames generated from a television ophthalmoscope in 1950s. However, it was not until the 1980s that some expert systems were applied to retinal images to quantify optic disc properties useful in detecting glaucoma. Subsequently, AI models have been broadly applied to different aspects of glaucoma including retinal and optic nerve image and visual field (VF) quantification, screening, referral, diagnosis, forecasting (prediction), prognosis, and monitoring.

Early machine learning models in glaucoma were based on neural networks and attempted to diagnose glaucoma from VFs in the 1990s.[4, 5] Thereafter, various machine learning models were applied to diagnose glaucoma based on fundus photographs, optical coherence tomography (OCT), OCT angiography, and other ocular and demographic parameters, followed by various deep learning models in the 2010s.[6]–[31]

## METHODS

In this review, we used search combinations of "artificial intelligence", "machine learning", "neural networks", "deep learning", "glaucoma screening", "glaucoma diagnosis", "glaucoma progression", "segmentation", and "image annotation" in Google and PubMed to review broad applications of AI in glaucoma. We categorized AI applications in glaucoma into four major groups: (1) applications in retinal imaging and VF quantification; (2) applications in screening, referral, diagnosis, and forecasting (prediction); (3) applications in monitoring and progression detection; and (4) applications in estimating functional parameters from structural factors. We then highlighted some of the limitations and challenges of integrating these AI models into clinical care.

## AI in Glaucoma Image and Data Quantification, and Characterization

Retinal imaging and VF testing in conjunction with clinical examinations form the primary basis for assessment and diagnosis of glaucoma.[32] While *color fundus photography* has long been used to document retinal status, recent *OCT imaging* provided three-dimensional views of retinal layers and optic nerve head structures.[33] In addition to these modalities, functional assessment typically performed via *standard automated perimetry (SAP)*[34] has remained a standard practice for diagnosis and prognosis of visual function in patients with glaucoma.[34, 35] These three imaging modalities comprise the major components of glaucoma assessment. As such, improvements in the quantification and characterization of retinal images and VFs could promote objectivity, improve consistency in glaucoma assessment, and set a common ground for research and clinical practice. For instance, interpreting vertical cup-to-disc ratio (CDR) may facilitate glaucoma diagnosis[36] as CDR is a major risk factor; likewise, monitoring RNFL thickness may facilitate prognosis as thinning of RNFL is a hallmark of glaucoma progression.[37] Quantification of VFs in the form of glaucoma-induced patterns of VF loss could also facilitate diagnosis and assist therapy adjustment and prognosis plan optimization based on the shape, type, and depth of defect with consideration of the patient's quality of the life.[38]

AI models have been proposed to quantify retinal images as early as the 1950s [Figure 1 & Figure 2: top row]. In conventional AI models (image processing and expert systems), the role of human expertise in hand-crafting algorithms to quantify glaucoma-induced changes and lesions from retinal images was critical. For instance, optic disc and cup boundaries were automatically detected based on various classical image processing techniques that typically require human expertise in the process. Retinal fundus image processing usually requires pre-processing steps to prepare and enhance the image for feature

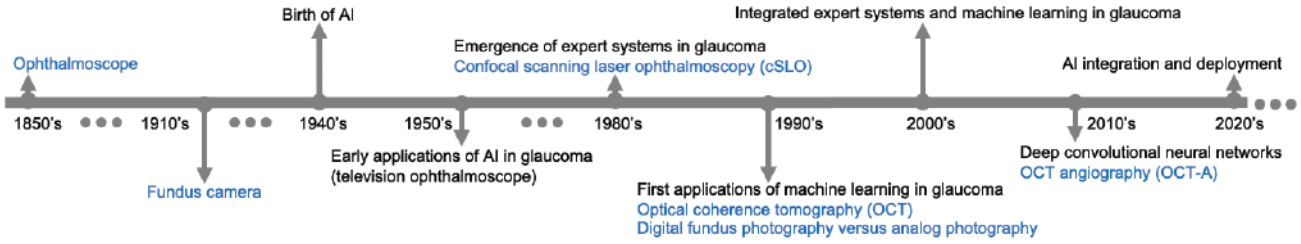


**Figure 1.** Timeline of major retinal imaging instruments and landmark artificial intelligence applications in glaucoma. Introduction of landmark imaging instruments are listed in blue and AI events are provided in black.
AI, artificial intelligence; OCT, optical coherence tomography; OCTA, OCT angiography.

extraction (identifying landmarks). Many of the image processing techniques include histograms equalization and morphological (shape) filtering, and active contours. More involved processes such as gradient vector flow was used to delineate optic disc and cup boundaries in early AI models.[6] As CDR is a major glaucoma risk factor, many of the follow-up AI models focused on localization and quantification of the optic disc and cup in fundus photographs to identify CDR. Hoover et al localized and quantified optic disc and cup based on the information derived from blood vessels.[39] Chrastek et al suggested an automated model for ONH segmentation and quantification based on morphological operations, Hough transform, and active contours.[11] Wong et al used several classical image processing steps to segment the optic cup and disc from retinal images then used a fusion network to combine quantified parameters and subsequently employed an SVM classifier to discriminate normal eyes from glaucomatous eyes.[40] Follow-up studies on fundus photographs also have applied broad classical image processing techniques including edge detection, morphological filtering, adaptive deformable filters, and active contours to quantify optic disc characteristics to assist glaucoma diagnosis [Figure 2: third row).41-45

Emerging deep CNN models however changed the paradigm from manual feature engineering to automatic end-to-end quantification of color fundus images (Fig. 2: fourth row]. One of the first applications of deep learning in quantifying optic disc and cup from fundus photographs was introduced in 2015.[12] They developed a deep learning model using two publicly available datasets of fundus images and segmented optic disc and cup and computed the degree of vessel kinking integrated with prior knowledge about retinal structures to quantify fundus images. Other models have obtained AUCs up to 0.92 in detecting glaucoma from the quantified retina and ONH characteristics based on fundus images.[46]

Fundus photographs were traditionally used to document retinal structure. However, with the introduction of OCT[47] in the 1990s, this modality soon became popular and is now an indispensable component of glaucoma assessment.[33] OCT quantification is thus highly rewarding yet challenging because OCT provides a significantly lower resolution compared to color fundus photographs, and lesions and characteristics are not typically as obvious as those in fundus photographs. Moreover, the shadows generated due to blood vessels pose additional quantification challenges.[33, 48] Nevertheless, OCT provides substantial retinal structural information in three dimensions and its quantification can be highly useful. For these reasons, OCT quantification and interpretation has always been an active area of research since its invention. Like color fundus photographs, the conventional AI methods to quantify OCT images typically include classical image preprocessing techniques such as linear or non-linear filtering, edge detection, and local texture analysis. Koozekanani et al developed an algorithm for OCT retinal layer segmentation based on classical edge detection and Markov modeling. Based on 1450 OCT B-scans, the derived retinal thickness measurements deviated from the ground truth thicknessed by less than 10 microns for ~74% of the B-scans and by less than 25 micron for ~99% of the B-scans.[49] Ishikawa et al proposed an algorithm based on adaptive thresholding technique to segment macular OCT images and subsequently used quantified parameters to diagnose glaucoma. Based on a dataset with about 60 OCT images, they obtained

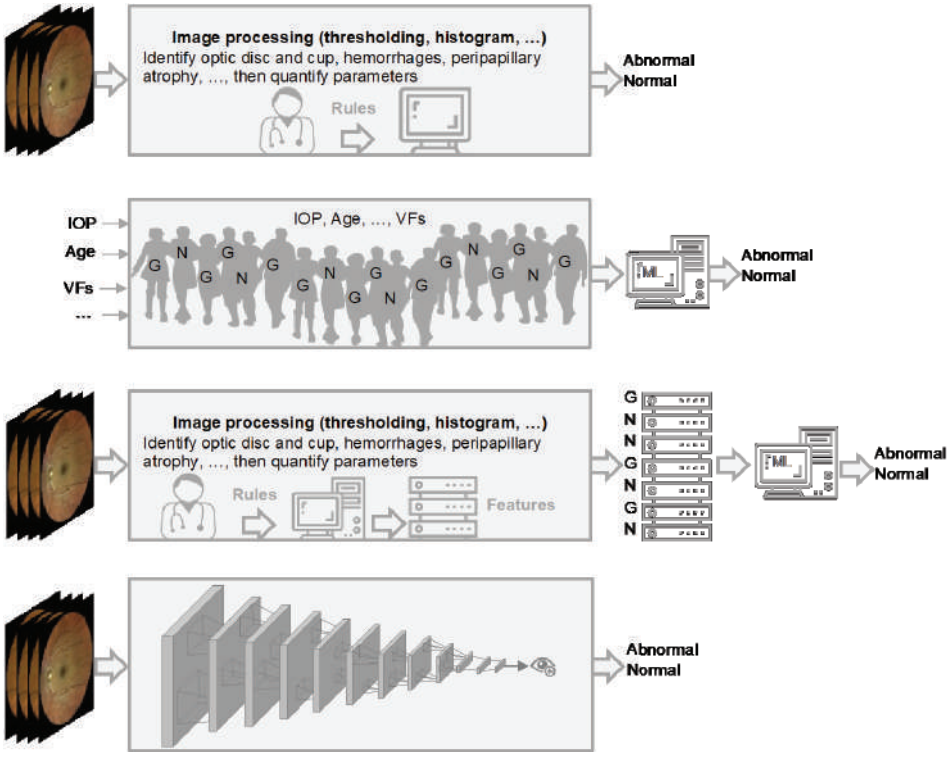


**Figure 2.** Evolution of AI in glaucoma. **First row**: Image processing and expert systems were used to identify glaucoma landmarks or features (such as cup-to-disc ratio or hemorrhages) from retinal images with the assistance of a glaucoma specialist and glaucoma landmarks are identified. **Second row**: Numerical parameters like raw visual fields (VFs), intraocular pressure (IOP), and age from normal and glaucomatous subjects (presented as *N* and *G*) are input to a conventional machine learning model (e.g., neural network) without glaucoma specialist assistance and diagnosis is made. **Third row**: Image processing and expert systems were used to quantify glaucoma landmarks (extract features) with the assistance of a glaucoma specialist then quantified parameters (features) from normal and glaucomatous subjects are fed to a conventional machine learning model to make diagnosis. **Fourth row**: Retinal image is fed to an end-to-end deep learning model and the diagnosis is made without assistance from a glaucoma specialist.

AUCs up to 0.97 for discriminating normal eyes from eyes with established glaucoma.[50] Follow-up models further improved the segmentation accuracy. For example, Kafieh et al developed an OCT segmentation model based on local image textures and diffusion mapping to quantify retinal layers. They evaluated their model using 23 OCT images collected from normal and glaucomatous eyes and obtained retinal layer quantifications with lower than ~8 microns of thickness error.[51]

Emerging deep CNN models however have transformed OCT image quantification from manual feature extraction and annotation to automatic end-to-end quantification. Recent deep learning models provide detailed quantifications of OCT layers as well as information regarding existing pathologies and underlying ocular condition.[13]–[17, 52, 53]

In terms of VFs, various methods have been proposed to summarize, quantify, and annotate VFs. Garway-Heath et al[54] developed a model to map VF test locations on optic nerve structure to better quantify the relationship between localized VF and retinal nerve fiber layer (RNFL) loss. Some groups focused on identifying local patterns of glaucomatous VF loss then classifying and quantifying the severity levels based on subjective assessments.[55, 56] However, manual identification and classification of VF patterns is labor-intensive and requires high levels of expertise that may be prone to inter-and intra-reader variability.[57, 58] Subsequently, numerous automated models based on conventional machine learning approaches were proposed to identify and classify patterns of VF defect using unsupervised Gaussian mixture modeling (GMM), archetypal analysis, or deep archetypal analysis.[22]–[31] Most of the AI models for quantifying and annotating VFs are based on conventional unsupervised learning. Figure 3 shows how classical archetypal analysis applied

can be used to decompose VFs into 18 prevalent patterns of VF loss [Figure 3: top panel] and decomposition of OCT circle scans to 16 prevalent patterns of RNFL loss [Figure 3: bottom panel]. Such a model can decompose VF or OCT data to a weighted combination of these prevalent patterns and even be used for subsequent detection of glaucoma progression.[22]–[31]

In terms of clinical applications, most of the commercially available OCT imaging instruments provide some level of OCT image quantification, interpretation, and visualization. The widely used Humphrey VF analyzer provides several summary parameters including mean deviation (MD), pattern standard deviation (PSD), and visual field index (VFI), and regional parameters such as glaucoma hemifield test (GHT). However, this is not the case for most (if not all) fundus cameras. But, as OCT is predominantly used in glaucoma clinical care, color fundus photograph quantification may not be a major limitation in clinical applications. Nevertheless, fundus cameras are usually cheaper and more portable than current commercialized OCT instruments, and thus may be more appropriate for community-based glaucoma screening. Thus, while innovative AI models may be applied to OCT and VF data to provide more objective and consistent parameters in glaucoma clinical practice, AI may augment color fundus photography in quantifying more specific and sensitive parameters to enhance community-based and glaucoma screening programs.

### *Clinical considerations*

The effectiveness of using optic nerve characteristics in detecting glaucoma has been investigated extensively. Damms et al observed that vertical CDR best suits glaucoma screening, whereas the rim area is more appropriate for detecting progression.[59] A follow-up study, however, found that localized rim area led to the highest specificity of 90% and sensitivity of 91% for discriminating glaucoma from normal eyes based on computerized raster tomography.[60] A recent study suggested vertical CDR as the most important feature for diagnosing glaucoma based on color fundus photographs.[36] Therefore, more accurate quantification of parameters such as CDR and RNFL thickness profiles may augment clinical care and improve more objective glaucoma assessment and diagnosis. Moreover, tracking the quantified parameters over time may facilitate a more objective and accurate monitoring and progression detection.

## Applications of AI in Glaucoma Screening, Referral, Diagnosis, and Forecasting

While the first applications of image processing in glaucoma dates back to the1950s, the first applications of machine learning models in glaucoma dates to the 1990s when several teams applied neural networks to VFs for glaucoma diagnose [Figure 2: second row].[4, 5] Numerous follow-up neural network-based models were proposed to diagnose glaucoma based on VFs.[61]–[64] As VFs were composed of numerical values of threshold sensitivity or total deviations, they provided the optimal input to neural networks which may explain the extensive utility of early neural network models for glaucoma diagnosis based on VFs. A study conducted by Chan and colleagues compared several machine learning models including multilayer perceptron (MLP), support vector machine (SVM), linear and quadratic discriminant analysis, mixture of Gaussian (MOG), and mixture of generalized Gaussian (MGG) in diagnosing glaucoma based on VFs and found that machine-learning-type classifiers provided higher accuracy compared to best VF indexes from the STATPAC software in diagnosing glaucoma.[7] Other teams utilized various machine learning classifiers such as SVM, discriminant analysis, bagging, and ensemble learning to identify glaucoma based on VFs.[8]–[10]

Raw VFs provide a small grid of numbers (typically fewer than 9*9), thus, in contrast to color fundus and OCT images, VFs are basically inappropriate for deep CNN analysis. As such, some researchers have applied deep CNN models on VF printouts (reports) rather than raw VF numbers. Li et al developed a deep CNN model based on over 4000 VF printouts and obtained an AUC up to about 0.87 in differentiating normal from glaucomatous VF while an SVM model achieved an AUC of 0.67 and glaucoma experts achieved an AUC up to 0.62.[65] A recent deep CNN models utilized over 16,000 VFs and obtained AUCs up to 0.93 for diagnosing glaucoma.[66]

Glaucoma is characterized by progressive structural loss of retinal ganglion cells (RGCs), therefore structural evaluation is a critical step

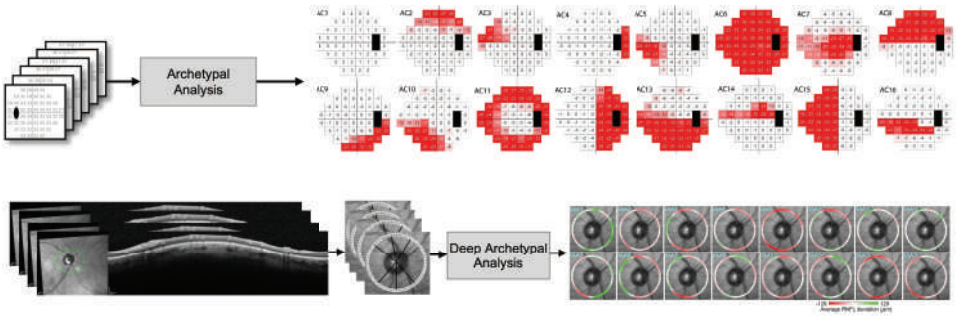


**Figure 3.** Visual field (VF) and optical coherence tomography (OCT) image quantification. Top: VFs were quantified to 18 prominent patterns of VF loss based on classical archetypal analysis. Bottom: OCT circle scans were quantified to 16 patterns of RNFL loss based on deep archetypal analysis.

in glaucoma assessment. Some early studies showed that RVM and SVM classifiers can discriminate glaucoma from normal eyes using RNFL thickness measurements derived from scanning laser polarimetry (SLP) instruments with AUROCs of up to 0.94.[67] Others generated ONH parameters (after a manual outlining of the optic disk border) such as cup's volume, depth, and shape as well as rim's characteristics from CSLO instruments to diagnose glaucoma.[68] While AI models were applied to SLP or cSLO-derived ONH and RNFL parameters (generated by the instruments), diagnostic AI models based on color fundus images were more involved as instruments typically did not provide quantified parameters. As a result, the AI models were required to first quantify characteristics (extract features) then learn those quantified features for glaucoma diagnosis. Bock et al developed image processing models (conventional AI) for glaucoma screening that first preprocessed color fundus photographs and generated different generic features and then performed dimension reduction to lower the number of features. These features were then combined, and a glaucoma risk index was generated, which achieved an AUC of 0.88 in screening glaucoma.[69] Other AI models used a combination of texture and higher order spectra features from color fundus photographs, then employed numerous machine learning models including SVM, naive Bayesian, and random-forest and obtained an accuracy up to 91% based on the random-forest classifier.[70] Cheng et al first segmented the optic disc and cup using histograms of pixel intensities, neighbor statistics, and incorporation of location pixel information to first compute CDR for glaucoma screening and thus obtained AUCs up to 0.82 based on two independent datasets.[71] More complex learning processes such as multi-task learning has been used to detect glaucoma and several other ocular conditions from fundus photographs.[72]

Deep learning models could, however, learn complex glaucoma features using several layers of neurons in an end-to-end process. One of the first deep CNN models in glaucoma used a network with four convolutional layers and two fully connected layers. This model obtained AUCs up to 0.88 for detecting glaucoma from fundus photographs based on two different publicly available datasets.[73] Some of the recent deep CNN models applied to fundus photographs have reached AUROCs up to 0.99 for glaucoma diagnosis.[74–76, 78] Other deep learning models have obtained AUC up to about 0.97 for glaucoma screening and AUC up to 0.94 for glaucoma referral.[36, 79] A recent meta-analysis paper analyzed the accuracy of seventeen deep learning-based studies that utilized 30 different patient cohorts and reported an AUC of 0.93 (95% CI 0.92–0.94) for diagnosing glaucoma based on color fundus photographs.[80]

As OCT has become a dominant imaging modality for glaucoma assessment,[33] numerous teams have explored the utility of glaucoma diagnosis based on OCT. Some studies have shown the usefulness of the OCT-derived RNFL parameters in distinguishing normal eyes from eyes with glaucoma without the utilization of AI models. Based on 94 normal subjects and patients with early glaucoma, Bowd et al obtained an AUC of 0.91 using COT parameters and showed the accuracy based on OCT was superior to

scanning laser polarimetry (SLP), frequency-doubling technology (FDT), and short-wavelength automated perimetry (SWAP) in discriminating normal eyes from eyes with early glaucoma.[81] Another study used RNFL thickness parameters of 95 age-matched normal and glaucomatous eyes and obtained accuracies up to about 90% in distinguishing normal eyes from glaucomatous eyes based on the commercially available OCT instruments of Stratus and Cirrus (Carl Zeiss Meditec, Dublin, CA).[82] These results were promising, and several follow-up studies showed that OCT can discriminate normal eyes from glaucomatous eyes with AUCs ranging from 0.89 to 0.96 based on RNFL or GCIPL thickness parameters derived from macula or ONH OCT images.[37, 83–87] These studies showed the capability of OCT-derived retinal parameters in diagnosing glaucoma without employing machine learning models.

The capability of machine learning models in improving the diagnostic accuracy for glaucoma based on OCT-derived retinal parameters were investigated further. Burgansky-Eliash et al evaluated five conventional machine learning classifiers including linear discriminant analysis, SVM, recursive partitioning and regression tree, generalized linear model, and generalized additive model based on OCT-derived parameters of 89 normal and glaucomatous eyes and obtained the best AUC of 0.98 (specificity of 95% and sensitivity of 92.5%) for discriminating normal eyes from glaucomatous eyes using an SVM classifier.[88] Follow-up AI models based on OCT-derived RNFL thickness measurements collected from 152 normal and glaucomatous eyes using SVM and ANN machine learning classifiers obtained AUCs up to about 0.99[89] and another neural network-based model evaluated RNFL-derived OCT segmentation strategies and obtained an AUC up to 0.85 for glaucoma diagnosis.[90]

Recent deep CNN models have also been applied to OCT-derived retinal parameters to diagnose glaucoma. Asaoka et al applied a deep learning model on over 4000 grids (8*8) of macular OCT-derived RNFL and ganglion complex layer (GCL) thickness profiles and obtained an AUC about 0.94.[18] Follow-up deep learning models have obtained AUCs up to 0.99 based on OCT-derived retinal parameters.[19–21] Deep learning approaches have also been applied to raw un-segmented OCT images for glaucoma diagnosis. Ran et al developed a multi-task three-dimensional (3D) deep learning model to diagnose glaucoma based on over 8000 raw volumetric OCT scans collected from multiple institutes and obtained AUCs in the range of 0.86 to 0.90.[91] A recent meta-analysis investigated five different deep learning studies that analyzed six cohorts of OCT and reported an AUC of about 0.96 (95% CI 0.94–0.99) for diagnosing glaucoma based on deep learning models. When averaged across the cohorts, the pooled sensitivity was 0.94 (95% CI 0.92–0.96) and pooled specificity was 0.95 (95% CI 0.91–0.97).[80]

Machine learning models have been applied to other retinal imaging modalities as well. OCT angiography (OCTA), a recent imaging technology in ophthalmology, provides high-resolution images of retinal vasculature structure and function that are appropriate for deep learning models.[92] OCTA-derived vasculature parameters have shown great promise in discriminating normal eyes from glaucomatous eyes without using any AI model.[93–95] As OCAT is a newer technology, a limited number of AI models have explored this modality to date. A recent study investigated the capability of deep learning and conventional machine learning classifiers to diagnose glaucoma based on 405 OCTA images and quantified parameters. The best AUC of the gradient boosting classifier (GBC) model based on quantified OCTA parameters was 0.89 while a deep learning model based on a VGG16 architecture achieved an AUC of 0.93 based on radial peripapillary capillary en face OCTA images of the ONH.

Most applications of AI models have been centered around glaucoma detection for screening and diagnosis purposes, while forecasting glaucoma could play an important role in identifying those with future disease development and potential vision loss. Thakur et al developed a deep learning model based on over 60,000 fundus photographs to forecast glaucoma before disease development. They achieved AUCs up to approximately 0.77 and 0.88 for forecasting glaucoma four to seven years and one to three years before onset, respectively. Their model achieved an AUC of about 0.95 once tested to diagnose glaucoma.[77] Other forecasting models are usually centered around predicting future VF or OCT parameters. Wen et al developed a model to forecast future VF tests (up to 5.5 years) from current VF tests using deep learning based on more than 30,000 VFs and obtained average

point-wise mean absolute errors (MAE) of about 2.5 dB.[96] Sedai and colleagues developed a deep learning model to forecast RNFL thickness measurements from raw OCT and quantified RNFL thickness measurements, VFs, and clinical data collected from multiple visits, and reached mean MAEs as low as about 1.8 micron in estimating global RNFL thickness across normal eyes, and eyes with suspect and established glaucoma.[97] Such validated models may facilitate personalized patient care by determining the most appropriate inter-visit schedule for timely interventions.

### *Clinical considerations*

While two autonomous AI-enabled models have received US FDA approvals for screening diabetic retinopathy and macular edema,[98, 99] no autonomous AI models have yet received FDA approval in glaucoma screening, diagnosis, or prognosis. It should be noted that most of the commercially available VF and OCT instruments already include some AI-enabled quantification and interpretation tools, and the evidence summarized above, strongly suggests that autonomous AI models would be warranted for glaucoma screening, diagnosis, and forecasting. Assistive AI models may benefit glaucoma clinical practice and augment clinical assessment while autonomous AI models may provide greater benefit to population-based screening. Nevertheless, various hurdles remain for full development and integration of assistive and autonomous AI models in glaucoma, as discussed in Section 6.

## Applications of AI in Glaucoma Prognosis and Monitoring

Detecting glaucoma-induced structural and functional loss is critical for preserving vision and maintaining quality of life of patients with glaucoma. However, identifying glaucoma-induced vision changes by inspecting a sequence of fundus photographs, OCT images, and VFs can be perplexing at both ends of the glaucoma spectrum - in the early stages of the disease, where structural and functional deficits are subtle; or in the late stage of the disease, where OCT is unable to provide required dynamic ranges (flooring effect) and VF presents significant VF variability.[100, 101] Early methods for detecting glaucoma progression introduced in the 1990s include: Advanced Glaucoma Intervention Study (AGIS) criteria;[102] Collaborative Initial Glaucoma Treatment Study (CIGTS) criteria,[103] and the widely used Guided Progression Analysis (GPA).[35] All these models provided event-based approaches utilizing ad-hoc rules to detect VF progression.

Point-wise linear regression (PLR)[104] and Permutation of PLR (PoPLR)[105] have provided trend-based approaches utilizing linear regression to identify VF progression. Other follow-up models used statistical analysis of summary or regional parameters such as VFI or mean deviation (MD) to detect glaucoma progression based on VFs.[106–108] More complex models based on structure–function relationship using dynamic estimates of the current glaucoma state and velocity of progression over time showed improved accuracy over the ordinary linear regression approaches.[108] These methods have used mathematical and statical approaches to detect progression.

Lin et al introduced one of the first applications of machine learning models in detecting glaucomatous progression based on VFs.[109] They obtained an AUC of 0.92 (average specificity and sensitivity of 88% and 86%, respectively) using a neural network with three hidden layers. Sample et al introduced one of the first unsupervised machine learning-based models to detect glaucoma progression.[110] They developed an unsupervised variational Bayesian model and identified several prominent patterns of VF loss. They identified the progression of glaucoma across these patterns. Most of the follow-up machine learning models also used unsupervised machine learning models to analyze VFs.[25, 28, 111, 112] As VF testing was an older technology compared to OCT, most of the early glaucoma progression models have been applied to VFs.

Wollstein et al investigated the utility of OCT-derived RNFL thickness measurements in detecting glaucoma progression and reported that OCT was more sensitive than VF in detecting glaucomatous progression.[113] Similarly, other studies also showed the utility of OCT in detecting glaucoma progression.[114] Yousefi et al evaluated the usefulness of several supervised machine learning models to detect glaucoma based on VFs and OCT parameters and reported the superiority of OCT in detecting glaucoma progression compared with VFs.[115] While unsupervised

archetypal analysis has been used for detecting glaucoma progression,[116] a recent study used deep archetypal analysis to identify patterns of VF loss and then used some of those patterns for detecting ocular hypertensive patients with future rapid glaucoma progression (rate of MD loss faster than –1 dB/year).[117] The application of deep CNN models in detecting glaucoma progression, however, has been limited. A recent study showed the effectiveness of a convolutional long short-term memory (LSTM) neural network that was trained and tested on over 670,000 VFs in identifying glaucoma progression from VFs with AUCs from 0.79 to 0.82.[118]

### *Clinical considerations*

Most of the early applications of AI in detecting glaucoma progression have been focused on VFs. This may be explained by two facts. First, the longer existence of VF testing technology in glaucoma care has resulted in the availability of more datasets with longer follow ups (compared to OCT). Second, VFs are already in numeric format and appropriate for most conventional machine learning models which is not the case for fundus images. AI-enabled models for detecting glaucoma progression based on fundus images do exist, but they are rare. This may reflect the fact that quantification of fundus images to provide appropriate input for most conventional machine learning models was challenging. In contrast to fundus imaging, OCT imaging already includes quantification such as retinal thickness profiles that are appropriate for most conventional machine learning models. With the advancement of deep learning models however, more innovative AI models would be desirable in order to fully exploit color fundus photographs as well as raw OCT images for detecting glaucoma progression in clinical practice.

Most current progression detection models utilize statistical approaches based on linear regression, and assume that glaucoma progresses linearly, while there is evidence that glaucomatous progression may be non-linear and rapid, particularly during the later stages.[119, 120] Additionally, most of these methods provide only information of whether the eye is progressed or not, without supplemental information on the type of pattern of loss. Therefore, unsupervised machine learning models may offer unbiased analysis of progression and provide explainable outcomes with information on local patterns of loss, rather than a sole binary outcome. As glaucoma is a multifactorial disease caused by a complex interaction of multiple factors, using a comprehensive set of input information may facilitate detection of glaucoma progression. However, no instrument/device yet provides a comprehensive analysis of glaucoma progression based on combined imaging and VF data along with ocular, clinical, and demographic factors. This is an unmet need and future AI models may facilitate detection of glaucoma using multiple sources of information.

## Applications of AI in Estimating Functional Parameters from Structural Factors

Advancements in AI models in glaucoma have posed critical questions regarding the feasibility of using objective OCT measurements to assess and monitor visual functional loss. A successful solution may replace subjective and tedious VF testing with objective and quick OCT imaging for glaucoma assessment. To that end, numerous teams have attempted to estimate global, regional, and point-wise VF parameters from raw OCT or OCT-derived measurements based on statistical models or machine learning approaches.[121–123] Some recent studies have utilized deep learning models to estimate global and local VF damage from raw OCT scans and quantified thickness measurements.[124–126] These studies have used scanning laser polarimetry (SLP)-derived RNFL thickness measurements to estimate VF threshold sensitives based on linear and non-linear regression, and obtained approximately 3.9 dB errors (Zhu et al),[121] OCT-derived retinal parameters to estimate VF sensitivities based on support vector regressor machines and achieved a root mean square error (RMSE) of about 3.7 dB,[122] OCT-derived RNFL to estimate VF sensitivities based on deep learning models and obtained RMSE of about 6.1 dB,[124] OCT-derived RNFL thickness measurements to estimate global VF mean deviation (MD) based on deep learning and achieved MAE of about 2.9 dB,[125] raw OCT images from macula and optic disc to estimate VF global parameters based on 3-D deep learning models and obtained RMSE about 2.4 dB and MAE of about 2.3 dB.[126] A follow-up model used an artificial neural network (ANN) model to estimate MD from OCT-derived RNFL parameters based

on four independent large datasets from different races, different instruments, and different scanning types and obtained MAE of about 4.0 dB and RMSE of approximately 5.2 dB with reasonable generalizability on other datasets.[127]

### *Clinical considerations*

Validated AI models may replace VF testing that can be tedious, subjective, and highly variable at later stages of the disease, with OCT imaging that is more objective, quick, and reproducible. Such models could generate quick outcomes and provide more objective glaucoma assessment. However, most of the current models for predicting VF parameters from OCT have several shortcomings. Some of these models underestimate or overestimate global or local VF parameters at both ends of the glaucoma spectrum. Additionally, while the overall error rate of these models may fall within the VF variability, still lower local error rates are required to reach a reasonable level for clinical applications. Finally, the generalizability of these models needs to be evaluated based on representative clinical data to gain clinical utility.

## Unresolved Challenges and Future Directions

As discussed in previous sections, AI models may perform a wide range of tasks such as retinal image and data annotation and interpretation, diagnosis, and prognosis, in order to enhance glaucoma research and clinical practice. Some of the AI models could generate outcomes more quickly, accurately, and consistently than more standard approaches. However, some of the AI models, particularly deep learning, have several limitations as listed below.

Unstable: Deep learning models could be fragile and sometimes even with slightly modifying (unrelated) regions of retina (e.g., by flipping pixels), the diagnosis outcome of the model may change.

Biased: Embedded bias in data could simply become integrated into the model. An AI model that has been trained on retinal images from glaucoma subjects at later stages will be biased and may simply miss patients at early stages of the disease.

Memory: Models may lose their previous ability if retrained on new data. An AI model that was trained on retinal images from glaucoma patients at the early stages of the disease may lose its capability if retrained on new data from subjects in later stages of the disease. The model may simply forget its previous capabilities.

Unexplainable: While there have been efforts in explaining the outcome of deep learning models, still explainablity is a critical challenge in applications in ophthalmology. Clinicians better trust models that explain reasons why they have made a decision rather than providing a sole binary diagnosis.

Uncertain: Except in rare cases,[128] most deep learning models only provide the likelihood of diagnosis and not certainty. In contrary to human expertise that may be wrong on challenging cases, a deep learning model be wrong on simple cases (provide a high likelihood on a definitely wrong decisions).

Foolish: Despite remarkable outcomes in some applications, deep learning models may make foolish mistakes. For instance, a model that has been developed to diagnose glaucoma based on fundus photographs may say a subject has glaucoma from an irrelevant input picture of the lung, while human experts won't make such simple mistakes.

Addressing some of these challenges are the bases of currently active research areas and innovative solutions are becoming increasingly available. In addition to technical challenges, other limitations have hindered widespread clinical utility of AI and deep learning models in glaucoma clinical practice. Some of these challenges are as follows.

Challenges related to glaucoma definitions:

Inconsistent definition of glaucoma: There is not yet a widespread consensus on glaucoma definition and different studies and guidelines have used different definitions.[129, 130]

Inconsistent definition of glaucoma progression: The problem is even worse for progression as there is no consensus on glaucoma-induced changes as well as a level that constitute a real change.

Challenges related to training and testing AI models:

Most of these reference datasets are annotated by non-ophthalmologists, ophthalmologists, or glaucoma experts with diverse levels of expertise and considerable intra-and inter-rater variability rates. Evaluating AI models based on

different datasets thus leads to different levels of performance.

The datasets may be selective and may not represent a diverse group of patients with different ethnicities, required phenotypes, or different severity levels thus generating selective bias.

Datasets are not from the targeted AI model. For instance, the AI model is for proposed for glaucoma screening, but training data is collected from subjects visiting a tertiary eye hospital.

Challenges related to integration of AI in glaucoma clinical practice:

Performance evaluation: Some of the AI model have reported studies that are not based on AI-related study design and reporting guidelines[131–133] leading to challenges in validating those models.

Acceptable performance (specificity and sensitivity): The required performance level of a model for glaucoma screening is different from a model targeted for glaucoma diagnosis or prognosis. These levels are not well-defined in glaucoma screening and diagnosis. For instance, as glaucoma is a low- prevalence disease, highly specific and sensitive models are required for screening.

In some AI models, it is confusing whether the model is assistive or autonomous and subsequently whether the AI model has been validated logically. While most of the AI models for retinal image quantification and interpretation are assistive AI tools, most of the diagnostic AI models are autonomous in generating a diagnosis. For instance, if a model is assistive, the evaluation phase requires involvement of the physicians/glaucoma specialists as well. Thus, evaluating the AI model alone limits clinical utility.

Other broad challenges related to integration of AI in glaucoma clinical practice:

Standards for oversight of Software: In different countries, it is still challenging to understand who will oversight an AI system in clinical practice? Developers, physicians, clinics, or providers? These need to be elucidated and each country's regulations may impact this differently.

Liability: It is vital to determine who is (are) responsible for a misdiagnosis or missed diagnosis. These are highly dependent on local regulations and legal systems as well.

Ethical considerations: The minimum requirement for AI models is to not to harm patient. The broader view is that these models would also need to benefit patients and improve clinical and patient outcome.

Reimbursement: Issues need to be resolved for reimbursement and revenue sharing with those who are involved in clinical care, if these AI systems are to receive widespread clinical utility.

Sharing and privacy: The minimum requirement for AI models is that they not violate patient safety and privacy. There are several additional aspects to be clarified, including dataset sharing and who owns the datasets used to train AI models.

## Summary

AI has shown tremendous potential in both research and clinical treatment of glaucoma. Various conventional AI and emerging deep learning models have been proposed to quantify retinal images and VFs in order to screen, diagnose, forecast, and prognose glaucoma. Some of the AI assistive models have already been integrated in some glaucoma imaging and VF instruments; however, no autonomous AI model has yet received US regulatory approvals to be used in glaucoma care. While there are many challenges regarding integration of AI in glaucoma clinics, a major challenge is the lack of a widely used reference standard for glaucoma, as most of the AI models are trained based on datasets that are subjectively evaluated based on different definitions of glaucoma or its progression. Other challenges include lack of standardized evaluation and reporting of the performance of AI models, targeted patient populations, and liability and ethical issues. Nevertheless, AI applications can provide major improvements in several important areas including *glaucoma research* by setting common grounds for reproducible factors, screening programs with highly specific and sensitive autonomous models for detecting glaucoma, clinical care with establishing assistive and autonomous glaucoma models for delineating hallmarks and diagnosis, and in clinical trial design by identifying subjects and even offering novel digital endpoints.

## Financial Support and Sponsorship

This work was supported by the National Institute of Health (NIH) grants EY033005, EY031725, and

a Challenge Grant from Research to Prevent Blindness (RPB), New York. The funders had no role in study design, data collection and analysis, decision to publish, or preparation of the manuscript.

## Conflicts of Interest

The author has no relevant conflict of interest to disclose.

## *REFERENCES*


1. Ting DS, Cheung GC, Wong TY. Diabetic retinopathy: Global prevalence, major risk factors, screening practices and public health challenges: A review. *Clin Exp Ophthalmol* 2016;44:260–277.
2. Gulshan V, Peng L, Coram M, Stumpe MC, Wu D, Narayanaswamy A, et al. Development and validation of a deep learning algorithm for detection of diabetic retinopathy in retinal fundus photographs. *JAMA* 2016;316:2402–2410.
3. De Fauw J, Ledsam JR, Romera-Paredes B, Nikolov S, Tomasev N, Blackwell S, et al. Clinically applicable deep learning for diagnosis and referral in retinal disease. *Nat Med* 2018;24:1342–1350.
4. Kelman SE, Perell HF, D'Autrechy L, Scott RJ. A neural network can differentiate glaucoma and optic neuropathy visual fields through pattern recognition. In: Mills RP, Heijl A, editors. Perimetry Update 1990/1991, Proceedings of the IXth International Perimetric Society Meeting. Amsterdam/New York: Kugler Publications; 1991. p. 291–295.
5. Nagata S, Kani K, Sugiyama A. A computer assisted visual field diagnosis system using neural netowrks. In: Mills RP, Heijl A, editors. Perimetry Update 1990/1991, Proceedings of the IXth International Perimetric Society Meeting. Amsterdam/New York: Kugler Publications; 1991. p. 291–295.
6. Mendels F, Heneghan C, Thiran J-P. Identification of the optic disk boundary in retinal images using active contours. 1999.
7. Chan K, Lee TW, Sample PA, Goldbaum MH, Weinreb RN, Sejnowski TJ. Comparison of machine learning and traditional classifiers in glaucoma diagnosis. *IEEE Trans Biomed Eng* 2002;49:963–974.
8. Bengtsson B, Bizios D, Heijl A. Effects of input data on the performance of a neural network in distinguishing normal and glaucomatous visual fields. *Invest Ophthalmol Vis Sci* 2005;46:3730–3736.
9. Bizios D, Heijl A, Bengtsson B. Trained artificial neural network for glaucoma diagnosis using visual field data: A comparison with conventional algorithms. *J Glaucoma* 2007;16:20–28.
10. Wroblewski D, Francis B, Chopra V, Kawji AS, Quiros P, Dustin L, et al. Glaucoma detection and evaluation through pattern recognition in standard automated perimetry data. *Graefes Arch Clin Exp Ophthalmol* 2009;247:1517–1530.
11. Chrastek R, Wolf M, Donath K, Niemann H, Paulus D, Hothorn T, et al. Automated segmentation of the optic nerve head for diagnosis of glaucoma. *Med Image Anal* 2005;9:297–314.
12. Lim G, Cheng Y, Hsu W, Lee ML. Integrated optic disc and cup segmentation with deep learning. Paper presented at: 2015 IEEE 27th International Conference on Tools with Artificial Intelligence (ICTAI); 2015 Nov 9-11 Nov.
13. Lee CS, Tyring AJ, Deruyter NP, Wu Y, Rokem A, Lee AY. Deep-learning based, automated segmentation of macular edema in optical coherence tomography. *Biomed Opt Express* 2017;8:3440–3448.
14. Kugelman J, Alonso-Caneiro D, Read SA, Vincent SJ, Collins MJ. Automatic segmentation of OCT retinal boundaries using recurrent neural networks and graph search. *Biomed Opt Express* 2018;9:5759–5777.
15. Masood S, Fang R, Li P, Li H, Sheng B, Mathavan A, et al. Automatic choroid layer segmentation from optical coherence tomography images using deep learning. *Sci Rep* 2019;9:3058.
16. Zhang H, Yang J, Zhou K, Li F, Hu Y, Zhao Y, et al. Automatic segmentation and visualization of choroid in OCT with knowledge infused deep learning. *IEEE J Biomed Health Inform* 2020;24:3408–3420.
17. Wu Q, Zhang B, Hu Y, Liu B, Cao D, Yang D, et al. Detection of morphologic patterns of diabetic macular edema using a deep learning approach based on optical coherence tomography images. *Retina* 2020.
18. Asaoka R, Murata H, Hirasawa K, Fujino Y, Matsuura M, Miki A, et al. Using deep learning and transfer learning to accurately diagnose early-onset glaucoma from macular optical coherence tomography images. *Am J Ophthalmol* 2019;198:136–145.
19. Lee J, Kim YK, Park KH, Jeoung JW. Diagnosing glaucoma with spectral-domain optical coherence tomography using deep learning classifier. *J Glaucoma* 2020;29:287–294.
20. Ran AR, Cheung CY, Wang X, Chen H, Luo LY, Chan PP, et al. Detection of glaucomatous optic neuropathy with spectral-domain optical coherence tomography: A retrospective training and validation deep-learning analysis. *Lancet Digit Health* 2019;1:e172–e182.
21. Thompson AC, Jammal AA, Berchuck SI, Mariottoni EB, Medeiros FA. Assessment of a segmentation-free deep learning algorithm for diagnosing glaucoma from optical coherence tomography scans. *JAMA Ophthalmol* 2020;138:333–339.
22. Sample PA, Chan K, Boden C, Lee TW, Blumenthal EZ, Weinreb RN, et al. Using unsupervised learning with variational bayesian mixture of factor analysis to identify patterns of glaucomatous visual field defects. *Investig Ophthalmol Vis Sci* 2004;45:2596–2605.
23. Goldbaum MH, Sample PA, Zhang Z, Chan K, Hao J, Lee TW, et al. Using unsupervised learning with independent component analysis to identify patterns of glaucomatous visual field defects. *Investig Ophthalmol Vis Sci* 2005;46:3676–3683.
24. Bowd C, Weinreb RN, Balasubramanian M, Lee I, Jang G, Yousefi S, et al.Glaucomatous patterns in frequency doubling technology (FDT) perimetry data identified by unsupervised machine learning classifiers. *PLoS One* 2014;9:e85941.

25. Yousefi S, Goldbaum MH, Balasubramanian M, Medeiros FA, Zangwill LM, Liebmann JM, et al. Learning from data: Recognizing glaucomatous defect patterns and detecting progression from visual field measurements. *IEEE Trans Biomed Eng* 2014;61:2112–2124.
26. Yousefi S, Goldbaum MH, Zangwill LM, Medeiros FA, Bowd C. Recognizing patterns of visual field loss using unsupervised machine learning. *Proc SPIE Int Soc Opt Eng* 2014;2014:90342M.
27. Elze T, Pasquale LR, Shen LQ, Chen TC, Wiggs JL, Bex PJ. Patterns of functional vision loss in glaucoma determined with archetypal analysis. *J R Soc Interface* 2015;12:20141118.
28. Yousefi S, Balasubramanian M, Goldbaum MH, Medeiros FA, Zangwill LM, Weinreb RN, et al. Unsupervised Gaussian mixture-model with expectation maximization for detecting glaucomatous progression in standard automated perimetry visual fields. *Transl Vis Sci Technol* 2016;5:2.
29. Wang M, Shen LQ, Pasquale LR, Boland MV, Wellik SR, De Moraes CG, et al. Artificial intelligence classification of central visual field patterns in glaucoma. *Ophthalmology.*
30. Thakur A, Goldbaum M, Yousefi S. Convex representations using deep archetypal analysis for predicting glaucoma. *IEEE J Transl Eng Health Med* 2020;8:3800107.
31. Gupta K, Thakur A, Goldbaum M, Yousefi S. Glaucoma precognition: Recognizing preclinical visual functional signs of glaucoma. Paper presented at: 2020 IEEE/CVF Conference on Computer Vision and Pattern Recognition Workshops (CVPRW); 2020 June 14–19.
32. Nadler Z, Wollstein G, Ishikawa H, Schuman JS. Clinical application of ocular imaging. *Optom Vis Sci* 2012;89:E543–E553.
33. Stein JD, Talwar N, Laverne AM, Nan B, Lichter PR. Trends in use of ancillary glaucoma tests for patients with open-angle glaucoma from 2001 to 2009. *Ophthalmology* 2012;119:748–758.
34. Alencar LM, Medeiros FA. The role of standard automated perimetry and newer functional methods for glaucoma diagnosis and follow-up. *Indian J Ophthalmol* 2011;59:S53–S58.
35. Bengtsson B, Heijl A. A visual field index for calculation of glaucoma rate of progression. *Am J Ophthalmol* 2008;145:343–353.
36. Phene S, Dunn RC, Hammel N, Liu Y, Krause J, Kitade N, et al. Deep learning and glaucoma specialists: The relative importance of optic disc features to predict glaucoma referral in fundus photographs. *Ophthalmology* 2019;126:1627–1639.
37. Bussel, II, Wollstein G, Schuman JS. OCT for glaucoma diagnosis, screening and detection of glaucoma progression. *Br J Ophthalmol* 2014;98:ii15–19.
38. Brusini P, Johnson CA. Staging functional damage in glaucoma: Review of different classification methods. *Surv Ophthalmol* 2007;52:156–179.
39. Hoover A, Goldbaum M. Locating the optic nerve in a retinal image using the fuzzy convergence of the blood vessels. *IEEE Trans Med Imaging* 2003;22:951–958.
40. Wong DW, Liu J, Lim JH, Tan NM, Zhang Z, Lu S, et al. Intelligent fusion of cup-to-disc ratio determination methods for glaucoma detection in ARGALI. *Annu Int Conf IEEE Eng Med Biol Soc* 2009;2009:5777–5780.
41. Aquino A, Gegundez-Arias ME, Marin D. Detecting the optic disc boundary in digital fundus images using morphological, edge detection, and feature extraction techniques. *IEEE Trans Med Imaging* 2010;29:1860–1869.
42. Haleem MS, Han L, Hemert JV, Li B, Fleming A, Pasquale LR, et al. A novel adaptive deformable model for automated optic disc and cup segmentation to aid glaucoma diagnosis. *J Med Syst* 2017;42:20.
43. Hu M, Zhu C, Li X, Xu Y. Optic cup segmentation from fundus images for glaucoma diagnosis. *Bioengineered* 2017;8:21–28.
44. Wang J, Wang Z, Li F, Qu G, Qiao Y, Lv H, et al. Joint retina segmentation and classification for early glaucoma diagnosis. *Biomed Opt Express* 2019;10:2639–2656.
45. Zhou W, Yi Y, Gao Y, Dai J. Optic disc and cup segmentation in retinal images for glaucoma diagnosis by locally statistical active contour model with structure prior. *Comput Math Methods Med* 2019;2019:8973287.
46. Fu H, Cheng J, Xu Y, Zhang C, Wong DWK, Liu J, et al. Disc-aware ensemble network for glaucoma screening from fundus image. *IEEE Trans Med Imaging* 2018;37:2493–2501.
47. Huang D, Swanson EA, Lin CP, Schuman JS, Stinson WG, Chang W, et al. Optical coherence tomography. *Science (New York, NY)* 1991;254:1178–1181.
48. Hood DC, Fortune B, Arthur SN, Xing D, Salant JA, Ritch R, et al. Blood vessel contributions to retinal nerve fiber layer thickness profiles measured with optical coherence tomography. *J Glaucoma* 2008;17:519–528.
49. Koozekanani D, Boyer K, Roberts C. Retinal thickness measurements from optical coherence tomography using a Markov boundary model. *IEEE Trans Med Imaging* 2001;20:900–916.
50. Ishikawa H, Stein DM, Wollstein G, Beaton S, Fujimoto JG, Schuman JS. Macular segmentation with optical coherence tomography. *Invest Ophthalmol Vis Sci* 2005;46:2012–2017.
51. Kafieh R, Rabbani H, Abramoff MD, Sonka M. Intra-retinal layer segmentation of 3D optical coherence tomography using coarse grained diffusion map. *Med Image Anal* 2013;17:907–928.
52. Gu Z, Cheng J, Fu H, Zhou K, Hao H, Zhao Y, et al. CE-Net: Context encoder network for 2D medical image segmentation. *IEEE T Med Imaging* 2019;38:2281–2292.
53. Wilson M, Chopra R, Wilson MZ, Cooper C, MacWilliams P, Liu Y, et al. Validation and clinical applicability of whole-volume automated segmentation of optical coherence tomography in retinal disease using deep learning. *JAMA Ophthalmol* 2021;139:964–973.
54. Garway-Heath DF, Poinoosawmy D, Fitzke FW, Hitchings RA. Mapping the visual field to the optic disc in normal tension glaucoma eyes. *Ophthalmology* 2000;107:1809–1815.
55. Brusini P. Clinical use of a new method for visual field damage classification in glaucoma. *Eur J Ophthalmol* 1996;6:402–407.
56. Keltner JL, Johnson CA, Cello KE, Edwards MA, Bandermann SE, Kass MA, et al. Classification of visual field abnormalities in the ocular hypertension treatment study. *Arch Ophthalmol* 2003;121:643–650.

57. Lichter PR. Variability of expert observers in evaluating the optic disc. *Trans Am Ophthalmol Soc* 1976;74:532–572.
58. Jampel HD, Friedman D, Quigley H, Vitale S, Miller R, Knezevich F, et al. Agreement among glaucoma specialists in assessing progressive disc changes from photographs in open-angle glaucoma patients. *Am J Ophthalmol* 2009;147:39–44 e31.
59. Damms T, Dannheim F. Sensitivity and specificity of optic disc parameters in chronic glaucoma. *Invest Ophthalmol Vis Sci* 1993;34:2246–2250.
60. Gundersen KG, Heijl A, Bengtsson B. Sensitivity and specificity of structural optic disc parameters in chronic glaucoma. *Acta Ophthalmol Scand* 1996;74:120–125.
61. Goldbaum MH, Sample PA, White H, Colt B, Raphaelian P, Fechtner RD, Weinreb RN. Interpretation of automated perimetry for glaucoma by neural network. *Invest Ophthalmol Vis Sci* 1994;35:3362–3373.
62. Madsen EM, Yolton RL. Demonstration of a neural network expert system for recognition of glaucomatous visual field changes. *Mil Med* 1994;159:553–557.
63. Spenceley SE, Henson DB, Bull DR. Visual field analysis using artificial neural networks. *Ophthalmic Physiol Opt* 1994;14:239–248.
64. Lietman T, Eng J, Katz J, Quigley HA. Neural networks for visual field analysis: How do they compare with other algorithms? *J Glaucoma* 1999;8:77–80.
65. Li F, Wang Z, Qu G, Song D, Yuan Y, Xu Y, et al. Automatic differentiation of glaucoma visual field from non-glaucoma visual filed using deep convolutional neural network. *BMC Med Imaging* 2018;18:35.
66. Huang X, Jin K, Zhu J, Xue Y, Si K, Zhang C, et al. A structure-related fine-grained deep learning system with diversity data for universal glaucoma visual field grading. *Front Med* 2022;9:832920.
67. Bowd C, Medeiros FA, Zhang ZH, Zangwill LM, Hao JC, Lee TW, et al. Relevance vector machine and support vector machine classifier analysis of scanning laser polarimetry retinal nerve fiber layer measurements. *Investig Ophthalmol Vis Sci* 2005;46:1322–1329.
68. Burgansky-Eliash Z, Wollstein G, Bilonick RA, Ishikawa H, Kagemann L, Schuman JS. Glaucoma detection with the Heidelberg retina tomograph 3. *Ophthalmology* 2007;114:466–471.
69. Bock R, Meier J, Nyul LG, Hornegger J, Michelson G. Glaucoma risk index: Automated glaucoma detection from color fundus images. *Med Image Anal* 2010;14:471–481.
70. Acharya UR, Dua S, Du X, Sree SV, Chua CK. Automated diagnosis of glaucoma using texture and higher order spectra features. *IEEE Trans Inf Technol Biomed: A publication of the IEEE Eng Med Biol Soc* 2011;15:449–455.
71. Cheng J, Liu J, Xu Y, Yin F, Wong DW, Tan NM, et al. Superpixel classification based optic disc and optic cup segmentation for glaucoma screening. *IEEE Trans Med Imaging* 2013;32:1019–1032.
72. Chen X, Xu Y, Yin F, Zhang Z, Wong DW, Wong TY, et al. Multiple ocular diseases detection based on joint sparse multi-task learning. *Annu Int Conf IEEE Eng Med Biol Soc* 2015;2015:5260–5263.
73. Xiangyu C, Yanwu X, Damon Wing Kee W, Tien Yin W, Jiang L. Glaucoma detection based on deep convolutional neural network. *Annu Int Conf IEEE Eng Med Biol Soc* 2015;2015:715–718.
74. Ting DSW, Cheung CY, Lim G, Tan GSW, Quang ND, Gan A, et al. Development and validation of a deep learning system for diabetic retinopathy and related eye diseases using retinal images from multiethnic populations with diabetes. *JAMA* 2017;318:2211–2223.
75. Li Z, He Y, Keel S, Meng W, Chang RT, He M. Efficacy of a deep learning system for detecting glaucomatous optic neuropathy based on color fundus photographs. *Ophthalmology* 2018;125:1199–1206.
76. Liu H, Li L, Wormstone IM, Qiao C, Zhang C, Liu P, et al. Development and validation of a deep learning system to detect glaucomatous optic neuropathy using fundus photographs. *JAMA Ophthalmol* 2019;137:1353–1360.
77. Thakur A, Goldbaum M, Yousefi S. Predicting glaucoma before onset using deep learning. *Ophthalmol Glaucoma* 2020;3:262–268.
78. Li F, Su Y, Lin F, Li Z, Song Y, Nie S, et al. A deep-learning system predicts glaucoma incidence and progression using retinal photographs. *J Clin Invest* 2022;132:e157968.
79. Liu S, Graham SL, Schulz A, Kalloniatis M, Zangerl B, Cai W, et al. A deep learning-based algorithm identifies glaucomatous discs using monoscopic fundus photographs. *Ophthalmol Glaucoma* 2018;1:15–22.
80. Aggarwal R, Sounderajah V, Martin G, Ting DSW, Karthikesalingam A, King D, et al. Diagnostic accuracy of deep learning in medical imaging: A systematic review and meta-analysis. *NPJ Digit Med* 2021;4:65.
81. Bowd C, Zangwill LM, Berry CC, Blumenthal EZ, Vasile C, Sanchez-Galeana C, et al. Detecting early glaucoma by assessment of retinal nerve fiber layer thickness and visual function. *Invest Ophthalmol Vis Sci* 2001;42:1993–2003.
82. Chang RT, Knight OJ, Feuer WJ, Budenz DL. Sensitivity and specificity of time-domain versus spectral-domain optical coherence tomography in diagnosing early to moderate glaucoma. *Ophthalmology* 2009;116:2294–2299.
83. Xu J, Ishikawa H, Wollstein G, Bilonick RA, Folio LS, Nadler Z, et al. Three-dimensional spectral-domain optical coherence tomography data analysis for glaucoma detection. *PLoS One* 2013;8:e55476.
84. Mwanza JC, Oakley JD, Budenz DL, Anderson DR, Cirrus Optical Coherence Tomography Normative Database Study G. Ability of cirrus HD-OCT optic nerve head parameters to discriminate normal from glaucomatous eyes. *Ophthalmology* 2011;118:241–248 e241.
85. Sung KR, Na JH, Lee Y. Glaucoma diagnostic capabilities of optic nerve head parameters as determined by Cirrus HD optical coherence tomography. *J Glaucoma* 2012;21:498–504.
86. Lisboa R, Paranhos A, Jr., Weinreb RN, Zangwill LM, Leite MT, Medeiros FA. Comparison of different spectral domain OCT scanning protocols for diagnosing preperimetric glaucoma. *Invest Ophthalmol Vis Sci* 2013;54:3417–3425.
87. Hatanaka Y, Muramatsu C, Sawada A, Hara T, Yamamoto T, Fujita H. Glaucoma risk assessment based on clinical data and automated nerve fiber layer defects detection. *Conference proceedings: Annu Int Conf IEEE Eng Med Biol Soc IEEE Eng Med Biol Soc Conf* 2012;2012:5963–5966.
88. Burgansky-Eliash Z, Wollstein G, Chu T, Ramsey JD, Glymour C, Noecker RJ, et al. Optical coherence tomography machine learning classifiers for glaucoma

detection: A preliminary study. *Invest Ophthalmol Vis Sci* 2005;46:4147–4152.

89. Bizios D, Heijl A, Hougaard JL, Bengtsson B. Machine learning classifiers for glaucoma diagnosis based on classification of retinal nerve fibre layer thickness parameters measured by Stratus OCT. *Acta Ophthalmol* 2010;88:44–52.
90. Larrosa JM, Polo V, Ferreras A, Garcia-Martin E, Calvo P, Pablo LE. Neural network analysis of different segmentation strategies of nerve fiber layer assessment for glaucoma diagnosis. *J Glaucoma* 2015;24:672–678.
91. Ran AR, Wang X, Chan PP, Chan NC, Yip W, Young AL, et al. Three-dimensional multi-task deep learning model to detect glaucomatous optic neuropathy and myopic features from optical coherence tomography scans: A retrospective multi-centre study. *Front Med* 2022;9:860574.
92. WuDunn D, Takusagawa HL, Sit AJ, Rosdahl JA, Radhakrishnan S, Hoguet A, et al. OCT angiography for the diagnosis of glaucoma: A report by the American Academy of Ophthalmology. *Ophthalmology* 2021;128:1222–1235.
93. Lee EJ, Lee KM, Lee SH, Kim TW. OCT angiography of the peripapillary retina in primary open-angle glaucoma. *Invest Ophthalmol Vis Sci* 2016;57:6265–6270.
94. Rao HL, Kadambi SV, Weinreb RN, Puttaiah NK, Pradhan ZS, Rao DAS, et al. Diagnostic ability of peripapillary vessel density measurements of optical coherence tomography angiography in primary open-angle and angle-closure glaucoma. *Br J Ophthalmol* 2017;101:1066–1070.
95. Yarmohammadi A, Zangwill LM, Diniz-Filho A, Suh MH, Manalastas PI, Fatehee N, et al. Optical coherence tomography angiography vessel density in healthy, glaucoma suspect, and glaucoma eyes. *Invest Ophthalmol Vis Sci* 2016;57:OCT451–OCT459.
96. Wen JC, Lee CS, Keane PA, Xiao S, Rokem AS, Chen PP, et al. Forecasting future Humphrey visual fields using deep learning. *PLoS One* 2019;14:e0214875.
97. Sedai S, Antony B, Ishikawa H, Wollstein G, Schuman JS, Garnavi R. Forecasting retinal nerve fiber layer thickness from multimodal temporal data incorporating OCT Volumes. *Ophthalmol Glaucoma* 2020;3:14–24.
98. Abramoff MD, Lavin PT, Birch M, Shah N, Folk JC. Pivotal trial of an autonomous AI-based diagnostic system for detection of diabetic retinopathy in primary care offices. *NPJ Digit Med* 2018;1:39.
99. Perez-Rueda A, Jimenez-Rodriguez D, Castro-Luna G. Diagnosis of subclinical keratoconus with a combined model of biomechanical and topographic parameters. *J Clin Med* 2021;10:2746.
100. Henson DB, Chaudry S, Artes PH, Faragher EB, Ansons A. Response variability in the visual field: Comparison of optic neuritis, glaucoma, ocular hypertension, and normal eyes. *Invest Ophthalmol Vis Sci* 2000;41:417–421.
101. Mikelberg FS, Parfitt CM, Swindale NV, Graham SL, Drance SM, Gosine R. Ability of the Heidelberg retina tomograph to detect early glaucomatous visual field loss. *J Glaucoma* 1995;4:242–247.
102. Advanced Glaucoma Intervention Study. 2. Visual field test scoring and reliability. *Ophthalmology* 1994;101:1445–1455.
103. Katz J. Scoring systems for measuring progression of visual field loss in clinical trials of glaucoma treatment. *Ophthalmology* 1999;106:391–395.
104. Gardiner SK, Crabb DP. Examination of different pointwise linear regression methods for determining visual field progression. *Invest Ophthalmol Vis Sci* 2002;43:1400–1407.
105. O'Leary N, Chauhan BC, Artes PH. Visual field progression in glaucoma: Estimating the overall significance of deterioration with permutation analyses of pointwise linear regression (PoPLR). *Invest Ophthalmol Vis Sci* 2012;53:6776–6784.
106. Gardiner SK, Demirel S. Detecting change using standard global perimetric indices in glaucoma. *Am J Ophthalmol* 2017;176:148–156.
107. Zhu H, Russell RA, Saunders LJ, Ceccon S, Garway-Heath DF, Crabb DP. Detecting changes in retinal function: Analysis with non-stationary Weibull error regression and spatial enhancement (ANSWERS). *PLoS One* 2014;9:e85654.
108. Hu R, Marin-Franch I, Racette L. Prediction accuracy of a novel dynamic structure-function model for glaucoma progression. *Invest Ophthalmol Vis Sci* 2014;55:8086–8094.
109. Lin A, Hoffman D, Gaasterland DE, Caprioli J. Neural networks to identify glaucomatous visual field progression. *Am J Ophthalmol* 2003;135:49–54.
110. Sample PA, Boden C, Zhang Z, Pascual J, Lee TW, Zangwill LM, et al. Unsupervised machine learning with independent component analysis to identify areas of progression in glaucomatous visual fields. *Invest Ophthalmol Vis Sci* 2005;46:3684–3692.
111. Goldbaum MH, Lee I, Jang G, Balasubramanian M, Sample PA, Weinreb RN, et al. Progression of patterns (POP): A machine classifier algorithm to identify glaucoma progression in visual fields. *Invest Ophthalmol Vis Sci* 2012;53:6557–6567.
112. Yousefi S, Kiwaki T, Zheng Y, Sugiura H, Asaoka R, Murata H, et al. Detection of longitudinal visual field progression in glaucoma using machine learning. *Am J Ophthalmol* 2018;193:71–79.
113. Wollstein G, Schuman JS, Price LL, Aydin A, Stark PC, Hertzmark E, et al. Optical coherence tomography longitudinal evaluation of retinal nerve fiber layer thickness in glaucoma. *Arch Ophthalmol* 2005;123:464–470.
114. Na JH, Sung KR, Lee JR, Lee KS, Baek S, Kim HK, et al. Detection of glaucomatous progression by spectral-domain optical coherence tomography. *Ophthalmology* 2013;120:1388–1395.
115. Yousefi S, Goldbaum MH, Balasubramanian M, Jung TP, Weinreb RN, Medeiros FA, et al. Glaucoma progression detection using structural retinal nerve fiber layer measurements and functional visual field points. *IEEE Trans Biomed Eng* 2014;61:1143–1154.
116. Wang M, Shen LQ, Pasquale LR, Petrakos P, Formica S, Boland MV, et al. An artificial intelligence approach to detect visual field progression in glaucoma based on spatial pattern analysis. *Invest Ophthalmol Vis Sci* 2019;60:365–375.
117. Yousefi S, Pasquale LR, Boland MV, Johnson CA. Machine-identified patterns of visual field loss and an association

with rapid progression in the ocular hypertension treatment study. *Ophthalmology* 2022;129:1402–1411.

118. Dixit A, Yohannan J, Boland MV. Assessing glaucoma progression using machine learning trained on longitudinal visual field and clinical data. *Ophthalmology* 2020;128:1016–1026.

119. Pathak M, Demirel S, Gardiner SK. Nonlinear trend analysis of longitudinal pointwise visual field sensitivity in suspected and early glaucoma. *Transl Vis Sci Technol* 2015;4:8.

120. Chen A, Nouri-Mahdavi K, Otarola FJ, Yu F, Afifi AA, Caprioli J. Models of glaucomatous visual field loss. *Invest Ophthalmol Vis Sci* 2014;55:7881–7887.

121. Zhu H, Crabb DP, Schlottmann PG, Lemij HG, Reus NJ, Healey PR, et al. Predicting visual function from the measurements of retinal nerve fiber layer structure. *Invest Ophthalmol Vis Sci* 2010;51:5657–5666.

122. Bogunovic H, Kwon YH, Rashid A, Lee K, Critser DB, Garvin MK, et al. Relationships of retinal structure and humphrey 24-2 visual field thresholds in patients with glaucoma. *Invest Ophthalmol Vis Sci* 2014;56:259–271.

123. Guo Z, Kwon YH, Lee K, Wang K, Wahle A, Alward WLM, et al. Optical coherence tomography analysis based prediction of Humphrey 24-2 visual field thresholds in patients with glaucoma. *Invest Ophthalmol Vis Sci* 2017;58:3975–3985.

124. Sugiura H, Kiwaki T, Yousefi S, Murata H, Asaoka R, Yamanishi K. Estimating glaucomatous visual sensitivity from retinal thickness with pattern-based regularization and visualization. *Kdd'18: Proc 24th Acm Sigkdd Int Conf Knowl Discov Data Min* 2018:783–792.

125. Christopher M, Bowd C, Belghith A, Goldbaum MH, Weinreb RN, Fazio MA, et al. Deep learning approaches predict glaucomatous visual field damage from oct optic nerve head en face images and retinal nerve fiber layer thickness maps. *Ophthalmology* 2020;127:346–356.

126. Yu HH, Maetschke SR, Antony BJ, Ishikawa H, Wollstein G, Schuman JS, et al. Estimating global visual field indices in glaucoma by combining macula and optic disc OCT scans using 3-dimensional convolutional neural networks. *Ophthalmol Glaucoma* 2021;4:102–112.

127. Huang X, Sun J, Majoor J, Vermeer KA, Lemij H, Elze T, et al. Estimating the severity of visual field damage from retinal nerve fiber layer thickness measurements with artificial intelligence. *Transl Vis Sci Technol* 2021;10:16.

128. Huang X, Sun J, Gupta K, Montesano G, Crabb DP, Garway-Heath DF, et al. Detecting glaucoma from multi-modal data using probabilistic deep learning. *Front Med* 2022;9:923096.

129. Prum BE, Jr., Rosenberg LF, Gedde SJ, Mansberger SL, Stein JD, Moroi SE, et al. Primary open-angle glaucoma preferred practice pattern((R)) guidelines. *Ophthalmology* 2016;123:P41–P111.

130. European Glaucoma Society Terminology and Guidelines for Glaucoma, 4th Edition - Chapter 2: Classification and terminology. Supported by the EGS Foundation: Part 1: Foreword; Introduction; Glossary; Chapter 2 Classification and terminology. *Br J Ophthalmol* 2017;101:73–127.

131. Sounderajah V, Ashrafian H, Golub RM, Shetty S, De Fauw J, Hooft L, et al. Developing a reporting guideline for artificial intelligence-centred diagnostic test accuracy studies: The STARD-AI protocol. *BMJ Open* 2021;11:e047709.

132. Cruz Rivera S, Liu X, Chan AW, Denniston AK, Calvert MJ. Guidelines for clinical trial protocols for interventions involving artificial intelligence: The SPIRIT-AI extension. *Nat Med* 2020;26:1351–1363.

133. Liu X, Rivera SC, Moher D, Calvert MJ, Denniston AK. Reporting guidelines for clinical trial reports for interventions involving artificial intelligence: The CONSORT-AI Extension. *BMJ* 2020;370:m3164.

Review Article

# Neuro-ophthalmic Manifestations of Coronavirus Disease 2019 and Its Vaccination: A Narrative Review

**Mohadeseh Feizi[1], MD; Danielle R. Isen[2], DO; Mehdi Tavakoli[2], MD**

[1]*Ophthalmic Research Center, Research Institute for Ophthalmology and Vision Science, Shahid Beheshti University of Medical Sciences, Tehran, Iran*
[2]*University of Alabama at Birmingham Heersink School of Medicine, Department of Ophthalmology and Visual Sciences, Birmingham, Alabama, USA*

**ORCID:**
*Mohadeseh Feizi: https://orcid.org/0000-0001-8558-8074*

## Abstract

Coronavirus disease 2019 (COVID-19) is a current pandemic caused by SARS-CoV-2 that has vastly affected the whole world. Although respiratory disease is the most common manifestation of COVID-19, the virus can affect multiple organs. Neurotropic aspects of the virus are increasingly unfolding, in so far as some respiratory failures are attributed to brainstem involvement. The neuro-ophthalmic manifestations of COVID-19 and the neuro-ophthalmic side effects of vaccination were reviewed. The major findings are that the SARS-CoV-2 infection commonly causes headaches and ocular pain. It can affect the afferent and efferent visual pathways by ischemic or inflammatory mechanisms. Optic nerve may be the origin of transient or permanent visual loss from papillophlebitis, idiopathic intracranial hypertension, or optic neuritis. Cerebrovascular strokes are not uncommon and may lead to cortical visual impairment or optic nerve infarction. SARS-CoV-2 may affect the pupillomotor pathways, resulting in tonic pupil (Adie's syndrome) or Horner's syndrome. Cranial neuropathies including third, fourth, sixth, and seventh nerve palsies have all been reported. Rhino-orbital mucormycosis superinfections in COVID-19 patients receiving steroids or other immunosuppressive therapies may result in unilateral or bilateral visual loss and ophthalmoplegia. Autoimmune conditions such as Guillain-Barré, Miller-Fisher syndrome, and ocular myasthenia have been reported.

**Keywords:** Corona Virus; COVID-19; Neuro-ophthalmology; Vaccination; Vision Loss

*J Ophthalmic Vis Res* 2023; 18 (1): 113–122

**Correspondence to:**
Mohadeseh Feizi, MD. Labbafinejad Medical Center, Shahid Beheshti University of Medical Sciences, Boostan 9 St., Pasdaran Ave., Tehran 16666, Iran.
E-mail: mohadeseh_feizi@yahoo.com

Received: 17-11-2021 Accepted: 30-08-2022

**Access this article online**

**Website:** https://knepublishing.com/index.php/JOVR

**DOI:** 10.18502/jovr.v18i1.12731

This is an open access article distributed under the Creative Commons Attribution License, which permits unrestricted use, distribution, and reproduction in any medium, provided the original work is properly cited.

**How to cite this article:** Feizi M, Isen DR, Tavakoli M. Neuro-ophthalmic Manifestations of Coronavirus Disease 2019 and Its Vaccination: A Narrative Review. J Ophthalmic Vis Res 2023;18:113–122.

© 2023 Feizi et al. This is an open access article distributed under the Creative Commons Attribution License | Published by Knowledge E

## INTRODUCTION

Coronavirus disease-2019 (COVID-19) is a novel β coronavirus of group 2B, first reported in December 2019 in Wuhan city, that rapidly disseminated all over the world, resulting in an immense pandemic.[1] The disease presents in a widely variable range from asymptomatic carriers or mild infection to severe acute respiratory syndrome (SARS), multi-organ failure, and death. Besides respiratory distress syndrome, SARS-CoV-2 may affect many other organs and cause cardiac or renal injury, dermatologic conditions, gastrointestinal symptoms, coagulopathy, severe inflammatory reaction, and central or peripheral nervous system involvement.[2] Up to one-third of patients with COVID-19 have neurological complications, and the incidence appears to be higher in patients with more severe infections.[3] The most common severe neurologic manifestations of COVID-19 are acute cerebrovascular disease and altered level of consciousness.[4] A retrospective study in Wuhan reported neurological symptoms in 36.4% of the hospitalized patients.[1] Neurologic manifestations are mainly reported to be associated with severe cases of COVID-19.[1, 5] Moreover, COVID-19-related cases of ischemic stroke involving visual pathways have resulted in prolonged hospitalizations and fatality.[6, 7] Findings have suggested that ischemic strokes in patients with COVID-19 disease are more severe and disabling than strokes in the uninfected subjects.[8] In contrast, isolated cranial neuropathies involving the eye are typically associated with mild to moderate COVID-19 disease that improves spontaneously or with local protocols.[9, 10]

A recent review reported that over 4% of patients with COVID-19 had ophthalmic findings requiring clinical attention.[11] Based on an initial study in Wuhan, visual impairment was described in 3 out of 214 (1.4%) hospitalized patients with COVID-19.[1]

Various neuro-ophthalmologic manifestations have been reported in patients with COVID-19 infection. In this article, we reviewed and categorized SARS-CoV-2-related neuro-ophthalmic presentations.

## Mechanisms of Neurologic Involvement in COVID-19

Several mechanisms have been postulated for neurologic involvement in COVID-19 disease. Direct viral invasion, hypoxia, hypercoagulable state, inflammatory reactions related to cytokine storm, delayed autoantibody formation, endothelial dysfunction, and retrograde axonal transport of the infection via cranial and peripheral nerves (most notably, the olfactory nerve) are the proposed underlying mechanisms for neuro-ophthalmic manifestations of COVID-19.[2, 5] It is thought that direct viral invasion is mediated by viral fusion to the angiotensin-converting-enzyme 2 (ACE-2) receptor, which is expressed on the surface of pulmonary type II alveolar epithelial cells as well as neurons and glial cells.[12] The SARS-COV-2 virus can affect nearly all neuro-ophthalmic pathways [Table 1]. COVID-19 can cause a wide range of pathologies within the afferent and efferent visual pathways. SARS-CoV-2 can cause central nervous system conditions such as seizures,[13] anosmia or ageusia,[14] altered level of consciousness, posterior reversible encephalopathy syndrome (PRES),[15, 16] neuromyelitis optica (NMO) spectrum disorder,[4, 17] myelin oligodendrocyte glycoprotein (MOG)-associated disease,[3, 18–22] acute disseminated encephalomyelitis (ADEM),[23] cerebral venous sinus thrombosis (CVST),[24, 25] and cerebrovascular strokes.[2, 6–8] It can also affect the peripheral nervous system, leading to conditions such as Guillain-Barré,[26] Miller Fisher syndrome,[27, 28] polyneuritis cranialis,[28] and myasthenia gravis.[29, 30]

SARS-CoV-2 is associated with pathologies of the afferent visual pathways including optic neuritis (idiopathic[5, 14, 31–33] or immune-mediated),[3, 4, 17–22] optic nerve infarction,[34] papillophlebitis,[35] and idiopathic intracranial hypertension.[36–38] The efferent visual pathways can be lesioned by COVID-19-related isolated cranial neuropathies,[9, 27, 39–41] nystagmus,[42–46] tonic pupil,[47–51] Horner's syndrome,[12, 13, 52] and opsoclonus-myoclonus-ataxia syndrome (OMAS).[53–55] Mucormycosis infections,[56] which are of exponentially increasing incidence in COVID-19 patients, can occur as a superinfection and result in lesions of the afferent or efferent visual pathways or even both.[57, 58]

## Interval Between Infection and Neuro-Ophthalmic Manifestations

Neuro-ophthalmic manifestations of COVID-19 may present either concurring with systemic and pulmonary symptoms or days to several weeks after their resolution. Timeline latency between acute viral symptoms and neuro-ophthalmic manifestation, auto-antibody formation, and good response to steroid therapy favor an immune-mediated mechanism.[49] Guillain-Barré, Miller Fisher syndrome, NMO, MOG-associated disease, ADEM, tonic pupil, rhombencephalitis, Bickerstaff encephalitis, myasthenia gravis (MG), and OMAS were all postulated to have delayed-immune mediated mechanisms related to COVID-19. The delayed immune response may be from antibodies directed against SARS-CoV-2 proteins that cross-react with cellular proteins through a mechanism known as molecular mimicry. Alternatively, COVID-19 infection may impair immunologic self-tolerance.[29]

## Headache/Ocular Pain

Ocular pain and headache are common and may be the initial manifestation of COVID-19 infection.[1, 11, 59] Headache was reported in 71% and ocular pain in 34% by healthcare workers in the Netherlands in patients with a positive SARS-CoV-2 polymerase chain reaction (PCR).[60] In another study, eye pain was amongst the most common of the ocular symptoms and seen in 16% of patients.[61] Photophobia and itchy eyes were seen at a similar frequency (18% and 17%, respectively).

Headache characteristics in COVID‐19 patients were moderate to severe, pulsating or pressing, bilateral, and mostly in the temporo-parietal, forehead, or periorbital regions. It has been postulated that an increase in pro-inflammatory cytokines, hypoxia, or activation of the trigeminal nerve endings from direct viral insult or vasculopathy explain the underlying pathophysiology of headache in COVID-19 disease.[62] However, the exact mechanism is not clear, and viral encephalitis and meningitis should be considered.

Overall, it seems that headache and periocular pain are the most prevalent neuro-ophthalmic presentations of COVID-19 but more comprehensive epidemiological studies are required to evaluate the prevalence of each neurological symptom.

## Optic Neuritis and Other Optic Nerve Disorders

Optic neuritis has been reported in association with COVID-19 infections in multiple cases where no other etiologies have been determined.[5, 14, 31–33] COVID-19 has also been the harbinger to optic neuritis in NMO spectrum disorder[4, 17] and MOG-related disease.[3, 18, 19, 21, 63, 64] Optic neuritis in association with COVID-19 infection has also been reported in the pediatric age group even in the context of demyelinating conditions.[65] COVID-19-related optic neuritis had a good response to intravenous (IV) corticosteroid therapy in all cases except four.[5, 14, 22, 32]

Optic neuritis was reported in conjunction with panuveitis in one case of COVID-19, which resulted in optic atrophy despite corticosteroid treatment. However, the patient only received oral prednisone without high-dose IV corticosteroids. The authors postulated that ischemic insult due to the prothrombotic capacity of COVID-19 or an inflammatory reaction resulted in optic atrophy in this case.[32]

Novi et al reported an adult patient with COVID-19 disease and bilateral retrobulbar optic neuritis with enhancing lesions in optic nerves, brain, and thoracic spine, consistent with ADEM.[23]

Cerebrovascular ischemia is a known complication of SARS-CoV-2 infection.[1] Optic nerve infarction due to internal carotid artery occlusion was reported in a 50-year-old COVID-positive male by Tavakoli et al.[34] Central retinal artery occlusion[66] or ophthalmic artery occlusion[67] due to internal carotid artery stroke have also been reported in COVID-19 disease.

There is one report of papillophlebitis in a 40-year-old male that occurred four weeks after the resolution of a typical COVID-19 infection with elevated D-dimer and fibrinogen levels. The authors proposed that the COVID-19 cytokine storm induced a hypercoagulable state and thrombotic microangiopathy, increasing the risk of papillophlebitis.[35]

Idiopathic intracranial hypertension can occur in adults with COVID-19 disease, but it is rare, and most of the cases have been reported in children.[36–38] Two of these cases were associated

with increased intracranial pressure inducing sixth nerve palsies in idiopathic intracranial hypertension due to COVID-19 multisystem inflammatory syndrome in children (MIS-C).[36, 37]

## Pupillary Abnormalities

Tonic (Adie's) pupil refers to parasympathetic denervation of the pupil sphincter, which causes poor constriction of the pupil to the light but the reaction to the accommodation remains relatively spared. Tonic pupil has been reported in association with COVID-19, including unilateral[47] and bilateral[48] cases. One patient with COVID-19-related bilateral tonic pupil also had inflammatory multifocal choroiditis.[68] Additionally, Adie-Holmes syndrome (with additional finding of loss of the deep tendon reflexes) has been described in a patient with COVID-19 infection.[69] Lastly, Ordás et al reported a case of tonic pupil with contralateral trochlear palsy in association with COVID-19 infection.[49]

Tonic pupil is often idiopathic, but it has been associated with other infections (e.g., syphilis, Lyme's disease, influenza or herpes viruses), autoimmune processes, trauma, choroidal and orbital tumors, and surgery.[47] In each of the above cases of tonic pupil,[47] there was a delay (ranging from two days to one month) between the onset of COVID-related respiratory symptoms and development of tonic pupil. Most of the authors hypothesized that tonic pupil in COVID-19 is secondary to a post-viral delayed immune-mediated injury rather than direct viral entry into the central nervous system. Moreover, a taper of prednisolone has been utilized for treatment with subsequent improvement in the tonic pupil.[50]

Horner's syndrome has also been rarely described in COVID-19 disease.[12, 13, 52] In each case, COVID-19 pneumonia involving the upper part of the lungs was the suggested etiology of Horner's syndrome, and no other causes were discovered with subsequent imaging studies.

## Central Visual Impairment and Visual Field Defects

COVID-19 disease can induce hypercoagulable and inflammatory states, increasing the risk of cerebrovascular stroke.[6, 70] There are reports of ischemic stroke involving the visual pathways in association with SARS-CoV-2 infection, resulting in homonymous field defects[2] or even cortical blindness from bilateral occipital infarcts.[7] Bondira et al reported a patient with COVID-19 disease and bilateral occipital strokes, resulting in a partial right homonymous hemianopsia and difficulty with reading.[6] Priftis et al presented a COVID-positive patient with a left occipito-temporal ischemic stroke, resulting in alexia without agraphia syndrome and right homonymous hemianopsia.[8]

COVID-induced PRES has been reported, resulting in transient cortical visual loss[15] or even hallucinatory palinopsia.[16] COVID-associated CVST has also been described but is uncommon, and only a few cases have been associated with blurry vision and papilledema.[24, 25] The disproportionally low frequency of reported visual involvement in COVID-associated CVST may be because of the severity of other symptoms or an altered level of consciousness.

In addition, there are reports of visual loss due to pituitary apoplexy in the context of acute COVID-19 infection.[71, 72]

## Cranial Nerve Palsies and Double Vision

Damage to third, fourth, sixth, and seventh cranial nerves have all occurred in timeline relation to COVID-19 infection. Cranial nerve involvement may develop as a primary and isolated insult or in the context of a more generalized condition such as Miller Fisher syndrome, Guillain-Barré, myasthenia gravis, venous sinus thrombosis, and increased intracranial pressure.

Isolated oculomotor palsy with and without pupillary involvement has been reported in association with COVID-19.[39, 40, 73] Similarly, isolated abducens palsy has been described in COVID-19.[9, 27] In these cases, there was no enhancement of the abducens nerve pathway on MRI, and patients had underlying systemic hypertension. Such findings raised the hypothesis that uncontrolled hypertension in the acute viral illness may cause abducens palsy. An alternative theory was that the abducens palsies occurred from the leptomeningeal invasion of SARS-CoV-2, given that two of these cases had optic nerve sheath enhancement on MRI. As previously mentioned, there is one case of unilateral trochlear nerve palsy with contralateral tonic pupil[49] and another with bilateral trochlear nerve palsy in the setting of COVID-related cerebral vasculitis.[74]

**Table 1.** A summary of reported neuro-ophthalmic manifestations of COVID-19.

| Clinical entity | Clinical characteristics | References |
|---|---|---|
| **Headache and ocular pain** | Common and may be the initial manifestations. Moderate to severe, pulsating/pressing, bilateral, temporo-parietal, forehead, or periorbital regions. | Mao L et al[1], 2020; Chwalisz BK et al, 2020[11]; Huang C et al[59], 2019 |
| **Optic neuritis** | Unilateral or bilateral, may be associated with neuromyelitis optica (NMO) spectrum disorders, myelin oligodendrocyte (MOG)-related disease, panuveitis, acute disseminated encephalomyelitis (ADEM). | Caudill GB et al [31], 2020; Benito-Pascual B et al[32], 2019; Marcos Aet al[5], 2020; Rodríguez-Rodríguez MS et al[14], 2021; Deane K et al[33], 2021; Novi G et al[23], 2020 |
| **Optic nerve infarction** | Vision loss due to internal carotid artery occlusion, optic nerve ischemia revealed on DWI sequence. | Tavakoli et al[34], 2019 |
| **Papillophlebitis** | Decreased visual field sensitivity, dilated and tortuous retinal vessels, disc edema, and retinal hemorrhage; decreased vision due to macular edema. | Insausti-García A et al[35], 2020 |
| **Idiopathic intracranial hypertension** | More reported in children than adults due to multisystem inflammatory syndrome (MIS). | Verkuil LD et al[36], 2020; Sofuoğlu AI et al[37], 2021; Khalid MF et al[38], 2021 |
| **Tonic Adie's pupil** | Unilateral or bilateral, associated with multifocal choroiditis; trochlea palsy. | Gopal M et al[47], 2021; Quijano-Nieto BA et al[48], 2021; Ortiz-Seller A et al[68], 2020; Kaya Tutar N et al[69], 2021; Ordás CM et al[49], 2020 |
| **Horner syndrome** | Associated with pneumonia involving the upper part of the lung. | Popiołek A et al[52], 2021; Naor MS et al[12], 2021; Portela-Sánchez S et al[13], 2021 |
| **Visual field defect and central visual impairment** | Cerebrovascular stroke resulting in homonymous visual field defect, cortical visual blindness, reading difficulties. | Tisdale AK et al[70], 2020; Bondira IP et al[6], 2021; Cyr DG et al[7], 2020; Priftis K et al[8], 2021 |
| **Posterior reversible encephalopathy syndrome (PRES)** | Transient cortical visual loss and hallucinatory palinopsia. | Kaya Y et al[15], 2020; Ghosh R et al[16], 2020 |
| **Cranial nerve palsy** | Isolated or multiple cranial nerve involvement including third, fourth, sixth, and seventh. Can occur in the context of Miller Fisher syndrome, Guillain-Barré, myasthenia gravis, venous sinus thrombosis, and increased intracranial pressure. | Ordás CM et al[49], 2020; Douedi S et al[39], 2021; Cicalese MP et al[73], 2022; John C et al[40], 2020; Greer CE et al[9], 2020; Dinkin M et al[27], 2020; de Oliveira R de MC et al[74], 2020; Gutiérrez-Ortiz C et al[28], 2020; Sansone P et al[26], 2021; Restivo DA et al[29], 2020; Mas Maresma L et al[30], 2020; Lima MA et al[10], 2020; Juliao Caamaño DS et al[75], 2020 |
| **Nystagmus and abnormal ocular movement** | Acquired nystagmus due to acute labyrinthitis, benign paroxysmal positional vertigo, rhombencephalitis, Bickerstaff encephalitis, opsoclonus-myoclonus-ataxia syndrome (OMAS). | Perret M et al[42], 2021; Picciotti PM et al[43], 2021; Wong P et al[44], 2022; Llorente Ayuso L et al[45], 2021; Nelson JL et al[53], 2022; Emamikhah M et al[54], 2021 |
| **Rhino-orbital-cerebral mucormycosis (ROCM)** | Mostly occurs in patients receiving high-dose corticosteroid; presented with peri-ocular edema, vision loss, ptosis, and ophthalmo-paresis. | Sen M et al[57], 2021; Pakdel F et al[58], 2022 |

Different medications for COVID-19-related cranial neuropathies such as hydroxychloroquine, azithromycin, corticosteroids, and IV immunoglobulin have been used. However, it is not known whether the neuro-ophthalmic benefit was conferred.

Cranial neuropathy in relation to COVID-19 has also been seen in the context of Miller Fisher syndrome, Guillain-Barré, and polyneuritis cranialis. Dinkin et al described a case of presumed Miller Fisher syndrome in a COVID-positive patient with a partial left pupil involving oculomotor nerve palsy,

bilateral abducens palsy, hyporeflexia, and gait ataxia.[27] The deficits partially improved following IV immunoglobulin infusions. Gutiérrez-Ortiz et al detailed a similar case of Miller Fisher syndrome in a patient with right fascicular oculomotor palsy, right internuclear ophthalmoparesis, ataxia, areflexia, albuminocytologic dissociation, anosmia, ageusia, and positive reverse transcriptase-PCR for SARS-CoV-2. Most of the deficits were resolved following IV immunoglobulin infusions. These authors described a second COVID-positive case with bilateral abducens palsy, areflexia, and albuminocytologic dissociation without ataxia or limb weakness secondary to polyneuritis cranialis.[28]

In a systematic review published by Sansone et al, of the 41 patients with SARS-CoV-2-related Guillain-Barré syndrome, 9 (22%) had diplopia, 7 (17%) had ocular palsy, and 13 (32%) had facial palsy. The average time between the onset of SARS-CoV-2 symptoms and the first neurological signs of Guillain-Barré syndrome was 10 days.[26]

COVID-19 has also been the harbinger of new diagnoses of myasthenia gravis. Restivo et al detailed three patients who developed diplopia, ptosis, or dysphagia and tested positive for elevated serum acetylcholine receptor antibodies following the SARS-CoV-2 infection.[29] Fatigability and other myasthenic symptoms started four to seven days after the initial COVID-19 manifestations.[29, 30] Similarity between SARS-CoV-2 epitopes and neuromuscular junction components is postulated to induce molecular mimicry, resulting in auto-antibody formation and subsequently post-COVID-19 myasthenia gravis.[29] Isolated peripheral facial nerve palsy has also been reported either during or at the onset of the SARS-CoV-2 clinical course. In one of the eight peripheral facial nerve palsy cases reported by Lima et al, ipsilateral abducens palsy was also present.[10] Facial diplegia has also been reported as a parainfectious complication of COVID-19 disease and was considered a rare variant of Guillain-Barré syndrome in the setting of concomitant albuminocytologic dissociation.[75]

## Abnormal Ocular Movements and Nystagmus

Acquired nystagmus has been seen in association with COVID-19,[76] and may be due to various underlying etiologies including acute labyrinthitis,[42] benign paroxysmal positional vertigo,[43] rhombencephalitis,[44] and Bickerstaff encephalitis.[45]

Several cases of OMAS have been described in COVID-positive patients.[53–55] In all patients who were tested, work-up with a paraneoplastic panel was unrevealing for other causes of OMAS. A variety of infections besides SARS-CoV-2 including human immunodeficiency virus (HIV), West Nile virus, Epstein Barr virus, and enterovirus have also been associated with OMAS.[53] Treatments used for COVID-associated OMAS include various combinations of the following: IV immunoglobulin, levetiracetam, sodium valproate, clonazepam, and corticosteroids. All cases were associated with a good therapeutic response and partial to complete recovery. Emamikhah et al stated that the dramatic effect of immunotherapy on recovery suggests an immune-mediated parainfectious mechanism for COVID-related OMAS.[54]

## Neuro-Ophthalmic Presentation Due to Secondary Mucormycosis

There is strong evidence that infection with SARS-CoV-2 increases the risk of secondary fungal infections, notably rhino-orbital-cerebral mucormycosis (ROCM). The incidence of ROCM increased to epidemic proportions during the second wave of the COVID-19 pandemic in India.[57] A retrospective, observational study was conducted in India involving 2826 patients with COVID-associated ROCM. The most common primary signs included periocular/facial edema (33%), loss of vision (21%), ptosis (12%), and proptosis (11%). Ocular movement restriction and diplopia were infrequent signs (3%). Most (87%) of the patients had received systemic corticosteroids prior to developing COVID-associated ROCM, and it was the most common risk factor for the condition followed by diabetes mellitus.

## Neuro-Ophthalmic Complications of COVID-19 Vaccines

There are several reports of neuro-ophthalmic complications following COVID-19 vaccination.[77–79] These complications occurred after all types of vaccines. They include acute ischemic stroke, intracranial hemorrhages, and cerebral venous sinus thrombosis.[78, 80]

Other reported neuro-ophthalmic complications include: bilateral arteritic anterior ischemic optic neuropathy (AAION),[81] post-vaccination cranial neuropathy, that is, third[73] and sixth[82–84] nerve palsies, facial palsy,[84–87] multiple cranial nerve palsies,[88] pupillary abnormalities such as Horner's syndrome, Holmes-Adie pupil, miosis and mydriasis,[78] eight nerve involvement and benign paroxysmal positional vertigo,[89] and post-vaccination optic neuritis.[90–92] In multiple sclerosis patients, BNT162b2 mRNA vaccine was reported to be associated with a transient increase of MS symptoms in 3.8% but none of them needed treatment.[93]

## SUMMARY

Coronavirus Disease 2019 and also all types of vaccines that have been made against it can affect the afferent and efferent visual pathways by ischemic or inflammatory mechanisms. The optic nerve may be the origin of transient or permanent visual loss from papillophlebitis, idiopathic intracranial hypertension, or optic neuritis. Cerebrovascular strokes are not uncommon and may lead to cortical visual impairment. The pupillomotor pathways and cranial nerve including the third, fourth, sixth, and seventh nerve may also be involved. Early detection of the neuro-ophthalmic features of COVID-19 disease/vaccine will assist in preventing vision loss and oculomotor deficits.

## Financial Support and Sponsorship

This article is authors' own work and has no sources of support.

## Conflicts of Interest

The authors have no financial interest in the subject of this article.

## *REFERENCES*

1. Mao L, Jin H, Wang M, Hu Y, Chen S, He Q, et al. Neurologic manifestations of hospitalized patients with coronavirus disease 2019 in Wuhan, China. *JAMA Neurol* 2020;77:683–690.
2. Tisdale AK, Dinkin M, Chwalisz BK. Afferent and efferent neuro-ophthalmic complications of coronavirus disease 19. *J Neuro-Ophthalmol* 2021;41:154–165.
3. Rojas-Correa DX, Reche-Sainz JA, Insausti-García A, Calleja-García C, Ferro-Osuna M. Post COVID-19 myelin oligodendrocyte glycoprotein antibody-associated optic neuritis. *Neuro-Ophthalmology* 2021;46:115–121.
4. Shaw VC, Chander G, Puttanna A. Neuromyelitis optica spectrum disorder secondary to COVID-19. *Br J Hosp Med* 2020;81:1–3.
5. da Silva Catharino AM, Neves MAO, Nunes NSM, do Nascimento JSF, do Nascimento JKF, Castro RRT, et al. COVID-19 related optic neuritis: Case report. *J Clin Neurol Neurosci* 2020;18:10.
6. Bondira IP, Lambert-Cheatham NA, Sakuru RC, Polinger-Hyman DJ, Pipitone BD, Arnold KE. Inability to read after prolonged COVID-19 hospitalization: MRI with clinical correlation. *J Neuro-Ophthalmol* 2021;41:e277–e278.
7. Cyr DG, Vicidomini CM, Siu NY, Elmann SE. Severe bilateral vision loss in 2 patients with coronavirus disease 2019. *J Neuro-Ophthalmol* 2020;40:403–405.
8. Priftis K, Prior M, Meneghetti L, Mercogliano T, Bendini M. Alexia without agraphia in a post COVID-19 patient with left-hemisphere ischemic stroke. *Neurol Sci* 2021;42:2179–2181.
9. Greer CE, Bhatt JM, Oliveira CA, Dinkin MJ. Isolated cranial nerve 6 palsy in 6 patients with COVID-19 infection. *J Neuroophthalmol* 2020;40:520–522.
10. Lima MA, Silva MT, Soares CN, Coutinho R, Oliveira HS, Afonso L, et al. Peripheral facial nerve palsy associated with COVID-19. *J Neurovirol* 2020;26:941–944.
11. Chwalisz BK, Dinkin MJ. Disease of the year: COVID-19 and its neuro-ophthalmic complications. *J Neuro-Ophthalmol* 2020;40:283–284.
12. Naor MS, Mathew PG, Sharon R. Transient Horner syndrome associated with COVID-19: A case report. *eNeurologicalSci* 2021;25:100349.
13. Portela-Sánchez S, Sánchez-Soblechero A, Melgarejo Otalora PJ, Rodríguez López Á, Velilla Alonso G, Palacios-Mendoza MA, et al. Neurological complications of COVID-19 in hospitalized patients: The registry of a neurology department in the first wave of the pandemic. *Eur J Neurol* 2021;28:3339–3347.
14. Rodríguez-Rodríguez MS, Romero-Castro RM, Alvarado-de la Barrera C, González-Cannata MG, García-Morales AK, Ávila-Ríos S. Optic neuritis following SARS-CoV-2 infection. *J Neurovirol* 2021;27:359–363.
15. Kaya Y, Kara S, Akinci C, Kocaman AS. Transient cortical blindness in COVID-19 pneumonia; a PRES-like syndrome: Case report. *J Neurol Sci* 2020;413:116858.
16. Ghosh R, Lahiri D, Dubey S, Ray BK, Benito-León J. Hallucinatory palinopsia in COVID-19-induced posterior reversible encephalopathy syndrome. *J Neuro-Ophthalmol* 2020;40:523–526.
17. de Ruijter NS, Kramer G, Gons RA, Hengstman GJ. Neuromyelitis optica spectrum disorder after presumed coronavirus (COVID-19) infection: A case report. *Mult Scler Relat Disord* 2020;46:102474.
18. Zhou S, Jones-Lopez EC, Soneji DJ, Azevedo CJ, Patel VR. Myelin oligodendrocyte glycoprotein antibody-associated optic neuritis and myelitis in COVID-19. *J Neuro-Ophthalmol* 2020;40:398–402.
19. Sawalha K, Adeodokun S, Kamoga GR. COVID-19-induced acute bilateral optic neuritis. *J Investig Med High Impact Case Rep* 2020;8:2324709620976018.

20. Žorić L, Rajović-Mrkić I, Čolak E, Mirić D, Kisić B. Optic neuritis in a patient with seropositive myelin oligodendrocyte glycoprotein antibody during the post-COVID-19 period. *Int Med Case Rep J* 2021;14:349–355.
21. Kogure C, Kikushima W, Fukuda Y, Hasebe Y, Takahashi T, Shibuya T, et al. Myelin oligodendrocyte glycoprotein antibody-associated optic neuritis in a COVID-19 patient: A case report. *Medicine* 2021;100:e25865.
22. Woodhall M, Mitchell JW, Gibbons E, Healy S, Waters P, Huda S. Case report: Myelin oligodendrocyte glycoprotein antibody-associated relapse with COVID-19. *Front Neurol* 2020;11:598531.
23. Novi G, Rossi T, Pedemonte E, Saitta L, Rolla C, Roccatagliata L, et al. Acute disseminated encephalomyelitis after SARS-CoV-2 infection. *Neurol Neuroimmunol Neuroinflamm* 2020;7:797.
24. Dakay K, Cooper J, Bloomfield J, Overby P, Mayer SA, Nuoman R, et al. Cerebral venous sinus thrombosis in COVID-19 infection: A case series and review of the literature. *J Stroke Cerebrovasc Dis* 2021;30:105434.
25. Klein DE, Libman R, Kirsch C, Arora R. Cerebral venous thrombosis: A typical presentation of COVID-19 in the young. *J Stroke Cerebrovasc Dis* 2020;29:104989.
26. Sansone P, Giaccari LG, Aurilio C, Coppolino F, Esposito V, Fiore M, et al. Post-infectious Guillain-Barré syndrome related to SARS-CoV-2 infection: A systematic review. *Life* 2021;11:1–16.
27. Dinkin M, Gao V, Kahan J, Bobker S, Simonetto M, Wechsler P, et al. COVID-19 presenting with ophthalmoparesis from cranial nerve palsy. *Neurology* 2020;95:221–223.
28. Gutiérrez-Ortiz C, Méndez-Guerrero A, Rodrigo-Rey S, San Pedro-Murillo E, Bermejo-Guerrero L, Gordo-Mañas R, et al. Miller Fisher syndrome and polyneuritis cranialis in COVID-19. *Neurology* 2020;95:e601–e605.
29. Restivo DA, Centonze D, Alesina A, Marchese-Ragona R. Myasthenia Gravis associated with SARS-CoV-2 infection. *Ann Intern Med* 2020;173:1027–1028.
30. Mas Maresma L, Barrachina Esteve O, Navarro Vilasaró M, Moreno-Ariño M. [Myasthenia gravis associated with SARS-CoV-2 infection: A conjunction of several factors]. *Rev Esp Geriatr Gerontol* 2020;55:360–361.
31. Caudill GB, Wolin MJ. Myelin oligodendrocyte glycoprotein and neuromyelitis optica/aquaporin-4 antibody negative COVID-19–associated optic neuritis. *J Neuro-Ophthalmol* 2022.
32. Benito-Pascual B, Gegúndez JA, Díaz-Valle D, Arriola-Villalobos P, Carreño E, Culebras E, et al. Panuveitis and optic neuritis as a possible initial presentation of the novel coronavirus disease 2019 (COVID-19). *Ocul Immunol Inflamm* 2020;28:922–925.
33. Deane K, Sarfraz A, Sarfraz Z, Valentine D, Idowu AR, Sanchez V. Unilateral optic neuritis associated with SARS-CoV-2 infection: A rare complication. *Am J Case Rep* 2021;22:e931665.
34. Tavakoli M, Sotoudeh M, Rezaei A, Saadatpour Z, Michael S, Vaphides LB. Optic nerve infarction in a patient with coronavirus disease 2019. *J Neuroophthalmol* 2021;42e347–e348.
35. Insausti-García A, Reche-Sainz JA, Ruiz-Arranz C, López Vázquez Á, Ferro-Osuna M. Papillophlebitis in a COVID-19 patient: Inflammation and hypercoagulable state. *Eur J Ophthalmol* 2020;32:NP168–NP172.
36. Verkuil LD, Liu GT, Brahma VL, Avery RA. Pseudotumor cerebri syndrome associated with MIS-C: A case report. *Lancet* 2020;396:532.
37. Sofuoğlu AI, Akçay N, Şevketoğlu E, Bektaş G. Pseudotumor Cerebri Syndrome as a neurologic involvement of multisystem inflammatory syndrome in children: A case report. *J Trop Pediatr* 2021;67:1–4.
38. Khalid MF, Micieli JA. Idiopathic intracranial hypertension associated with SARS-CoV-2 B.1.1.7 variant of concern. *Can J Neurol Sci* 2022;49:472–473.
39. Douedi S, Naser H, Mazahir U, Hamad AI, Sedarous M. Third cranial nerve palsy due to COVID-19 infection. *Cureus* 2021;13:e14280.
40. Fitzpatrick JC, Comstock JM, Longmuir RA, Donahue SP, Fitzpatrick JM, Bond JB. Cranial nerve III palsy in the setting of COVID 19 infection. *J Neuro-Ophthalmology* 2020;41:e286–e287.
41. Belghmaidi S, Nassih H, Boutgayout S, El Fakiri K, El Qadiry R, Hajji I, et al. Third cranial nerve palsy presenting with unilateral diplopia and strabismus in a 24-year-old woman with COVID-19. *Am J Case Rep* 2020;21:e925897.
42. Perret M, Bernard A, Rahmani A, Manckoundia P, Putot A. Acute labyrinthitis revealing COVID-19. *Diagnostics* 2021;11:482.
43. Picciotti PM, Passali GC, Sergi B, De Corso E. Benign paroxysmal positional vertigo (BPPV) in COVID-19. *Audiology Res* 2021;11:418–422.
44. Wong P, Craik S, Newman P, Makan A, Srinivasan K, Crawford E, et al. Lessons of the month 1: A case of rhombencephalitis as a rare complication of acute COVID-19 infection. *Clin Med* 2020;20:293–294.
45. Llorente Ayuso L, Torres Rubio P, Beijinho do Rosário RF, Giganto Arroyo ML, Sierra-Hidalgo F. Bickerstaff encephalitis after COVID-19. *J Neurol* 2021;268:2035–2037.
46. García-Romo E, Blanco R, Nicholls C, Hernández-Tejero A, Fernández-de-Arévalo B. COVID-19 presenting with nystagmus. *Arch Soc Esp Oftalmol* 2021;96:224–226.
47. Gopal M, Ambika S, Padmalakshmi K. Tonic pupil following COVID-19. *J Neuro-Ophthalmol* 2021;41:e764–e766.
48. Quijano-Nieto BA, Córdoba-Ortega CM. [Tonic pupil after COVID-19 infection]. *Arch Soc Esp Oftalmol* 2021;96:353–355.
49. Ordás CM, Villacieros-Álvarez J, Pastor-Vivas AI, Corrales-Benítez Á. Concurrent tonic pupil and trochlear nerve palsy in COVID-19. *J Neurovirol* 2020;26:970–972.
50. Kaya Tutar N, Kale N, Tugcu B. Adie-Holmes syndrome associated with COVID-19 infection: A case report. *Indian J Ophthalmol* 2021;69:773–774.
51. Ortiz-Seller A, Martínez Costa L, Hernández-Pons A, Valls Pascual E, Solves Alemany A, Albert-Fort M. Ophthalmic and neuro-ophthalmic manifestations of coronavirus disease 2019 (COVID-19). *Ocul Immunol Inflamm* 2020;28:1285–1289.
52. Popiołek A, Chyrek-Tomaszewska A, Kłopocki J, Dura M, Pulkowski G. Horner's syndrome in the course of COVID-19: A case report. *Med Res J* 2021;6:274–275.

53. Nelson JL, Blume GM, Bansal SK, Kaufman JR, Woods FR, Zhang X, et al. Postinfectious SARS-CoV-2 opsoclonus-myoclonus-ataxia syndrome. *J Neuro-Ophthalmol* 2022;42:251–255.
54. Emamikhah M, Babadi M, Mehrabani M, Jalili M, Pouranian M, Daraie P, et al. Opsoclonus-myoclonus syndrome, a post-infectious neurologic complication of COVID-19: Case series and review of literature. *J Neurovirol* 2021;27:26–34.
55. Shah PB, Desai SD. Opsoclonus myoclonus ataxia syndrome in the setting of COVID-19 infection. *Neurology* 2021;96:33.
56. Veisi A, Bagheri A, Eshaghi M, Rikhtehgar MH, Rezaei Kanavi M, Farjad R. Rhino-orbital mucormycosis during steroid therapy in COVID-19 patients: A case report. *Eur J Ophthalmol* 2021;32:NP11–NP16.
57. Sen M, Honavar SG, Bansal R, Sengupta S, Rao R, Kim U, et al. Epidemiology, clinical profile, management, and outcome of COVID-19-associated rhino-orbital-cerebral mucormycosis in 2826 patients in India - Collaborative OPAI-IJO study on mucormycosis in COVID-19 (COSMIC), Report 1. *Indian J Ophthalmol* 2021;69:1670–1692.
58. Pakdel F, Zand A, Sharifi A, Asadi M, Abri Aghdam K. Challenges and pitfalls in the management of rhino-orbital mucormycosis in ophthalmology: A highlighted problem in the COVID-19 era. *J Ophthalmic Vis Res* 2022;17:424–431.
59. Huang C, Wang Y, Li X, Ren L, Zhao J, Hu Y, et al. Clinical features of patients infected with 2019 novel coronavirus in Wuhan, China. *Lancet* 2020;395:497–506.
60. Tostmann A, Bradley J, Bousema T, Yiek WK, Holwerda M, Bleeker-Rovers C, et al. Strong associations and moderate predictive value of early symptoms for SARS-CoV-2 test positivity among healthcare workers, the Netherlands, March 2020. *Euro Surveill* 2020;25:2000508.
61. Pardhan S, Vaughan M, Zhang J, Smith L, Chichger H. Sore eyes as the most significant ocular symptom experienced by people with COVID-19: A comparison between pre-COVID-19 and during COVID-19 states. *BMJ Open Ophthalmol* 2020;5:e000632.
62. Bolay H, Gül A, Baykan B. COVID-19 is a real headache! *Headache* 2020;60:1415–1421.
63. Colantonio MA, Nwafor DC, Jaiswal S, Shrestha AK, Elkhooly M, Rollins S, et al. Myelin oligodendrocyte glycoprotein antibody-associated optic neuritis and myelitis in COVID-19: A case report and a review of the literature. *Egypt J Neurol Psychiat Neurosurg* 2022;58:62.
64. Assavapongpaiboon B, Apinyawasisuk S, Jariyakosol S. Myelin oligodendrocyte glycoprotein antibody-associated optic neuritis with COVID-19 infection: A case report and literature review. *Am J Ophthalmol Case Rep* 2022;26:101491.
65. Fernández Alcalde C, Granados Fernández M, Nieves Moreno M, Calvo Rey C, Falces Romero I, Noval Martín S. COVID-19 ocular findings in children: A case series. *World J Pediatr* 2021;17:329–334.
66. Murchison AP, Sweid A, Dharia R, Theofanis TN, Tjoumakaris SI, Jabbour PM, et al. Monocular visual loss as the presenting symptom of COVID-19 infection. *Clin Neurol Neurosurg* 2021;201:106440.
67. Deshpande G, Giri P. Acute monocular vision loss as presenting symptom of delayed stroke from internal carotid occlusion in COVID-19. *Indian J Ophthalmol* 2021;69:1325–1327.
68. Ortiz-Seller A, Martínez Costa L, Hernández-Pons A, Valls Pascual E, Solves Alemany A, Albert-Fort M. Ophthalmic and neuro-ophthalmic manifestations of coronavirus disease 2019 (COVID-19). *Ocul Immunol Inflamm* 2020;28:1285–1289.
69. Kaya Tutar N, Kale N, Tugcu B. Adie-Holmes syndrome associated with COVID-19 infection: A case report. *Indian J Ophthalmol* 2021;69:773–774.
70. Tisdale AK, Chwalisz BK. Neuro-ophthalmic manifestations of coronavirus disease 19. *Curr Opin Ophthalmol* 2020;31:489–494.
71. Katti V, Ramamurthy LB, Kanakpur S, Shet SD, Dhoot M. Neuro-ophthalmic presentation of COVID-19 disease: A case report. *Indian J Ophthalmol* 2021;69:992–994.
72. Solorio-Pineda S, Almendárez-Sánchez CA, Tafur-Grandett AA, Ramos-Martínez GA, Huato-Reyes R, Ruiz-Flores MI, et al. Pituitary macroadenoma apoplexy in a severe acute respiratory syndrome-coronavirus-2-positive testing: Causal or casual? *Surg Neurol Int* 2020;11:304.
73. Cicalese MP, Ferrua F, Barzaghi F, Cerri F, Moro M, Aiuti A, et al. Third cranial nerve palsy in an 88-year-old man after SARS-CoV-2 mRNA vaccination: Change of injection site and type of vaccine resulted in an uneventful second dose with humoral immune response. *BMJ Case Rep* 2022;15:e246485.
74. Oliveira RM, Santos DH, Olivetti BC, Takahashi JT. Bilateral trochlear nerve palsy due to cerebral vasculitis related to COVID-19 infection. *Arq Neuropsiquiatr* 2020;78:385–386.
75. Juliao Caamaño DS, Alonso Beato R. Facial diplegia, a possible atypical variant of Guillain-Barré Syndrome as a rare neurological complication of SARS-CoV-2. *J Clin Neurosci* 2020;77:230–232.
76. García-Romo E, Blanco R, Nicholls C, Hernández-Tejero A, Fernández-de-Arévalo B. COVID-19 presenting with nystagmus. *Arch la Soc Española Oftalmol* 2021;96:224–226.
77. Ng XL, Betzler BK, Ng S, Chee SP, Rajamani L, Singhal A, et al. The eye of the storm: COVID-19 vaccination and the eye. *Ophthalmol Ther* 2022;11:81–100.
78. Petzold A. Neuro-ophthalmic implications of severe acute respiratory syndrome coronavirus 2 (SARS-CoV-2) related infection and vaccination. *Asia Pac J Ophthalmol* 2022;11:196–207.
79. Eleiwa TK, Gaier ED, Haseeb A, ElSheikh RH, Sallam AB, Elhusseiny AM. Adverse ocular events following COVID-19 vaccination. *Inflamm Res* 2021;70:1005–1009.
80. Patone M, Handunnetthi L, Saatci D, Pan J, Katikireddi SV, Razvi S, et al. Neurological complications after first dose of COVID-19 vaccines and SARS-CoV-2 infection. *Nat Med* 2021;27:2144–2153.
81. Maleki A, Look-Why S, Manhapra A, Foster CS. COVID-19 recombinant mRNA vaccines and serious ocular inflammatory side effects: Real or coincidence? *J Ophthalmic Vis Res* 2021;16:490–501.
82. Pawar N, Ravindran M, Padmavathy S, Chakrabarty S. Acute abducens nerve palsy after COVID-19 vaccination in a young adult. *Indian J Ophthalmol* 2021;69:3764–3766.

83. Karam EZ, Ríos Macias P, Chahin G, Kattah JC. Inflammatory sixth nerve palsy post-COVID-19 vaccination: Magnetic resonance imaging findings. *Neuro-Ophthalmol* 2022;46:314–318.
84. Veisi A, Najafi M, Hassanpour K, Bagheri A. Facial and abducens nerve palsies following COVID-19 vaccination: Report of two cases. *Neuro-Ophthalmology* 2022;46:203–206.
85. Ish S, Ish P. Facial nerve palsy after COVID-19 vaccination - A rare association or a coincidence. *Indian J Ophthalmol* 2021;69:2550–2552.
86. Shemer A, Pras E, Einan-Lifshitz A, Dubinsky-Pertzov B, Hecht I. Association of COVID-19 vaccination and facial nerve palsy: A case-control study. *JAMA Otolaryngol Head Neck Surg* 2021;147:739–743.
87. Ozonoff A, Nanishi E, Levy O. Bell's palsy and SARS-CoV-2 vaccines. *Lancet Infect Dis* 2021;21:450–452.
88. Mungmunpuntipantip R, Wiwanitkit V. Multiple cranial nerve palsies and COVID-19 vaccination. *Acta Neurol Scand* 2022;145:375.
89. Barreto RG, Yacovino DA, Teixeira LJ, Freitas MM. Teleconsultation and teletreatment protocol to diagnose and manage patients with benign paroxysmal positional vertigo (BPPV) during the COVID-19 pandemic. *Int Arch Otorhinolaryngol* 2021;25:e141–e149.
90. Roy M, Chandra A, Roy S, Shrotriya C. Optic neuritis following COVID-19 vaccination: coincidence or side-effect? - A case series. *Indian J Ophthalmol* 2022;70:679–683.
91. García-Estrada C, Gómez-Figueroa E, Alban L, Arias-Cárdenas A. Optic neuritis after COVID-19 vaccine application. *Clin Exp Neuroimmunol* 2022;13:72–74.
92. Alvarez LM, Ning Neo Y, Davagnanam I, Ashenhurst M, Acheson J, Abdel-Hay A, et al. Post vaccination optic neuritis: Observations from the SARS-CoV-2 pandemic. *SSRN Electron J* 2021.
93. Dreyer-Alster S, Menascu S, Mandel M, Shirbint E, Magalashvili D, Dolev M, et al. COVID-19 vaccination in patients with multiple sclerosis: Safety and humoral efficacy of the third booster dose. *J Neurol Sci* 2022;434:120155.

Case Report

# Retrocorneal Scleral Patch Supported Glue: A Technique for Management of Corneal Perforation and Corneoscleral Melt following Pterygium Surgery

**Ashok Sharma[1], MS; Rajan Sharma[1], MS; Verinder S. Nirankari[2], MD**

*Ashok Sharma, MS. Cornea Centre, SCO 2463 - 2464, Sector 22C, Chandigarh 160022, India*

**ORCID:**

*Ashok Sharma: https://orcid.org/0000-0003-0169-7033*

## Abstract

**Purpose:** To describe a new method of treatment of corneal perforation with extensive corneoscleral melt.

**Case Report:** A 42-year-old man presented with moderate-sized (3.5 mm) corneal perforation with extensive corneo-limbo-scleral ulceration following bare sclera excision of pterygium. No prior use of antimetabolites or postoperative beta radiation noted. We considered retrocorneal sclera patch supported cyanoacrylate application. The sclera was thinned to one-third thickness and a patch (4.5×4.5 mm) was punched. The sclera patch was placed on the iris, behind the corneal perforation, adequately covering it from inside. A minimal amount of adhesive was applied on the retrocorneal sclera patch and margin of corneal perforation. The ulcerating sclera was covered with double layered amniotic membrane. Topical antibiotic, steroid, and cycloplegic drops were instilled thrice daily. Corneal perforation healed and no recurrence occurred during the 18 months' follow-up.

**Conclusion:** Retrocorneal scleral patch supported cyanoacrylate is effective for corneal perforation with corneo-scleral melt.

**Keywords:** Corneal Perforation; Cyanoacrylate Tissue Adhesive; Pterygium Surgery; Scleral Necrosis; Scleral Patch

*J Ophthalmic Vis Res* 2023; 18 (1): 123–129

**Correspondence to:**

Ashok Sharma, MS. Cornea Centre, SCO 2463 - 2464, Sector 22C, Chandigarh 160022, India.
E-mail: asharmapgius@yahoo.com

Received: 01-11-2021 Accepted: 15-02-2022

**Access this article online**

**Website:** https://knepublishing.com/index.php/JOVR

**DOI:** 10.18502/jovr.v18i1.12732

This is an open access article distributed under the Creative Commons Attribution License, which permits unrestricted use, distribution, and reproduction in any medium, provided the original work is properly cited.

**How to cite this article:** Sharma A, Sharma R, Nirankari VS. Retrocorneal Scleral Patch Supported Glue: A Technique for Management of Corneal Perforation and Corneoscleral Melt following Pterygium Surgery . J Ophthalmic Vis Res 2023;18:123–129.

© 2023 Sharma et al. This is an open access article distributed under the Creative Commons Attribution License | Published by Knowledge E

## INTRODUCTION

Pterygium excision with conjunctival autograft, pterygium excision with amniotic membrane graft, and pterygium excision with combined conjunctival autograft and amniotic membrane graft have been advocated for primary or recurrent pterygium.[1] The bare sclera technique, although technically simple and easy, is associated with a high incidence of recurrence (62%) and is no longer favored.[2] Pterygium excision with conjunctival autograft is the preferred treatment modality for primary pterygium.

Scleral necrosis has been reported following the bare sclera excision technique and the use of beta radiation and antimetabolites (thiotepa and mitomycin C) in the postoperative period.[2, 3] Cases of scleral necrosis following the bare sclera technique without the use of beta radiation and antimetabolites have also been reported.[3] Corneal ulceration may be treated with amniotic membrane graft, deep anterior lamellar keratoplasty, or therapeutic penetrating keratoplasty.[4] Scleral ulceration may be treated with amniotic membrane graft, conjunctival autograft, Tenon's capsule graft, and scleral graft.[5] Moderate corneal perforation, extensive corneo-limbo-scleral melt is an extremely rare complication of pterygium surgery and poses a management challenge. In the presence of the extensive corneo-limbo-scleral ulceration, deep anterior lamellar keratoplasty or therapeutic penetrating keratoplasty could not be considered. Application of cyanoacrylate tissue adhesive alone also was not feasible, as perforation was large. We report such a case successfully managed with retrocorneal sclera patch augmented cyanoacrylate tissue adhesive application.

## CASE REPORT

A 42-year-old man presented with persistent pain, redness, watering and diminution of vision in the right eye for three weeks. Referring ophthalmologist performed pterygium surgery using bare sclera technique and patient was fine for four weeks and then developed symptoms. The referring ophthalmologist treated the patient with topical antibiotic and steroid for three weeks. Observing no response, the patient was referred to. No antimetabolites or postoperative beta radiation were used in this case. The operating surgeon had used heat cautery on the sclera. Patient did not reveal any history suggestive of systemic autoimmune disorder. At the time of presentation, his visual acuity was 4/60 in the right eye and 6/6 in the left eye. Intraocular pressure in the left eye was 16 mmHg. Slit-lamp biomicroscopy revealed large area of corneal perforation (3.5×3.5 mm) and extensive corneo-limbo-scleral necrosis [Figure 1]. The left eye did not reveal any abnormality.

The material obtained on corneal scrapings were subjected to the detailed microbiological tests. Direct microscopy and cultures of the scraping material did not reveal any bacterial or fungal pathogen. Hematological investigations including complete blood count, erythrocyte sedimentation rate, rheumatoid factor, anti-nuclear antibody, ant-DNA antibodies, liver function tests, renal function tests, C-reactive protein and antineutrophil cytoplasmic antibodies were normal. Serology markers of human immunodeficiency virus 1 and 2, varicella-zoster virus, hepatitis B surface antigen, hepatitis C and venereal disease research laboratory test were non-reactive. Chest radiography and the Montoux test were normal.

### Surgical Technique

Retrocorneal scleral patch augmented cyanoacrylate tissue adhesive application was done under peribulbar anesthesia, in the operating room using surgical microscope. The right eye was prepared and draped aseptically. The ocular surface was exposed using Barraquer eye speculum. The area of corneo-limbo-scleral ulceration was cleaned and the debris was removed. The size of the corneal perforation was

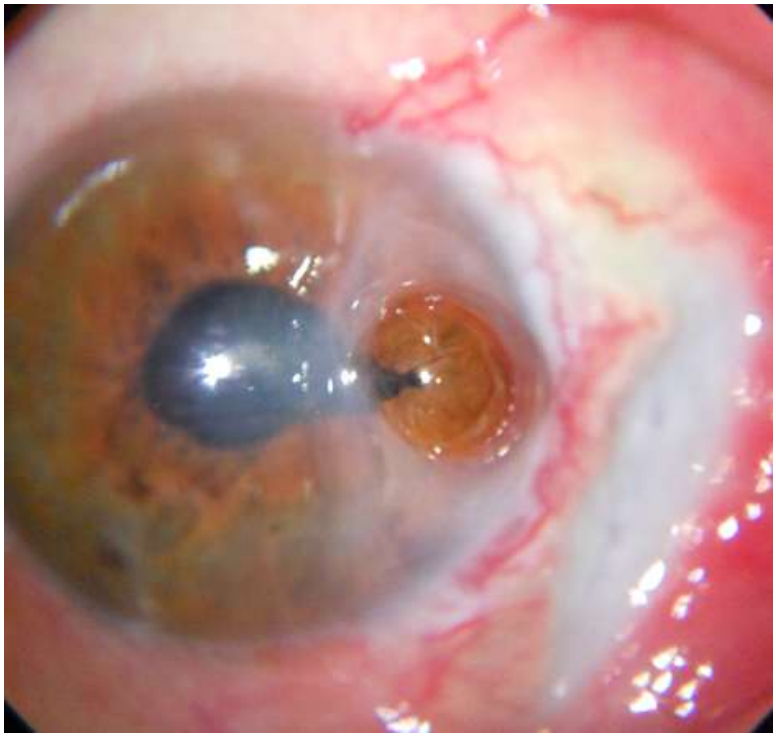

**Figure 1.** Corneal perforation (3.5 mm) with iris presenting at the site with extensive corneo-limbo-scleral melt.

measured with Castroviejo calipers. The corneal perforation measured 3.5×3.5 mm [Figure 2a]. The donor sclera was obtained from eyes not suitable for optical PKP. Donor sclera obtained from the local eye bank and stored in pure glycerin was taken out and placed in the normal saline for 15 min. The sclera was placed in the solution containing amikacin sulphate 2% (Alfakim 500 mg/2 ml Ranbaxy India) and vancomycin hydrochloride 5% (Vanking 500 mg/vial Neon Laboratories India) for 5 min. The sclera was thinned to one-third of its thickness and a patch (4.5×4.5 mm) was punched out with skin biopsy punch [Figure 2b]. The scleral patch was thinned to one-third of its thickness with crescent knife. The adhesions between the iris and the margin of corneal perforation were lysed. A small iridotomy was performed. The scleral patch was placed on the iris, beneath the corneal perforation [Figure 2c]. The scleral patch and the surrounding cornea surface were dried with Weck-cel ophthalmic sponge. Isoamyl 2-cyanoacrylate (Amcrylate; Concord Drugs Ltd, Hayathnagar, Andhara Pradesh, India) was drawn into a 2 ml disposable syringe with a 26 gauge needle. The minimal amount of cyanoacrylate tissue adhesive (Amcrylate; Concord Drugs Ltd, Hayathnagar, Andhara Pradesh India) was applied on the retrocorneal sclera patch and margin of the corneal perforation [Figure 2d]. The cyanoacrylate tissue adhesive was allowed to polymerize [Figure 2e]. An air bubble was placed in the anterior chamber. The ulcerating limbus and the sclera were covered with double-layered amniotic membrane graft. Amniotic membrane graft was sutured with Vicryl 8 '0' suture. A bandage contact lens was placed [Figure 2f].

The patient was put on topical moxifloxacin 0.5% (Vigamox; Alcon Laboratories, Inc., Fort Worth, TX) four times a day, atropine sulfate 1% (Atropine; Jawa Pvt. Ltd., Gurgaon, Haryana, India) three times a day, and carboxymethylcellulose 1% (Refresh Liquigel; Allergan, Pithampur, Madhya Pradesh, India) four times a day. After 72 hr, topical prednisolone 1% (Allergan Ltd, West-port, Co, Mayo, Ireland) four times a day was added. The patient was given intravenous methylprednisolone (1 gr)

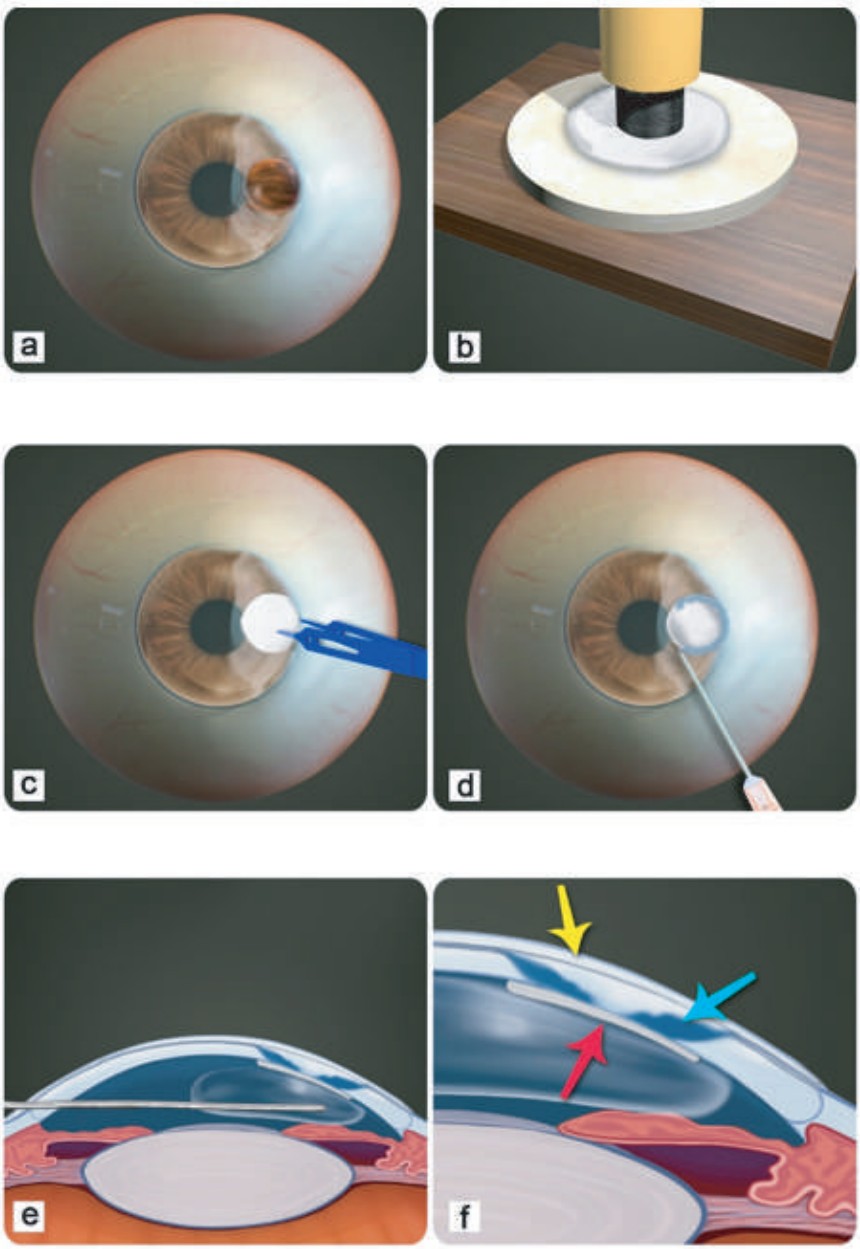


**Figure 2.** Diagramatic presentation of retrocorneal sclera patch supported cyanoacrylate tissue adhesive application: (a) Corneal perforation (3.5×3.5 mm), corneal, limbal and sclera melt; (b) Punching of sclera patch (4.5×4.5 mm) using a skin bopsy punch; (c) Placing the thinned sclera patch behind the corneal perforation; (d) Application of minimum quantity of cyanoacrylate tissue adhesive at the margin of perforation on the sclera patch; (e) Injecting an air bubble in the anterior chamber; (f) At completion of surgical procedure, retrocorneal sclera patch (red arrow), cyanoacrlate tissue adhesive (blue arrow), and bandage contact lens (yellow arrow).

daily for three days followed by oral prednisolone 60 mg daily for two weeks and tapered over six weeks.

At 72 hr, the scleral patch, cyanoacrylate tissue adhesive plug, and double layered amniotic membrane graft were in place [Figure 3a]. At two weeks, corneal perforation was sealed and scleral necrosis started healing [Figure 3b]. At eight weeks' follow-up, cyanoacrylate tissue adhesive plug became lose and the scleral patch developed vascularization. The cyanoacrylate tissue adhesive plug was carefully separated from the underlying sclera patch and removed. At 12 weeks, the corneal perforation healed and the patient developed

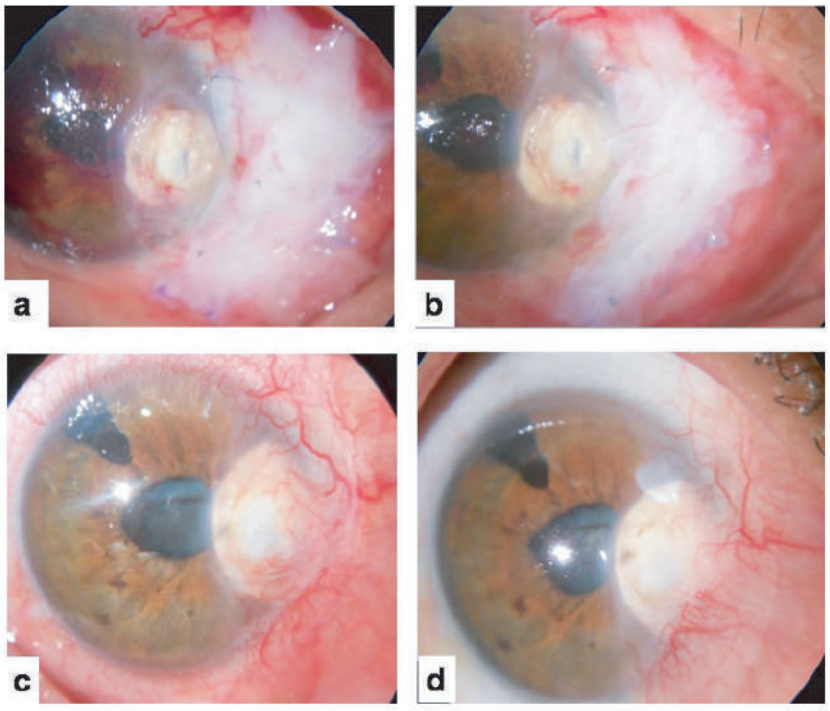


**Figure 3.** (a) Sealed corneal perforation 72 hr after surgery (scleral patch, CTA plug, and double layered AMG in place). (b) Corneal perforation sealed and corneo-limbo-scleral necrosis at healing stage at two-weeks' follow-up. (c) Healed corneal perforation (sclera patch in place) and pseudo-pterygium at 12 weeks' follow-up. (d) Healed corneal perforation (sclera patch in place) and pseudo-pterygium at 18 months' follow-up.

pseudo-pterygium. At 20 weeks, patient was diagnosed as suffering from intumescent cataract. Cataract surgery was performed. He was advised excision of the pseudo-pterygium but was reluctant [Figure 3c]. During the 18 months' follow-up, patient did not develop any recurrence, the scleral patch remained in place and the patient had pseudo-pterygium [Figure 3d].

## DISCUSSION

Retrocorneal scleral patch supported cyanoacrylate tissue adhesive application healed the corneal perforation and the amniotic membrane graft healed the corneo-limbo-scleral melt following pterygium surgery. Cyanoacrylate tissue adhesive is the gold standard treatment for corneal perforation.[6] Cyanoacrylate tissue adhesive application used alone was not feasible because of the size (3.5 mm) of the perforation and also due to the risk of its inadvertent access into the anterior chamber.[7] Due to extensive corneo-scleral ulceration around the corneal perforation, we did not consider scleral patch augmented cyanoacrylate tissue adhesive application technique.[8] In this technique, the partial thickness scleral patch is placed on the perforation anteriorly, and cyanoacrylate tissue adhesive is applied on the margin and surface of the scleral patch.[8] In another technique for moderate corneal perforations due to rheumatoid arthritis, a partial thickness scleral patch was placed in the intracorneal lamellar pocket and then cyanoacrylate tissue adhesive was applied.[9] Since our patient had extensive corneal and sclera melt surrounding the corneal perforation, both these techniques could not be executed. The only option left to the authors was to place a sclera patch on the iris, behind the corneal perforation and then apply the cyanoacrylate tissue adhesive to seal the perforation. To the best of authors' knowledge, this technique has not

been reported in literature. Amniotic membrane,[10] Tenon's capsule,[11] and cornea have also been used as tissue scaffolds to support cyanoacrylate tissue adhesive in treatment of moderate corneal perforations.

Bare-sclera technique of pterygium excision is not a favored treatment option.[2] Most corneal surgeons prefer pterygium excision with conjunctival auto graft (CAG for both primary and recurrent pterygium.[1] Bare sclera technique has high recurrence rate (60–80%).[2] Bare sclera was previously combined with either post-op beta radiation or anti-metabolites (thiotepa or mitomycin-c). However, the use of both postoperative beta radiation and thiotepa/mitomycin-C has been reported to cause scleral necrosis.[2] In most cases of scleral necrosis, mitomycin has been used several times more than the recommended concentration and dosage.[1] These agents are used to reduce the recurrence of pterygium excision. The underlying pathogenesis of sclera melt include obliterative endarteritis and inhibition of mitosis in capillary endothelium. Therefore, the use of mitomycin with bare sclera technique is not advocated. Low-dose mitomycin-C associated with pterygium excision and limbal conjunctival grafts have been found to be successful.[1] However, scleral necrosis and corneal melt have been reported following bare sclera technique in the absence of the use of postoperative beta radiation or anti-metabolite.[3] In our patient, the primary operating surgeon did not use any postoperative beta radiation or anti-metabolite. Several ocular and systemic comorbidities can also predispose an inclination to sclera/cornea melt. Our patient did not have any collagen vascular disorder including rheumatoid arthritis or Wegner's granulomatosis.

To speculate the etiopathogenesis in our patient is difficult. Underlying etiopathogenesis may be infection, ischemia, or inflammation. Infective etiology was ruled out as all microbiological tests were negative. Primary ischemic etiology was unlikely as the patient had not received intra/postoperative mitomycin C. Light cautery application to bleeding vessels in the sclera bed could be held responsible for severe ischemia and scleral melt. It appears that bare sclera technique causing exposure of sclera was responsible for inducing inflammation that resulted in ischemia and ulceration. Clinical presentation and signs in our case simulate surgery-induced necrosis of the sclera.

In our patient, in addition to retrocorneal sclera patch augmented cyanoacrylate tissue adhesive application, double layered amniotic membrane graft was applied. Amniotic membrane graft coupled with intravenous methylprednisolone and later oral prednisolone decreased inflammation, arrested corneal scleral ulceration, promoted healing and epithelization. Patients not responding to corticosteroids or developing complications of oral steroids may need immunosuppressive agents.

In summary, this case report demonstrates that retrocorneal sclera patch augmented cyanoacrylate tissue adhesive healed the moderate sized (3.5 mm) corneal perforation in association with extensive corneo-limbo-scleral melt following pterygium surgery.

## Financial Support and Sponsorship

None.

## Conflicts of Interest

There are no conflicts of interest.

## *REFERENCES*

1. Sharma A, Gupta A, Ram J, Gupta A. Low-dose intraoperative mitomycin-C versus conjunctival autograft in primary pterygium surgery: Long term follow-up. *Ophthalmic Surg Lasers* 2000;31:301–307.
2. Tan DT, Chee SP, Dear KB, Lim AS. Effect of pterygium morphology on pterygium recurrence in a controlled trial comparing conjunctival autografting with bare sclera excision. *Arch Ophthalmol* 1997;115:1235–1240.

3. Alsagoff Z, Tan DT, Chee SP. Necrotising scleritis after bare sclera excision of pterygium. *Br J Ophthalmol* 2000;84:1050–1052.
4. Ti SE, Tan DT. Tectonic corneal lamellar grafting for severe scleral melting after pterygium surgery. *Ophthalmology* 2003;110:1126–1136.
5. Siatiri H, Mirzaee-Rad N, Aggarwal S, Kheirkhah A. Combined tenonplasty and scleral graft for refractory pseudomonas scleritis following pterygium removal with mitomycin C application. *J Ophthalmic Vis Res* 2018;13:200–202.
6. Saini JS, Sharma A, Grewal SP. Chronic corneal perforations. *Ophthalmic Surg* 1992;23:399–402.
7. Sharma A, Kaur R, Kumar S, Gupta P, Pandav S, Patnaik B, et al. Fibrin glue versus N-butyl-2-cyanoacrylate in corneal perforations. *Ophthalmology* 2003;110:291–298.
8. Sharma A, Mohan K, Sharma R, Nirankari VS. Scleral patch graft augmented cyanoacrylate tissue adhesive for treatment of moderate-sized noninfectious corneal perforations (3.5–4.5 mm). *Cornea* 2013;32:1326–1330.
9. Sharma A, Sharma R, Nirankari VS. Intracorneal scleral patch supported cyanoacrylate application for corneal perforations secondary to rheumatoid arthritis. *Indian J Ophthalmol* 2021;69:69–73.
10. Kitagawa K, Okabe M, Yanagisawa S, Zhang XY, Nikaido T, Hayashi A. Use of a hyperdried cross-linked amniotic membrane as initial therapy for corneal perforations. *Jpn J Ophthalmol* 2011;55:16–21.
11. Sharma N, Singhal D, Maharana PK, Vajpayee RB. Tuck-in tenon patch graft in corneal perforation. *Cornea* 2019;38:951–954.

Case Report

# A Multifaceted Approach to Treatment of Recalcitrant Cutaneous Periorbital Juvenile Xanthogranuloma

**Alexandra Van Brummen[1], MD; Sarah Jacobs[2], MD; Shu Feng[1], MD; Emily Li[1,3], MD; Arash J. Amadi[1], MD**

[1]*Department of Ophthalmology, University of Washington, Seattle, WA, USA*
[2]*Department of Ophthalmology, University of Alabama, Birmingham, AL, USA*
[3]*Wilmer Eye Institute, Johns Hopkins University, Baltimore, MD, USA*

**ORCID:**
*Alexandra Van Brummen: https://orcid.org/0000-0003-4383-5035*
*Arash J. Amadi: https://orcid.org/0000-0001-6560-0013*

## Abstract

**Purpose:** To demonstrate novel treatments for patients with high juvenile xanthogranuloma (JXG) eyelid lesion burden.
**Case Report:** A 14-year-old girl was referred to the oculoplastic surgery service for management of worsening extensive bilateral eyelid and adnexal lesions in the setting of JXG. The patient underwent intra-lesional steroid injections, serial excisions, and reconstruction with skin grafts. She was subsequently treated with $CO_2$ laser-assisted topical steroid application, which resulted in lesion regression.
**Conclusion:** A novel multimodal approach to treatment of severe periocular JXG, incorporating surgical debulking, skin autograft, CO2 laser, and intra-lesional steroids, can be effective for lesion control.

**Keywords:** $CO_2$ Laser; Juvenile Xanthogranuloma; Laser-assisted Steroid Delivery

*J Ophthalmic Vis Res* 2023; 18 (1): 130–134

The material was previously presented at the ASOPRS Spring 2017 Meeting in Vancouver, British Colombia.

## INTRODUCTION

Juvenile xanthogranuloma (JXG) represents one of the most common manifestations of non-Langerhans cell histiocytosis.[1] Patients typically present with red–yellow papules or nodules, which occur more extensively in the pediatric population compared to adult patients.[1, 2] JXG lesions most commonly present cutaneously, however, they can affect intraocular structures in 0.3–10% of pediatric cases.[3] In rare cases, JXG has also been reported to involve pulmonary, pericardial,

**Correspondence to:**
Alexandra Van Brummen, MD. Department of Ophthalmology, University of Washington, School of Medicine, 325 9th Ave., PO Box 359608, Seattle, WA 98104, USA.
E-mail: avanbrum@uw.edu

Received: 03-05-2021 Accepted: 25-02-2022

Access this article online

**Website:** https://knepublishing.com/index.php/JOVR

**DOI:** 10.18502/jovr.v18i1.12733

This is an open access article distributed under the Creative Commons Attribution License, which permits unrestricted use, distribution, and reproduction in any medium, provided the original work is properly cited.

**How to cite this article:** Van Brummen A, Jacobs S, Feng S, Li E, Amadi AJ. A Multifaceted Approach to Treatment of a Recalcitrant Cutaneous Periorbital Juvenile Xanthogranuloma. J Ophthalmic Vis Res 2023;18:130–134.


© 2023 Van Brummen et al. This is an open access article distributed under the Creative Commons Attribution License | Published by Knowledge E

testicular, hepatic, central nervous system, and skeletal system tissues.[4] Management varies depending on the location involved and the extent of disease burden, spanning a range from observation to topical steroid application to surgical excision with or without radiation treatment.[2, 3] The authors present a rare case of JXG with extensive periorbital soft tissue involvement that required multi-modal management including surgical excision, skin grafting, and laser-assisted drug delivery of intra-lesional steroids. Collection and evaluation of protected patient health information was in compliance with the Health Insurance Portability and Accountability Act of 1996 and adhered to the ethical principles outlined in the Declaration of Helsinki as amended in 2013. Informed consent for use of photos was obtained from the patient.

## CASE REPORT

A 14-year-old female presented to ophthalmology clinic as a referral for JXG involving the bilateral eyelids and sinus passages. The skin lesions were first noted around age eight and increased in size until age ten. She had previously undergone surgical debulking for extensive JXG infiltration of the sinonasal mucosa. On examination, her Snellen visual acuity was 20/20 bilaterally. Intraocular pressure and extraocular motility were normal. She had numerous protuberant lesions on the upper and lower eyelids bilaterally [Figures 1 & 2A]. Full dilated examination ruled out ocular involvement.

Per patient preference, the periocular skin lesions were observed for a year after presentation to ophthalmology department. When no spontaneous lesion regression occurred during that time, the patient agreed to proceed with serial lesion excision with skin grafting, one eyelid at a time, each separated by a two-week interval. Full-thickness skin autografts were obtained from retro-auricular skin for the bilateral lower eyelids and upper inner arm skin for the upper eyelids. Intralesional injections of triamcinolone acetonide (40 mg/mL) were given in the upper eyelids at two-week intervals prior to lesion excision (at four and two weeks preoperatively in the right upper lid; and six, four, and two weeks preoperatively in the left upper lid). Silicone scar gel was utilized postoperatively to help with scar modulation of the skin grafts on all four eyelids, starting postoperative week three and continuing through postoperative month three. The patient healed well without excessive trichiasis or other recurrence of lesions [Figure 2B]. At postoperative month three, the patient had persistent lesions along the outer perimeter of her skin graft sites. She underwent serial treatments of $CO_2$ laser resurfacing (four total treatments, given at two-to-three-month intervals), utilizing the Lumens UltraPulse $CO_2$ laser (Lumenis, Yokne'am Illit, Israel). For each treatment, the SCAAR-Fx setting (5% density, 80 mJ, 200 Hz) was applied to the preseptal region and DeepFx setting (10% density, 15 mJ, 250 Hz) was applied to the entire periocular zone. Immediately after the laser application, topical triamcinolone acetonide (40 mg/mL) was massaged into the treated skin, which allows for laser-assisted drug delivery.[5] The patient demonstrated further improvement after $CO_2$ laser resurfacing [Figure 2C].

At the most recent follow-up 39 months after lesion excision, examination revealed lesion regrowth on the superonasal upper lids [Figure 2D]. The involved areas were small, and the patient was not bothered by them functionally or cosmetically. Her exam otherwise demonstrated well-healed skin grafts and an overall acceptable outcome. Further treatment with intra-lesional steroids was offered, but the patient deferred them in pursuit of naturopathic treatments.

## DISCUSSION

JXG is the most common non-Langerhans cell histiocytosis, typically presenting in childhood with red–yellow papules or nodules.[1, 2] On histopathology, involved skin cells, derived from dermal dendrites, express CD1a but do not exhibit reactivity for S-100 protein or contain Birbeck granules.[2] The disease can present with systemic involvement, affecting the brain, eye, lungs, liver, spleen, and other organs.[2] Failure to recognize systemic involvement can result in fatal consequences for patients. Freyer et al described a case initially characterized as isolated cutaneous JXG, subsequently found to have intracranial disease when the patient developed seizures one month after initial diagnosis, warranting systemic treatment with chemotherapy.[2] Conditions including neurofibromatosis type I (NF-1) and juvenile myelomonocytic leukemia can additionally present with JXG.[3] In patients younger than three years of age, 18% of those diagnosed


**Figure 1.** Demonstration of extensive upper and lower lid lesions (A, B, C) with satellite lesions extending towards upper brow.

with NF-1 were also found to have JXG.[3, 6] In addition, patients with NF-1 and JXG have a 20 to 30 times higher risk of developing comorbid juvenile myelomonocytic leukemia.[3, 7] Diagnosis of JXG warrants further serologic evaluation with a complete blood count and comprehensive metabolic panel to screen for hepatic, renal, and hematopoietic abnormalities.

Achieving sustained regression of JXG lesions remains a clinical challenge. Surgical excision and chemotherapy with vinblastine, methotrexate, and others play roles in systemic management.[2] For intracranial lesions, the treatment of choice has typically been described as surgical excision, at times supplemented by radiation.[8]

Sustained regression of isolated cutaneous lesions also poses a clinical challenge. Some suggest a period of observation as cutaneous lesions have been known to spontaneously regress.[1] For persistent cases, the mainstay of treatment includes intra-lesional or topical corticosteroids.[3, 9] Elner et al reviewed six cases demonstrating improvement in symptoms of orbital and eyelid xanthogranuloma, including improvement of lid ptosis and diplopia, with triamcinolone acetonide 40 mg/mL injections alone.[9] Similarly, Kuruvilla et al described regression of an eyelid JXG lesion in an infant in response to intra-lesional steroid injection.[10] However, neither reported complete resolution of clinical evidence of disease; rather, they described partial regression, which alleviated disease symptoms. In addition, the lesion burden of the described patients was mild compared to the case presented in our report.

For more severe cases with larger or multiple lesions, treatment modalities extend beyond corticosteroids. One author described elimination of multiple JXG lesions without recurrence after $CO_2$ laser treatment.[11] Others have also described successful use of $CO_2$ laser in treatment of necrobiotic xanthogranuloma lesions in the setting of lymphoplasmacytic lymphoma.[12] Finally, surgical excision has been described in some cases of cutaneous lesions as well, especially in cases of large disfiguring or debilitating lesions in young children.[3]

In summary, the authors present a multifaceted approach to treatment of cutaneous periorbital JXG recalcitrant to local corticosteroid treatment alone. A combination of intra-lesional steroid injection, surgical lesion debulking, skin graft reconstruction, and $CO_2$ laser skin resurfacing with laser-assisted drug delivery produced great improvement in the patient's functional and cosmetic concerns, maintained for several years before partial relapse. Because a multipronged approach to treatment was used, it is not possible to discern with certainty that the laser-assisted steroid delivery was the main reason for improvement, as the steroid injections may also have contributed to the results. Future investigation includes optimization

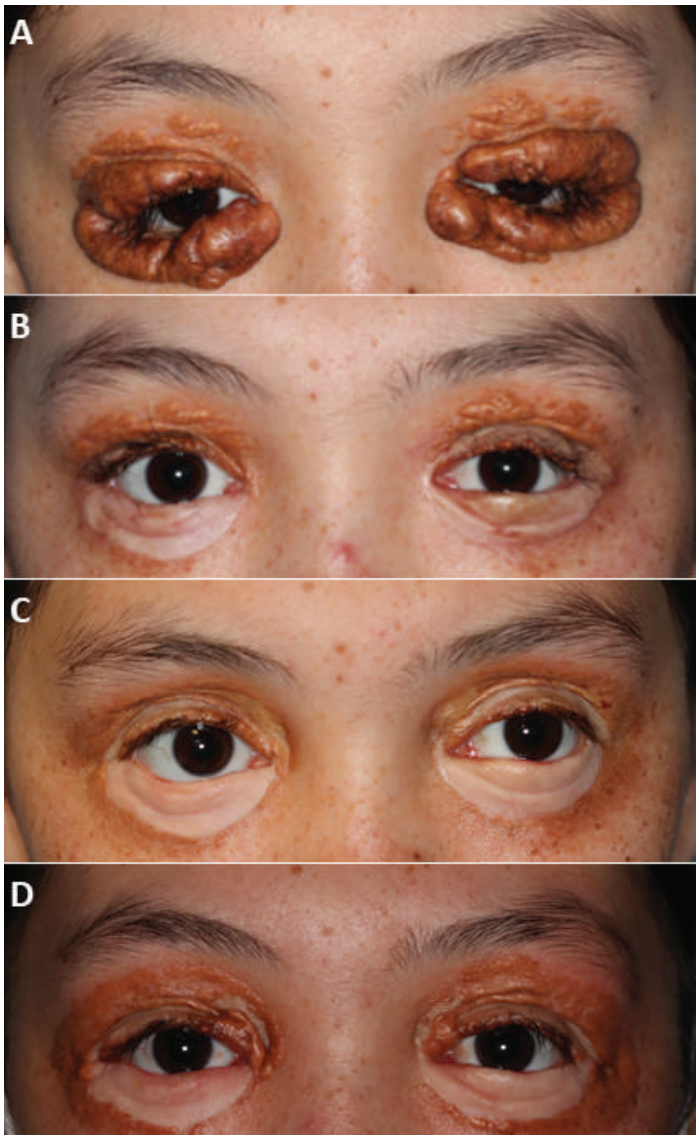


**Figure 2.** Periorbital lesions preoperatively (A) compared to status post-surgical excision and intralesional steroid application (B). (C) Postoperative month three after $CO_2$ laser resurfacing. (D) Demonstration of persistent regression of lesions 39 months postoperatively, with only mild recurrence.

of $CO_2$ laser treatment regimen (total number of treatments, treatment interval, and subsequent maintenance treatments for localized lesion recurrence) and steroid delivery.

## Declaration of patient consent

The patient agreed to the publication of this case report and photos, and a signed University of Washington media release for publication was completed.

## Financial Support and Sponsorship

EL is the endowed James L. Hargiss, M.D., Ophthalmic Plastic and Reconstructive Surgery Fellow and the Rayment Endowed Fellow in Ophthalmology. The department is funded by an unrestricted grant from Research to Prevent Blindness.

## Conflicts of interest

The authors have no financial or conflicts of interest disclosures.

## REFERENCES


1. Wollina U, Burgdor WHC, Haroske G. Disseminated Juvenille Xanthogranuloma. *JDDG* 2006;4:45–48.
2. Freyer DR, Kennedy R, Bostrom BC, Kohut G, Dehner LP. Juvenile xanthogranuloma: Forms systemic disease and their clinical implications. *J Pediatr* 1996;129:227–237.
3. Samara WA, Khoo CTL, Say EAT, Saktanasate J, Eagle Jr RC, Shields JA, et al. Juvenile xanthogranuloma involving the eye and ocular adnexa. *Ophthalmology* 2015;122:2130–2138.
4. Chang MW, Frieden IJ, Good W. The risk of intraocular juvenile xanthogranuloma: Survey of current practices and assessment of risk. *J Am Acad Dermatol* 1996;34:445–449.
5. Park JH, Chun JY, Lee JH. Laser-assisted topical corticosteroid delivery for treatment of keloids. *Lasers Med Sci* 2017;32:601–608.
6. Cambiaghi S, Restano L, Caputo R. Juvenile xanthogranuloma associated with neurofibromatosis 1:14 patients without evidence of hematologic malignancies. *Pediatr Dermatol* 2004;21:97–101.
7. Zvulunov A, Barak Y, Metzker A. Juvenile xanthogranuloma, neurofibromatosis, and juvenile chronic myelogenous leukemia: World statistical analysis. *Arch Dermatol* 1995;131:904–908.
8. Vijapura JA, Fulbright JM. Use of radiation in treatment of central nervous system juvenile xanthogranulomatosis. *Pediatr Hematol Oncol* 2012;29:440–445.
9. Elner V, Mintz R, Demirci H, Hassan AS. Local corticosteroid treatment of eyelid and orbital xanthogranuloma. *OPRS* 2006;22:36–40.
10. Kuruvilla R, Excaravage GK, Finn AJ, Dutton JJ. Infiltrative subcutaneous juvenile xanthogranuloma of the eyelid in a neonate. *OPRS* 2009;25:330–332.
11. Klemke CD, Held B, Dippel E, Goerdt S. Multiple juvenile xanthogranulomas successfully treated with CO2 laser. *JDDG* 2007;5:30–33.
12. Vieira V, Del Pozo J, Martinez W, Veiga-Barreiro JA, Fonseca E. Necrobiotic xanthogranuloma associated with lymphoplasmacytic lymphoma. Palliative treatment with carbon dioxide laser. *Eur J Dermatol* 2005;15:182–185.

Photo Essay

# Tantalum Surgical Clip Presenting As an Intraorbital Foreign Body

**George P. Kung[1], BS; Jeremy D. Clark[2], MD; Austin Gerber[2], MD; Niloofar Piri[1], MD**

[1]*Department of Ophthalmology, Saint Louis University School of Medicine, St. Louis, Missouri*
[2]*Department of Ophthalmology and Visual Sciences, Kentucky Lions Eye Center, University of Louisville, Louisville, Kentucky*

**ORCID:**
*Niloofar Piri: https://orcid.org/0000-0002-0685-028X*
*George Kung: https://orcid.org/0000-0001-8554-5613*

*J Ophthalmic Vis Res* 2023; 18 (1): 135–137

## PRESENTATION

An 87-year-old female presented to the emergency room after she was partially run over by a truck and sustained multiple injuries including skull and facial trauma. Facial bones CT scan was significant for a large, metallic intraorbital foreign body on the left side [Figure 1]. Per radiology, an intraocular foreign body (IOFB) could not be ruled out. Ophthalmology department was consulted to evaluate. She had a history of scleral buckling in the left eye for rhegmatogenous retinal detachment in the 1990s, with chronic mild low vision at baseline.

Her near corrected visual acuity was 20/20 OD and 20/60 OS; intraocular pressures were 14 OD, 11 mmHg OS. A relative afferent pupillary defect was present on the left. Examination revealed left upper lid hematoma, lower lid ecchymosis, deep laceration above eyebrow, superior subconjunctival hemorrhage, and pseudophakia. Fundus exam on the left revealed no vitreous hemorrhage, 360 high buckle effect, temporal cryopexy scars, and small hemorrhage on the buckle. No intraocular penetration site was seen, and foreign body appeared to be intraorbital only.

**Correspondence to:**

Niloofar Piri, MD. Department of Ophthalmology, Saint Louis University School of Medicine, 1008 South Spring Ave, St. Louis, MO 63110, USA.
E-mail: niloofar.piri@health.slu.edu

Received: 05-02-2022 Accepted: 01-06-2022

**Access this article online**

**Website:** https://knepublishing.com/index.php/JOVR

**DOI:** 10.18502/jovr.v18i1.12734

Laceration was the suspected entry site. Clinical exam was not concerning for IOFB, but given the large, and irregular shape of the foreign body in addition to embedding on the globe with air track, the decision was made to proceed with exploratory orbitotomy and foreign body removal.

Superior orbitotomy through upper lid crease was performed with opening of the septum. Exploration and irrigation failed to retrieve any foreign body. Intraoperative skull X-ray was performed, which revealed the presence of a small metallic foreign body in the superonasal orbit in a regular shape similar to a surgical clip [Figures 2A & 2B].

Surgical plan was changed, and superior 120° peritomy was performed with isolation of the superior rectus muscle. Metallic foreign body was revealed to be a tantalum surgical clip. Upon contact with the retina surgeon's office, it was confirmed to be a non-magnetic tantalum clip used to secure the scleral buckle.

## DISCUSSION

While ophthalmologists have moved onto the usage of sutures or silicone sleeves to secure

This is an open access article distributed under the Creative Commons Attribution License, which permits unrestricted use, distribution, and reproduction in any medium, provided the original work is properly cited.

**How to cite this article:** Kung GP, Clark JD, Gerber A, Piri N. Tantalum Surgical Clips Presenting As an Intraorbital Foreign Body. J Ophthalmic Vis Res 2023;18:135–137.

© 2023 Kung et al. This is an open access article distributed under the Creative Commons Attribution License | Published by Knowledge E

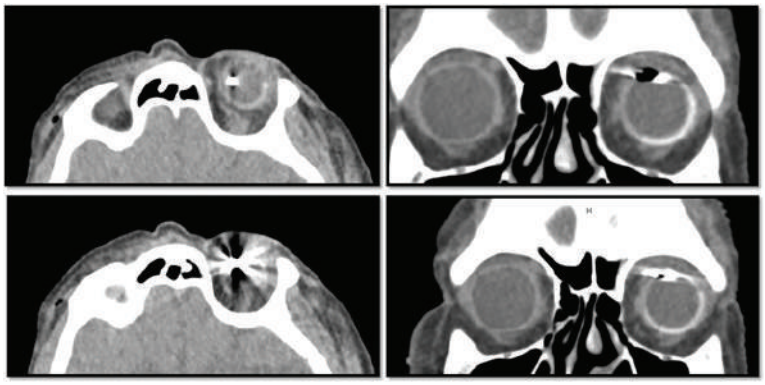

**Figure 1.** Orbital CT scan. Axial sections with suspected intraocular hyperdense metallic foreign body (Left panel). Large metallic foreign body with irregular borders complicated by streak artifact and air track superonasally embedding into the sclera (Right panel).
CT, computed tomography.

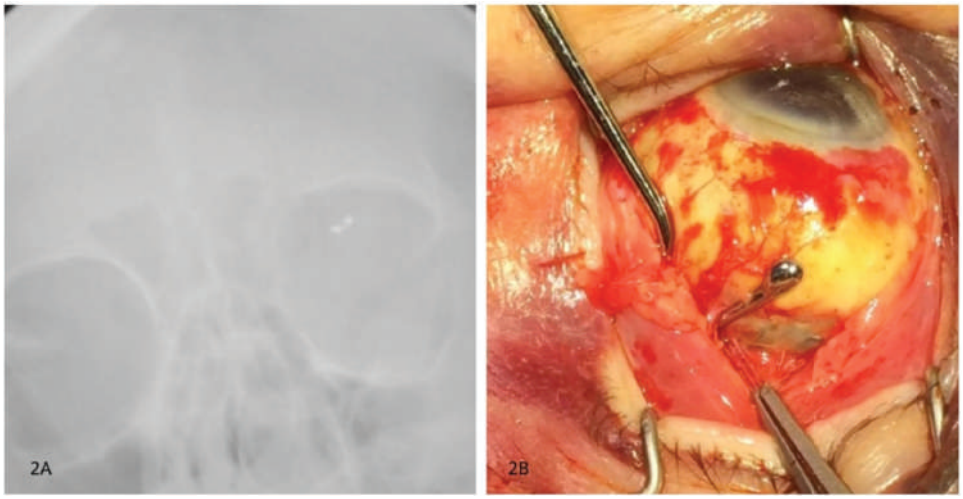


**Figure 2.** (A) Intraoperative X-ray demonstrating metallic foreign body in left orbit to be symmetric surgical clip. (B) Metallic surgical clip used to secure buckle located superonasally.

scleral buckles in the past two decades, tantalum clips were a common option in historical scleral buckle surgery.[1]

The properties of tantalum posed a unique diagnostic challenge in this case. While radiopaque on X-rays, tantalum has the disadvantage of producing streak artifacts on CT.[1–3] The irregular margins of the foreign body produced by the artifact on CT made it difficult to not only see the shape of the clip but also localize its location. Plain radiographs are not a typical part of foreign body workup due to their underestimation of common radiolucent foreign bodies such as wood or plastic.[4, 5] Had an X-ray been considered in the context of the patient's surgical history and artifact on CT, the surgical clip likely would have been identified earlier and surgery been avoided.

In summary, foreign bodies can present a complex problem when initial diagnostic imaging is uncertain. In patients with a historical scleral buckle procedure, consider the presence of tantalum clips as a possibility.

## Financial Support and Sponsorship

None.

## Conflicts of Interest

None.

## REFERENCES


1. Wilkinson CP, Michels RG, Rice TA. Michels retinal detachment. Mosby; 1997. p. 1163.
2. Gross SC, Kowalski JB, Lee SH, Terry B, Honickman SJ. Surgical ligation clip artifacts on CT scans. *Radiology* 1985;156:831–832.
3. Schepens CL, Hartnett ME, Hirose T. Schepens' retinal detachment and allied diseases. Butterworth-Heinemann; 2000. p. 792.
4. Pinto A, Brunese L, Daniele S, Faggian A, Guarnieri G, Muto M, et al. Role of computed tomography in the assessment of intraorbital foreign bodies. *Semin Ultrasound CT MRI* 2012;33:392–395.
5. Bryden FM, Pyott AA, Bailey M, McGhee CNJ. Real time ultrasound in the assessment of intraocular foreign bodies. *Eye* 1990;4:727–731.

Letter

# What is the Real Cost of Intraoperative Floppy Iris Syndrome in Cataract Surgery?

**Argyrios Tzamalis, MD, PhD; Chrysanthos D. Christou, MD; Efthymia Prousali, MD; Asimina Mataftsi, MD, PhD; Nikolaos Ziakas, MD, PhD**

*2nd Department of Ophthalmology, Aristotle University of Thessaloniki, Papageorgiou General Hospital, Thessaloniki, Greece*

**ORCID:**

*Argyrios Tzamalis: https://orcid.org/0000-0002-3172-8542*

*J Ophthalmic Vis Res* 2023; 18 (1): 138–140

## Dear Editor,

Since its original description by Chang and Campbell in 2005, intraoperative floppy iris syndrome (IFIS) has been widely established as one of the most challenging conditions for cataract surgeons.[1] Numerous studies have been published proving that the appearance of IFIS significantly increases the risk of intraoperative complications.[2] However, there is no report so far in the literature dealing with the economic impact of IFIS in cataract surgery.

We conducted a retrospective analysis of the medical and financial records of all cases that underwent phacoemulsification surgery in a tertiary-care ophthalmology department during year 2019. Data regarding patient demographics, phacoemulsification metrics, surgical time, complications, and postoperative follow-ups were retrieved from the electronic patient records and the cost of all consumables charged in every case was recorded from the individual billing form that was automatically produced for every surgery. The surgical duration was recorded by an independent theatre nurse in each case. The timer was started upon the first incision and the endpoint was defined as the removal of the surgical drape. The study was performed according to the Tenets of the Declaration of Helsinki after approval of the Institutional Review Board.

In total, 1294 cases of 1178 cataract patients (mean age = 73.8 ± 8.9 years), with ($n$ = 48) or without ($n$ = 1246) a recorded IFIS of any severity, were identified and enrolled in a multivariate analysis. As per our departmental policy, the presence of IFIS was defined and further classified as the intraoperative occurrence of any of the following three signs according to the grading system proposed by Chang and Campbell: progressive miosis; billowing of the iris; iris prolapse through incisions.[3] Patients with one of these three clinical signs were designated as having IFIS. The average cost of surgical consumables charged among all cataract operations was 362.1 ± 90.9 €, while the mean

**Correspondence to:**

Argyrios Tzamalis, MD, PhD, MA, FEBO. 2nd Department of Ophthalmology, Aristotle University of Thessaloniki, Papageorgiou General Hospital, Thessaloniki, 56429 Greece.
E-mail: argyriostzamalis@yahoo.com

Received: 05-12-2021 Accepted: 29-09-2022

Access this article online

**Website:** https://knepublishing.com/index.php/JOVR

**DOI:** 10.18502/jovr.v18i1.12735

This is an open access article distributed under the Creative Commons Attribution License, which permits unrestricted use, distribution, and reproduction in any medium, provided the original work is properly cited.

**How to cite this article:** Tzamalis A, Christou CD, Prousali E, Mataftsi A, Ziakas N. What is the Real Cost of Intraoperative Floppy Iris Syndrome in Cataract Surgery?. J Ophthalmic Vis Res 2023;18:138–140.



© 2023 Tzamalis et al. This is an open access article distributed under the Creative Commons Attribution License | Published by Knowledge E

**Table 1.** Average cost of surgical consumables and surgical duration in all cataract surgeries along with respective comparison between cases with and without IFIS.

| | IFIS (n = 48) | Non-IFIS (n = 1246) |
|---|---|---|
| **Cost of surgical consumables (Euros - €)** | 420.2 ± 146.6 | 359.9 ± 87.5 |
| **Surgical time (min)** | 30.9 ± 23.2 | 21.4 ± 14.8 |
| **Extra cost from surgical consumables per case (Euros - €)** | 60.3 | |
| **Extra cost from prolonged surgical time per case (Euros - €)** | 41.04 | |
| **Total extra cost per case (Euros - €)** | **101.34** | |

*Assessed with Student's *t*-test.
IFIS, intraoperative floppy iris syndrome

**Table 2.** Average cost of surgical consumables and surgical duration in uneventful cataract surgeries along with respective comparison between cases with or without IFIS.

| | IFIS (*n* = 39) | Non-IFIS (*n* = 1199) |
|---|---|---|
| **Cost of surgical consumables (Euros - €)** | 384.2 ± 48.3 | 352.8 ± 47.1 |
| **Surgical time (minutes)** | 23.2 ± 11.6 | 16.7 ± 8.4 |
| **Extra cost from surgical consumables per case (Euros - €)** | 31.4 | |
| **Extra cost from prolonged surgical time per case (Euros - €)** | 28.08 | |
| **Total Extra cost per case (Euros - €)** | **59.48** | |

Assessed with Student's *t*-test.
IFIS, intraoperative floppy iris syndrome

duration of surgery was 21.75 ± 15.1 min (′). No statistically significant differences in cost or surgical time were noted regarding age, gender, medical history, medication intake, or other ophthalmic conditions such as pseudoexfoliation, glaucoma, and cataract grading ($P > 0.05$). Cases that developed IFIS demonstrated a significantly higher cost of surgical consumables (CostIFIS = 420.2 ± 146.6 € vs CostNON-IFIS = 359.9 ± 87.5 €, $P < 0.0001$) as well as a longer duration of surgery (TimeIFIS = 30.9 ± 23.2′ vs TimeNON-IFIS = 21.4 ± 14.8′, $P < 0.0001$) [Table 1]. This difference remained significant even when excluding all complicated cases (4.32% in total; 18.75% in IFIS cases) such as posterior capsular rupture, zonular dehiscence, nucleus drop, and iris trauma [Table 2]. Notably, no pupillary expansion devices were used in any of the cases included in the analysis. The increased cost in cases of IFIS was mainly due to the use of additional consumables such as extra OVDs, dyes, single-use instruments, as well as anterior vitrectomy in complicated cases.

Moreover, we attempted to assess the additional cost that the aforementioned longer duration of surgery had imposed in cases with IFIS. The cost of operating time in cataract surgery has already been evaluated in several cost-effectiveness analyses, ranging from 0.56 to 2.36 €/min (average = 1.21) in European countries[3] and from 8.3 to 11.24 US dollars ($)/min in the United States.[4, 5] The cost per minute of surgical time was evaluated by the departmental accounting officers and found to be 4.32 €/min. It was calculated by dividing the total minutes of all surgeries into their non-supply cost (sum of salaries and wages of all hospital personnel included in cataract surgery) for the single fiscal year of 2019, based on previous reports.[4, 5] Subsequently, the appearance of IFIS imposed an extra cost of 28.08 € per patient as an average in non-complicated surgeries and 41.04 € per patient when all cases were considered. Summing up increased consumables and increased duration resulted in a total extra cost of 59.48 € in uneventful cases and 101.34 € when complicated cases were also included [Tables 1 & 2].

It is of note that the average surgical duration of phacoemulsification in this study was found to be somewhat longer than in other similar studies.

This may be attributed to the fact that our analysis also included cases performed by trainees, who, as expected, required more time to complete the surgery. However, the occurrence of IFIS and the respective intraoperative complications rate did not yield any statistically significant difference between senior surgeons and trainees ($P$ = 0.43 and $P$ = 0.17, respectively).

Further limitations of this study include its retrospective nature that may have had an impact on our results. Although an electronic record is automatically produced for each surgery, it is possible that some cases of mild IFIS may have been ignored or misidentified and consequently, not recorded. Moreover, our study included cases performed by surgeons of various experience levels, and, thus, differences in phacoemulsification techniques and consumables used may have induced some bias. However, all surgeons that participated in the study initially utilized the same phaco technique (divide & conquer) and device (Centurion Vision System, Alcon).

In conclusion, the appearance of IFIS seems to have a substantial economic impact in cataract surgery as it increases the cost of surgical consumables and the time needed to complete the procedure, even in uneventful cases. Cataract surgeons should be aware of cases prone to develop IFIS and they are justified from a financial point of view to use all appropriate measures to prevent and manage floppy iris avoiding extra costs and devastating ocular complications.

## Financial Support and Sponsorship

None.

## Conflicts of Interest

None.

## *REFERENCES*

1. Chang DF, Campbell JR. Intraoperative floppy iris syndrome associated with tamsulosin. *J Cataract Refract Surg* 2005;31:664–673.
2. Enright JM, Karacal H, Tsai LM. Floppy iris syndrome and cataract surgery. *Curr Opin Ophthalmol* 2017;28:29–34.
3. Chang DF, Campbell JR, Colin J, Schweitzer C, Study Surgeon Group. Prospective masked comparison of intraoperative floppy iris syndrome severity with tamsulosin versus alfuzosin. *Ophthalmology* 2014;121:829–834.
4. Fattore G, Torbica A. Cost and reimbursement of cataract surgery in Europe: A cross-country comparison. *Health Econ* 2008;17:S71–S82.
5. Hosler MR, Scott IU, Kunselman AR, Wolford KR, Oltra EZ, Murray WB. Impact of resident participation in cataract surgery on operative time and cost. *Ophthalmology* 2012;119:95–98.
6. Taravella MJ, Davidson R, Erlanger M, Guiton G, Gregory D. Time and cost of teaching cataract surgery. *J Cataract Refract Surg* 2014;40:212–216.